NASA CR 135045

EXPERIMENTAL CLEAN COMBUSTOR PROGRAM

Noise Measurement Addendum

PHASE II FINAL REPORT

by

J.J. Emmerling
K.L. Bekofske

GENERAL ELECTRIC COMPANY

Prepared For

National Aeronautics and Space Administration

NASA-Lewis Research Center

Contract NAS 3-18551

1. Report No.	2. Government Accession No.	3. Recipient's Catalog No.
NASA CR 135045		

4. Title and Subtitle	5. Report Date
Phase II - Experimental Clean Combustor Program - Noise Addendum Final Report	January 1976
	6. Performing Organization Code

7. Author(s)	8. Performing Organization Report No.
J.J. Emmerling K.L. Bekofske	R75AEG147-13
	10. Work Unit No.

9. Performing Organization Name and Address	11. Contract or Grant No.
General Electric Company 1 Jimson Road Cincinnati, Ohio 45215	NAS3-18551
	13. Type of Report and Period Covered
	Contractor Report

12. Sponsoring Agency Name and Address	14. Sponsoring Agency Code
National Aeronautics and Space Administration Washington, D.C. 20546	

15. Supplementary Notes

Project Manager, R.G. Huff, V/STOL and Noise Division
NASA-Lewis Research Center, Cleveland, Ohio

16. Abstract

Combustor noise measurements were performed using wave guide probes. Test results from two full-scale annular combustor configurations in a combustor test rig are presented. A CF6-50 combustor represented a current design and a Double Annular combustor represented the advanced Clean Combustor configuration. The overall acoustic power levels were found to correlate with the steady state heat release rate and inlet temperature. The data taken under Phase I of this program were also found to agree with the correlation.

A theoretical analysis for the attenuation of combustor noise propagating through a turbine was extended from a subsonic relative flow condition to include the case of supersonic flow at the discharge side. The predicted attenuation from this analysis was compared to both engine data and extrapolated component combustor data. The attenuation of combustor noise through the CF6-50 turbine was found to be greater than 14 dB by both the analysis and the data.

17. Key Words (Suggested by Author(s))	18. Distribution Statement
Combustor Noise Turbine Attenuation Clean Combustor Core Engine Noise Noise	Unclassified - Unlimited

19. Security Classif. (of this report)	20. Security Classif. (of this page)	21. No. of Pages	22. Price*
Unclassified	Unclassified	166	

TABLE OF CONTENTS

LIST OF ILLUSTRATIONS

LIST OF ILLUSTRATIONS (Continued)

LIST OF ILLUSTRATIONS (Continued)

LIST OF ILLUSTRATIONS (Continued)

LIST OF ILLUSTRATIONS (Continued)

LIST OF ILLUSTRATIONS (Continued)

LIST OF ILLUSTRATIONS (Concluded)

LIST OF TABLES

SECTION 1.0

SUMMARY

In an examination of component combustor noise data it was found that a sound power level correlation could be arrived at based on the steady state heat release rate and inlet temperature. This correlation is presently valid only for component rig and the configurations tested. Before this correlation can be applied to engine data, the effect of blade row attenuation and exhaust nozzle termination must be defined.

The sound pressure levels and spectral shapes of two combustors were recorded. The CF6-50 was the baseline combustor. This combustor design is currently being used in the CF6-50 engine. The Double Annular Combustor configuration D13 was one of the final clean combustor design configurations tested under Phase II. The two combustors were tested at pressures up to 9.5 atmospheres. Phase I testing was conducted at pressures of 4.8 atmospheres or less. Only configuration D13 was tested at both the higher Phase II pressures and the lower Phase I levels. A combustor noise prediction correlation was arrived at based on this configuration and was found to be in good agreement with the other configurations.

The analysis of noise attenuation due to turbine blade rows was extended to include the supersonic relative flow condition. The predicted attenuation based on this analysis was calculated to be greater than 34dB for the CF6-50. However, this level of attenuation has not been verified by test data. Work in this area has been initiated under NASA contract number NAS3-19435.

SECTION 2.0

INTRODUCTION

Low frequency noise radiating from the core exhaust of gas turbine engines contributes to an engine's overall perceived noise level, particularly at approach. The lower frequency core noise is related to the engine's combustor. In order to predict and possibly reduce combustor noise at the source it was necessary to determine the controlling parameters. This was accomplished utilizing component combustor test data. A relationship was identified which correlated the overall combustor noise power levels to easily determinable aerodynamic and thermodynamic parameters. This empirical relationship may make it possible to extrapolate the noise level for an annular combustor in a component test rig to actual engine conditions. It remains to be seen whether this equation is valid for a combustor installed in an engine.

In calculating the overall noise levels it was assumed that the measured pressure fluctuations in the combustor were dominated by acoustic waves rather than convected disturbances. This assumption was believed to be correct, however it remains to be verified.

The information contained here in Phase II is a continuation of the work presented under Phase I of this program. The purpose of this phase was to 1) measure noise from two combustors, 2) correlate these and the data from Phase I with their respective aerodynamic and thermodynamic parameters and 3) analyze the effect of turbine blade row attenuation. Two combustors were chosen for testing. The CF6-50 was selected as a current design combustor. This permitted data taken from this combustor to be evaluated against farfield noise levels from the CF6-50 engine. The Double Annular configuration D13 was selected as an advanced design clean combustor. The data from this configuration was compared to the current design in order to determine the effect of the design change on the noise.

This report supplies supplemental information to the Experimental Clean Combustor Program Phase II Final Report (Reference 1). The test point data and the corresponding reading numbers in this Noise Addendum and in Reference 1 are the same.

SECTION 3.0

INSTRUMENTATION

Both the aerodynamic and acoustic instrumentation were located at two axial planes in the component combustor test rig (see Figure 1). The upstream location was designated engine station 3.0 which is typically the compressor discharge plane in an engine (see Figure 2). The downstream instrumentation was located directly behind the combustor and was designated engine station 3.9. Reference to a station 4.0 refers to a plane immediately downstream of the combustor where the turbine first stage nozzle would be in an engine.

Acoustic data were taken utilizing waveguide probes and kulite sensors. The upstream acoustic waveguide probe was 50.8 cm long and was located at 45° F.L.A. (Forward Looking Aft) from the top centerline. The downstream acoustic probe sensing holes were located at the combustion exit. For the Double Annular Combustor test a wall static probe 35.56 cm long was located at 84° F.L.A. This probe was flush with the inside of the deflector plate and was axially located in the same plane as the body of the downstream waveguide probe.

The aerodynamic data were taken using standard instrumentation available in the CF6-50 component combustor rig. Information regarding details of the aerodynamic instrumentation of the test facility can be found in Reference 1.

3.1 ACOUSTIC WAVEGUIDE PROBE DESIGN

Due to the high temperature environment of a combustor the acoustic data were acquired through the use of waveguide probes. This permitted the pressure transducers to be located in a relatively lower temperature area. A waveguide probe consisted of a hollow tube with three parts: the sensing end, the transducer, and the infinite or ρc termination. The probe functioned by sensing pressures at the sensing end and permitted the pressure to propagate through the waveguide tube, past the transducer, to be dissipated without reflection in the infinite or ρc termination. The sensing end may be either a wall static pressure tap installed with the end termination flush with a test duct wall, or may extend into the flow in the duct. The probe design whose sensing end extends into the flow from a side wall was bent 90 degrees into the direction of the flow and a bullet nose tip was inserted in it's end. Pressure entered the waveguide through 36 radial holes immediately behind the tip. The sum of the areas of the sensing holes corresponded to the cross sectional area of the waveguide, thereby minimizing any pressure loss due to area changes. From the sensing end the pressure waves passed through the waveguide tube past the transducer. The Kulite transducer was mounted in a compression fitting tee so that the diaphram was essentially flush with the inside wall of the waveguide. The Kulite that was used for recording data was model XGE-1S-375V-200D. Once past the transducer the

Figure 1. Combustor Test Rig Layout.

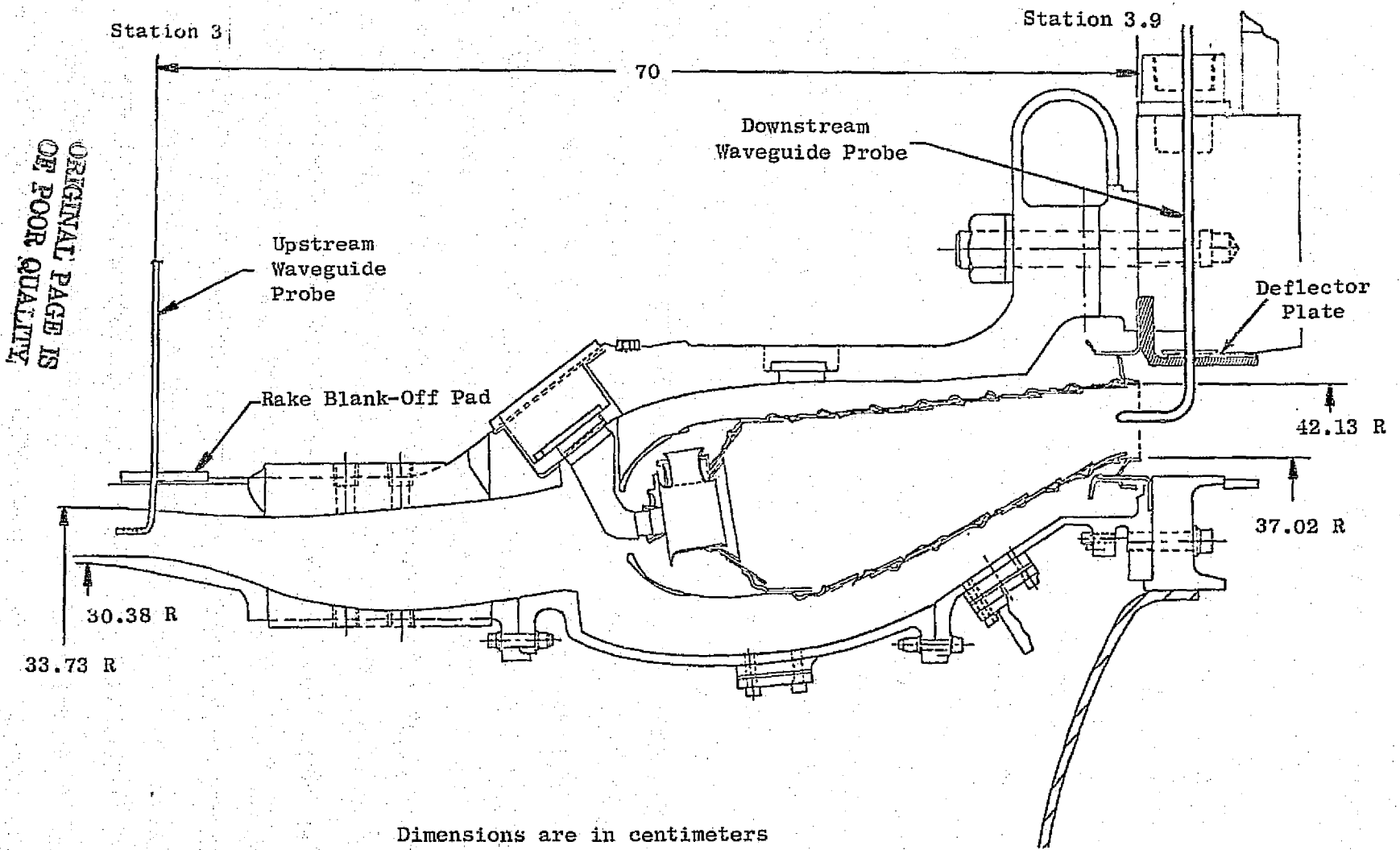

Figure 2. Top-Half Cross Section of Experimental Clean Combustor Test Rig Showing the Acoustic Probe Locations.

pressure waves were dissipated by air viscous loss in a continuation of the waveguide, which was over 12 meters long. This long length of waveguide was called the infinite or ρc termination because waves could not be reflected back from it. Reflected waves had to be eliminated because they would generate standing waves through the waveguide which would generate misleading levels at the transducer.

The waveguides consisted of 6.35 mm diameter tubes with 0.71 mm wall thickness. The upstream probe was made of stainless steel and was capable of operating at temperatures up to 1000° K, pressures up to 200 atmospheres and Mach numbers over 0.5. The downstream probe was sheathed in a water jacket which incorporated tip impingement cooling. Details of the downstream probe are shown in Figure 3. This probe was capable of operating at temperatures over 1600° K, pressures up to 200 atmospheres and Mach numbers of 0.4. In order to meet that condition the cooling water pressure differential through the probe was kept at 6.8 atmospheres. At that pressure the water flow rate was four liters per minute.

3.2 ACOUSTIC WAVEGUIDE PROBE CALIBRATION

The waveguide probe with the water cooled casing was tested in a waveguide probe calibration facility (Figure 4). The calibration consisted of measuring the sound pressure level difference between the probes sensing holes and the transducer end. A small (1.27 mm dia.) reference Kulite was temporarily attached to the probe tip next to the static sensing holes. The location was such that the phase associated with the distance between the sensing holes and the Kulite was less than nine percent of the wavelength at 5000 Hz. The percent of phase difference becomes smaller at lower frequencies. The reference Kulite had a flat response from 20 to over 10,000 Hz. A B&K type 4134 microphone was connected to the probe's transducer end. The probe tip and reference Kulite were then placed in the plane wave tube which was excited at one end by a loudspeaker driver. The speaker was used to generace pure tone levels from 50 to over 5000 Hz. In order to keep a constant sound pressure level at the probe sensing holes, the reference Kulite was connected to a feed back compressor circuit. The signal from both the Kulite and the microphone were filtered with a 20 Hz constant bandwidth filter centered around the speaker driver frequency. The measured difference in level between the two transducers was the probe loss, see Figure 5. The calculated loss also shown on the plot was based on the Iberall method (Ref. 2). It was observed that the measured response and calculated response in general were within one dB. It was therefore concluded that the effect of the small transducer near the sensing holes was negligible. The tabulation of probe attenuations used in correcting the one-third octave band data is listed in Table I.

3.3 EFFECT OF FLOW ON ACOUSTIC PROBES

Since the probes were to be immersed in the combustor flow, a test was conducted in order to evaluate the impact of any probe-generated noise on the measuring transducer. The waveguide probes were mounted in a 12.7 by

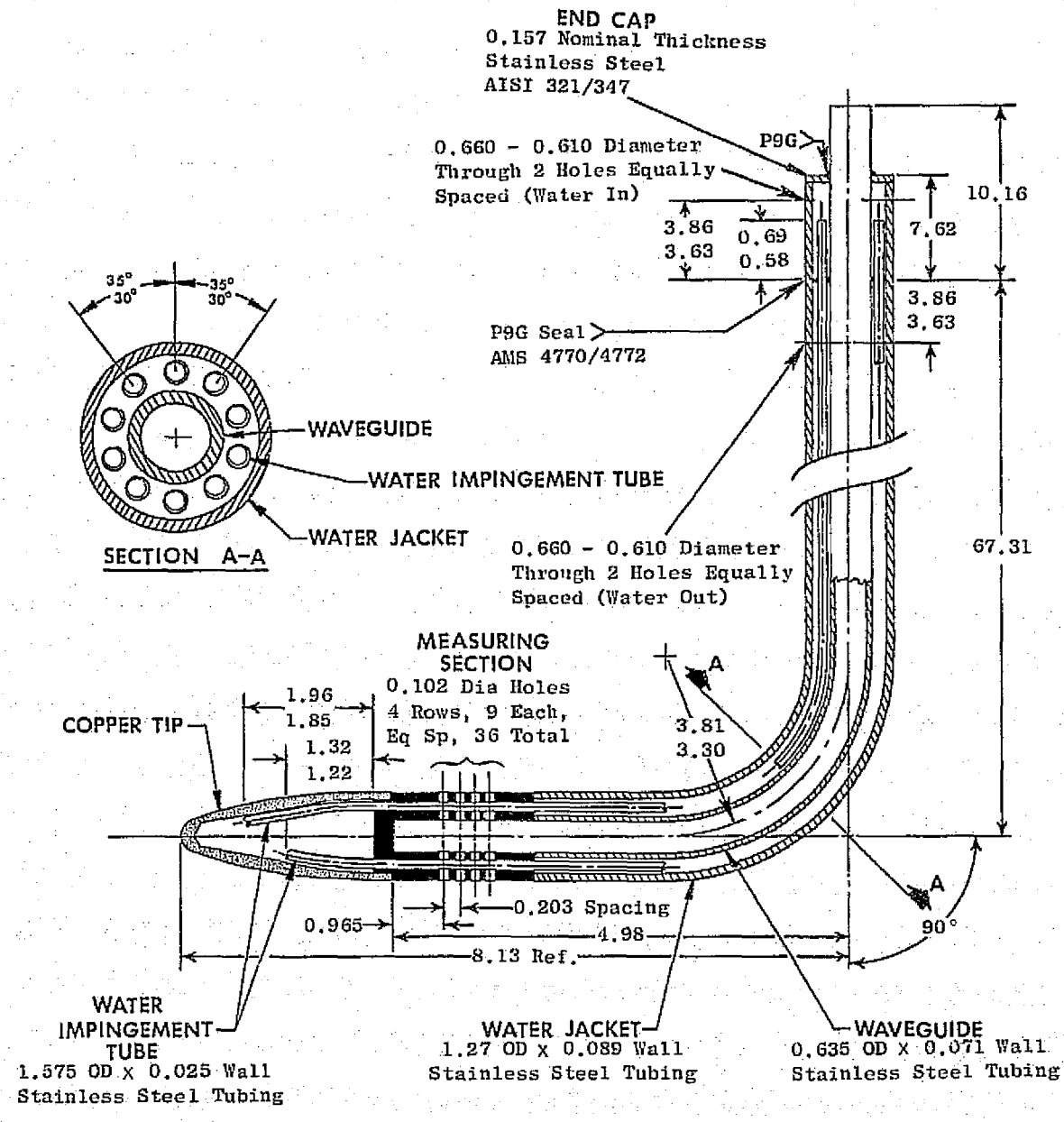

Figure 3. Water Cooled Acoustic Waveguide Probe.

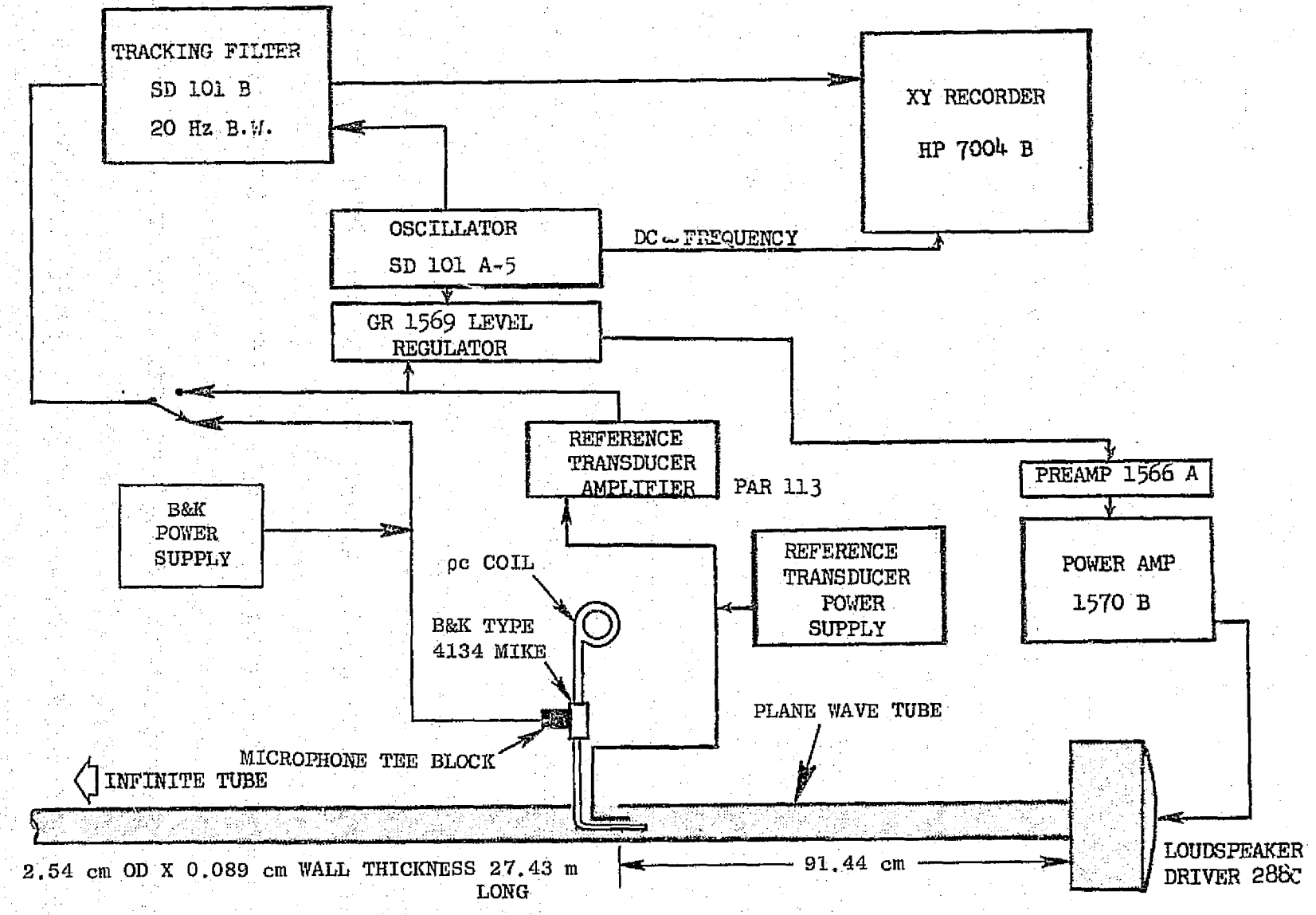

Figure 4. Acoustic Probe Calibration Instrumentation.

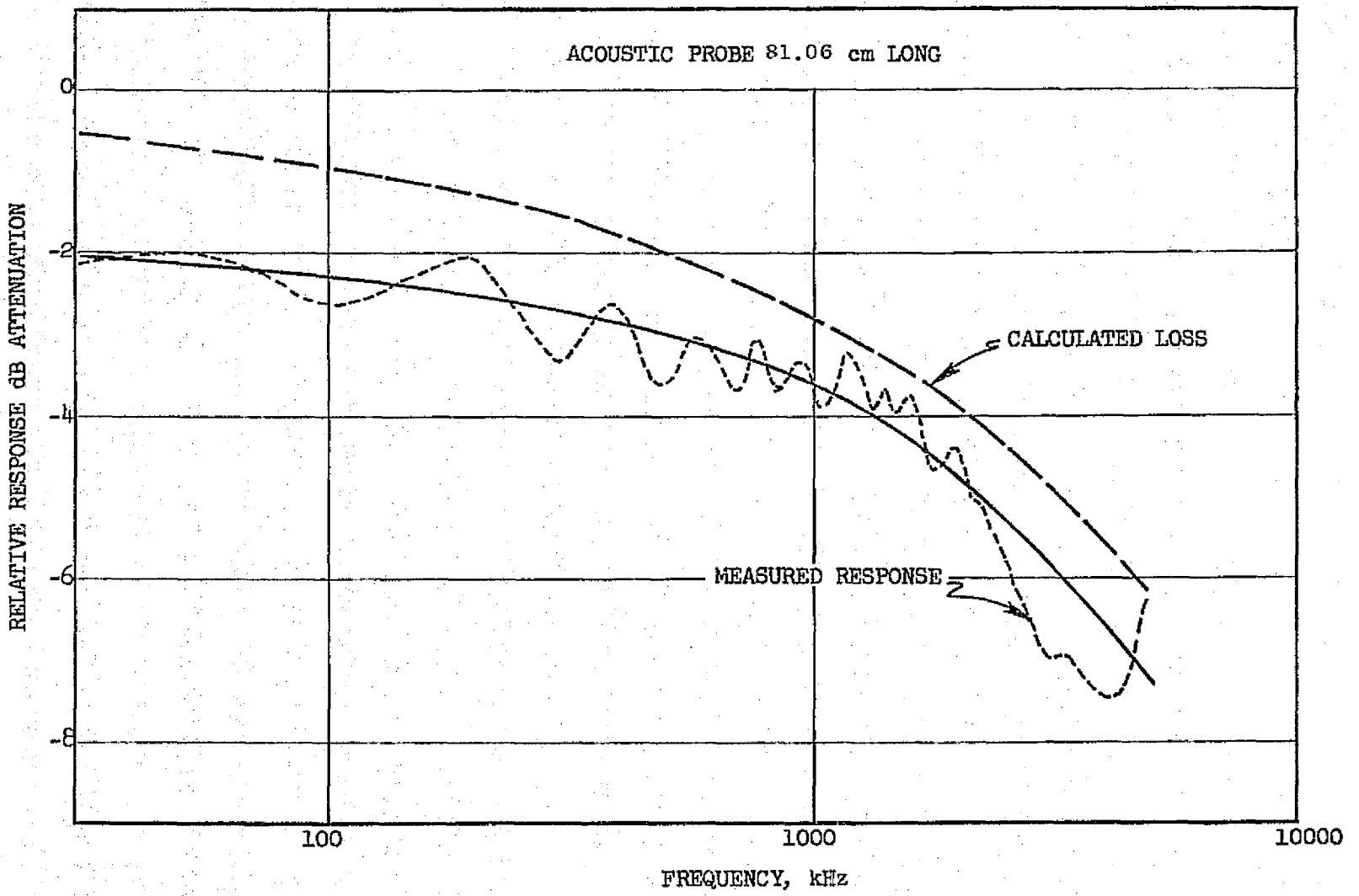

Figure 5. Waveguide Probe Loss Vs. Frequency.

Table I. Tabulation of Waveguide Probe Attenuation.

Frequency	Upstream Waveguide Probe	Downstream Water-Cooled Waveguide Probe	Downstream Wall Static Waveguide
31.5	0.30	2.0	0.21
40	0.34	2.1	0.24
50	0.38	2.1	0.27
63	0.43	2.1	0.30
80	0.48	2.2	0.34
100	0.54	2.3	0.38
125	0.60	2.3	0.42
160	0.68	2.4	0.47
200	0.76	2.5	0.53
250	0.85	2.6	0.60
315	0.96	2.7	0.67
400	1.07	2.9	0.75
500	1.20	3.0	0.84
630	1.35	3.2	0.94
800	1.51	3.4	1.06
1000	1.70	3.6	1.19
1250	1.91	3.9	1.33
1600	2.14	4.3	1.50
2000	2.40	4.8	1.68
2500	2.69	5.3	1.88
3150	3.02	6.0	2.11
4000	3.39	6.7	2.37
5000	3.80	7.3	2.66
6300	4.27	8.3	2.99
8000	4.79	9.2	3.35
10000	5.37	10.3	3.79

Frequency in Hz, Attenuation in dB

6.1 cm duct, which simulated the combustor annulus passage height. The duct had a muffled upstream plenum and three flow-straightening screens, see Figure 6. From the plenum to the duct the flow was accelerated, in order to generate a thin boundary layer. The measured centerline turbulence levels were low, on the order of 1.1%. The noise level of this facility was also low. The overall sound pressure level measured at the wall without the probe installed was 120 dB at a Mach number of 0.3.

The two probes that were used in the combustor noise test were each in turn mounted in the duct. The sound pressure level spectra for each were measured over the range of Mach numbers from 0.1 to 0.3, Figure 7. At the 0.3 Mach number the 1.27 cm diameter downstream probe had an overall sound pressure level of 129.3 dB while the 0.635 cm diameter upstream probe had 132 dB OASPL. The difference in level between the two probes was probably due to the difference in the shape of the probe tips. The flow-generated noise over the probes was on the order of 130 dB, ten dB more than the facility noise. Also, the overall pressure levels measured in the combustor test were all over 145 dB. The measured combustor overall pressure levels were therefore 15 dB or more over probe generated noise levels. It appeared that probe flow noise would not influence the combustor noise measurements.

The effect of water flowing through the passages in the downstream probe water jacket was also tested. Figure 8(a) shows that the effect of the water flowing through the probe was negligible when compared to the water off. The peak level was also very low, less than 80 dB. This test was performed while the probe was still installed in the flow noise duct. A peak in the spectra was observed at 315 Hz, which also occurred in the flow noise spectra. The peak was not, however observed with the wall microphone. Furthermore a test (Volume II of Reference 4) was conducted with nothing in the duct. An average of eight microphones located in the room around the duct and a flow Mach number of 0.3 produced similar peaks, Figure 8(b), at 315 and 2500 Hz which were comparable to Figure 7. The peaks therefore appeared to be standing waves related to the duct.

3.4 THE ACOUSTIC MEASUREMENT SYSTEM

The electrical system (Figure 9) consisted of Kulites connected to low noise Princeton Applied Research amplifiers which fed into a Lockheed wide-band FM tape recorder. The Kulites were Model XCEL-31-13-100D which have a flat frequency response from 20 to over 10,000 Hz. The wall static probe that was used in the Double Annular combustor test as well as the waveguide probes were all operated in this manner.

A backflow purge was used on all of the probes. The purge consisted of connecting the end of the pc termination to a higher static pressure upstream of the combustor. The flow rate was restricted with a 3.18 mm diameter tube, 30.5 cm long. A back pressure of less than 0.9 atmospheres produced less than 24.8 liters per minute air flow for two probes. The peak 1/3-octave levels at this condition was less than 110 dB. This level was considered negligible for this test. The actual pressure across the system

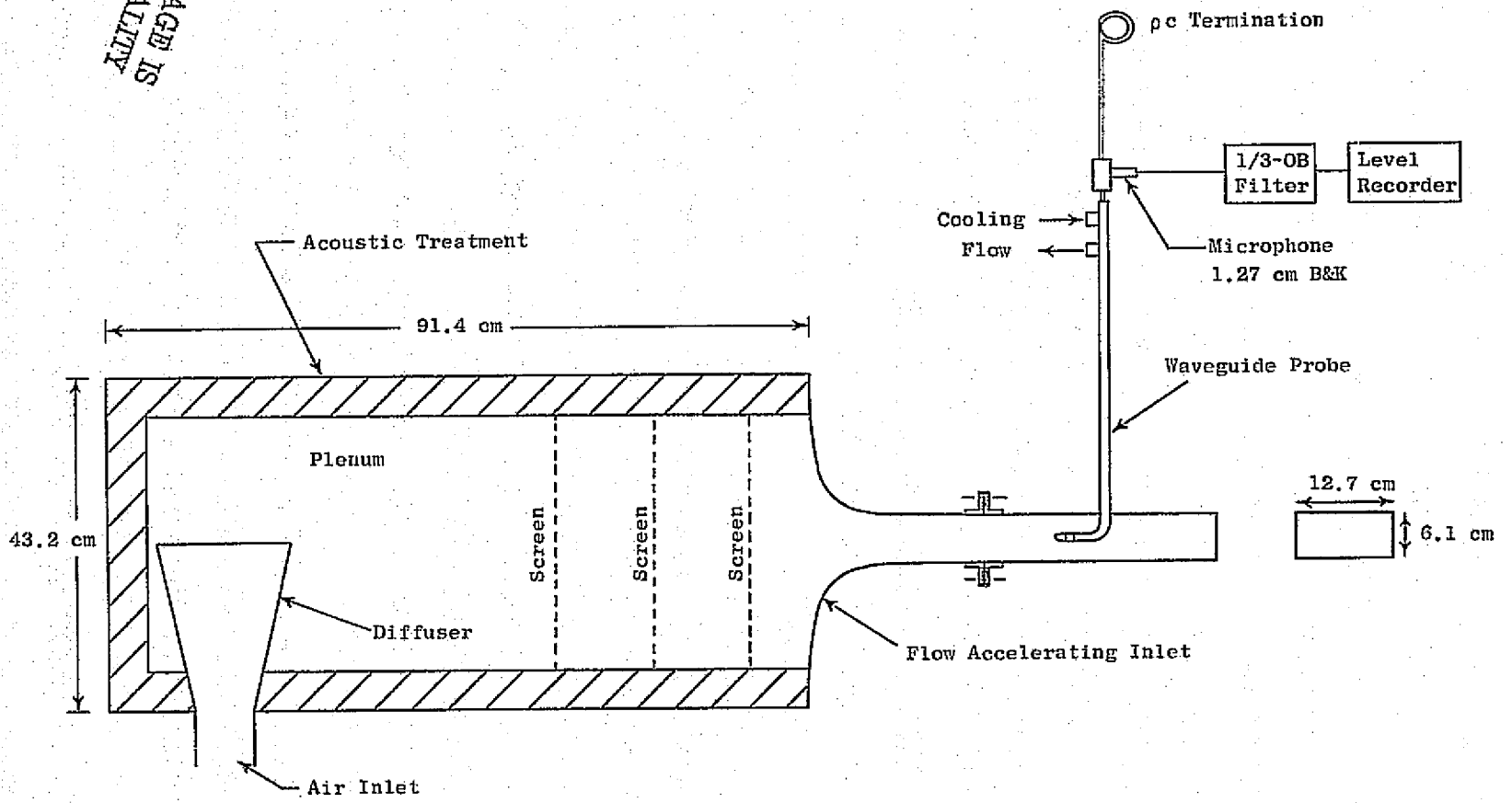

Figure 6. Acoustic Duct Facility for Probe Flow Noise Mesurement.

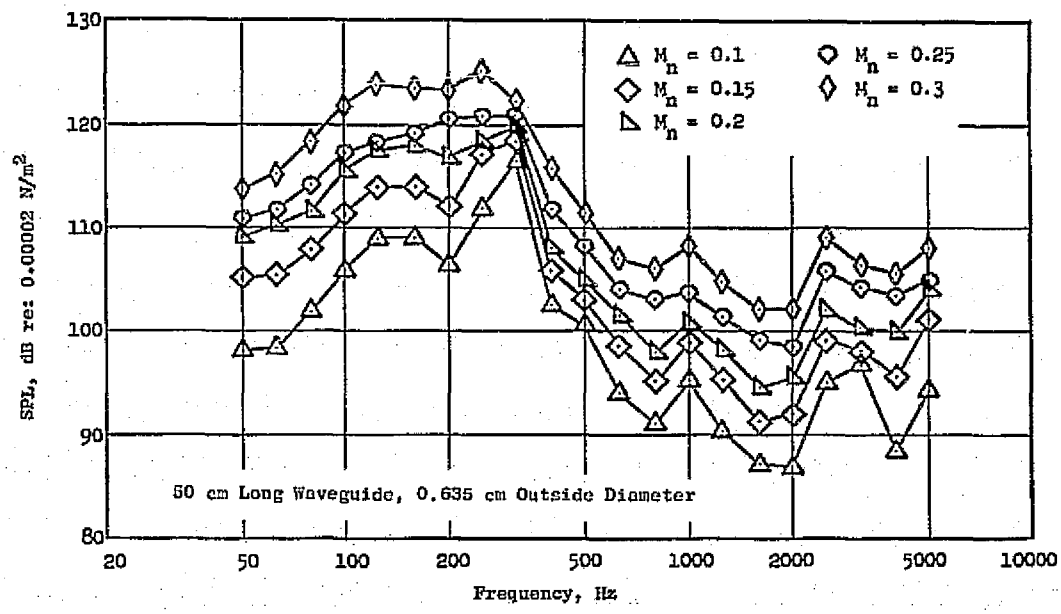

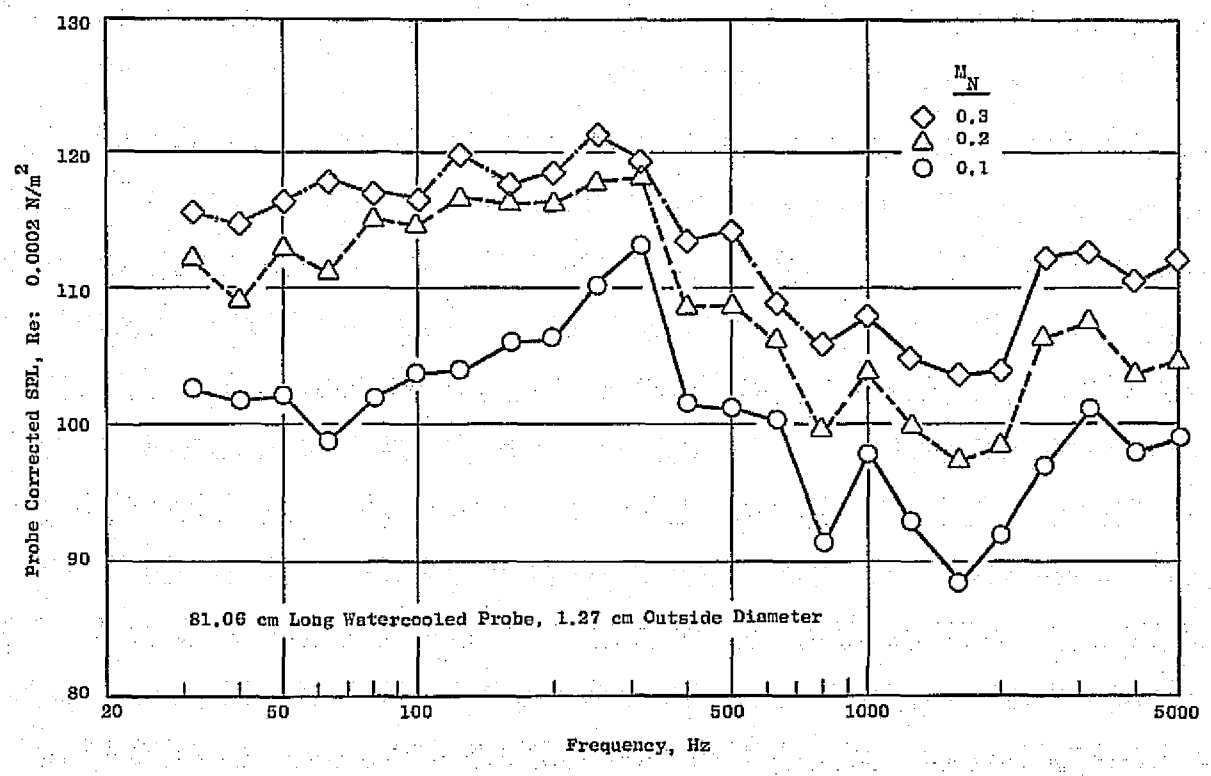

Figure 7. Effect of Air Flow on Probe Measured Levels.

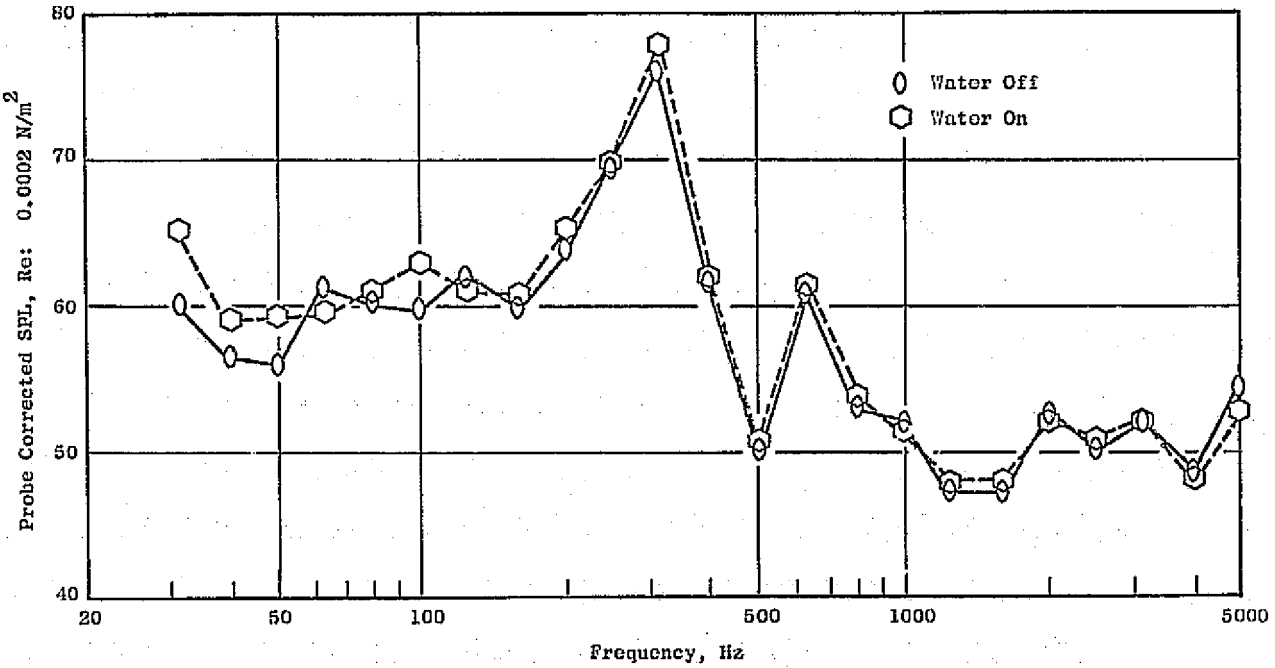

(a) Effect of Cooling Water on the 81.06 cm Probe

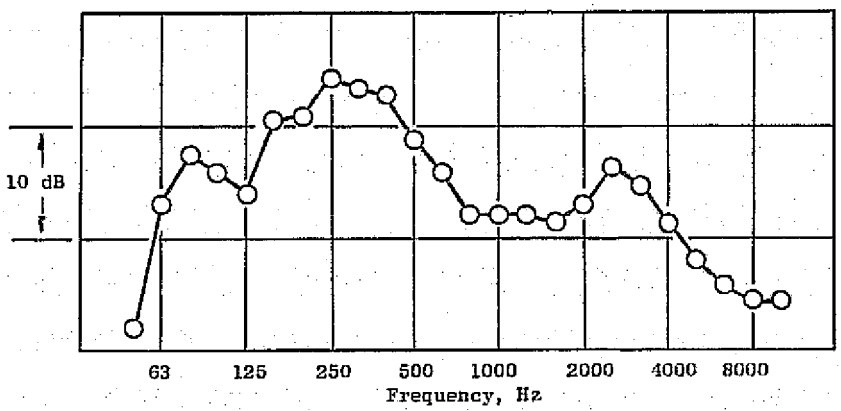

(b) 1/3-Octave Band Spectrum Measured in Room with Duct Mach No. = 0.3

Figure 8. Effects of Cooling Water and Duct Flow.

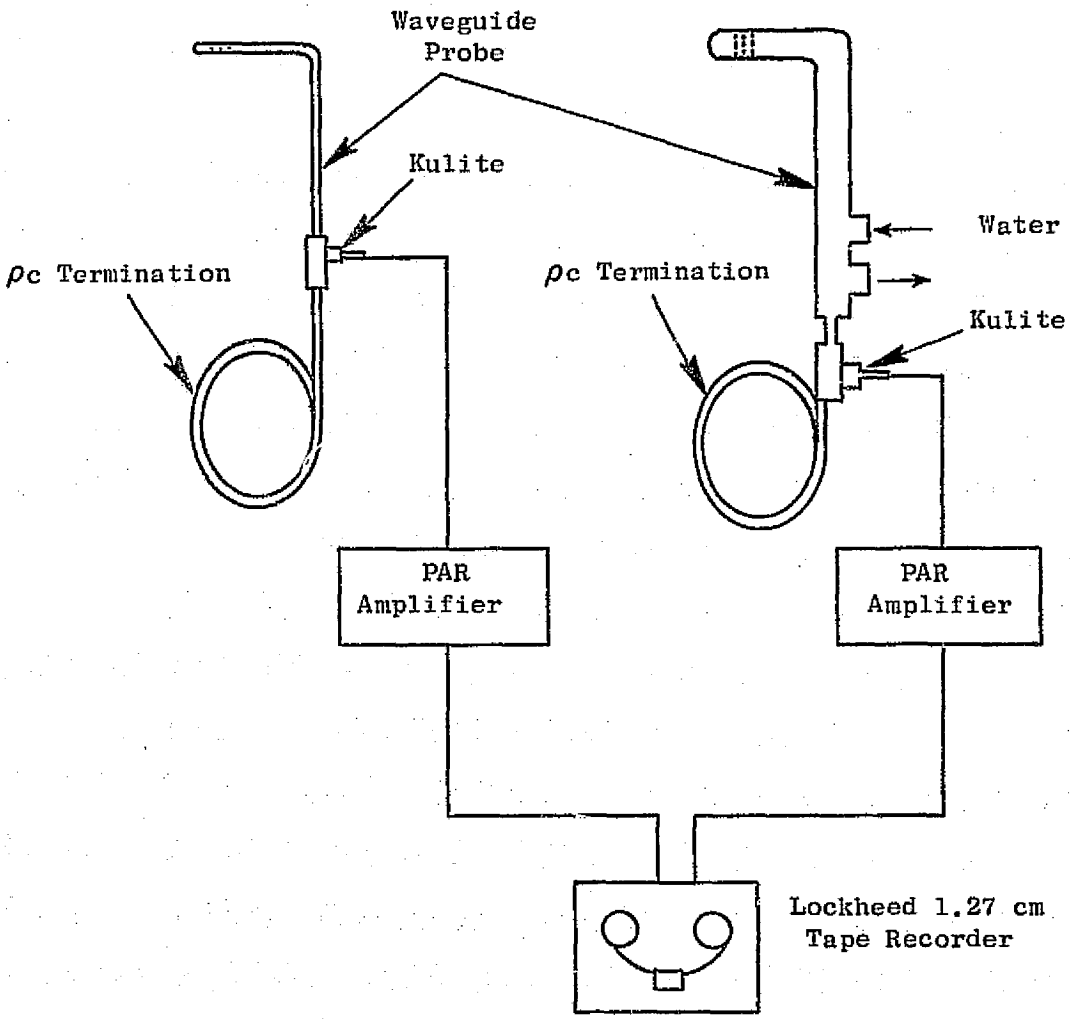

Figure 9. Electrical Schematic.

during the combustor tests varied with air flow rate. However, it did not exceed the 0.9 atmosphere level. Therefore the purge noise levels would be even lower. This system was the same as the one used under Phase I (Reference 3) whose spectral shape and levels can be seen in Figure 10.

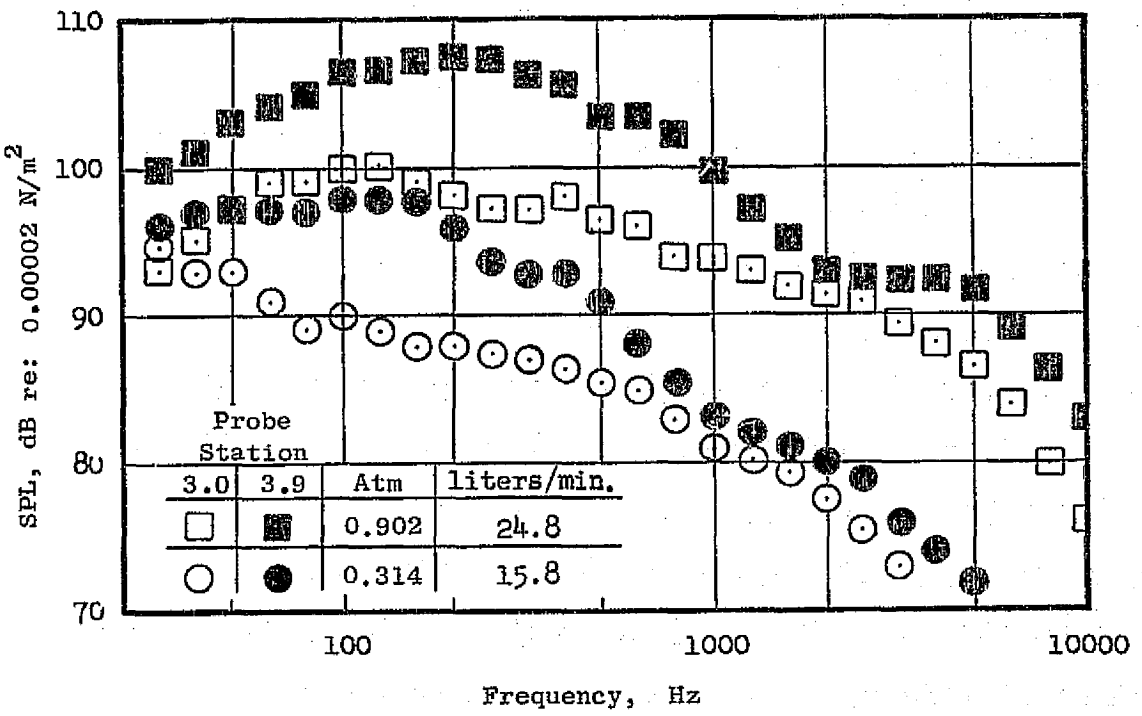

Figure 10. Back Flow Purge Internal Flow Noise Spectrum.

SECTION 4.0

COMBUSTOR DESIGNS

4.1 THE CF6-50 ENGINE

The CF6-50 engine is one of two versions of the CF6 high bypass ratio turbofan engine. The other model, the CF6-6D, is the power plant for the McDonnell-Douglas DC-10 Series 10 Tri-Jet aircraft. The CF6-50 is the higher power version of the two engines and is being utilized in the McDonnell-Douglas DC-10 Series 30 Tri-Jet long range intercontinental aircraft, the Boeing 747, and the Airbus Industrie A300B aircraft. Some of the overall specifications of the CF6-50A engine are:

Weight	3780 kg
Length (cold)	482 cm
Max. Dia. (cold)	272 cm
Fan/Comp. Stages	1-(3)/14
HPT/LPT Stages	2/4
Thrust/Weight	5.95
Pressure Ratio	30:1
Airflow	660 kg/s
Max. SLS Thrust	218 kN
SFC	0.389
Cruise Mach Number/Alt	0.85/10.5 km
Thrust	48 kN
SFC	0.654
Bypass Weight flow Ratio (Fan/Core)	4.1

The smoke emission levels of this engine are low and virtually invisible at all operating conditions. The favorable fuel economy and high thrust-to-weight ratio made this engine an attractive selection as a baseline vehicle.

4.2 CF6-50 COMBUSTOR

The CF6-50 combustor is a high performance combustor incorporating a low pressure loss step diffuser, carbureting swirl-cup-dome design and a short burning length. The step diffuser has a pressure loss of about one percent of the total pressure and does not vary significantly over the engine cycle. These features have made it possible for this combustor to have low smoke emissions and high combustion efficiency at all operating conditions, a low pressure loss, and low exit temperature pattern factors. The design of the step diffuser provides a uniform, steady airflow distribution into the combustor. Its shorter burning length which requires less liner cooling air improves the exit temperature pattern factor and profile.

The flow at the compressor discharge plane has a Mach number of 0.27. This high velocity flow is diffused in a relatively long, area-rule prediffuser with an area ratio of 2.0. The top half cross section, Figure 11(a), illustrates the combustion system layout. The production CF6-50 combustor incorporates 30 vortex-inducing axial swirler cups, one for each of its corresponding fuel nozzles.

The air that flowed through the prediffuser passage was $\dot{W}_3$. The air which passed through the combustor exit was $\dot{W}_c$. The difference between the two was the simulated turbine bleed air. Past the prediffuser passage the air flow was split into three streams, outer, center and inner. The combustion air flow $\dot{W}_c$ entered the combustion zone through either swirl cups, dilution holes, or film cooling slots. The outer and inner flow streams were smoothly accelerated around the combustor cowling and entered the combustion zone through the outer and inner liner passages which consisted of holes and slots. Thirty percent of $\dot{W}_c$ was liner cooling flow which centered the combustion reaction zone through film slots. The center stream flowed into the combustor primary zone through the dome cowling to the swirl cups. The cowling opening was oversized and provided free-stream diffusion of the dome flow. This resulted in higher pressure recovery in the center stream. The higher pressure recovery generated higher pressure drops across the dome and therefore higher velocities through the swirl cups and other dome flow openings.

The combustion process of chemically reacting a liquid fuel with air, for heat release, is by nature nonhomogeneous. The local fuel-air ratio will be a function of the location in the combustor. When the fuel enters the primary zone close to the swirl cups, the fuel-air ratio is close to stoichiometric and decreases from that value as you travel axially down the combustor. The dillution holes and film cooling slots dilute the primary zone mixture, and to an extent react with it. Figure 11(b) shows the details of the air flow splits. It may be useful to determine this spatial function of the fuel-air ratio in order to assess its effect on the noise. However, in order to simplify this study of combustor noise, the fuel-air ratio that passed through the combustor exit was used.

Relevant design parameters for the CF6-50 combustor are shown in Table II. The space rate listed in the table is the heat released in the combustor. It is defined as the actual heat release, in joules per hour, divided by the product of the total enclosed combustor volume down to Station 4 (in cubic meters) and the burner total pressure in atmospheres.

$$\text{Space rate} = \frac{\text{heat release}}{\text{volume} \times \text{pressure}}$$

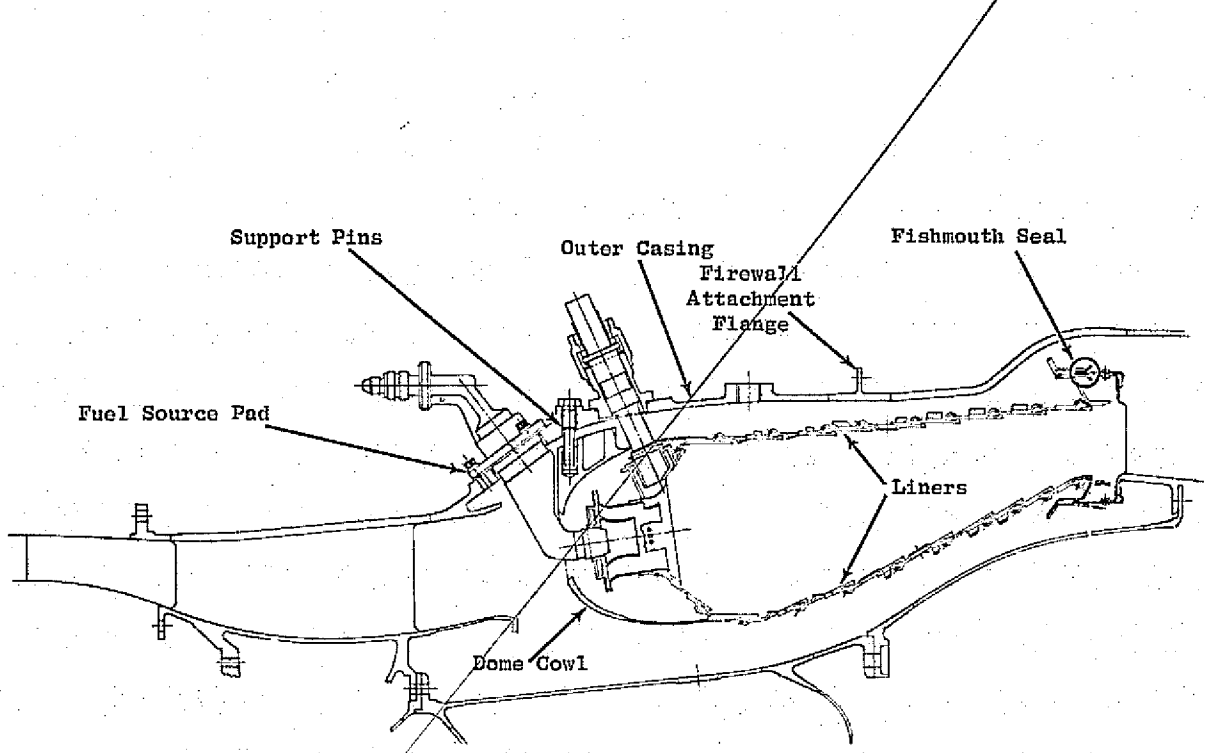

(a) CF6-50 Combustor Mechanical Design Features

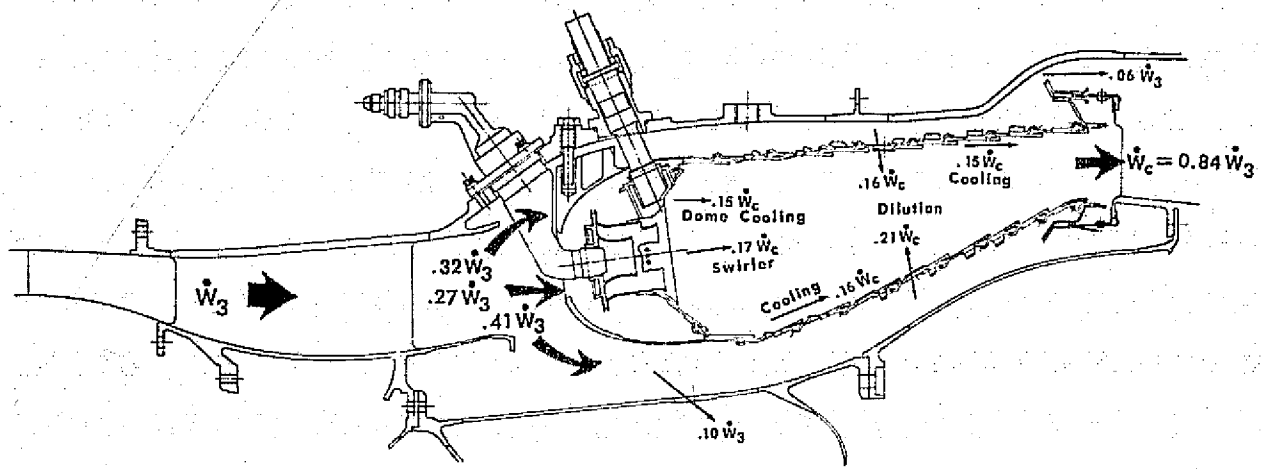

(b) CF6-50 Combustor Air Flow Paths

Figure 11. CF6-50 Combustor Design Features.

Table II. CF6-50 Combustor Design Parameters.

Combustor Airflow ($\dot{W}_c$)	103.42 kg/s
Compressor Exit Mach Number	0.27
Overall System Length	75.95 cm
Burning Length (L_B)	34.8 cm
Dome Height (H_D)	11.43 cm
L_B/H_D	3.0
Reference Velocity	25.9 m/s
Reference Area	3729 cm^2
Space Rate	2.2×10^{11} J/hr-m^3-atm
$\Delta P_T/P_{T_3}$	4.3% (Total)
Number of Fuel Nozzles	30
Fuel Nozzle Spacing (B)	6.91 cm
L_B/B	5.0
B/H_D	0.60

4.3 DOUBLE ANNULAR COMBUSTOR

The general arrangement of the Double Annular Combustor design approach is shown in Figures 12 and 13 and its geometric parameters are tabulated in Table III. The dome assembly consisted of two annular spectacle plates separated by a small centerbody. Assembled in the spectacle plates was an array of 60 air swirlers (30 in each annulus). The air swirler components consisted of a primary air swirler/venturi casting, a counter-rotating secondary air swirler, a flameshield and a retainer ring. The air swirler assemblies were attached to the dome spectacle plates with a radial slip joint arrangement to accommodate mechanical stack-up and thermal growth between the fuel injectors and the combustor assembly. The flameshields were impingement cooled. The centerbody and dome panels were film cooled using wiggle strip construction.

The cooling liners were modified production CF6-50 liners. The cooling flow metering hole areas were reduced and the dilution holes were modified, Figure 14.

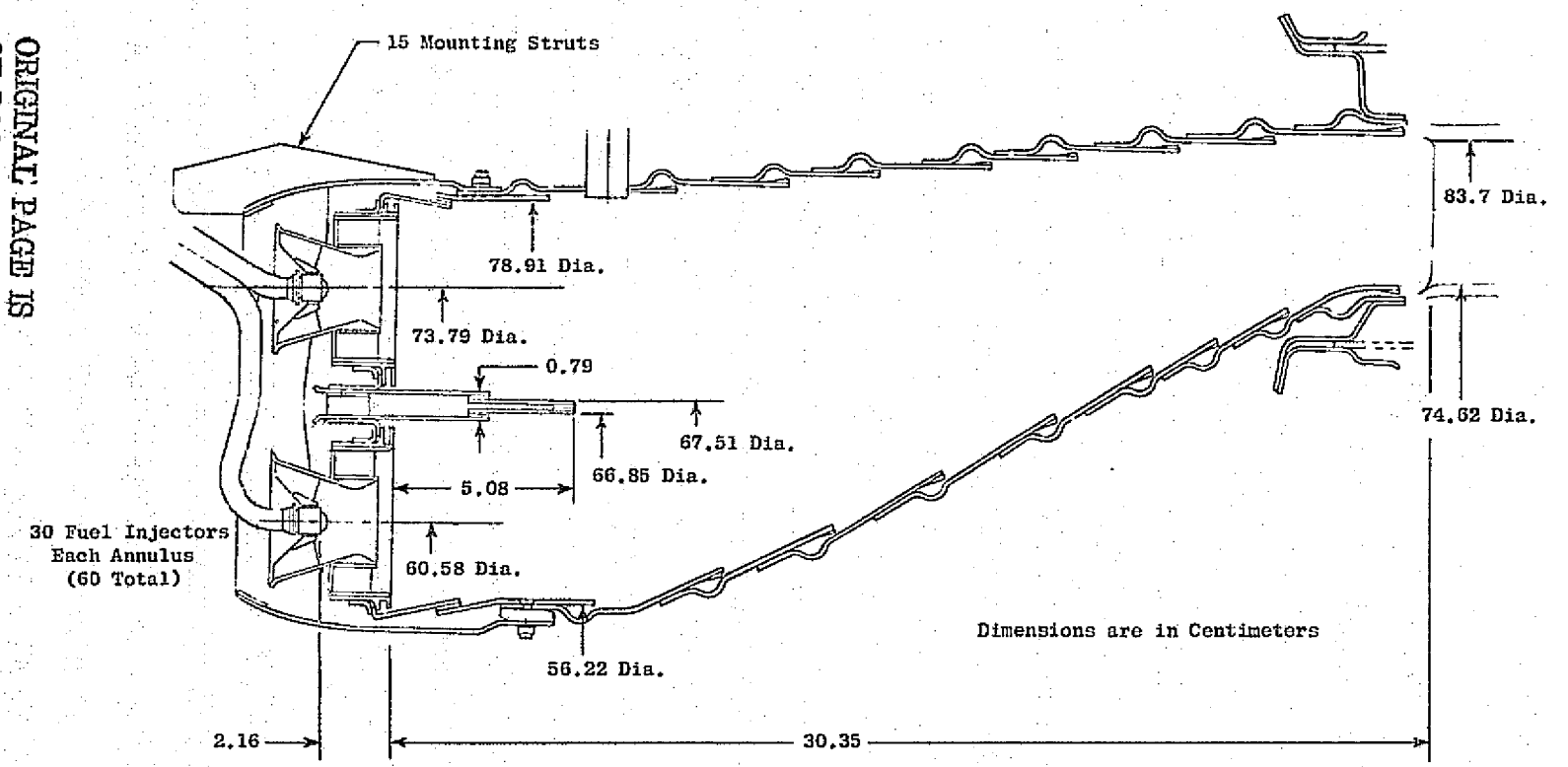

Figure 12. General Arrangement, Double Annular Combustor.

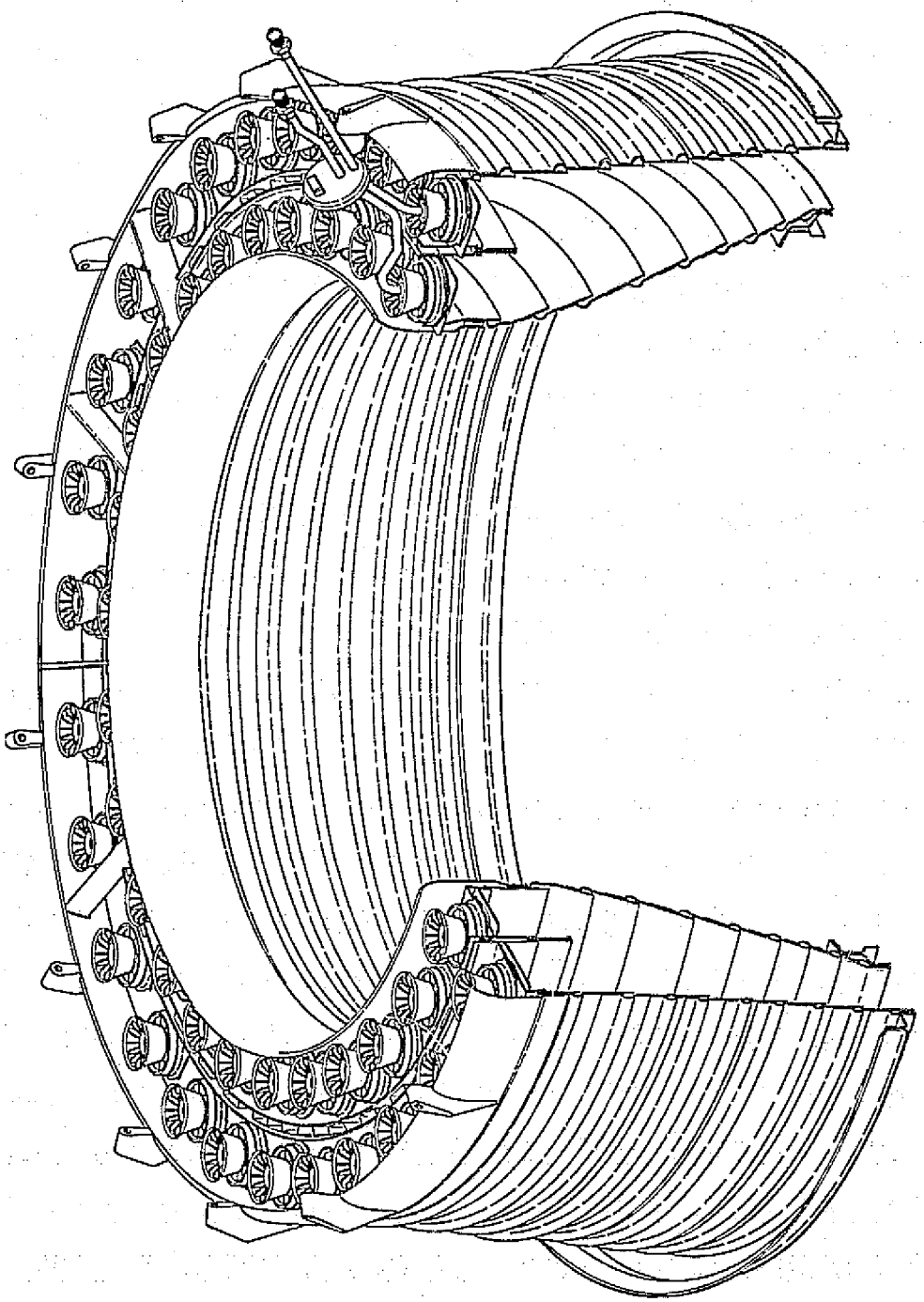

Figure 13. Double Annular Combustor.

Table III. Geometric Design Parameters, Double-Annular Combustor.

		Outer Annulus	Inner Annulus	Overall
Dome Height (1)	cm	5.69	5.33	11.35
Burning Length	cm	5.08(2)	5.08(2)	30.35
Fuel Injector Spacing	cm	7.73	6.34	-
Area(1)	cm^2	1311	1028	2409
Volume	cm^3	6541(2)	5097(2)	54,991

(1) at trailing edge of centerbody

(2) from flameshields to trailing edge of centerbody

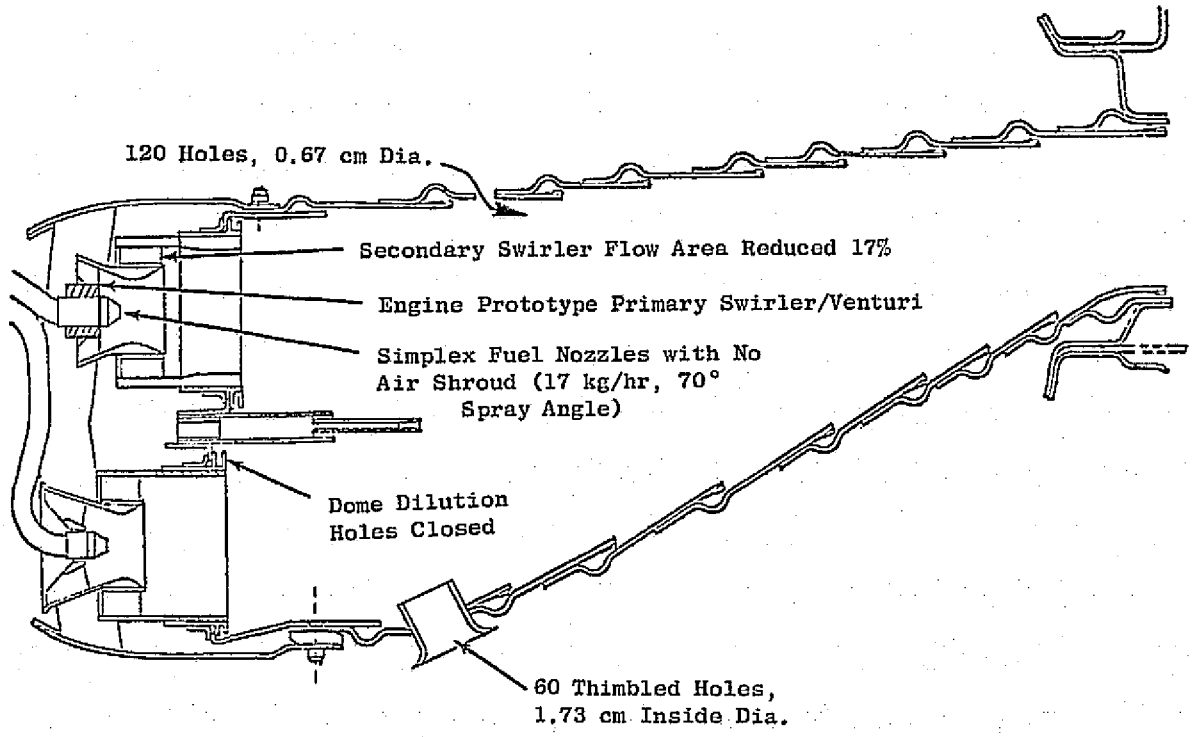

Figure 14. Details of Double Annular Combustor D13.

SECTION 5.0

EXPERIMENTAL RESULTS

The results presented here consist of tables of the aerodynamic data and one-third octave band sound pressure levels. Plots of the sound pressure spectra are also presented.

5.1 AERODYNAMIC DATA

The aerodynamic data consist of the fuel-air ratio, total and static pressures and total temperatures at both upstream and downstream locations in the combustor, the air and fuel flow rates and the fuel temperature for each reading number. A total of eight data points were recorded for the CF6-50 combustor, four fuel-air ratios at both the approach and takeoff inlet conditions. The dry loss, zero fuel air ratio test points could not be taken due to a cokeing problem with the fuel nozzles. A low fuel air ratio was substituted. The aerodynamic data are listed in Table IV. The combustor pressure levels were higher than those tested under Phase I. Thus a one to one comparison of this combustor to any of the Phase I configurations is not recommended.

The Double Annular aerodynamic data are listed in Table V. A total of eighteen data points were recorded encompassing approach and takeoff inlet conditions comparable to those taken for both the CF6-50 and the Phase I combustors. The 3.4 and 4.7 atm pressures correspond to Phase I approach and takeoff while the 6.8 and 9.5 atm pressures correspond to the CF6-50 Phase II approach and takeoff pressures respectively. The aerodynamic data listed in Table V are presented in terms of successive reading numbers with the exception of readings 748 and 699. Those two readings were included in their group of similar inlet conditions. This order is maintained consistent through the reporting of the acoustic data-tabulations and their plots.

5.2 ACOUSTIC DATA

The one-third octave band sound pressure levels from 31.5 to 10,000 Hz and the calculated overall sound pressure level based on that spectrum are listed in Tables VI and VII for the CF6-50 and Double Annular combustors respectively. All of the levels have been corrected for probe losses. The notation U, indicates the upstream probe, D the downstream probe and the subscript W indicates the wall static probe.

During the Double Annular combustor test it was not possible to get data from the upstream probe for all of the readings. However, data taken with a wall static probe at the downstream location have been substituted. Reliable data from the upstream probe were obtained for readings 748, 723, 726, 727 and 728. The CF6-50 combustor noise spectra are plotted on Figures 15 to 22. The Double Annular combustor were plotted on Figures 23 to 45.

Table IV. CF6-50 Aerodynamic Data.

RDG.	f/a	(atm.)				(kgm/sec)	(Kgm/hr)	(° K)		
		P_{T3}	P_{S3}	$P_{T3.9}$	$P_{S3.9}$	W_c	W_f	T_{T3}	$T_{T3.9}$	T_{fuel}
317	.0141	6.87	6.41	6.45	6.29	29.9	1521	661	1174	295
318	.0169	6.80	6.40	6.43	6.27	30.4	1852	659	1266	295
319	.0197	6.87	6.48	6.51	6.33	30.6	2171	659	1358	295
320	.0240	7.28	6.86	6.88	6.71	30.2	2607	659	1489	294
321	.0229	9.59	9.11	9.16	9.00	33.1	2733	811	1583	294
322	.0199	9.53	9.10	9.15	9.00	33.0	2361	818	1496	295
323	.0169	9.59	9.11	9.15	9.01	32.9	1999	819	1402	295
324	.0138	9.53	9.09	9.14	9.00	33.2	1651	819	1304	296

Table V. Double Annular, D-13, Aerodynamic Data.

RDG.	f/a	(atm.)				(kgm/sec)	(kgm/hr)	(°K)		
		P_{T3}	P_{S3}	$P_{T3.9}$	$P_{S3.9}$	W_c	W_f	T_{T3}	$T_{T3.9}$	T_F
705	.0118	6.84	6.50	6.48	6.37	28.0	1186	627	1064	304
706	.0098	6.82	6.48	6.46	6.36	28.0	997	627	995	304
707	.0078	6.83	6.48	6.48	6.38	28.1	791	627	924	304
708	.0059	6.84	6.50	6.48	6.39	27.9	590	627	852	304
709	.0136	4.84	4.60	4.59	4.52	17.0	833	816	1291	302
710	.0170	4.77	4.54	4.52	4.45	16.6	1017	815	1401	301
711	.0200	4.77	4.55	4.51	4.43	16.6	1195	821	1502	301
748	.0234	4.72	4.51	4.47	4.38	16.5	1387	820	1604	302
712	.0140	3.45	3.29	3.28	3.22	13.9	701	630	1139	302
713	.0122	3.43	3.26	3.26	3.21	13.7	602	629	1077	301
714	.0101	3.44	3.28	3.27	3.22	13.8	499	628	1004	301
715	.0081	3.43	3.27	3.25	3.20	13.8	401	632	937	301
716	.0061	3.42	3.26	3.25	3.20	13.8	304	631	865	301
699	.0229	9.55	9.09	9.05	8.88	33.4	2752	819	1587	303
723	.0230	9.53	9.07	9.01	8.84	33.3	2756	816	1589	304
726	.0199	9.55	9.14	9.04	8.88	33.1	2373	820	1499	304
727	.0170	9.54	9.07	9.04	8.89	33.1	2021	820	1405	304
728	.0140	9.53	9.07	9.02	8.88	33.1	1667	820	1306	303

Table VI. One-Third Octave Band Sound Pressure Levels, CF6-50 Combustor.

Rdg.	317		318		319		320		321		322		323		324	
Probe	U	D	U	D	U	D	U	D	U	D	U	D	U	D	U	D
Frequency																
31.5	131.3	131.5	131.0	133.0	131.0	133.3	130.3	133.3	132.5	135.5	132.9	135.3	132.0	135.0	132.3	135.5
40	130.4	131.2	130.4	131.7	130.4	132.0	129.9	132.2	132.9	135.5	132.1	135.5	132.4	136.0	132.1	135.7
50	130.8	132.1	130.8	133.1	130.8	132.1	129.8	132.9	133.5	137.4	133.0	137.6	133.3	137.9	133.0	137.4
63	130.8	133.1	130.8	134.4	131.0	134.1	131.3	135.4	134.0	140.4	133.5	138.9	133.3	138.9	133.5	138.1
80	130.9	134.6	131.1	134.6	131.1	134.6	130.6	135.3	132.4	139.8	132.4	138.1	131.9	138.6	131.9	137.3
100	132.9	135.2	133.1	135.7	133.4	135.9	132.4	136.7	133.9	139.4	133.1	137.7	133.4	137.9	133.4	137.2
125	135.8	136.0	135.8	135.3	135.8	134.5	135.3	135.3	137.5	137.0	137.8	136.3	137.8	136.0	137.8	136.8
160	135.0	138.3	135.0	138.0	135.2	138.3	135.0	138.5	134.5	138.5	134.7	137.5	134.7	138.0	135.0	138.5
200	137.0	138.3	136.7	137.3	136.7	136.8	136.0	137.0	138.0	136.8	138.2	136.0	138.2	135.5	138.0	136.0
250	134.6	139.1	134.1	138.1	133.9	137.9	134.6	137.9	134.6	138.1	134.6	137.6	134.6	137.6	134.1	137.1
315	140.5	140.8	139.8	139.0	140.0	138.5	140.3	140.0	139.5	140.0	138.3	138.5	138.3	138.3	138.0	138.3
400	146.1	146.3	146.6	146.5	146.1	145.5	149.1	149.3	146.1	143.8	145.3	143.0	145.3	142.8	145.1	143.3
500	152.0	151.7	152.5	153.2	152.5	153.0	157.3	158.0	151.3	149.5	152.3	148.7	152.0	148.7	152.3	148.2
630	151.0	149.7	151.2	150.2	150.5	150.4	148.7	148.7	148.7	148.2	148.0	146.4	147.7	146.7	147.2	146.4
800	151.8	149.4	152.5	149.6	151.8	148.1	149.5	147.1	153.3	149.9	153.0	148.1	153.0	148.4	152.5	148.4
1000	148.0	147.6	148.0	147.3	148.5	147.1	148.2	147.1	151.7	149.1	150.7	147.3	151.0	147.3	150.5	147.3
1250	145.0	149.4	144.6	149.1	145.0	149.1	145.5	148.4	150.3	150.1	149.8	148.9	149.5	149.1	149.5	149.1
1600	142.8	147.1	142.8	147.6	142.8	147.4	144.1	145.9	144.1	147.4	143.1	146.4	143.1	146.4	142.8	146.1
2000	140.4	146.0	141.1	145.8	140.4	144.5	141.6	143.3	143.4	145.8	142.1	145.0	142.4	145.5	141.9	145.5
2500	137.0	145.7	137.8	145.7	137.0	144.7	138.8	143.2	140.5	146.9	139.0	145.9	138.8	146.2	138.8	146.4
3150	136.2	144.0	136.4	144.0	136.2	143.2	135.9	141.7	138.9	146.0	137.9	145.5	137.4	145.7	138.2	146.2
4000	134.1	141.7	134.1	142.0	133.9	141.2	132.9	140.0	137.6	143.5	138.1	142.7	138.1	142.7	138.9	144.2
5000	129.6	140.1	129.6	140.3	129.8	139.8	129.3	139.1	133.3	143.3	134.0	141.3	134.0	141.8	134.8	142.1
6300	121.8	133.2	122.8	133.7	122.8	133.5	122.8	132.2	126.3	136.7	126.8	133.5	126.1	134.0	126.8	133.2
8000	114.9	126.2	115.1	126.7	115.1	125.4	116.6	125.2	119.6	129.0	118.4	124.9	117.9	125.7	118.1	125.4
10000	108.1	121.2	109.9	120.7	108.9	119.2	112.1	119.4	113.6	123.9	113.4	119.2	112.6	119.2	113.1	120.7
OASPL	158.1	161.4	158.5	159.1	158.2	158.7	159.9	160.5	159.2	158.8	158.9	157.6	158.8	157.8	158.6	157.8

Table VII. One-Third Octave Band Sound Pressure Levels, Double Annular Configuration D13.

RDG.	705		706		707		708		709		710	
Probe	D	Dw	D	Dw	D	Dw	D	Dw	D	Dw	D	Dw
Frequency												
31.5	137.3	135.5	137.6	135.2	137.6	135.2	138.1	135.5	136.1	132.5	135.8	133.0
40	139.3	134.6	139.8	134.6	140.0	135.1	139.5	135.3	139.0	133.6	138.3	136.8
50	140.7	140.3	141.2	140.1	141.7	140.1	140.7	139.8	139.7	136.1	139.5	137.6
63	142.2	137.8	141.9	137.5	141.7	137.3	140.4	137.3	139.4	133.0	139.7	137.8
80	140.9	138.4	140.6	137.9	141.1	137.4	139.9	137.4	139.4	132.2	138.4	139.7
100	139.0	135.3	139.5	135.5	139.0	135.0	138.8	135.3	139.0	132.3	136.5	137.0
125	139.1	135.4	139.6	135.4	139.1	134.9	137.1	135.6	136.8	132.9	136.1	136.4
160	138.1	135.9	137.9	135.4	137.1	134.6	136.6	134.6	134.1	133.9	134.4	136.6
200	138.8	137.3	138.3	136.8	137.3	135.5	136.6	137.0	133.6	134.8	134.1	138.0
250	138.9	137.6	137.9	137.4	136.2	135.9	135.4	136.9	133.9	135.9	135.2	138.9
315	140.5	138.9	140.3	138.4	139.0	136.7	137.5	137.2	136.8	135.7	137.0	139.7
400	144.1	141.4	145.4	141.4	142.4	139.1	140.6	138.9	139.6	136.6	141.1	140.9
500	144.6	143.6	147.1	145.9	144.1	143.9	140.1	141.4	137.6	138.9	140.6	142.9
630	148.2	144.1	151.7	146.6	154.2	147.1	146.2	142.4	143.0	139.9	142.5	144.1
800	146.2	145.6	147.5	145.8	150.5	147.8	146.7	145.8	142.5	142.3	143.2	145.1
1000	148.4	145.4	148.6	146.1	148.1	145.1	147.1	145.1	143.9	140.6	144.1	143.6
1250	147.2	143.3	149.0	145.6	148.0	145.1	144.2	143.1	143.2	141.1	145.2	143.8
1600	145.5	143.6	146.2	145.4	147.2	146.1	144.0	144.9	142.7	141.6	143.0	143.6
2000	145.8	141.9	147.6	143.1	149.1	143.9	146.3	141.9	142.3	141.6	142.3	142.9
2500	146.3	139.5	148.8	140.0	149.8	141.3	147.0	140.0	143.3	139.8	143.5	141.3
3150	145.5	137.8	147.0	140.6	149.3	143.3	147.8	143.6	145.0	140.1	145.5	140.6
4000	141.3	134.6	144.0	137.1	146.5	138.9	146.5	141.4	146.5	141.9	146.3	141.9
5000	138.2	130.7	139.4	131.5	141.7	131.7	141.4	134.0	147.2	139.2	147.7	139.7
6300	135.6	129.7	135.6	130.7	136.6	129.5	135.1	130.0	142.9	130.2	143.4	134.7
8000	137.1	130.0	137.1	130.5	138.4	129.7	135.9	129.7	139.1	126.2	139.1	131.2
10000	140.8	129.7	141.8	130.5	141.6	129.7	137.6	127.7	140.3	124.0	139.8	129.2
OASPL	157.6	154.4	159.2	155.5	160.2	155.7	157.1	154.5	155.8	152.2	156.2	154.8

Table VII. One-Third Octave Band Sound Pressure Levels, Double Annular Configuration D13 (Continued).

RDG.	711		748			712		713		714		715	
Probe	D	Dw	U	D	Dw	D	Dw	D	Dw	D	Dw	D	Dw
Frequency													
31.5	134.8	132.7	129.0	129.1	146.7	138.1	131.0	140.8	132.0	139.8	131.7	138.0	131.2
40	137.5	136.1	129.1	129.5	146.1	139.0	132.1	139.3	134.8	139.7	132.3	139.3	134.1
50	138.7	136.8	129.4	130.0	145.6	139.5	132.8	139.7	133.8	139.2	134.6	139.2	132.8
63	139.4	136.8	129.6	132.4	145.5	141.7	130.5	141.9	132.3	140.4	133.0	138.7	132.3
80	138.1	137.9	129.0	131.9	145.2	137.4	129.7	139.9	132.7	139.1	134.2	137.6	134.4
100	137.3	136.5	130.4	131.5	145.8	134.5	129.5	137.0	132.8	138.8	132.5	137.0	132.5
125	135.8	135.6	133.3	131.6	145.1	133.8	129.6	134.8	132.9	137.1	131.9	136.1	132.1
160	135.1	135.9	131.3	135.6	145.4	131.9	130.4	130.6	132.6	135.6	132.6	134.9	131.4
200	134.3	137.0	135.5	135.1	145.8	131.1	130.8	130.8	134.0	134.6	135.0	134.1	133.3
250	136.7	138.6	134.3	138.2	145.6	131.4	132.1	131.4	133.9	136.4	135.1	133.4	133.6
315	138.3	139.2	140.2	140.3	145.9	135.8	132.7	133.5	134.2	137.5	135.7	135.5	135.2
400	141.9	141.1	146.2	142.4	146.6	136.4	134.9	135.4	136.1	138.1	137.1	136.6	136.1
500	141.6	142.4	147.2	143.4	146.9	136.6	136.1	135.9	137.1	137.6	138.1	137.9	137.4
630	144.0	143.6	149.0	146.0	147.9	138.5	136.4	138.0	137.9	139.2	139.1	138.2	139.1
800	145.0	145.3	151.5	146.7	148.6	138.0	137.8	137.2	138.8	140.5	138.6	138.0	137.8
1000	145.6	144.9	151.6	147.1	149.4	139.4	136.4	139.4	137.4	140.1	136.4	140.4	135.4
1250	145.2	143.6	148.1	147.5	148.8	137.5	133.6	137.5	136.3	140.2	136.3	139.4	135.8
1600	143.5	142.9	143.4	146.7	148.6	136.0	132.6	135.5	134.6	139.2	134.4	137.7	133.9
2000	142.6	142.9	143.6	144.3	148.1	134.8	131.4	138.8	134.1	139.3	134.1	138.6	133.4
2500	142.5	141.3	143.3	142.5	148.8	134.3	128.0	134.8	131.5	138.8	132.0	137.5	131.0
3150	144.5	140.1	138.7	143.5	150.1	134.8	126.1	134.0	130.3	136.5	130.8	134.5	131.1
4000	145.3	140.4	134.3	143.3	149.9	130.5	124.6	130.5	128.9	134.0	129.4	131.0	129.4
5000	146.4	139.0	134.3	144.7	151.5	129.9	123.2	127.4	127.7	133.4	126.7	128.7	125.7
6300	141.4	132.7	129.7	141.1	152.0	130.4	121.2	126.1	126.7	135.1	125.2	128.1	124.2
8000	137.1	130.5	131.1	137.6	153.5	132.9	121.7	127.6	126.7	139.1	125.7	130.4	123.5
10000	137.3	129.0	135.0	136.1	152.0	135.6	121.5	132.1	126.5	141.3	125.5	135.1	123.2
OASPL	156.0	154.5	158.0	156.6	162.8	150.6	146.4	150.9	148.3	152.7	148.6	151.1	148.0

Table VII. One-Third Octave Band Sound Pressure Levels, Double Annular Configuration D13 (Concluded).

RDG.	716		699		723			726			727			728		
Probe	D	Dw	D	Dw	U	D	Dw	U	D	Dw	U	D	Dw	U	D	Dw
Frequency																
31.5	143.6	131.7	139.6	141.0	138.3	136.6	141.0	138.3	136.8	138.0	138.5	137.6	136.7	138.5	137.3	136.5
40	143.3	136.6	139.3	137.3	135.4	136.8	138.8	135.4	137.0	135.8	134.9	136.8	135.8	135.1	136.5	135.3
50	141.7	135.1	141.5	141.6	136.9	138.0	138.6	136.4	137.7	137.6	137.4	139.5	137.8	137.4	140.0	138.6
63	140.2	134.8	145.2	142.5	138.1	140.7	138.0	137.1	139.9	138.5	137.1	140.9	139.0	137.9	141.2	139.0
80	138.9	137.4	144.6	146.4	140.0	140.1	139.4	139.8	139.6	140.2	139.3	139.9	139.4	139.5	140.6	139.2
100	138.3	134.8	142.5	144.3	137.4	138.8	139.5	136.9	137.8	139.8	137.4	138.0	138.5	137.1	138.0	138.3
125	136.8	133.6	142.8	142.6	141.0	139.8	139.9	139.8	137.8	140.9	139.8	138.1	139.6	139.5	138.1	138.4
160	134.9	132.6	144.1	142.1	138.3	141.9	141.1	137.5	140.4	141.1	137.5	139.4	140.6	137.5	139.1	139.9
200	133.3	135.3	144.8	142.3	141.2	140.8	140.3	141.5	140.3	141.3	141.2	139.8	139.8	141.2	139.8	139.3
250	134.2	135.6	146.7	143.9	139.3	143.4	142.1	138.8	142.7	142.6	138.0	142.2	141.1	137.8	140.9	140.6
315	135.3	136.7	147.3	145.7	145.7	145.3	144.2	144.9	144.5	144.2	143.7	142.8	143.8	142.9	141.5	141.7
400	134.9	137.6	149.6	147.4	152.4	148.6	146.1	151.7	148.4	147.1	150.2	146.4	144.9	148.4	144.4	143.6
500	135.1	138.1	152.2	149.4	153.7	149.9	148.1	155.2	150.6	150.1	156.2	151.1	149.9	151.2	145.6	146.6
630	137.7	140.1	154.7	151.4	154.0	151.5	150.1	154.0	150.2	150.4	154.5	151.7	150.6	153.5	149.5	148.4
800	136.0	138.8	154.7	151.6	157.2	153.5	150.3	154.7	151.5	150.8	155.2	150.7	149.3	156.7	151.2	150.1
1000	138.6	136.4	153.9	152.4	157.4	153.1	151.4	157.1	152.6	151.9	154.9	150.6	149.9	156.1	150.1	148.4
1250	137.8	135.8	153.2	149.3	154.1	154.0	149.8	155.1	154.2	150.3	155.1	153.0	149.6	154.4	150.7	147.8
1600	137.2	134.4	152.2	149.6	150.7	152.7	150.1	151.2	151.0	150.6	151.4	152.2	150.6	151.4	151.5	149.6
2000	137.6	133.6	152.1	149.6	151.6	151.1	149.9	152.1	150.6	151.4	152.6	150.1	151.4	152.6	149.8	150.6
2500	136.0	131.3	151.0	147.5	151.3	150.0	146.8	151.0	150.5	146.5	150.8	150.5	146.8	150.3	151.3	146.0
3150	133.5	131.6	149.3	145.3	146.9	151.0	146.1	147.7	151.8	147.8	147.7	151.8	147.8	147.4	152.3	147.8
4000	130.8	129.9	148.0	146.6	143.3	152.3	146.6	142.6	152.5	148.6	142.8	153.8	149.4	142.8	153.8	149.6
5000	127.4	127.0	148.7	146.0	142.8	152.7	145.7	142.8	153.4	147.5	142.3	153.9	147.0	142.6	154.2	146.7
6300	127.1	125.0	144.6	138.2	147.5	148.6	137.7	137.5	148.9	140.0	137.2	149.6	139.7	137.7	149.9	139.7
8000	130.4	124.7	142.6	134.5	133.3	145.1	133.2	133.1	144.9	135.2	132.8	144.6	136.5	133.1	143.4	136.2
10000	134.6	123.5	142.6	132.2	134.3	143.6	132.5	133.5	143.8	132.7	133.5	142.6	134.2	133.8	142.6	135.5
OASPL	151.8	149.3	163.7	161.1	164.2	163.3	160.2	164.0	163.0	161.0	163.8	163.0	160.5	163.4	162.5	159.6

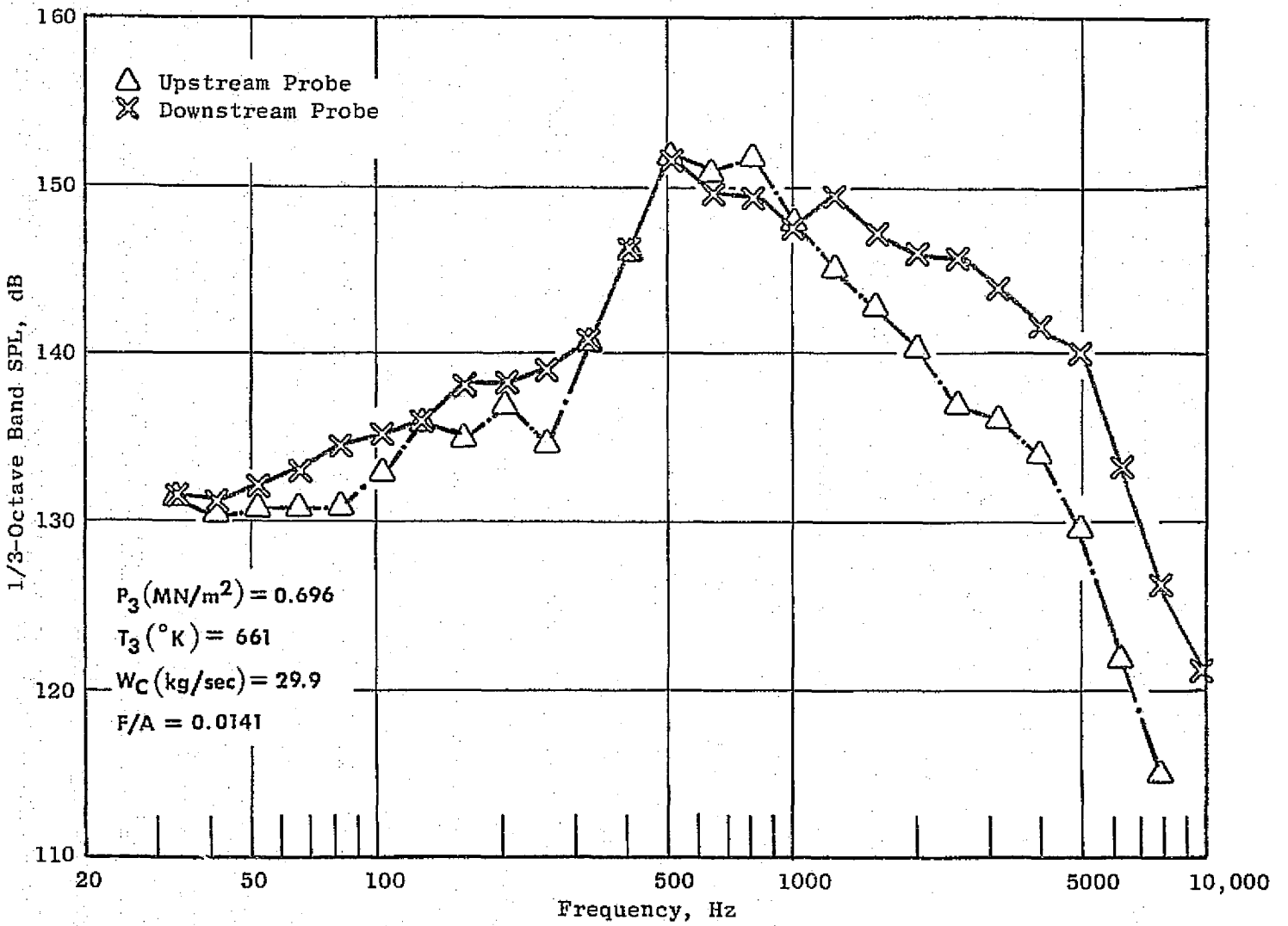

Figure 15. CF6-50 Combustor Noise, Reading 317.

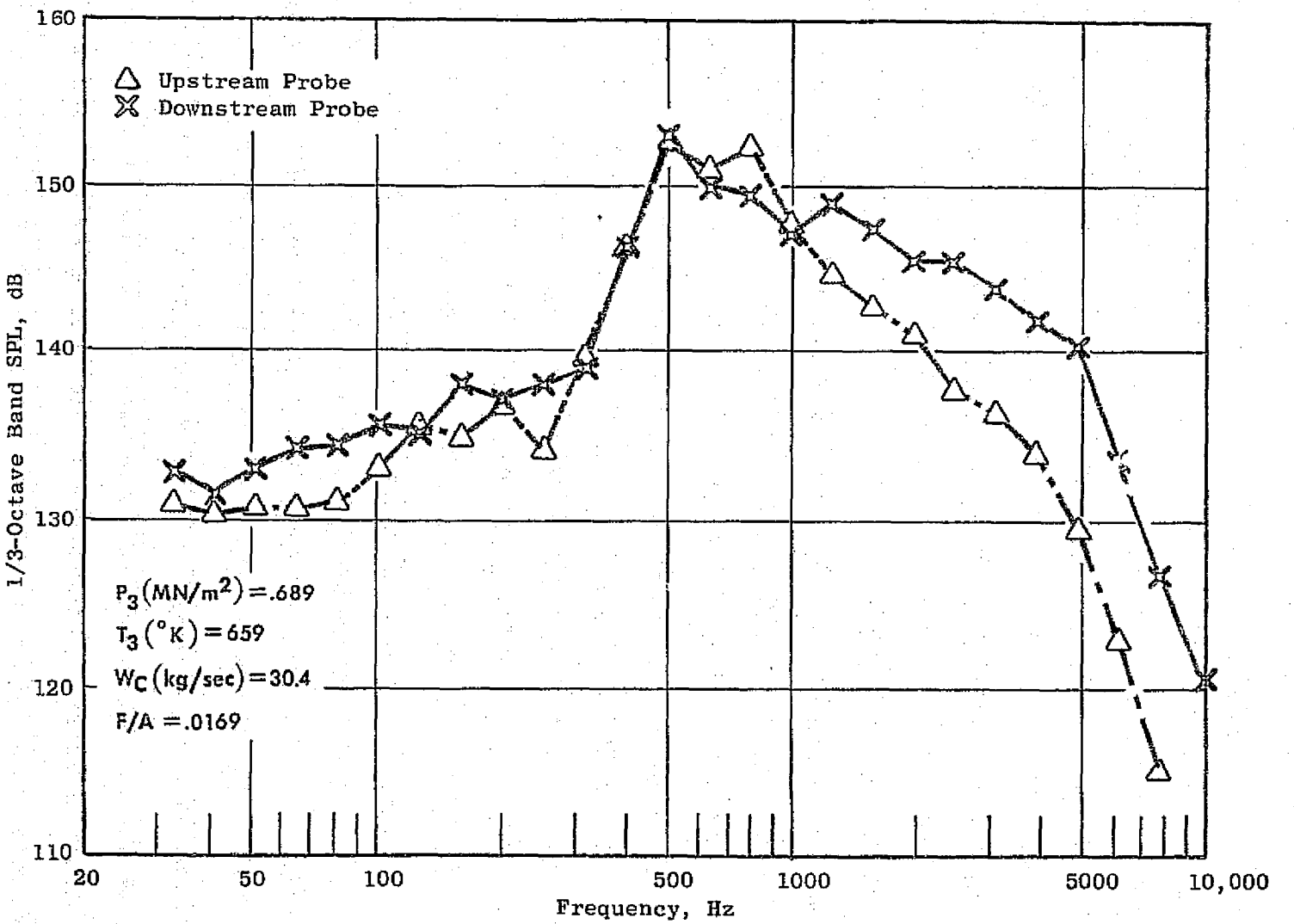

Figure 16. CF6-50 Combustor Noise, Reading 318.

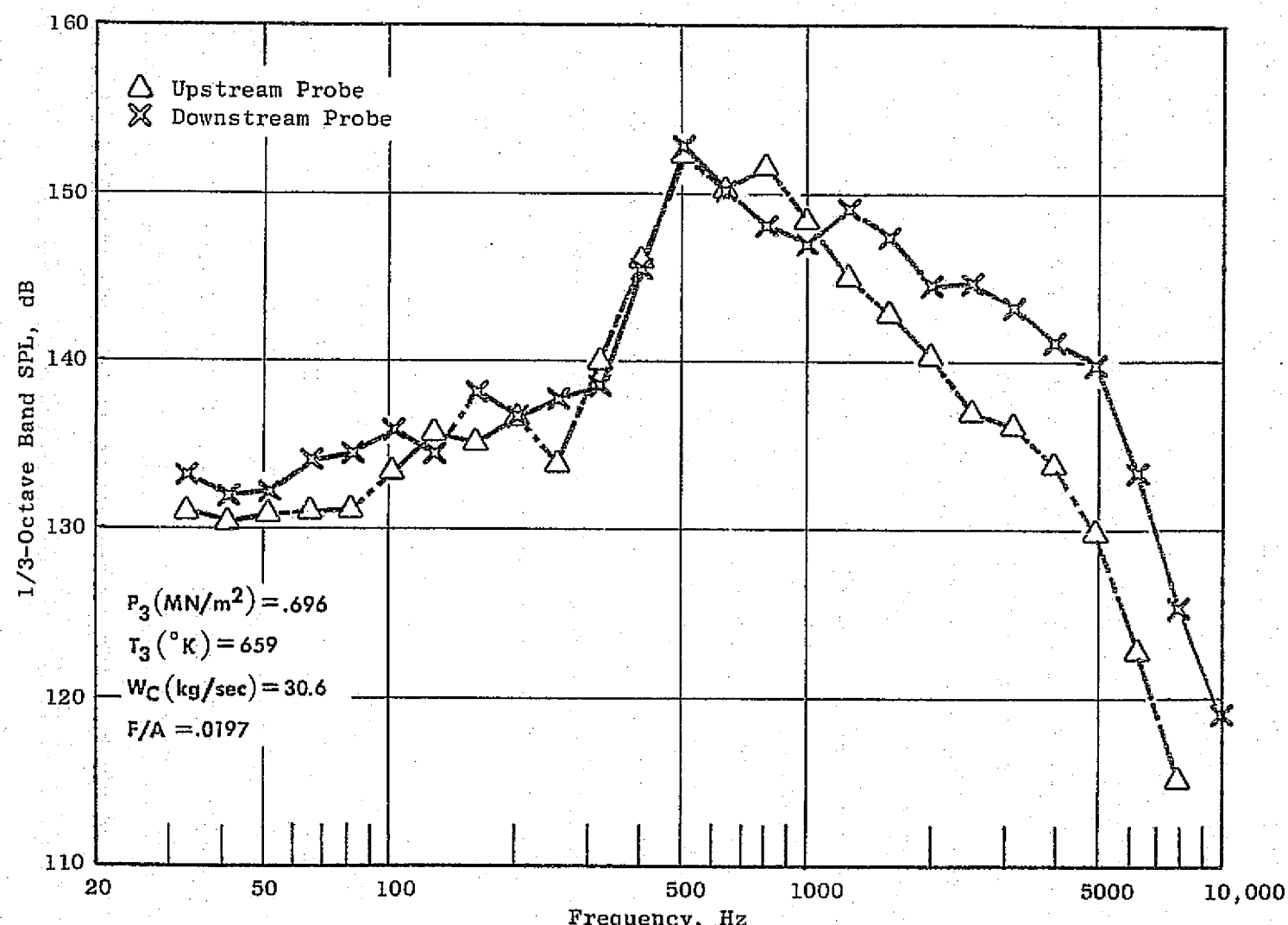

Figure 17. CF6-50 Combustor Noise, Reading 319.

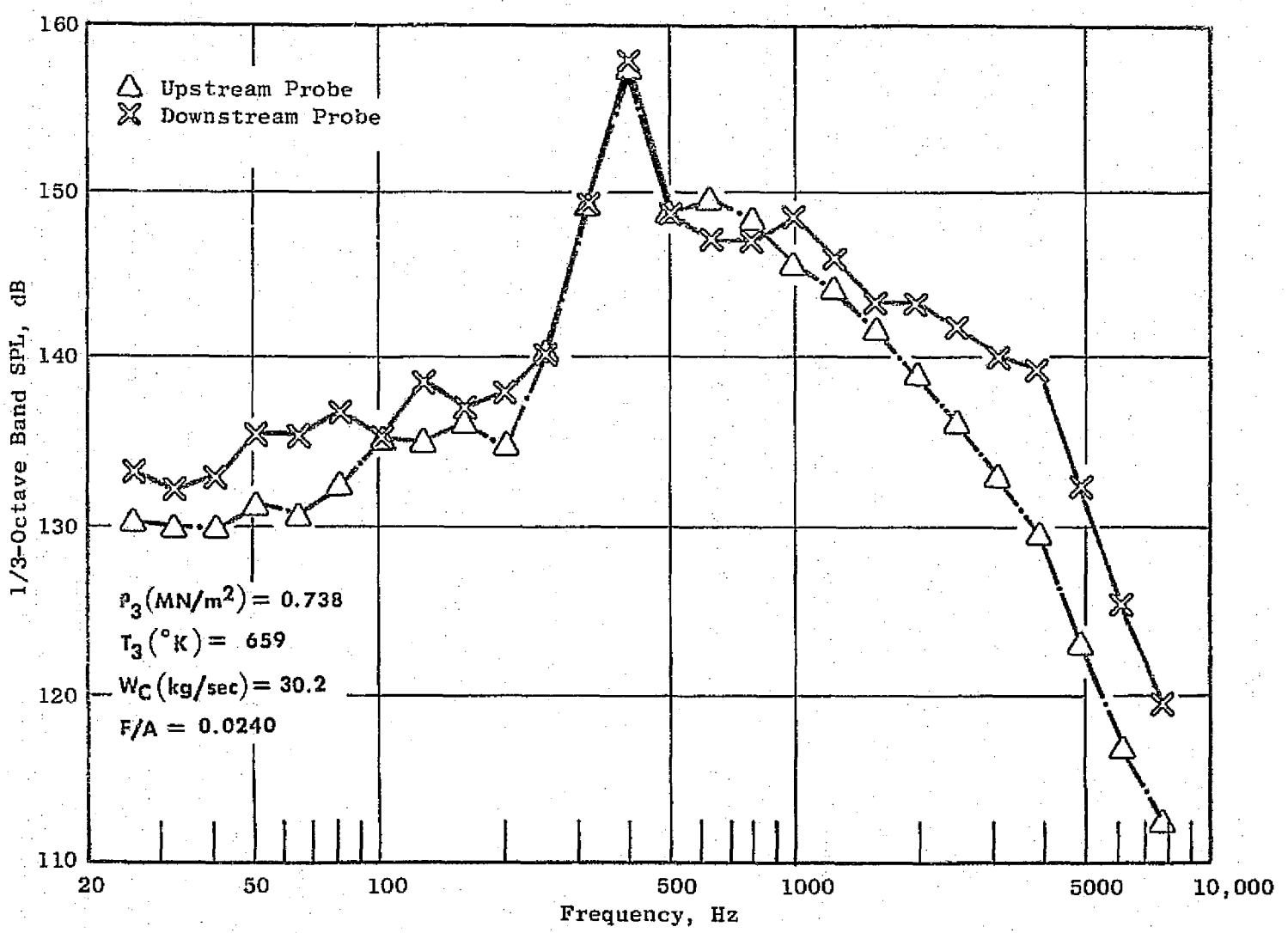

Figure 18. CF6-50 Combustor Noise, Reading 320.

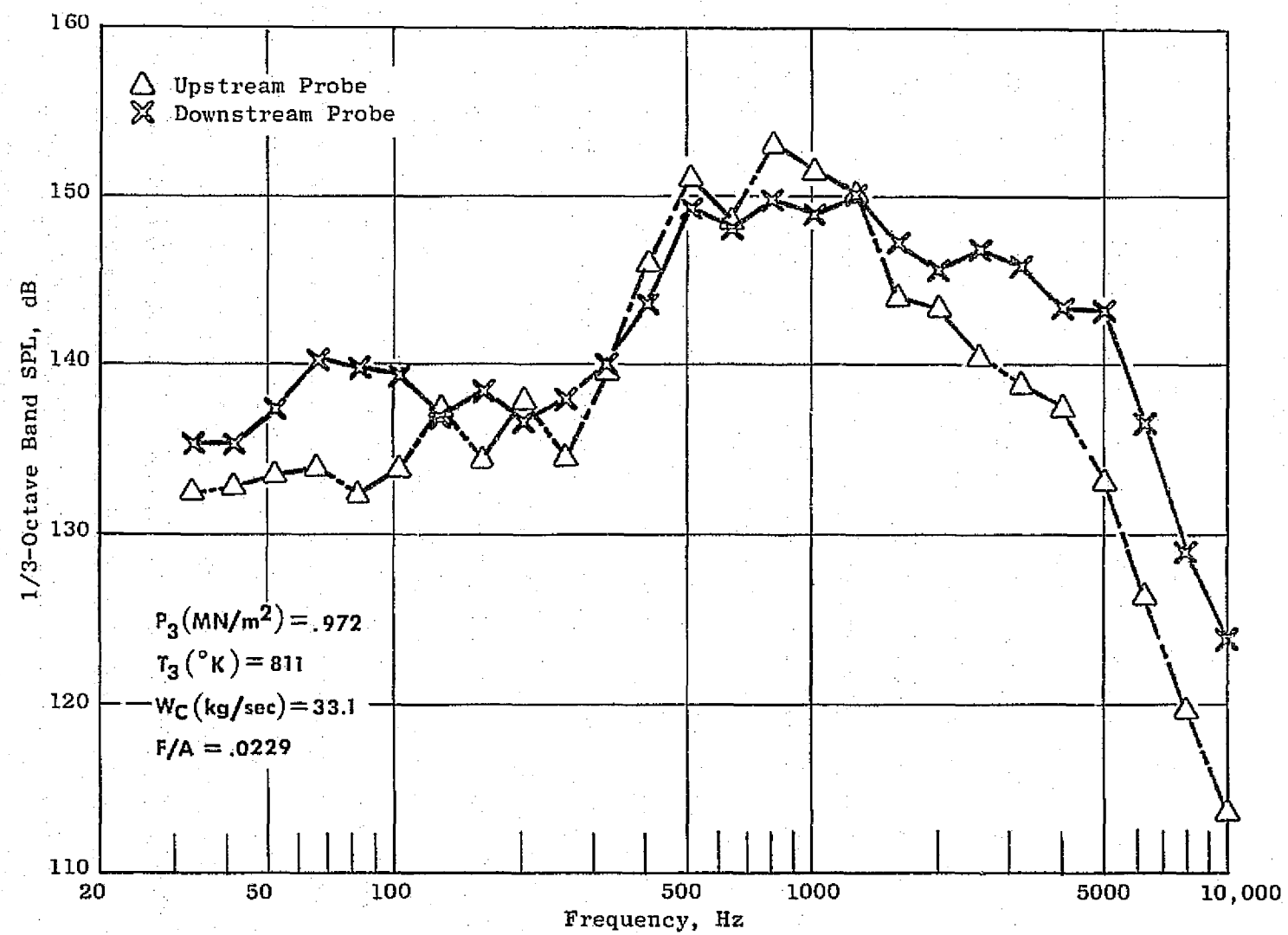

Figure 19. CF6-50 Combustor Noise, Reading 321.

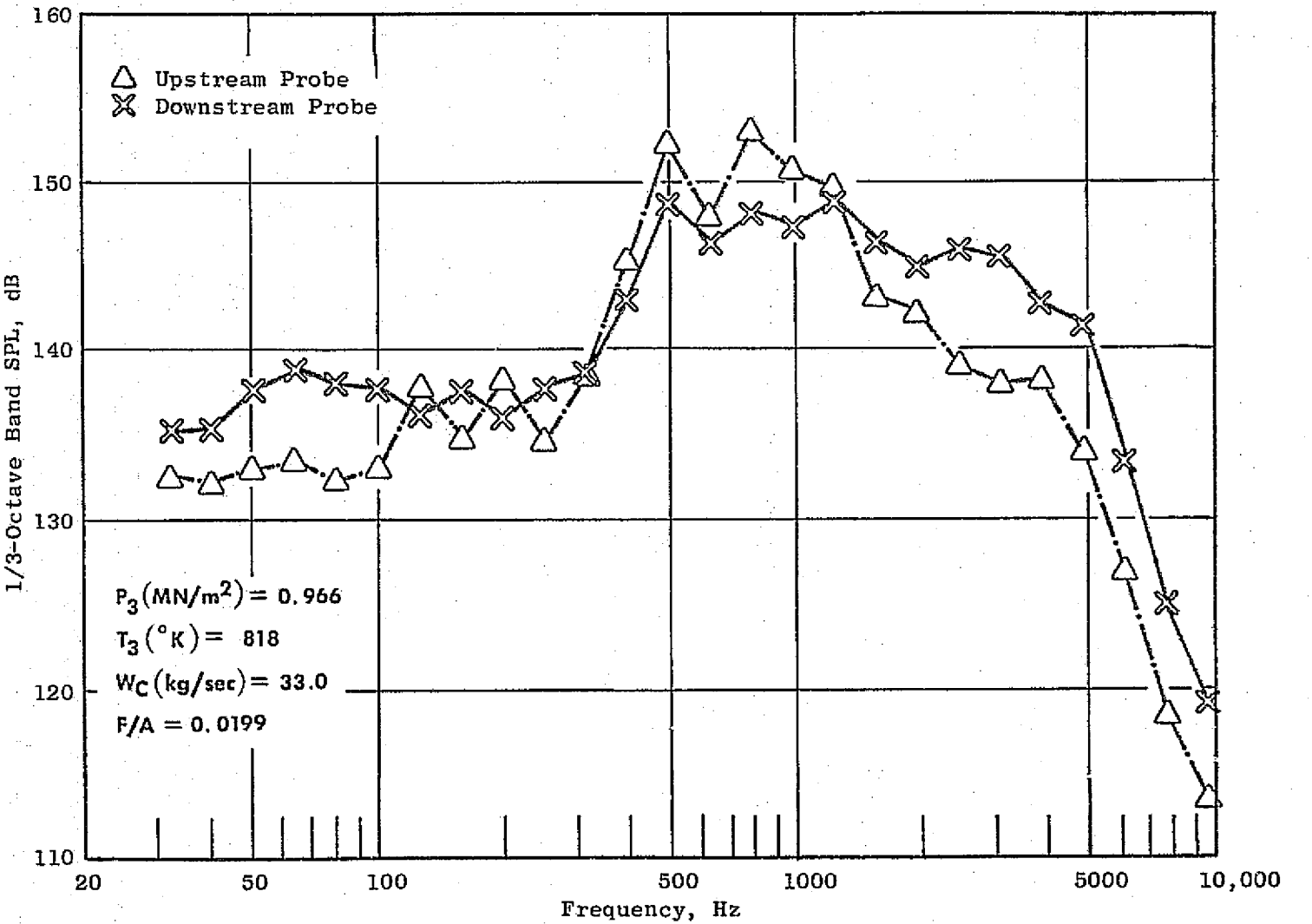

Figure 20. CF6-50 Combustor Noise, Reading 322.

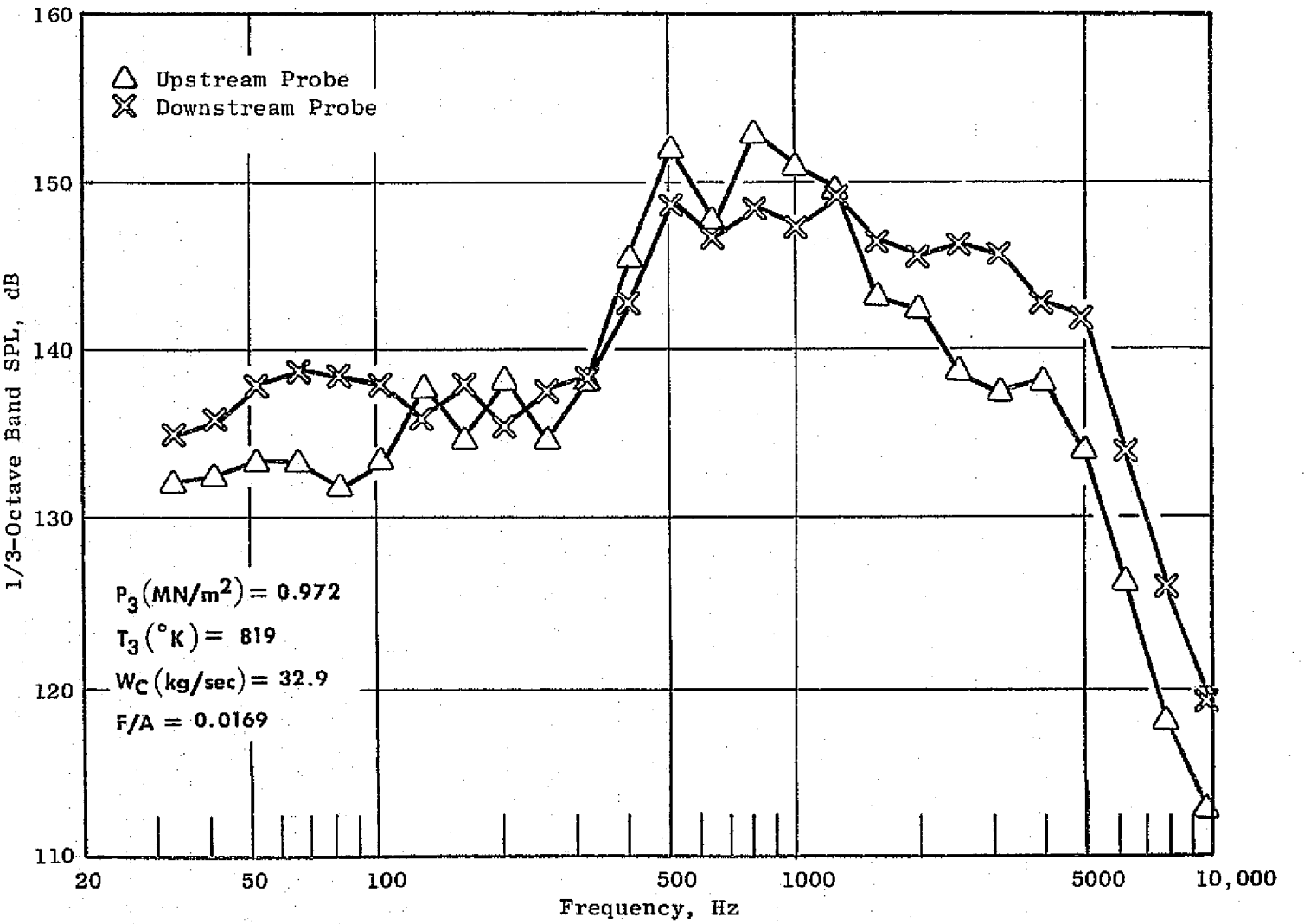

Figure 21. CF6-50 Combustor Noise, Reading 323.

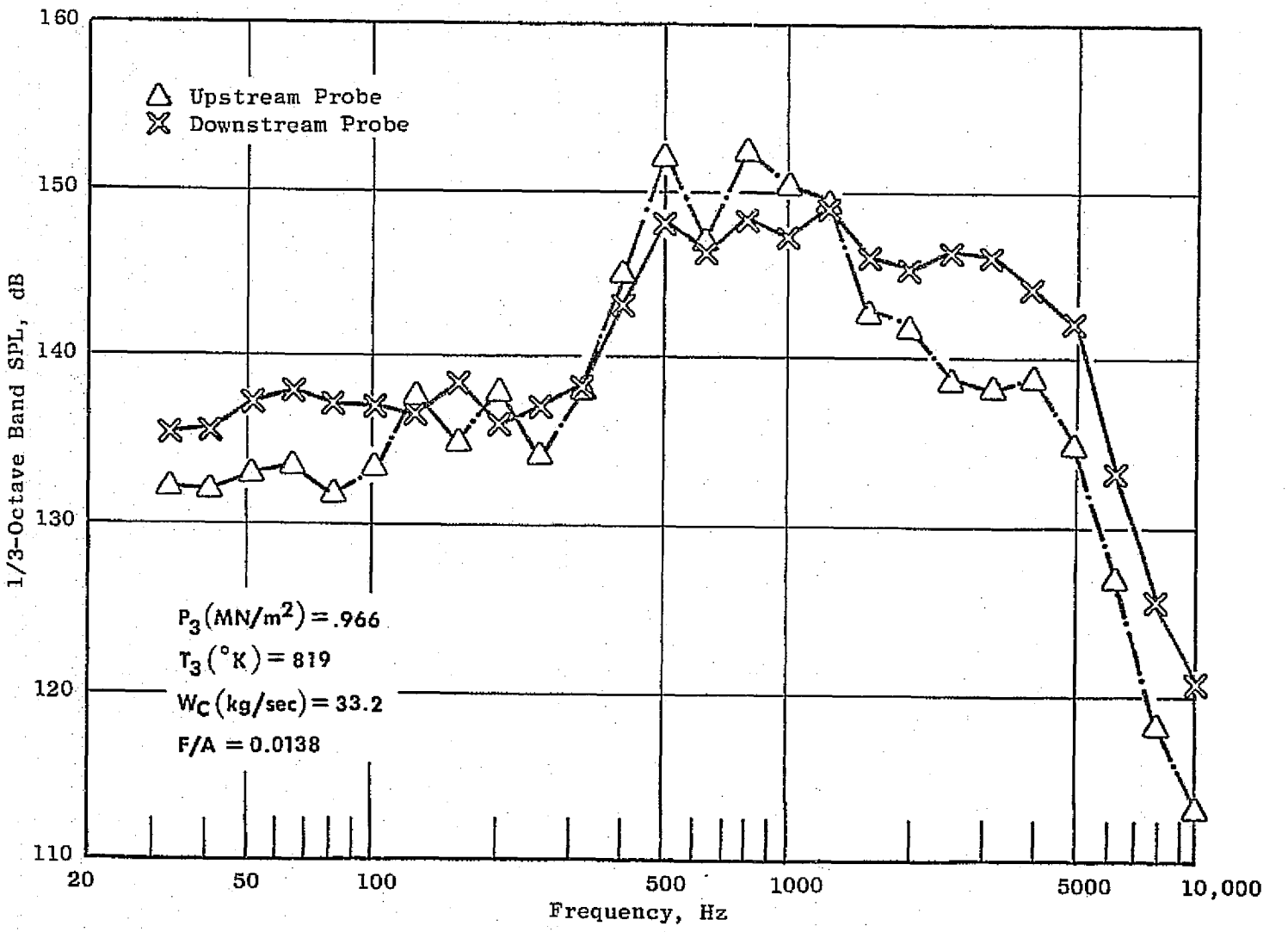

Figure 22. CF6-50 Combustor Noise, Reading 324.

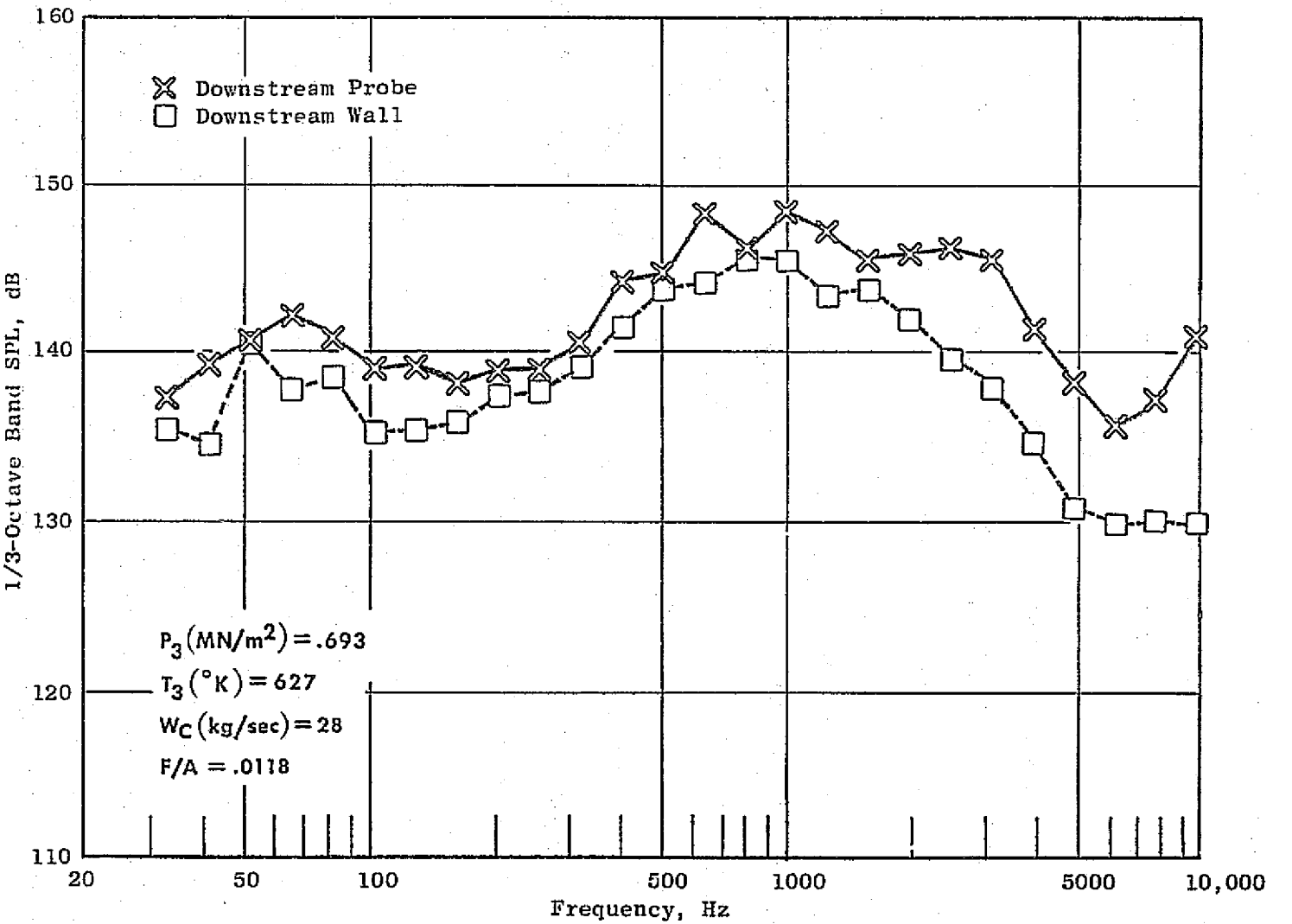

Figure 23. Double Annular, D13, Combustor Noise Reading 705.

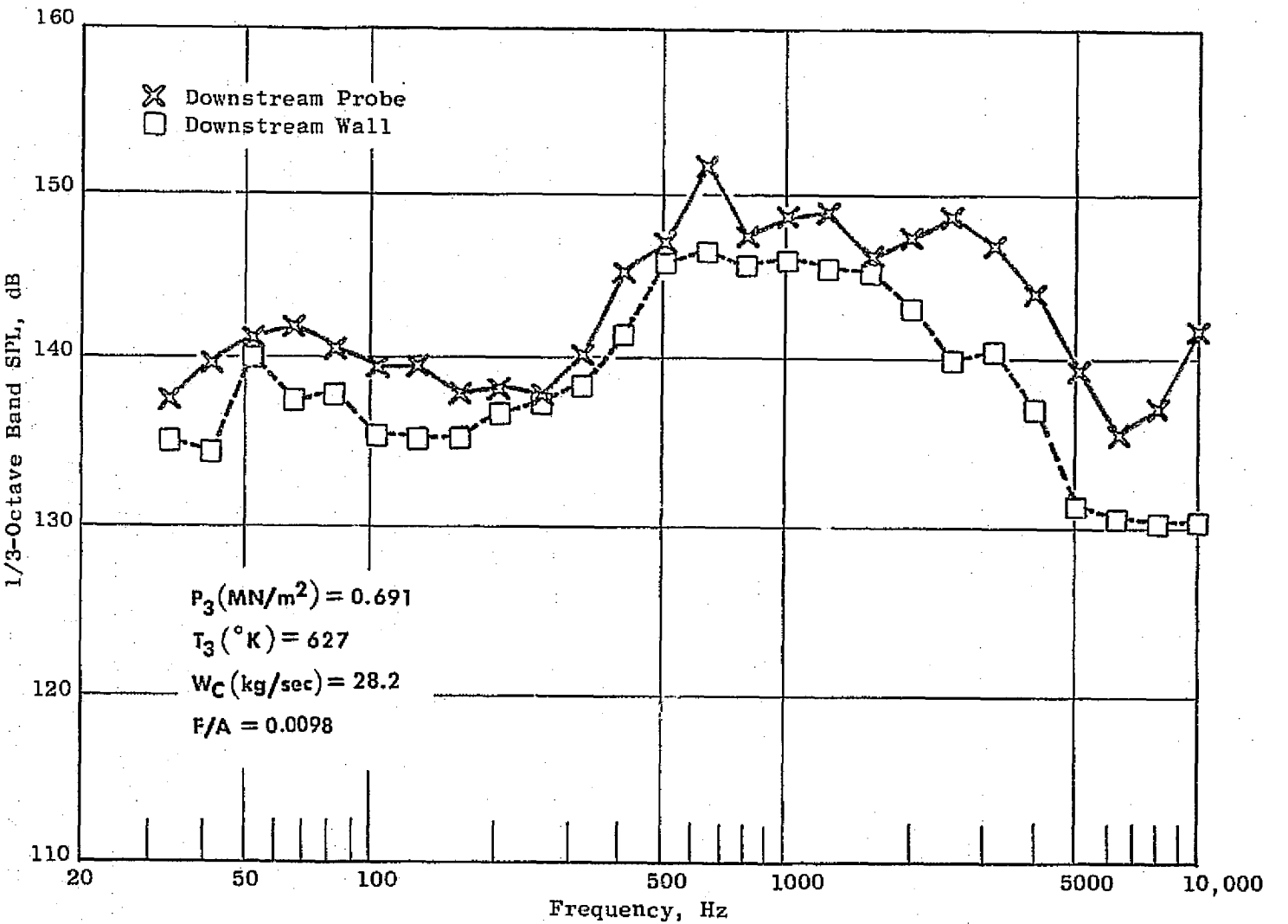

Figure 24. Double Annular, D13, Combustor Noise Reading 706.

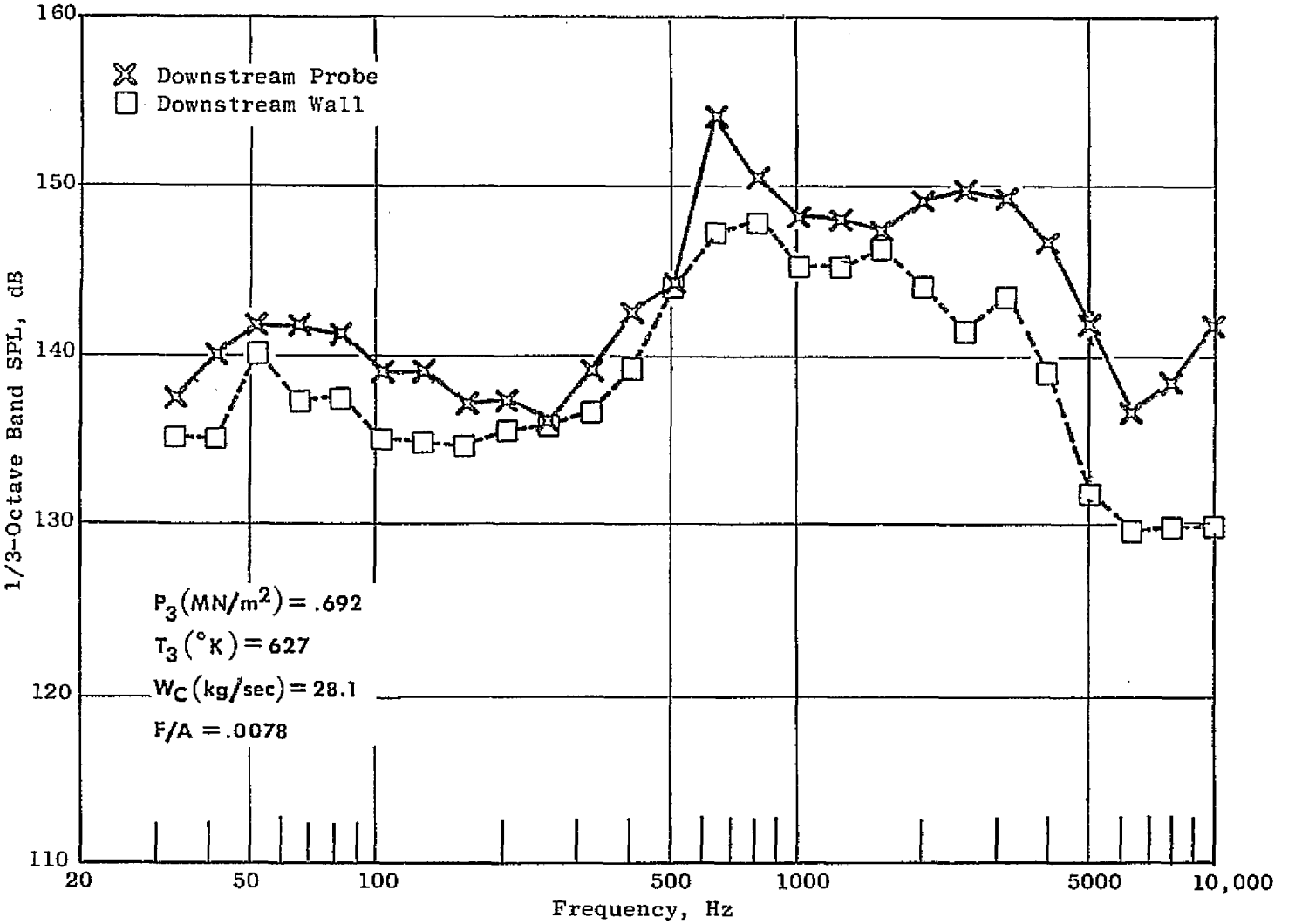

Figure 25. Double Annular, D13, Combustor Noise Reading 707.

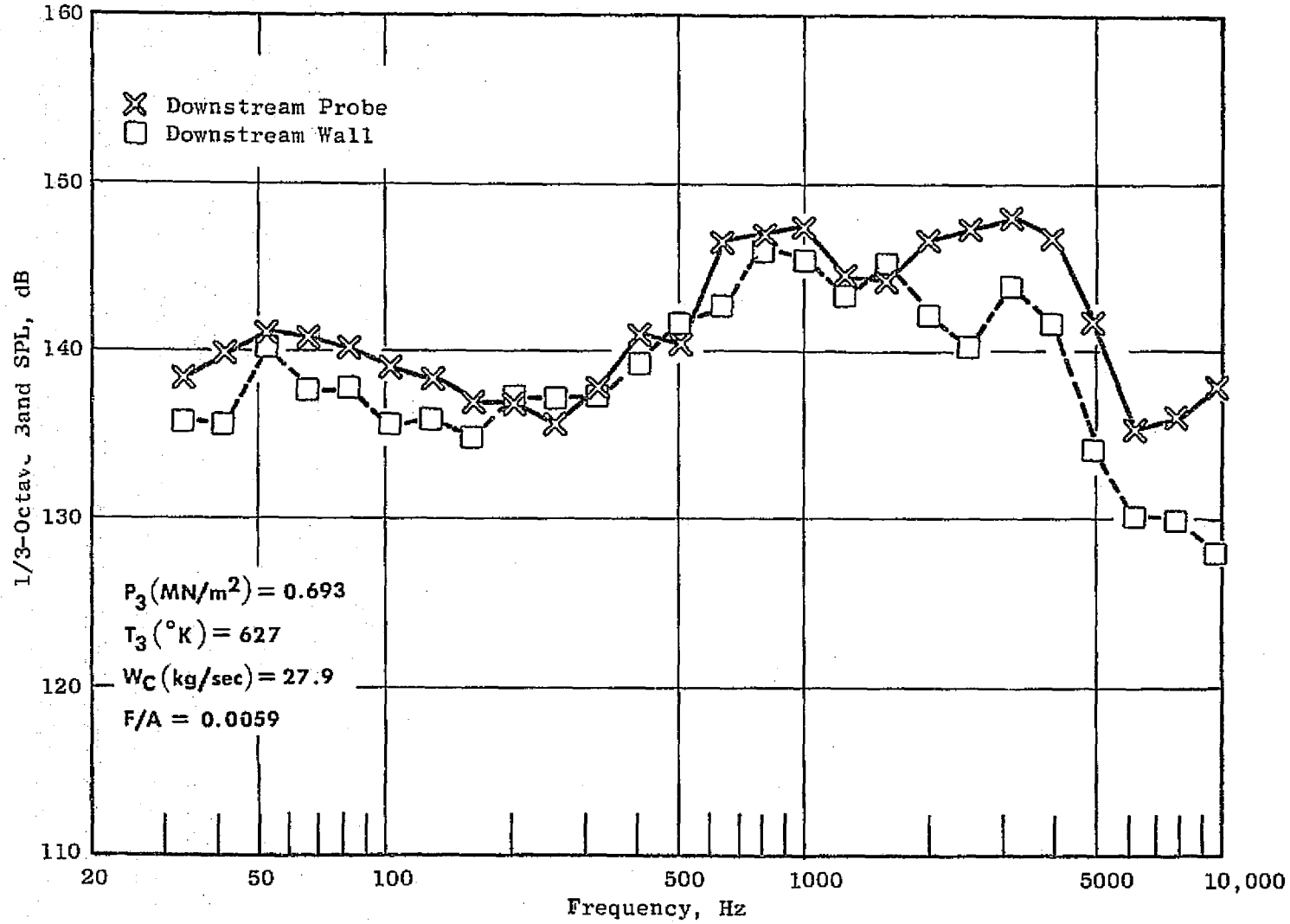

Figure 26. Double Annular, D13, Combustor Noise Reading 708.

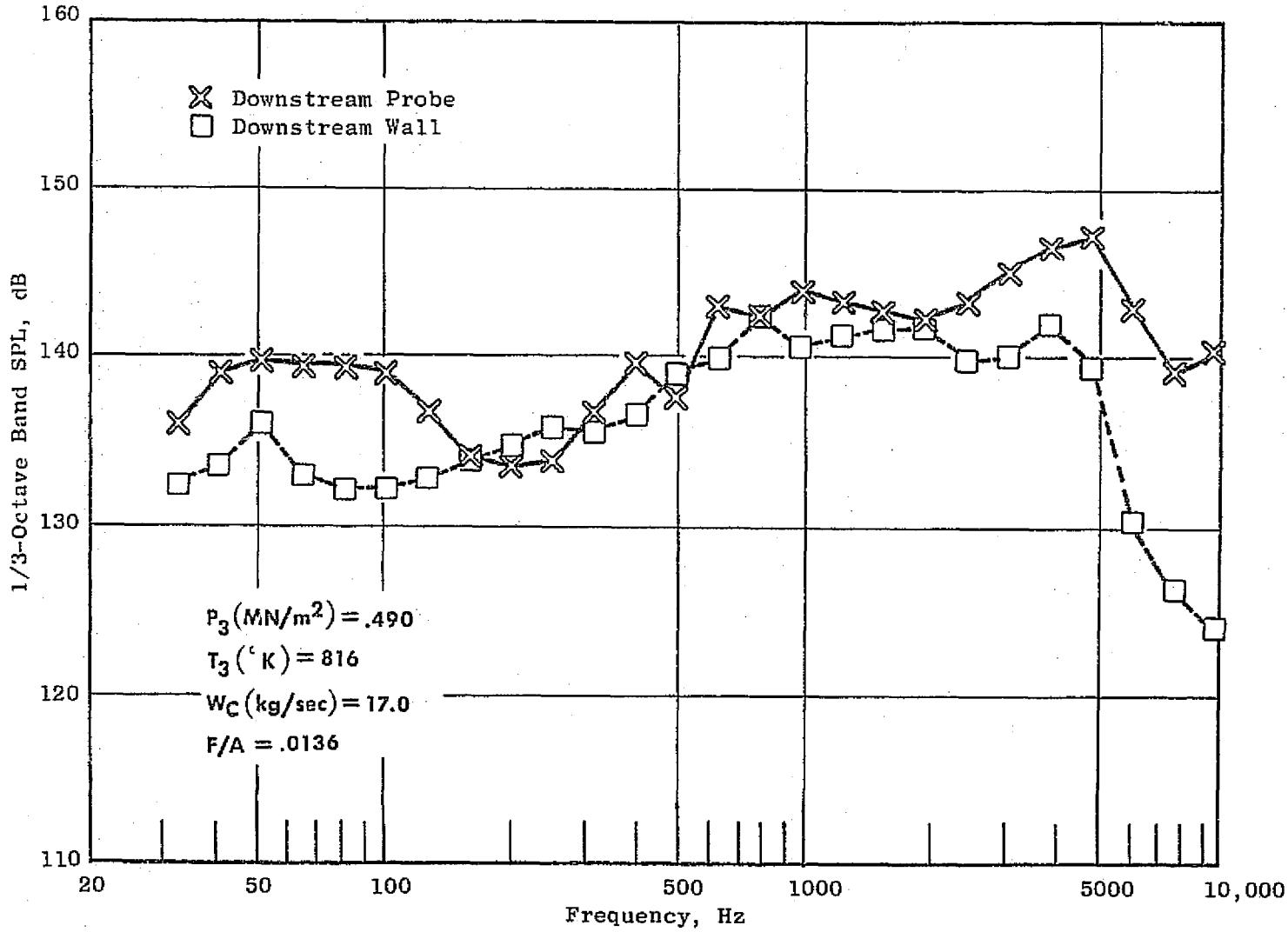

Figure 27. Double Annular, D13, Combustor Noise Reading 709.

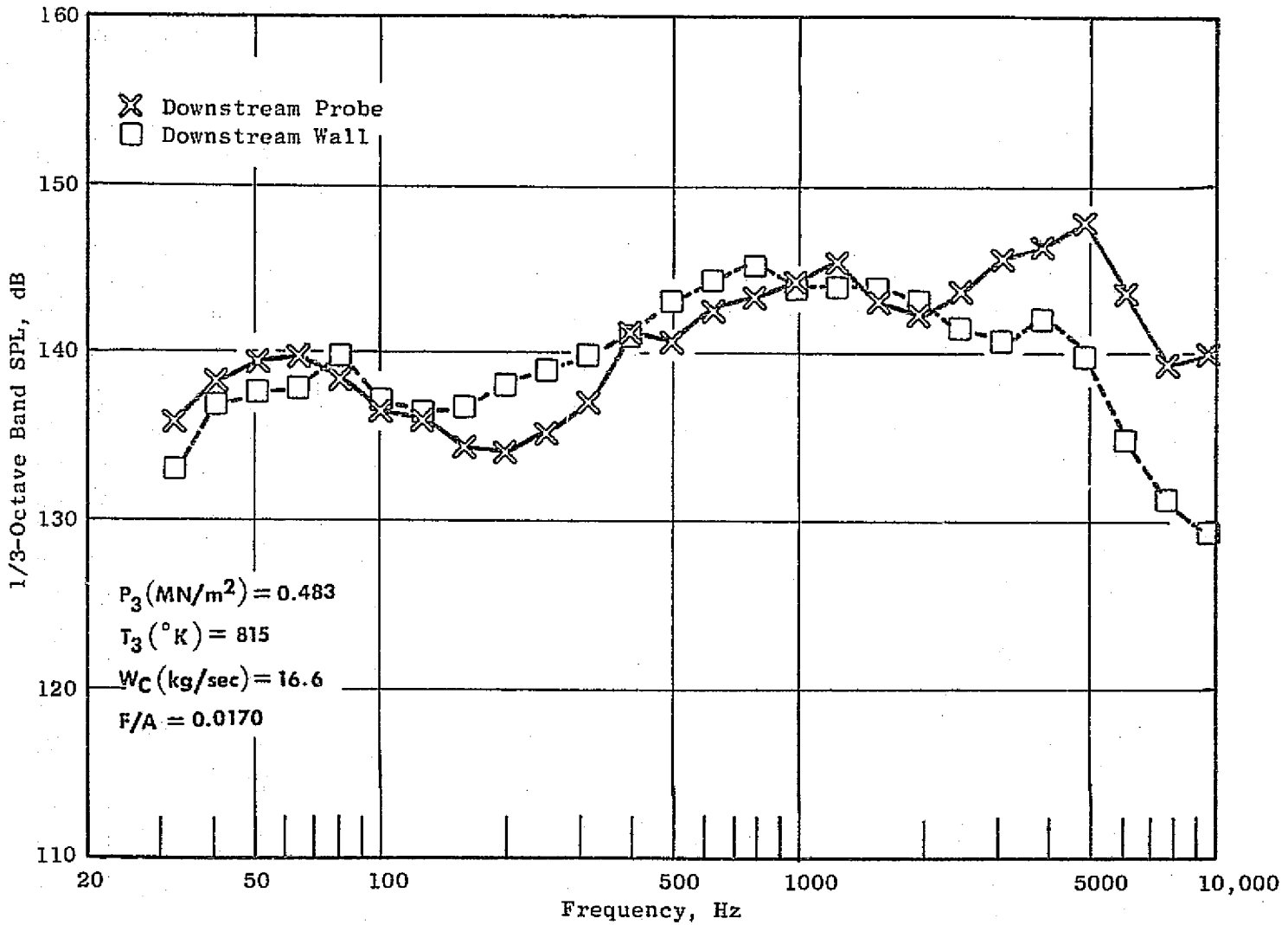

Figure 28. Double Annular, D13, Combustor Noise Reading 710.

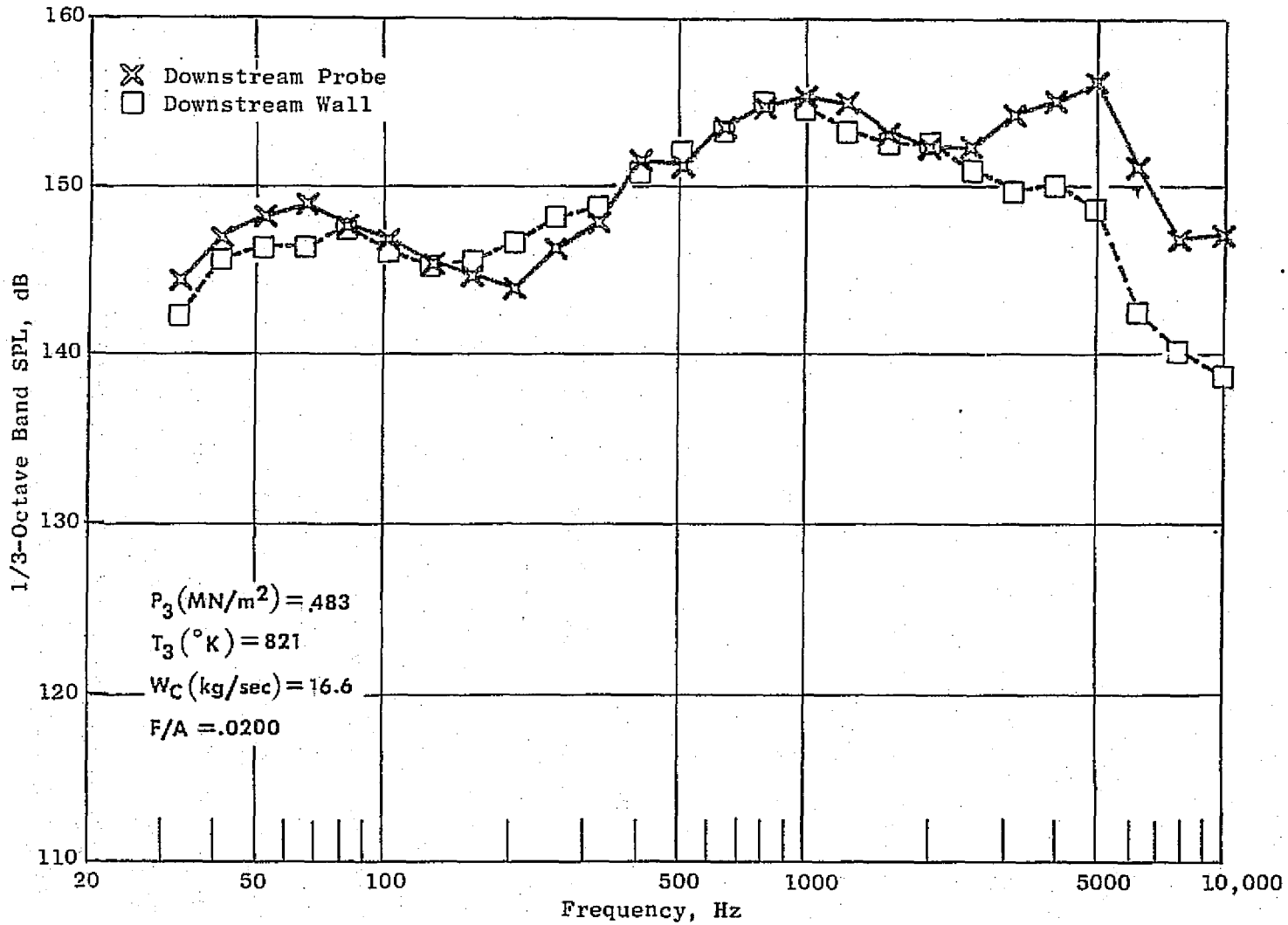

Figure 29. Double Annular, D13, Combustor Noise Reading 711.

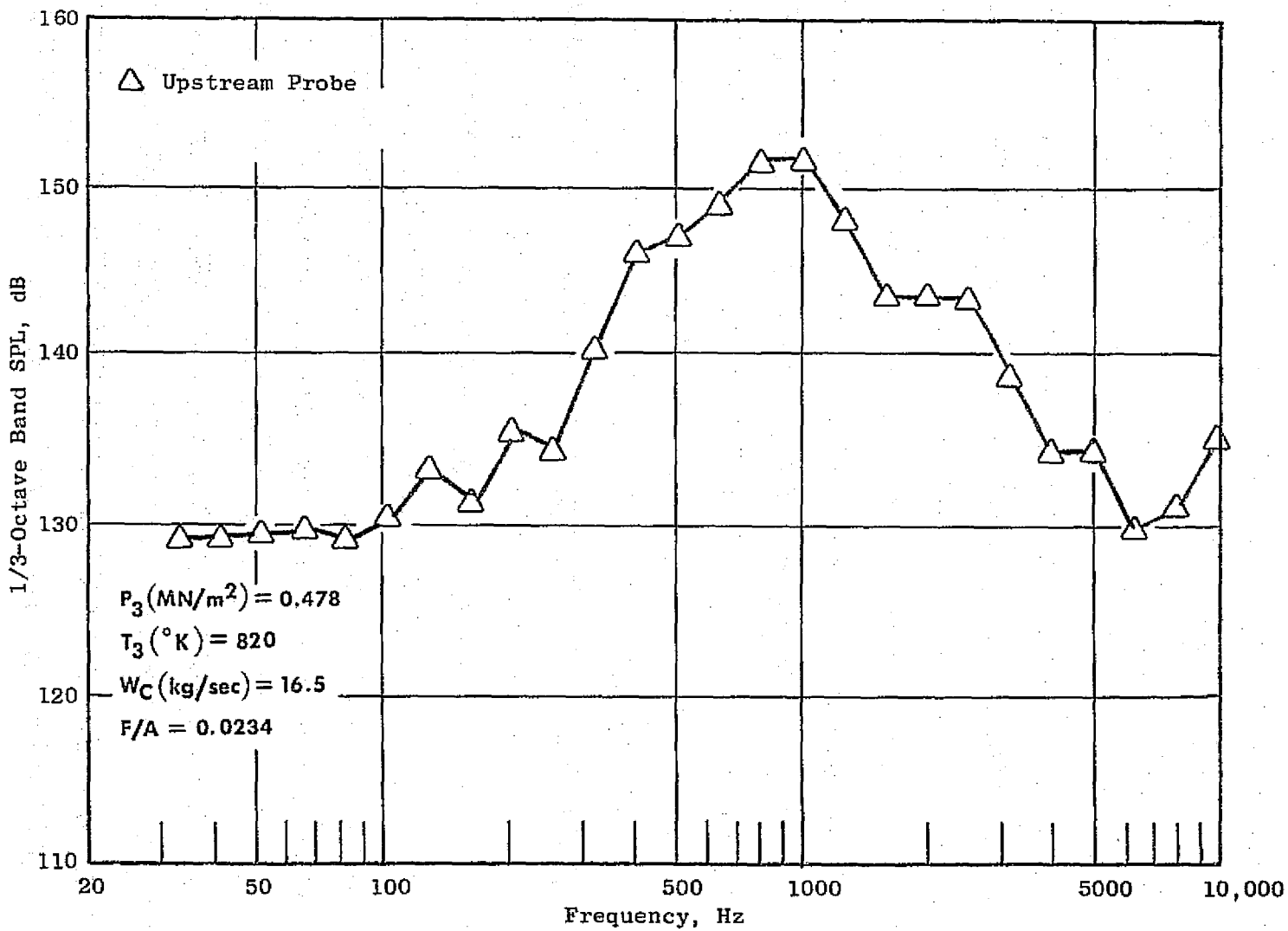

Figure 30. Double Annular, D13, Combustor Noise, Upstream Probe Reading 748.

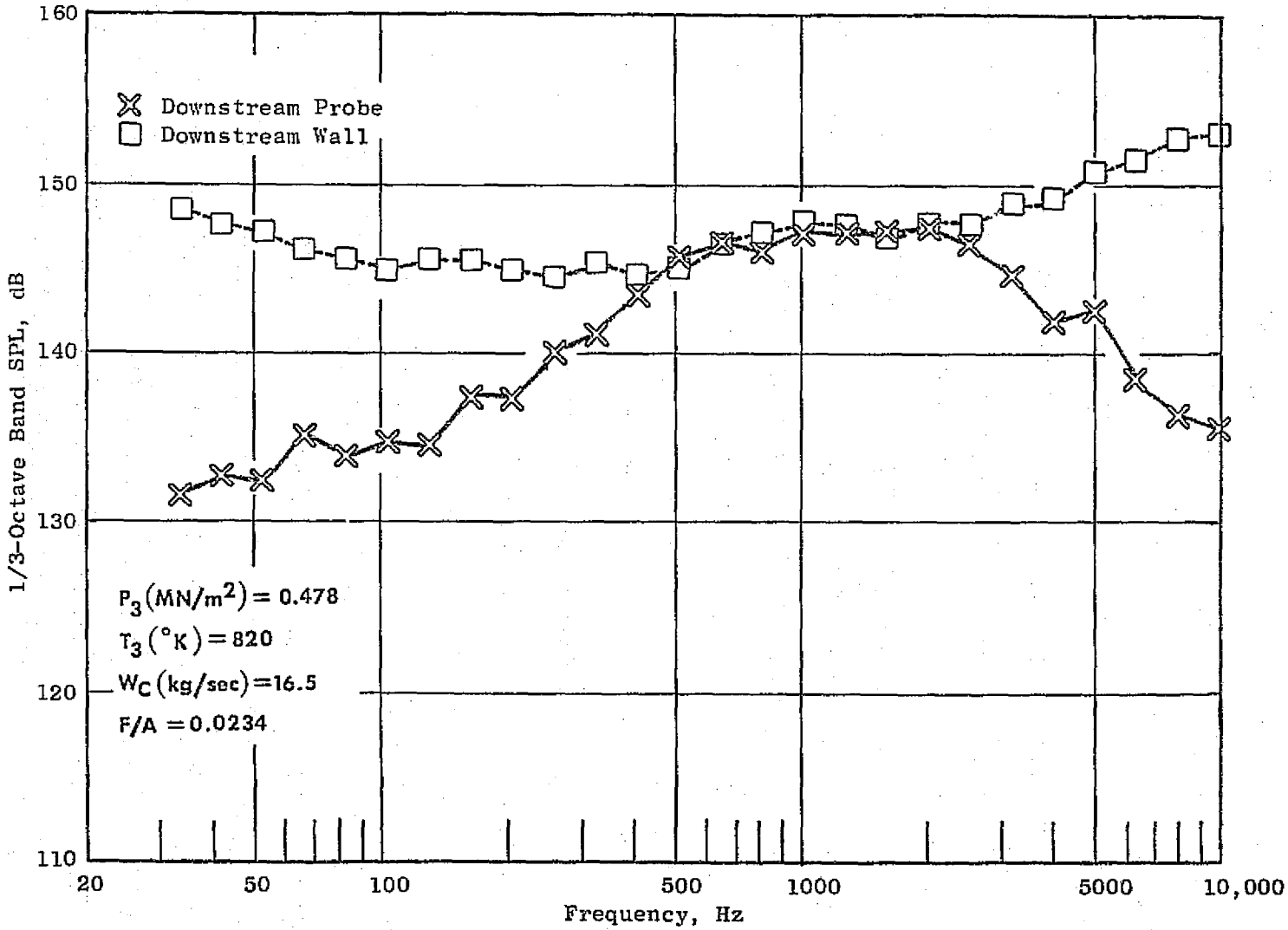

Figure 31. Double Annular, D13, Combustor Noise Reading 748.

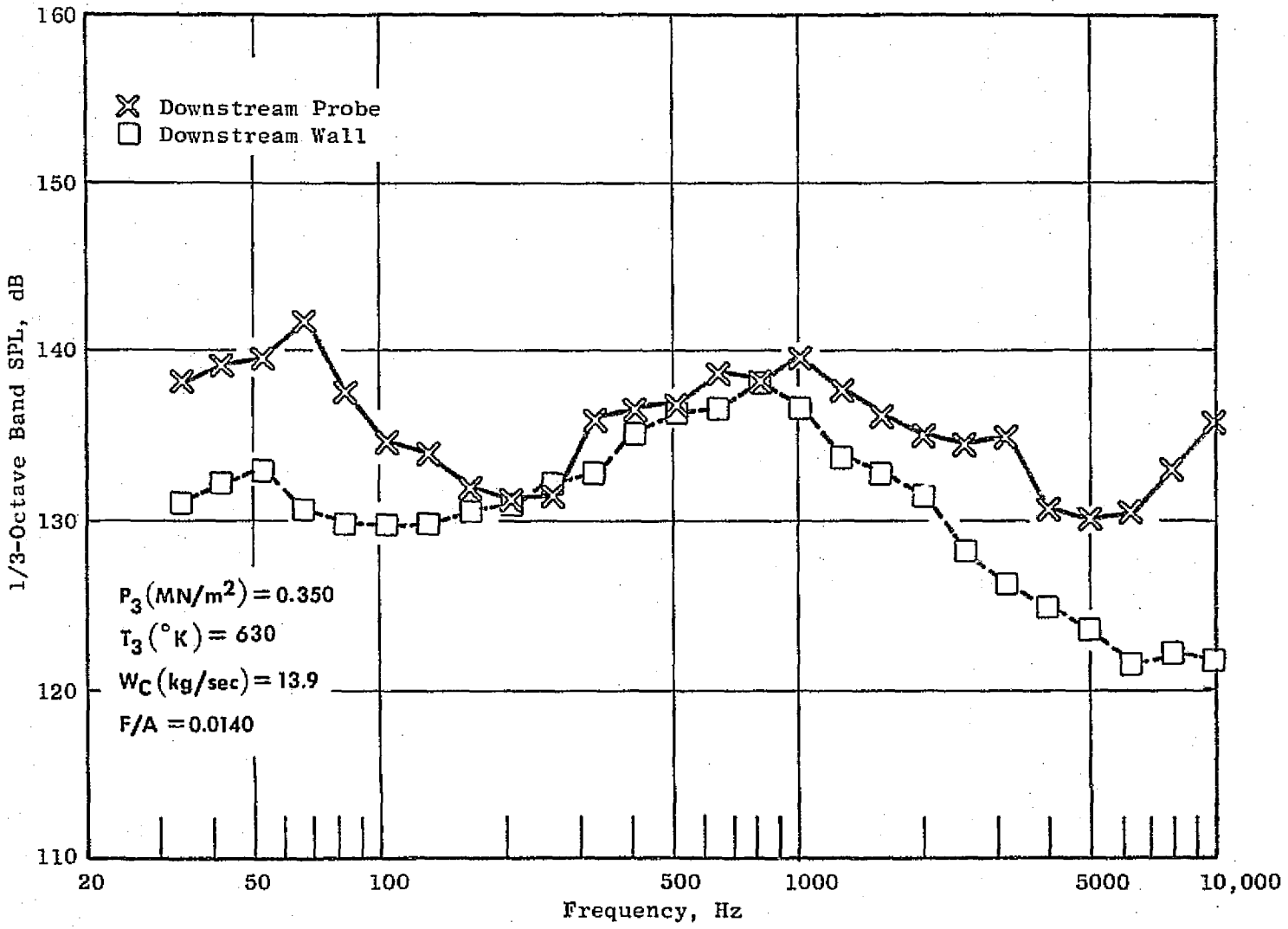

Figure 32. Double Annular, D13, Combustor Noise Reading 712.

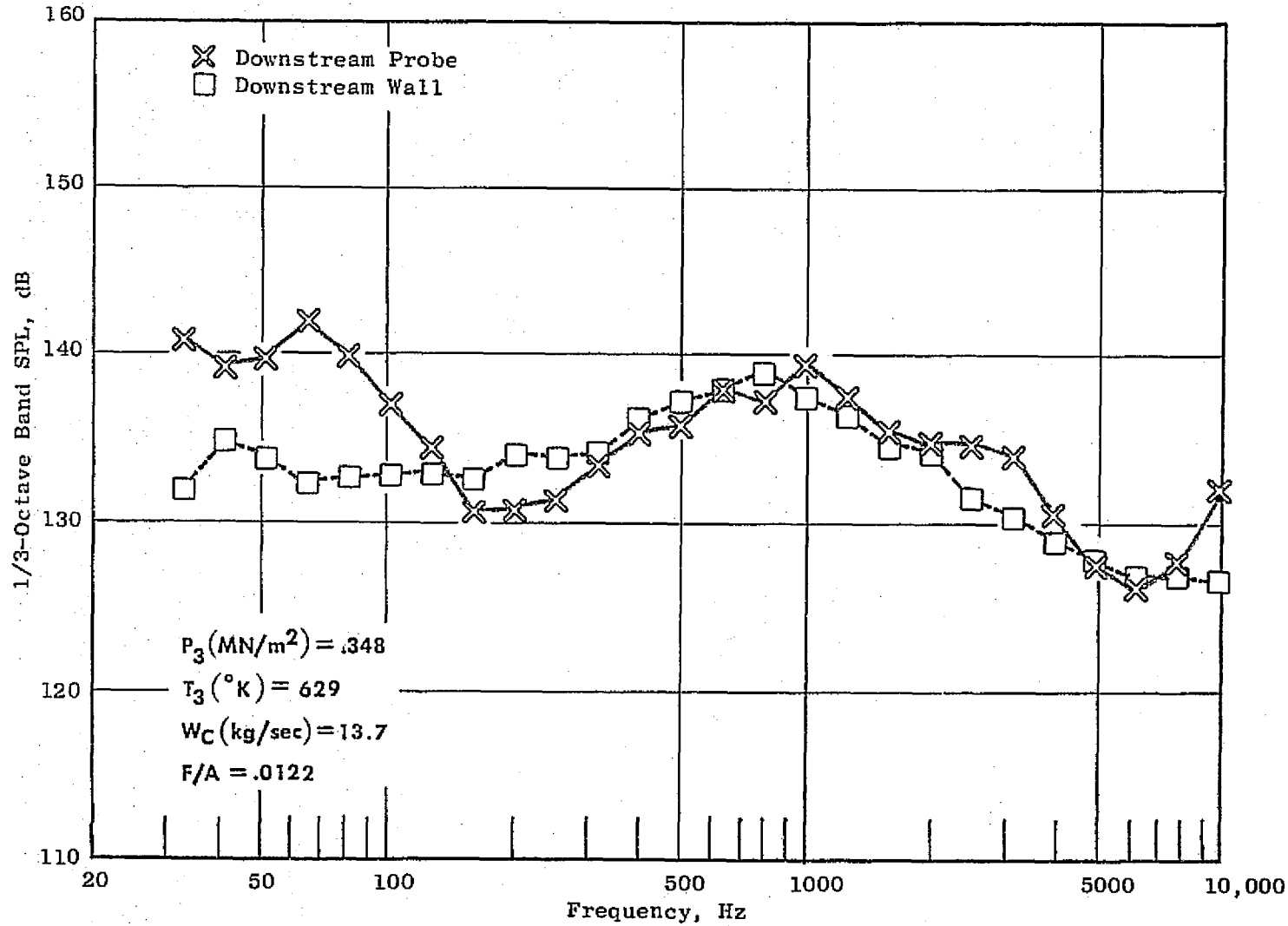

Figure 33. Double Annular, D13, Combustor Noise Reading 713.

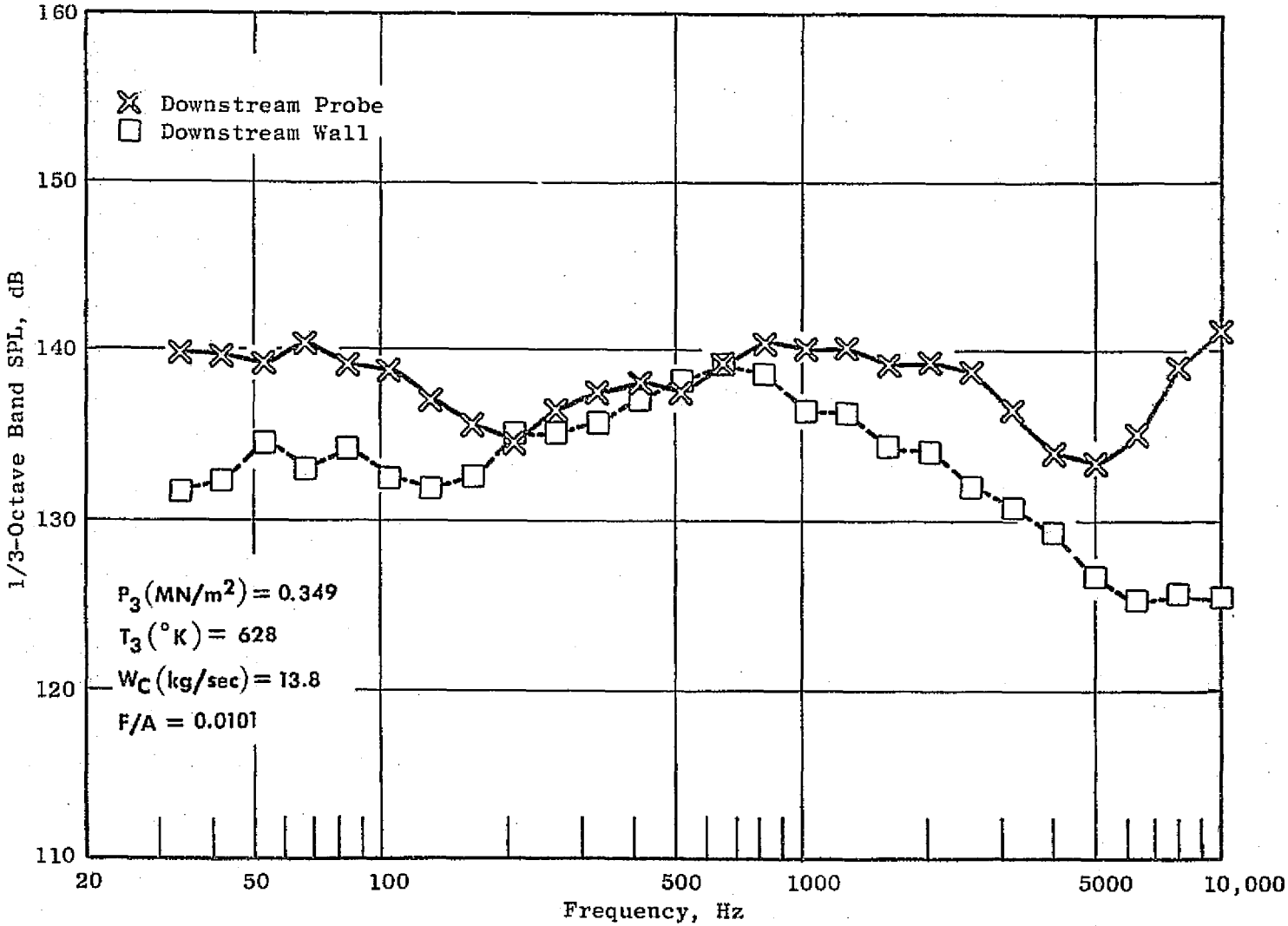

Figure 34. Double Annular, D13, Combustor Noise Reading 714.

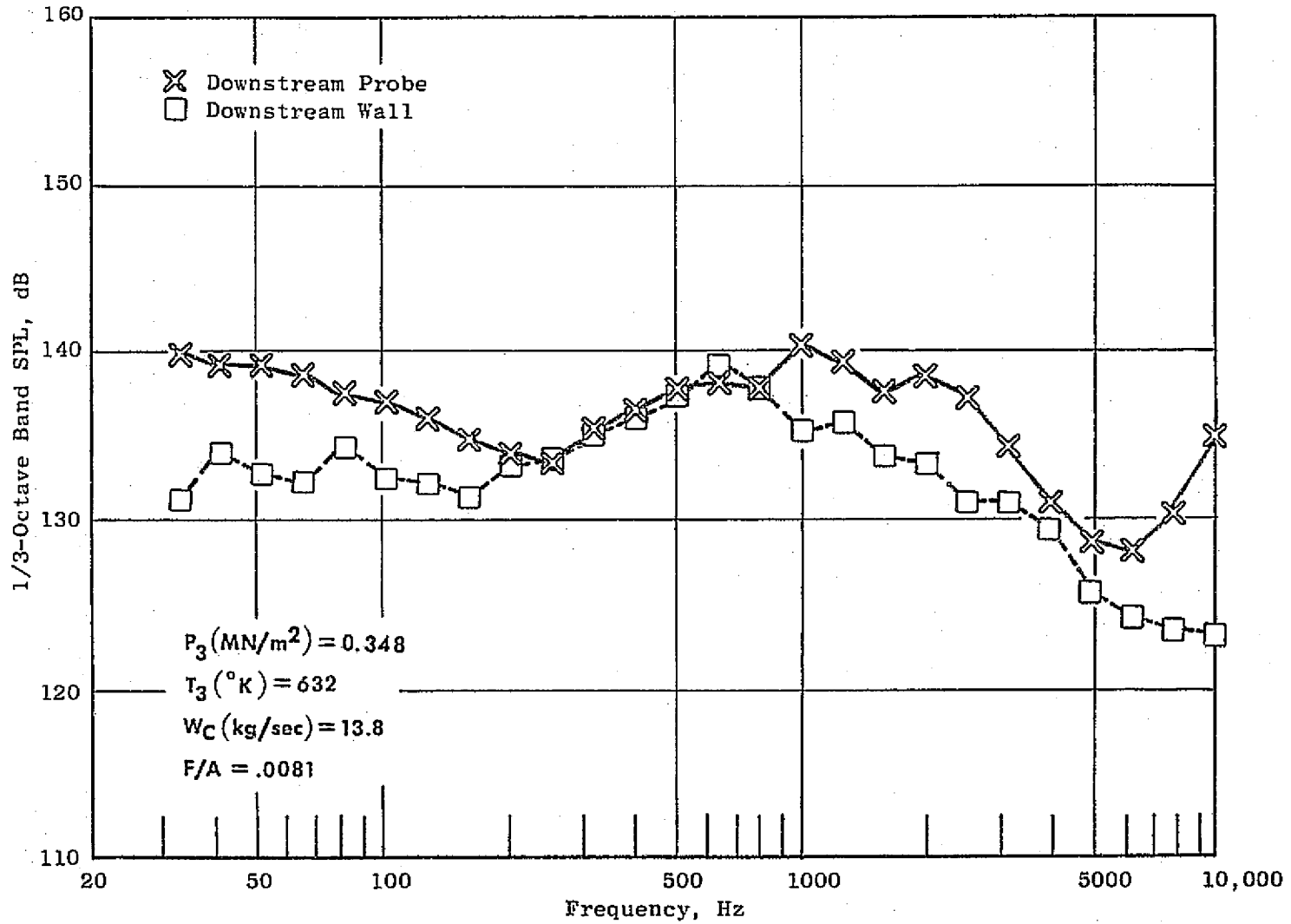

Figure 35. Double Annular, D13, Combustor Noise Reading 715.

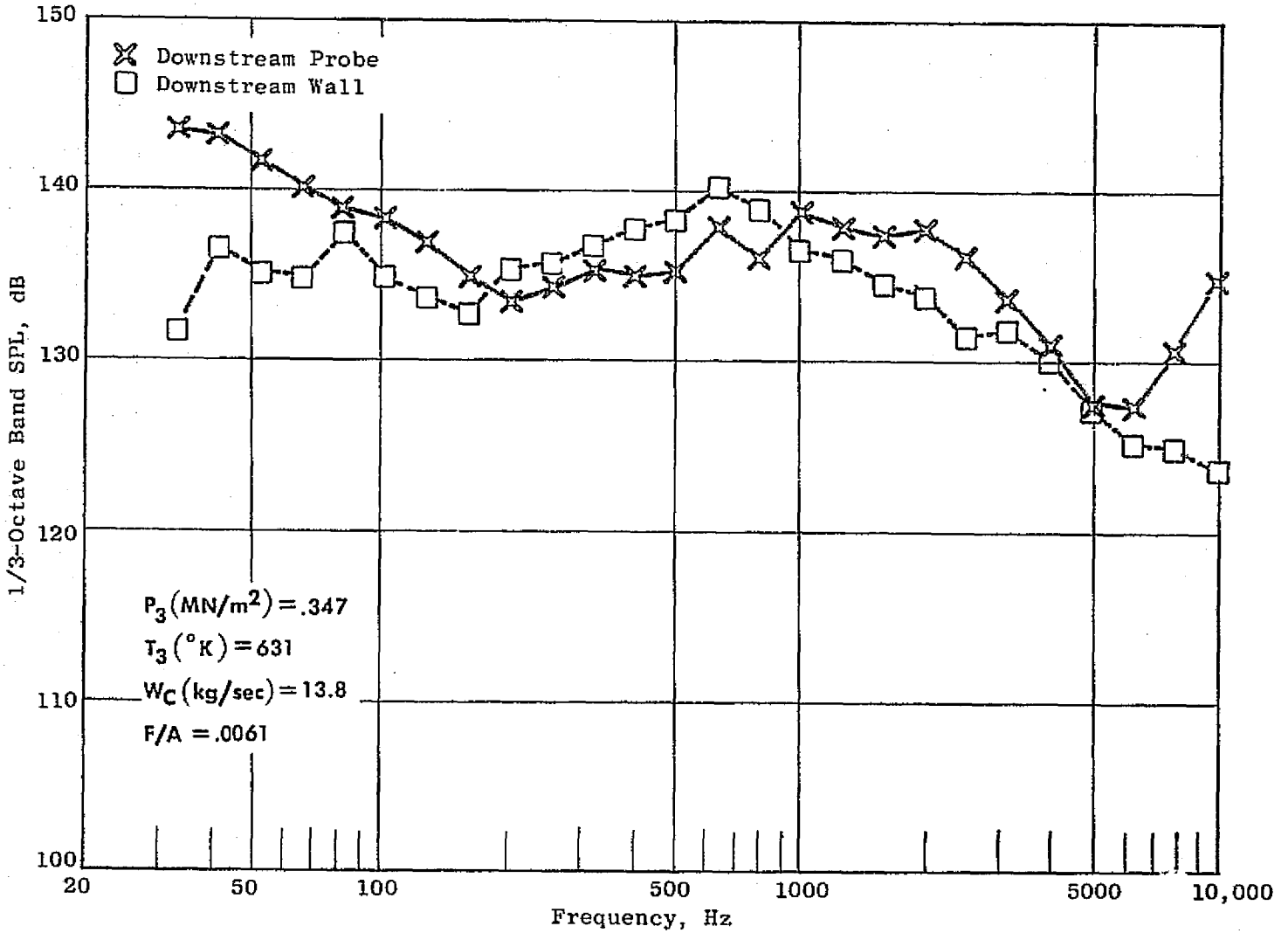

Figure 36. Double Annular, D13, Combustor Noise Reading 716.

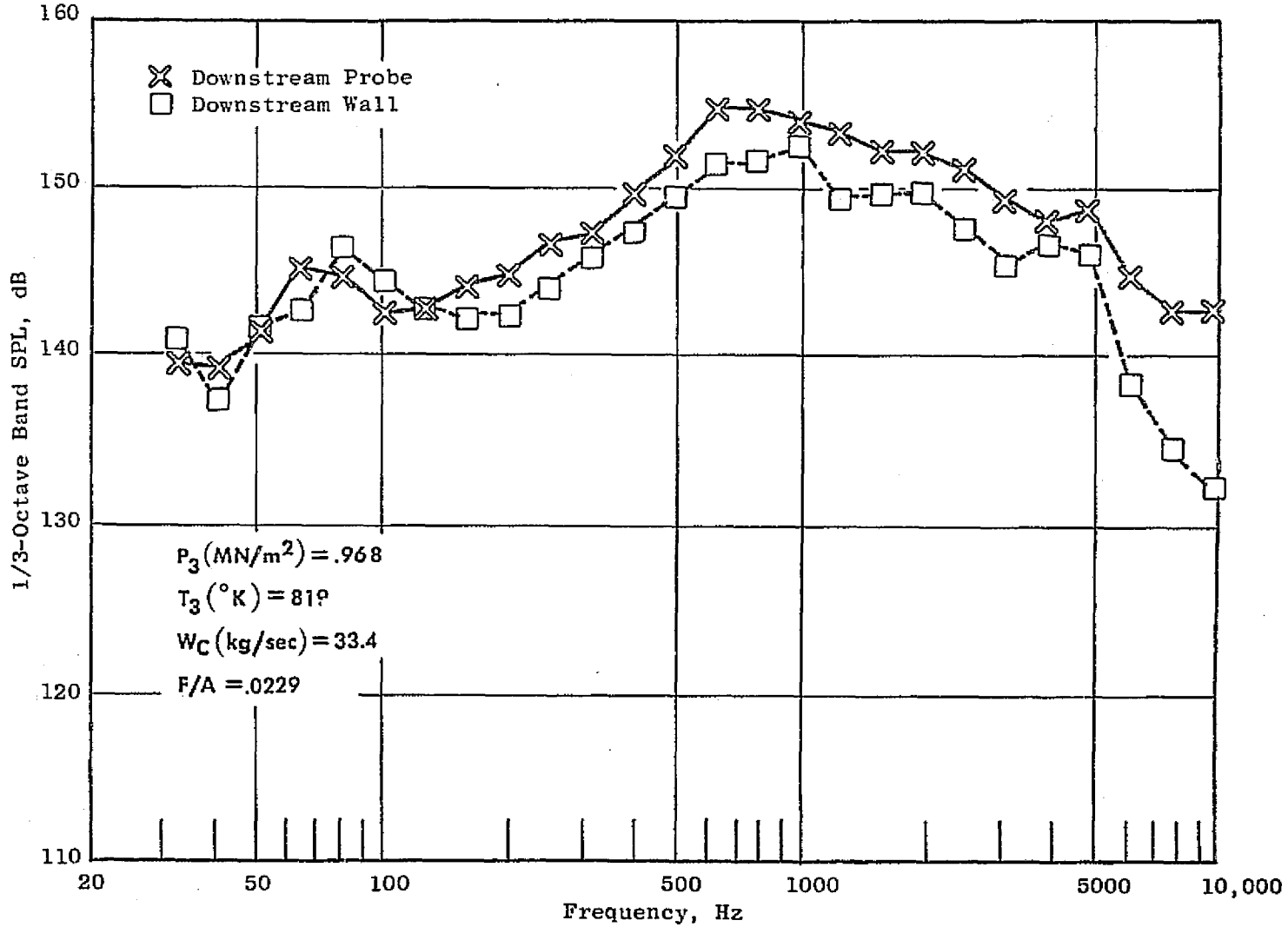

Figure 37. Double Annular, D13, Combustor Noise Reading 699.

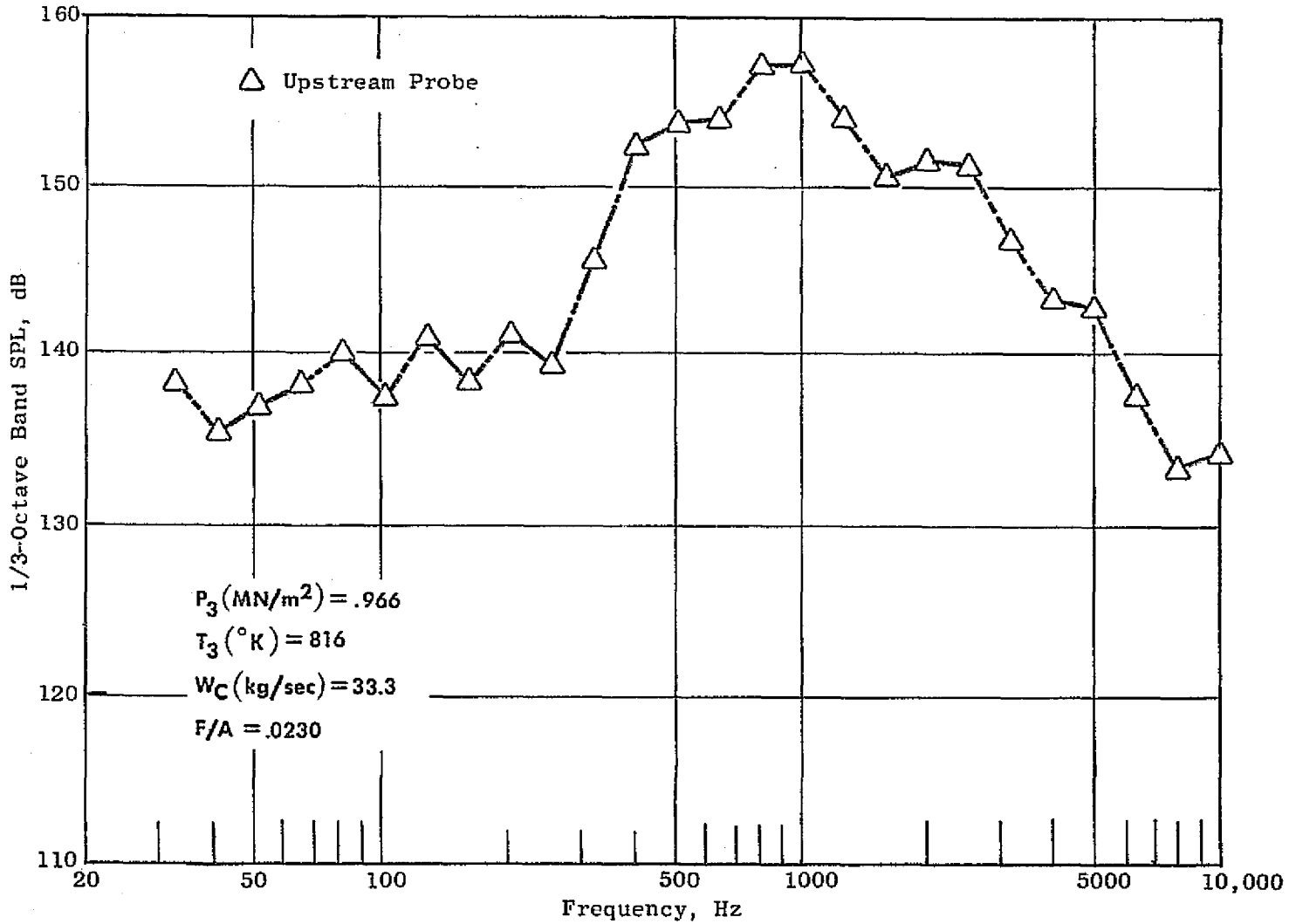

Figure 38. Double Annular, D13, Combustor Noise, Upstream Probe Reading 723.

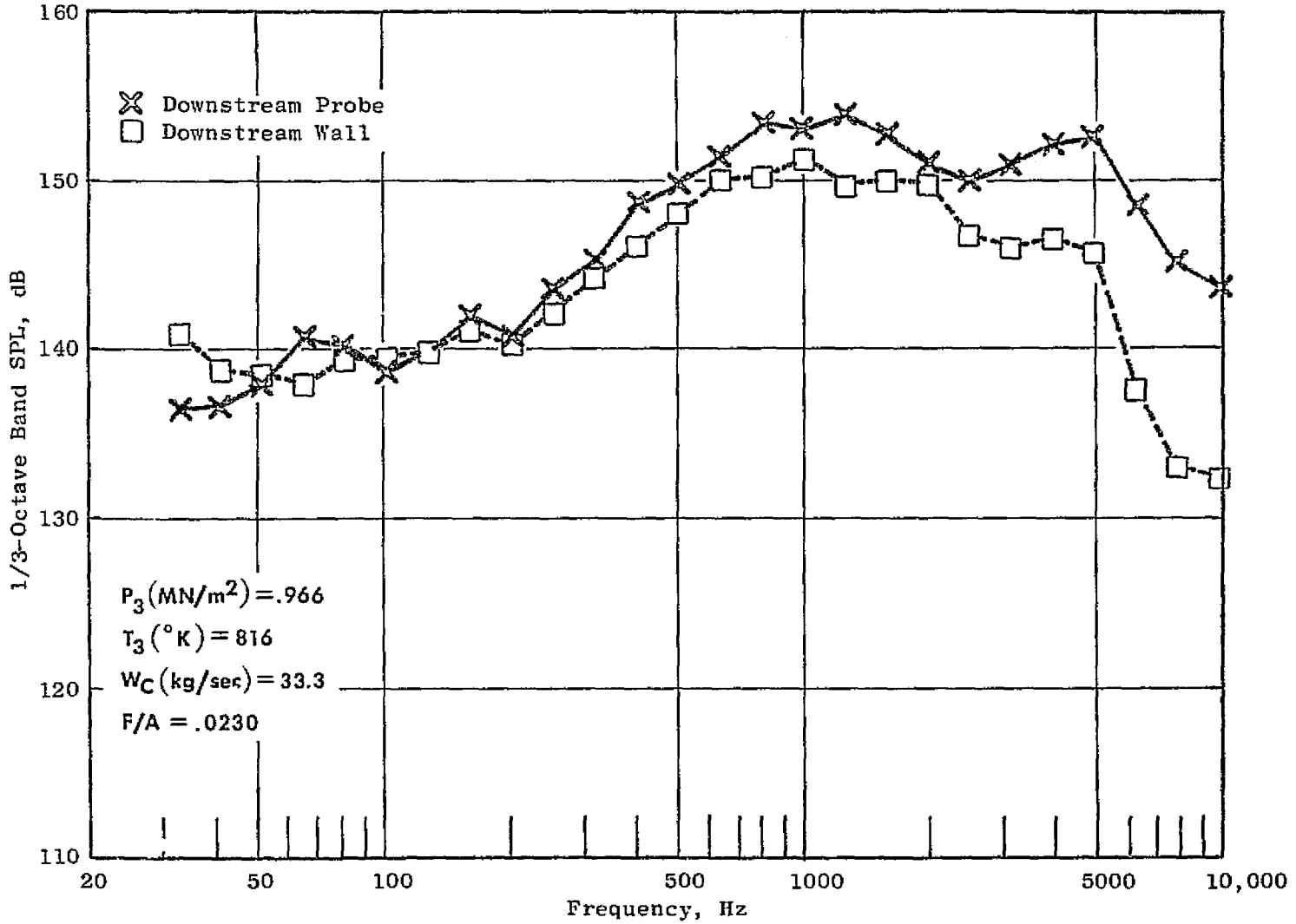

Figure 39. Double Annular, D13, Combustor Noise Reading 723.

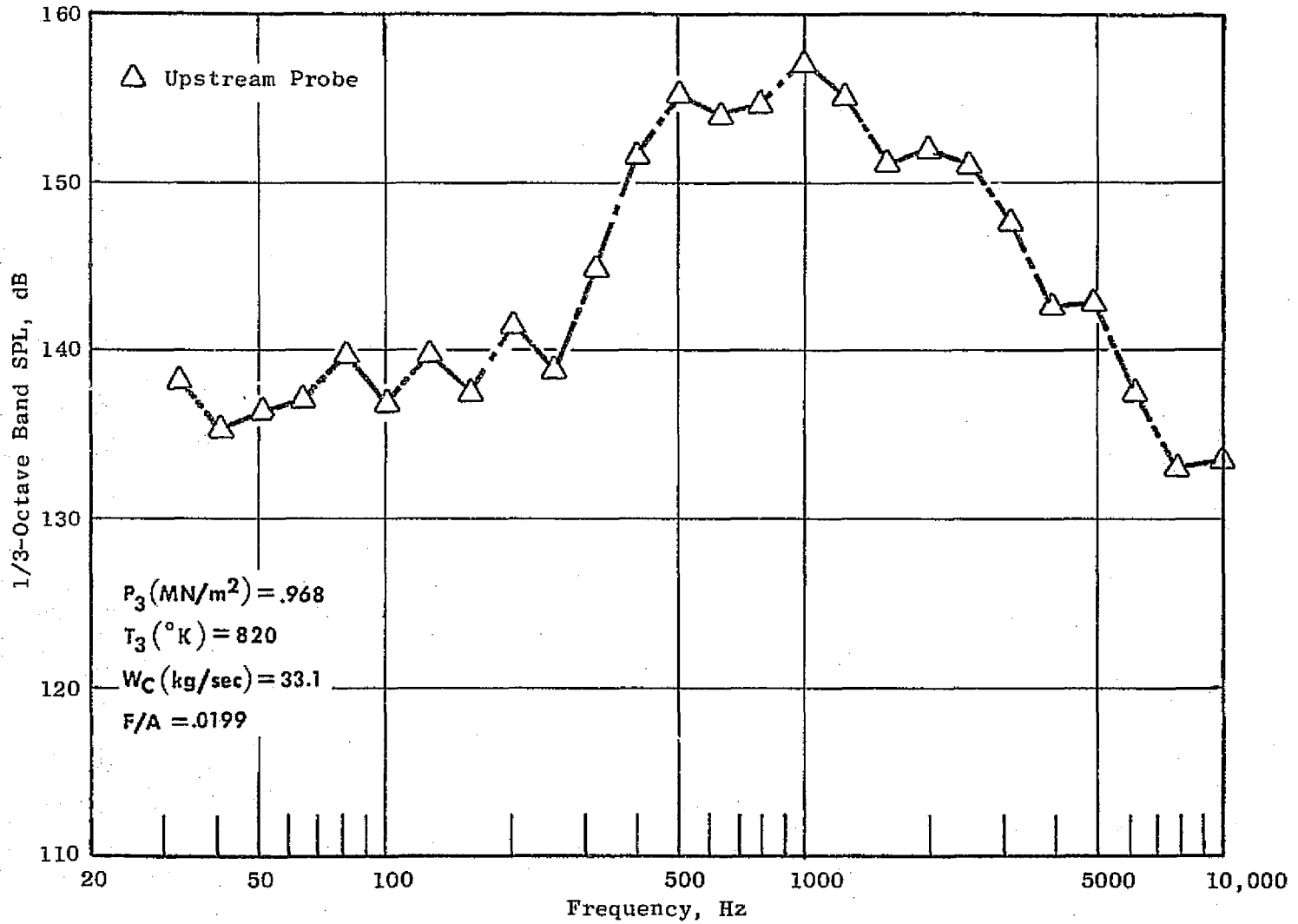

Figure 40. Double Annular, D13, Combustor Noise, Upstream Probe Reading 726.

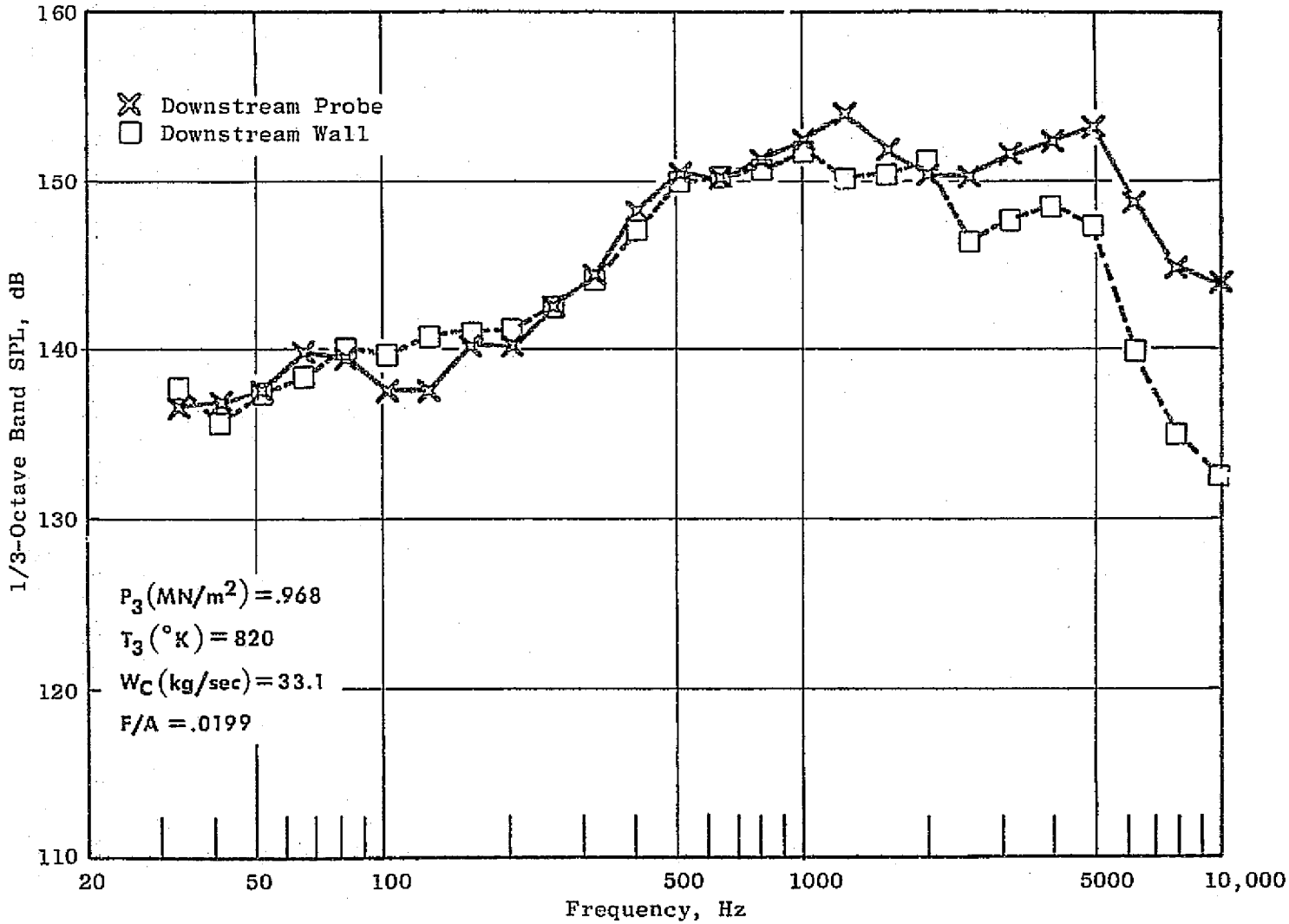

Figure 41. Double Annular, D13, Combustor Noise Reading 726.

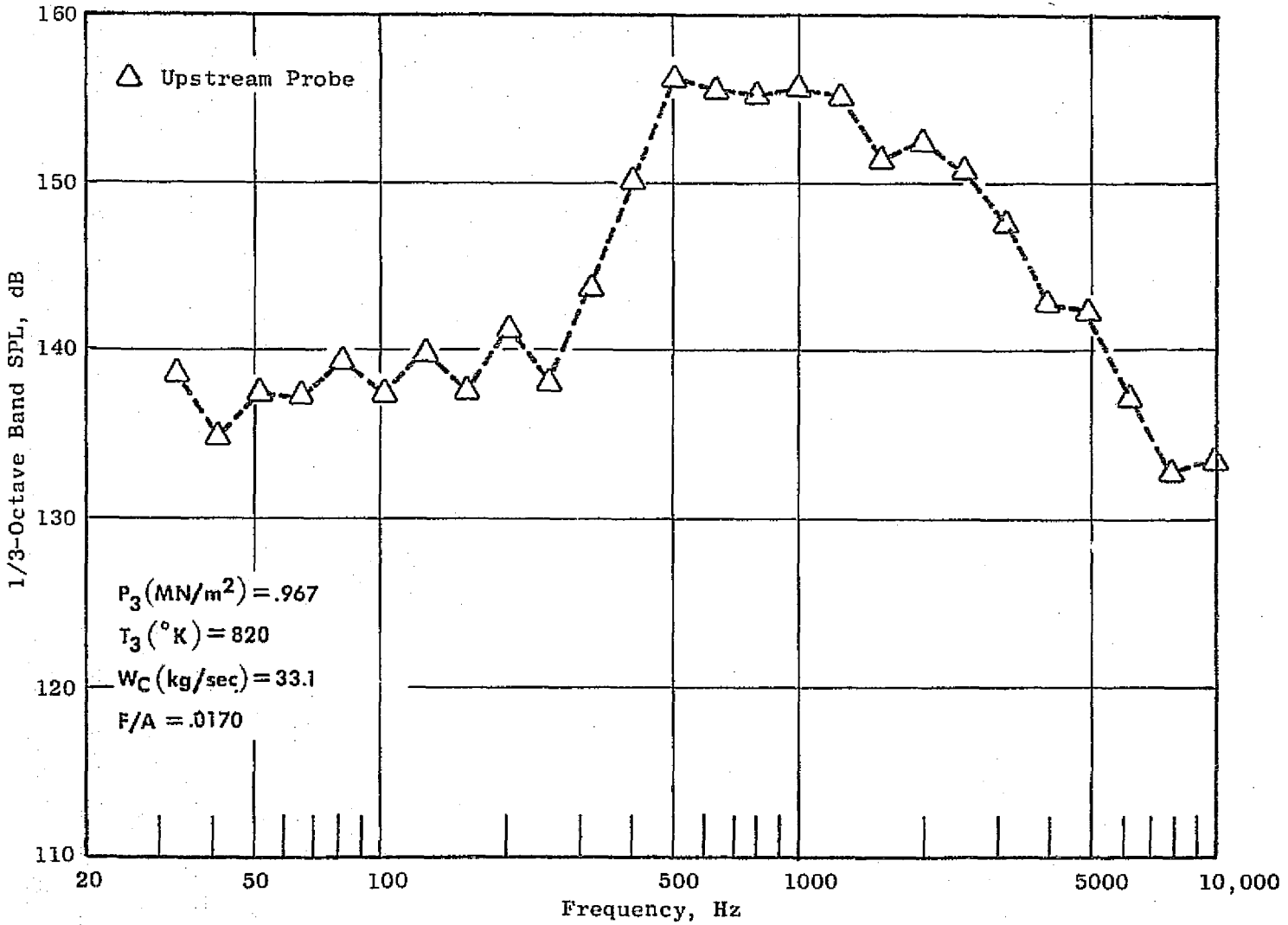

Figure 42. Double Annular, D13, Combustor Noise, Upstream Probe Reading 727.

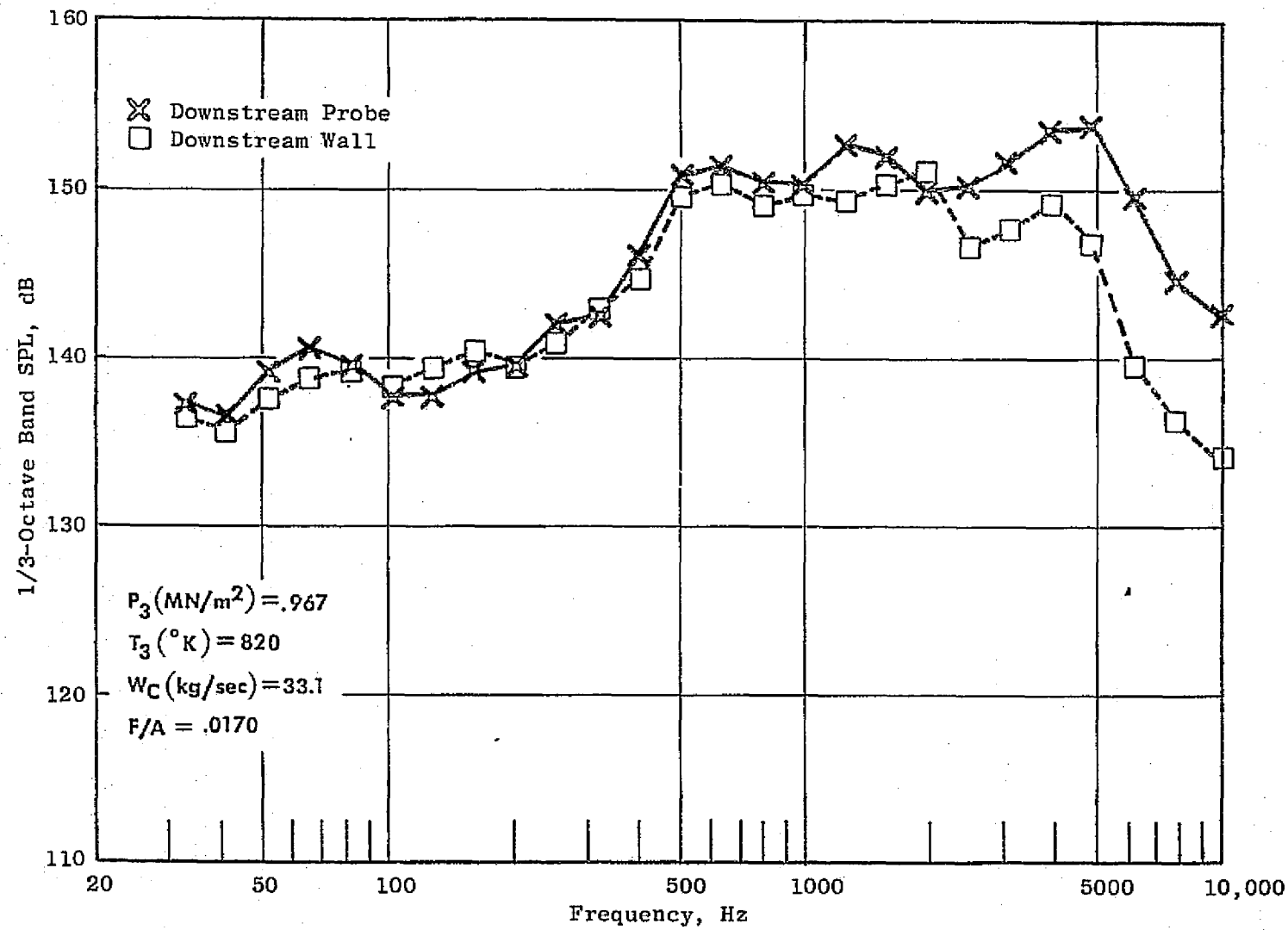

Figure 43. Double Annular, D13, Combustor Noise Reading 727.

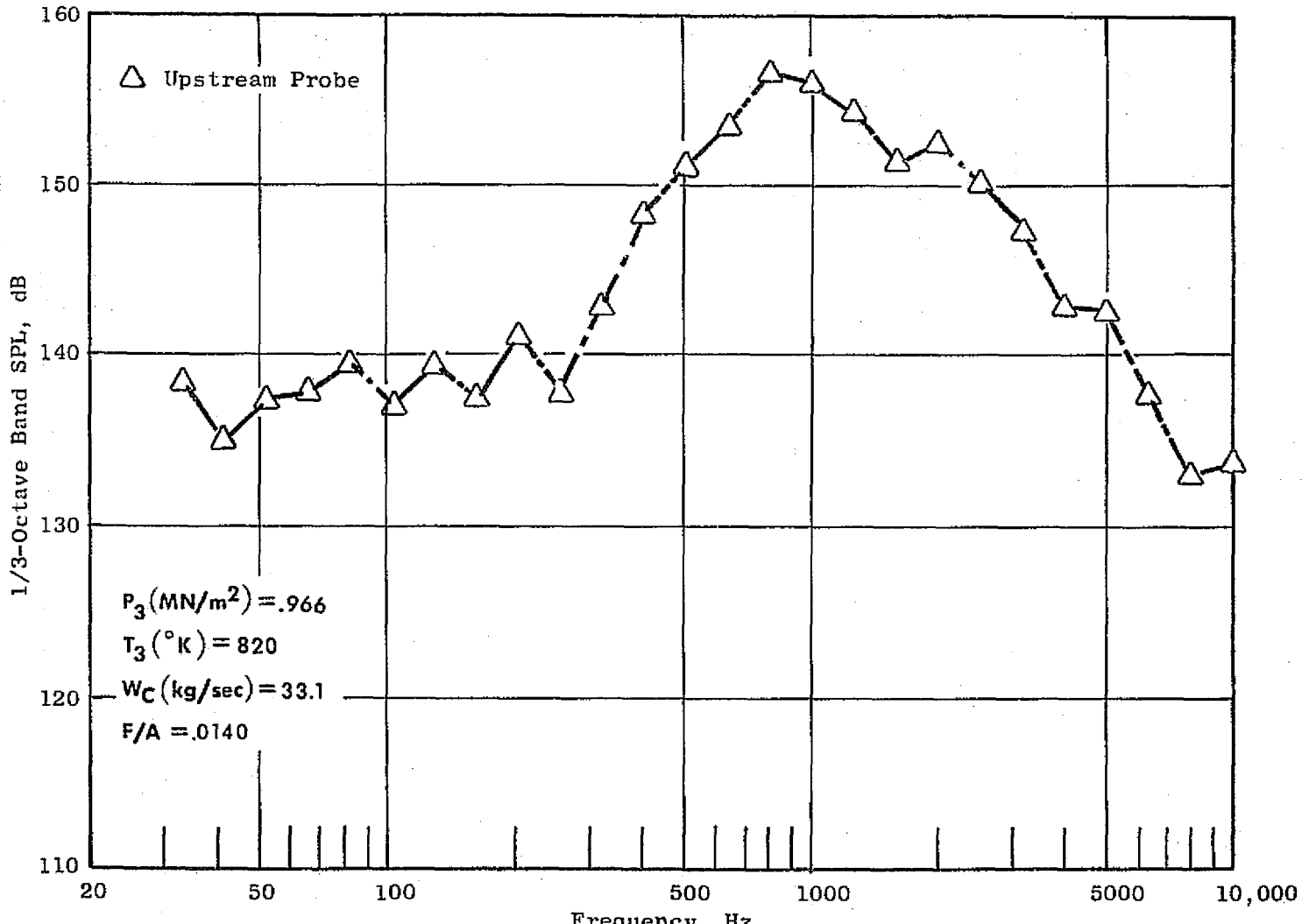

Figure 44. Double Annular, D13, Combustor Noise, Upstream Probe Reading 728.

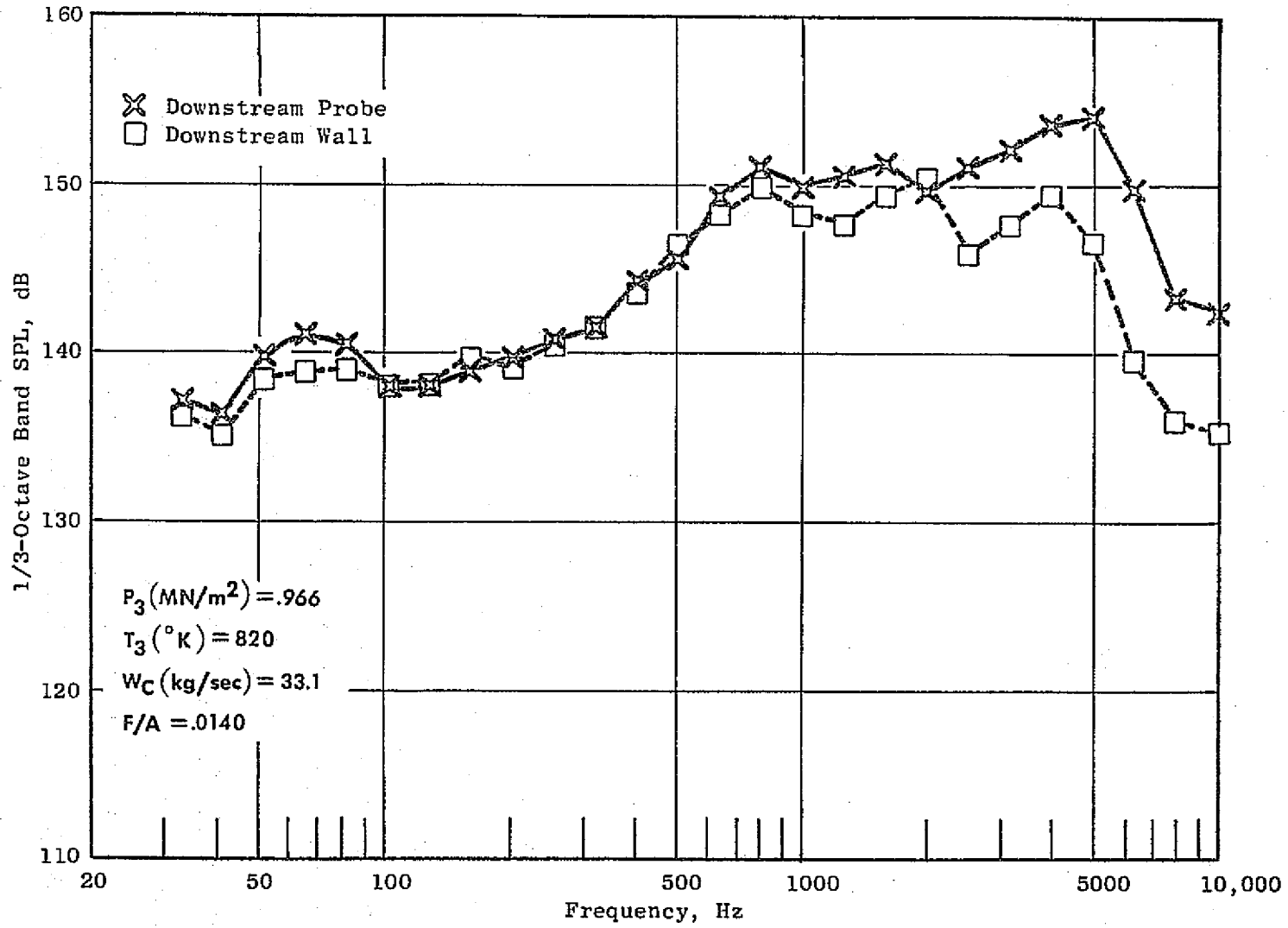

Figure 45. Double Annular, D13, Combustor Noise Reading 728.

SECTION 6.0

DISCUSSION OF RESULTS

Under Phase I of this program six combustors were tested and two additional combustors have been tested under Phase II. Comparisons of the noise characteristics of the Phase II data with five of the six combustors from Phase I were performed. Effects of the various aerodynamic parameters were observed. There was also an additional set of data introduced by the downstream wall static probe utilized in the Double Annular Configuration D-13 test. An evaluation of this data is also presented.

The comparison of the upstream to downstream probe spectra was illustrated in Section 5.2 (Figures 15 to 22). There appeared to be good agreement at the lower frequencies and peak levels. However, above 1000 Hz there was some divergence in the levels seen by the two probes. The difference in the spectral shapes is believed to be due to the propagation path differences for each probe. The downstream probe was directly exposed to the combustor noise source while the upstream probe saw the blockage of the combustor dome and cowl and the impedance change due to an area change in the step diffuser. Thus, the following analysis deals primarily with the probes downstream of the combustor.

In some spectra there was what appeared to be a pure tone which usually occurred in the 500 Hz band. Examples can be seen in Figures 18 and 25. It appears to be a damped resonance in the combustion system. However, it could not be ascertained whether it was caused by the combustor or the test facility. This analysis will not be concerned with resonances but with the broad band noise.

6.1 SOUND PRESSURE LEVEL SPECTRA

The combustor noise spectra were examined with the intent of determining the effect of probe type, fuel-air ratio, and configuration change on the noise levels. A comparison to the engine prediction spectra was also made.

Configuration D-13 had two probes downstream of the combustor, the water cooled waveguide probe which was immersed in the flow and the wall probe which was flush with the air flow path. Spectral comparisons of the two probes can be seen in Figures 23 to 47. The majority of the wall data agree with the probe within a few dB. In Figure 46 the difference in OASPL was 3.1 dB. However, a test condition did occur, Figure 47, where the wall acoustic signal appears to be overcome by the local boundary layer, resulting in a flatter spectrum. The levels of the two probes agree somewhat from 400 to 2500 Hz, which provides the peak acoustic levels, but diverges at both the higher and lower frequencies. For readings 712, 714 and 715 at the low 3.43 atm pressure level (Figures 32, 34 and 35) the situation seems to have

reversed itself. The probe levels indicate higher levels than the wall below 250 Hz and above 1000 Hz. With only one exception the shapes of the spectral data from the two probes were similar, with the wall probe overall sound pressure level being on the average 2.9 dB less than the water cooled waveguide probe. The evaluation of combustor noise was based on the signals from the downstream water cooled probe in order to be consistent with the data previously recorded.

The effect of the fuel-air ratio can be seen in Figures 48 to 51 for both approach and takeoff inlet conditions at both the Phase I and Phase II pressure ranges. As the fuel-air ratio is increased the noise levels appear to increase in some regions of the spectrum and decrease in others; however, the net effect on the overall power level, Figure 52, indicates a consistent increase in noise level with an increase in fuel-air ratio for the same inlet conditions. At the fuel-air ratios below 0.014 the effect of this parameter was masked somewhat by the presence of pure tones at the 6.83 atm pressure and by other broad band noise sources at the 3.44 atm pressure level. It can never the less be concluded that the fuel-air ratio or its resulting temperature rise should be included into a correlation which predicts the overall power level.

Figure 52 also indicates that the Double Annular D-13 takeoff levels are consistently higher than the CF6-50, while the approach levels appeared to fall on the same line. Comparing the takeoff spectra, Figure 53 (for the same 0.0139 fuel-air ratio) shows a greater increase in D-13 level over the CF6-50 occurring at frequencies greater than 630 Hz. With the fuel-air ratio increased to 0.0229 (Figure 54) the difference is uniform across the spectrum. At this higher fuel-air ratio the spectra were roughly similar and peaking in the 630 to 1000 Hz range.

Since the Double Annular combustor was tested at the lower Phase I (Reference 3) pressure levels also, it can be directly compared to spectra for the Double Annular combustor Configuration II-11. At both takeoff and approach, Figures 55 and 56, there is good agreement for both the spectral shape and level.

The two combustors were compared to the engine prediction spectrum and spectral envelope (Reference 4). The prediction spectrum had been used for predicting combustor noise from an engine. The actual engine data were found to fall in a range between the prediction spectrum and the spectral envelope which forms an upper bound to the range of data. The frequency at which the peak was set for engine data was 400 Hz ± a 1/3-octave band. From examining the component combustor spectra it was observed that indeed the spectra do fall in the same shape range between the prediction spectrum and spectral envelope. However the frequency at which the peak occurred was 1000 Hz, for all of the data from both the CF6-50 and D-13 (see Figure 57). There was good agreement from 200 Hz to 4000 Hz. The combustor noise peak occurring at 1000 Hz was in general true for the configurations tested under Phase I. Some typical examples were shown in Figure 58.

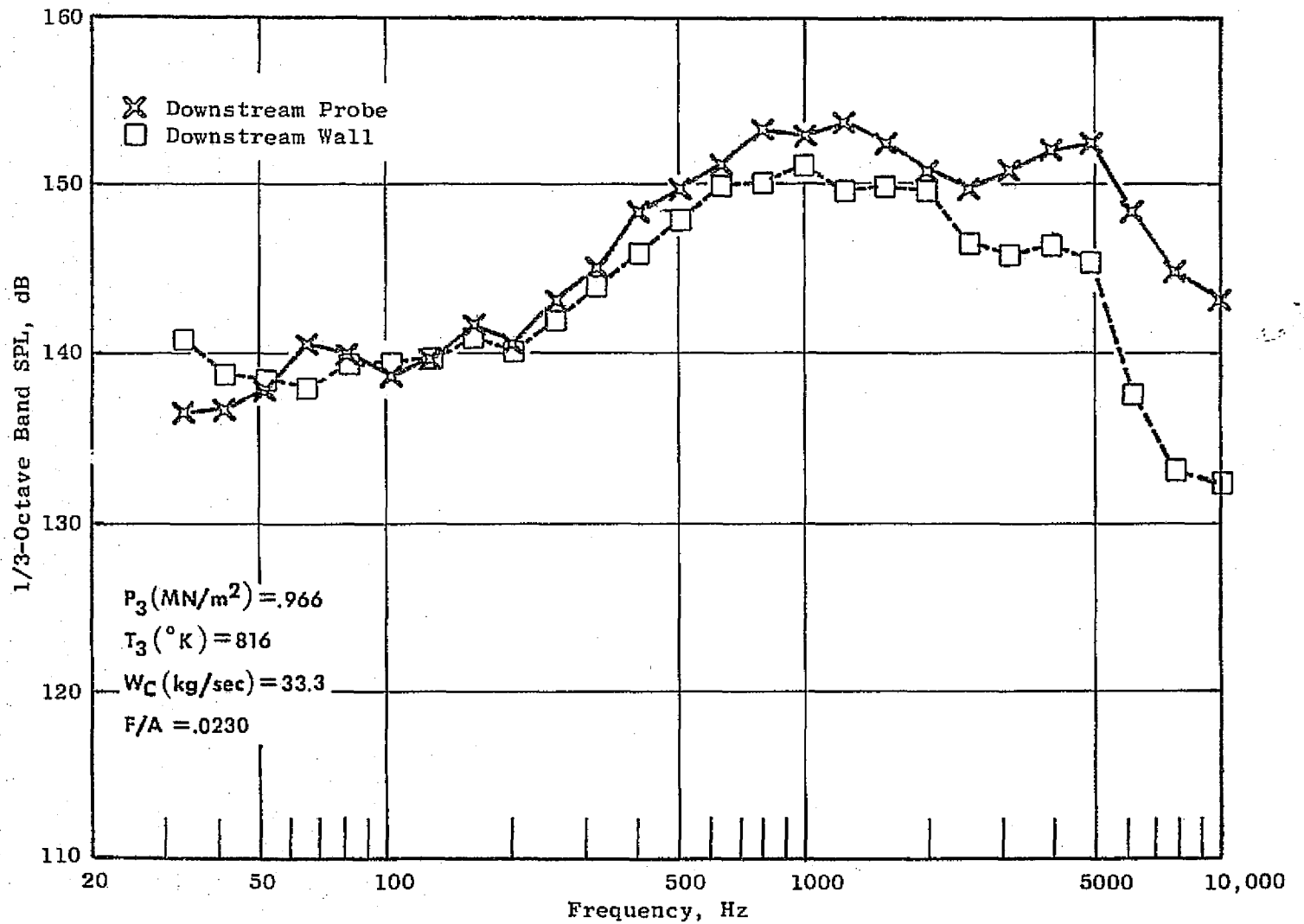

Figure 46. Comparison of Downstream Probe to Wall Spectra, Reading 723.

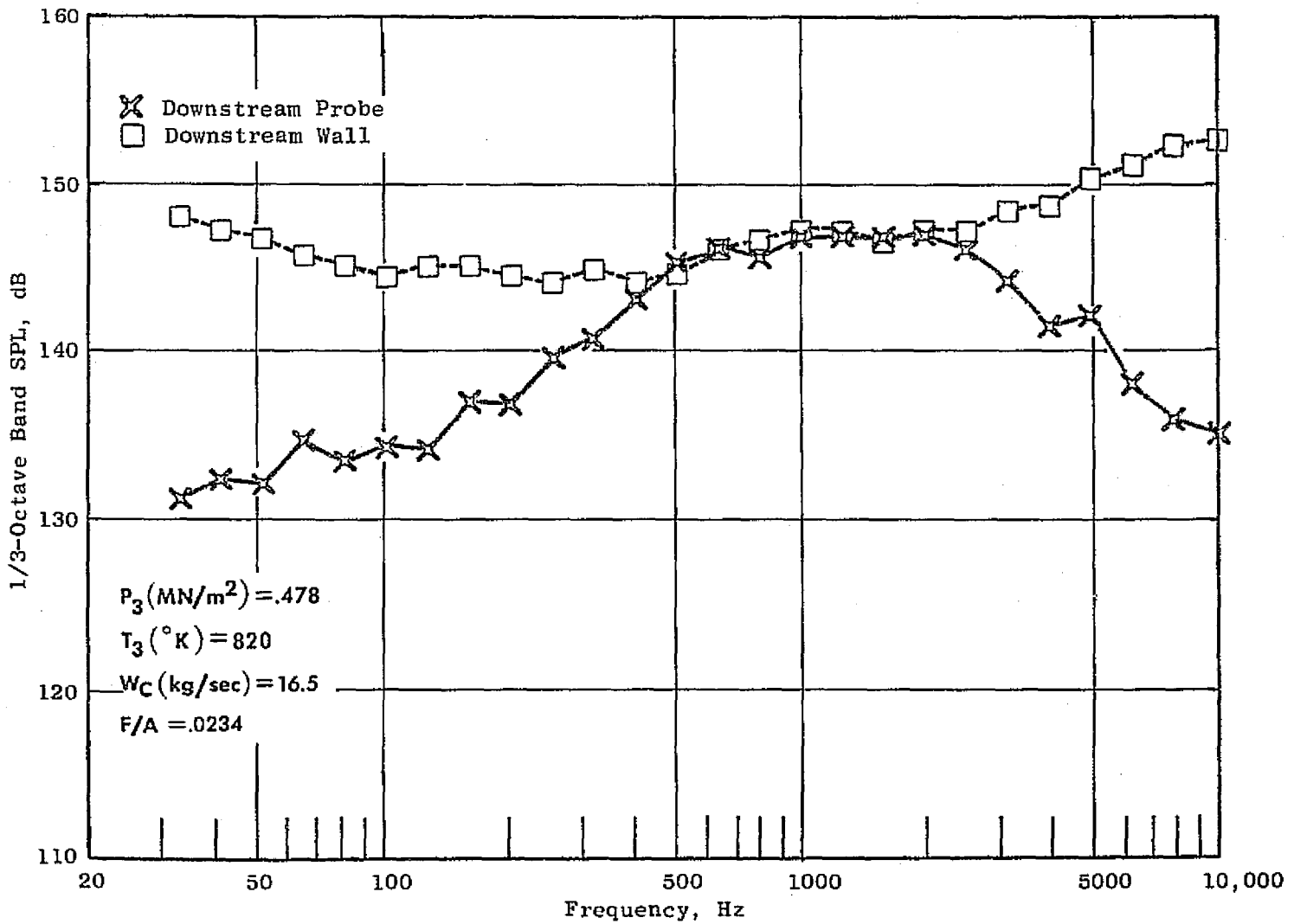

Figure 47. Comparison of Downstream Probe to Wall Spectra, Reading 748.

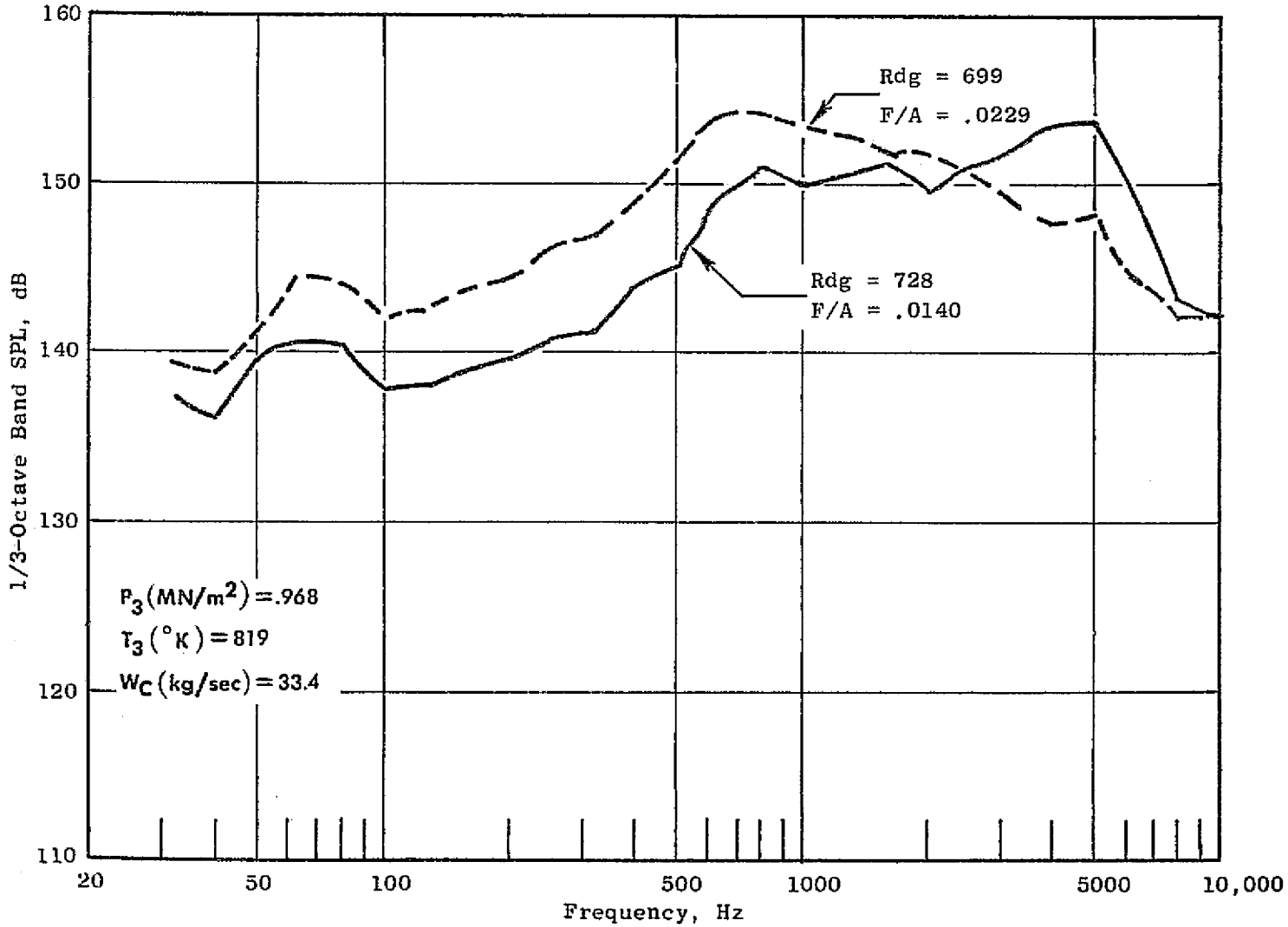

Figure 48. Effect of Fuel-Air Ratio on D13 at a Takeoff Inlet Condition.

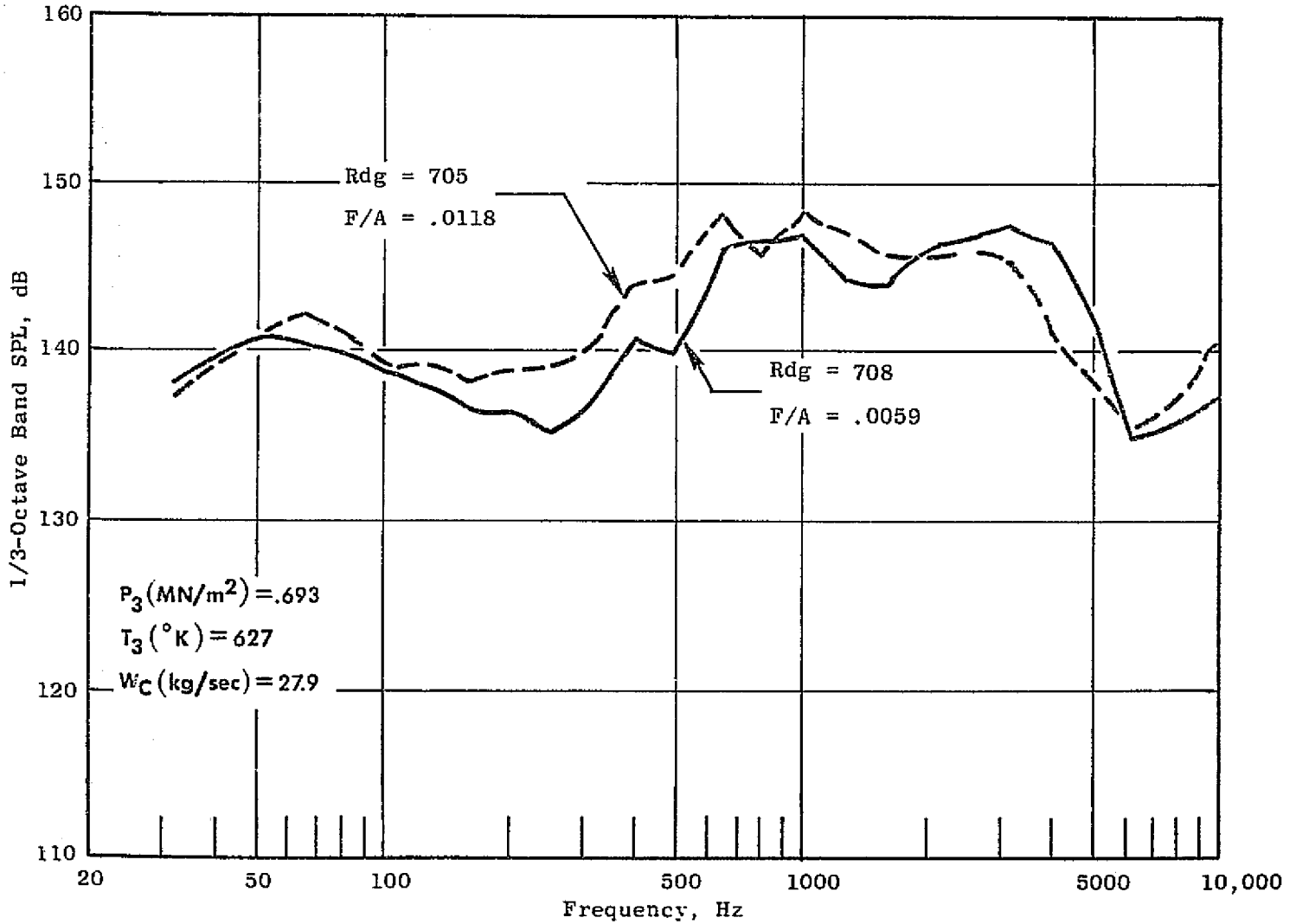

Figure 49. Effect of Fuel-Air Ratio on D13 at an Approach Inlet Condition.

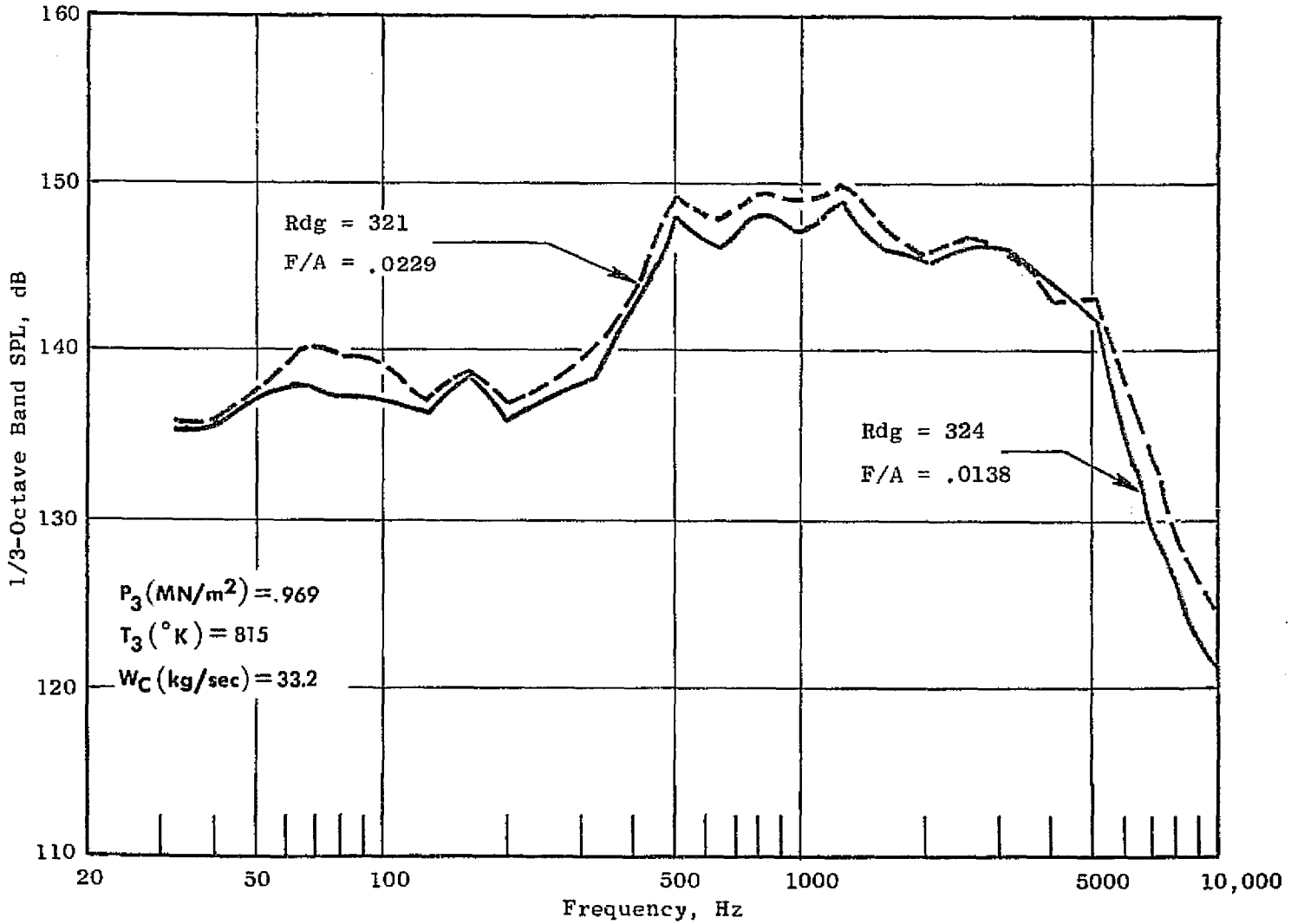

Figure 50. Effect of Fuel-Air Ratio on CF6-50 at a Takeoff Inlet Condition.

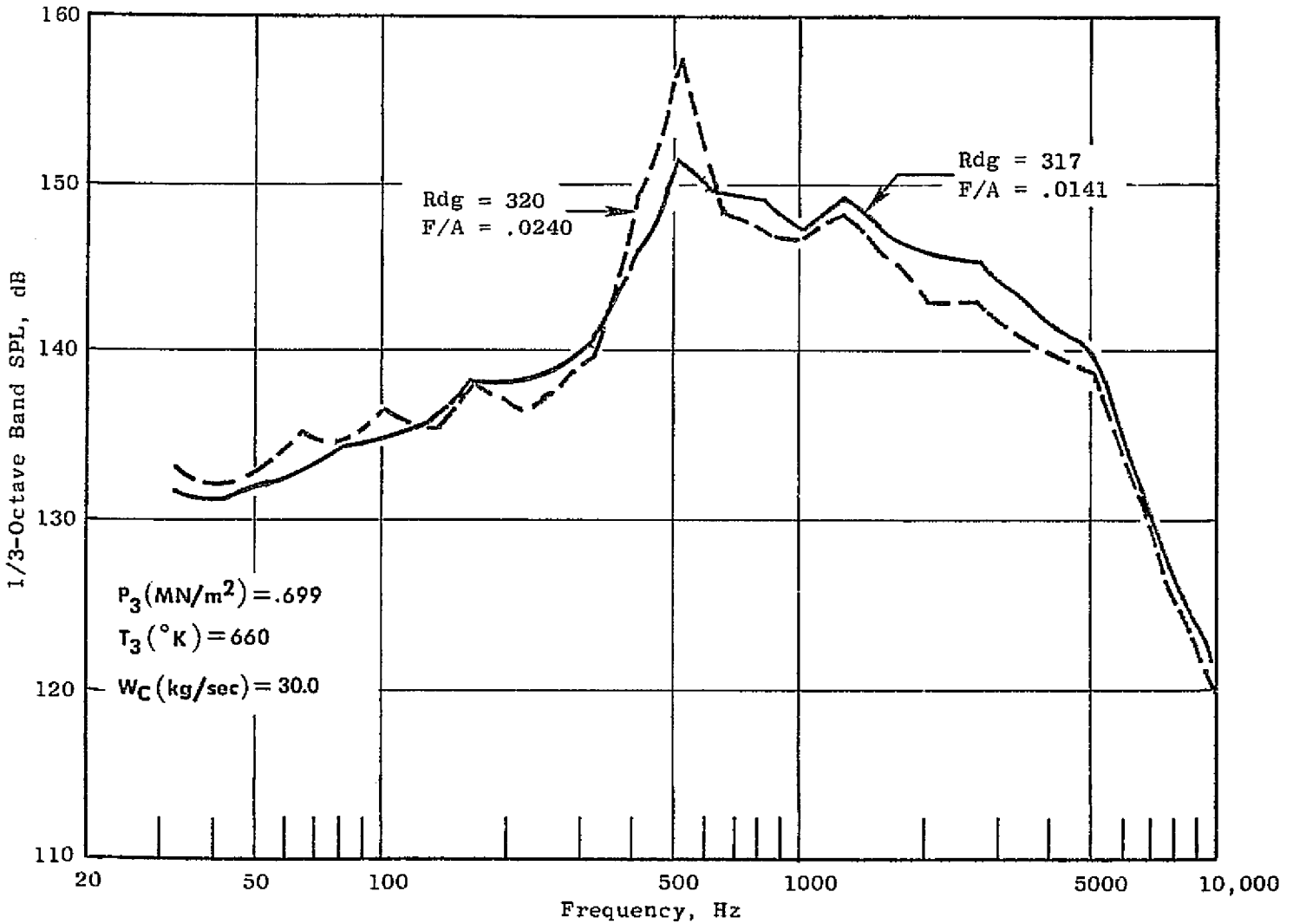

Figure 51. Effect of Fuel-Air Ratio on CF6-50 at an Approach Inlet Condition.

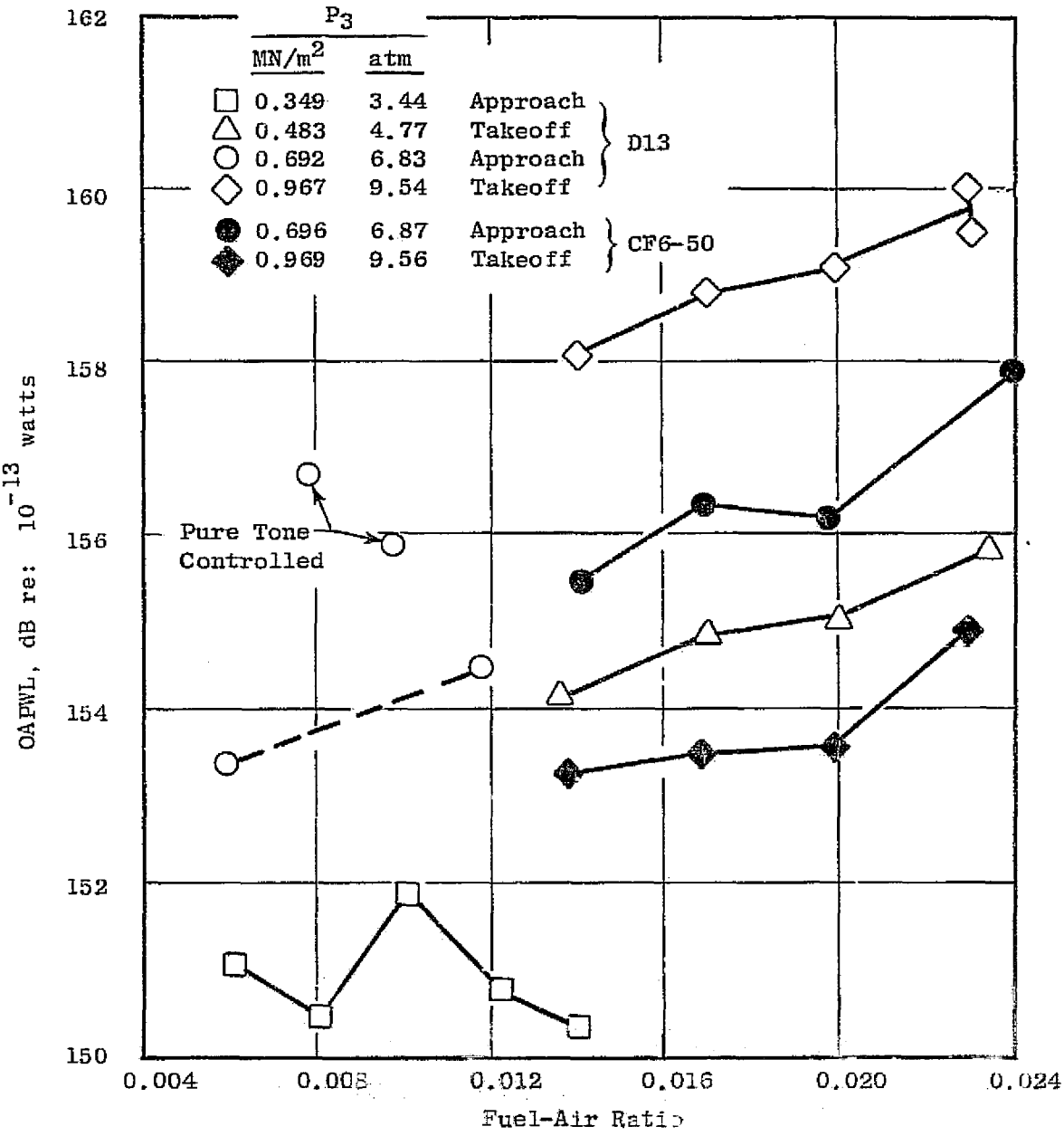

Figure 52. Effect of Fuel-Air Ratio on the Overall Power Level.

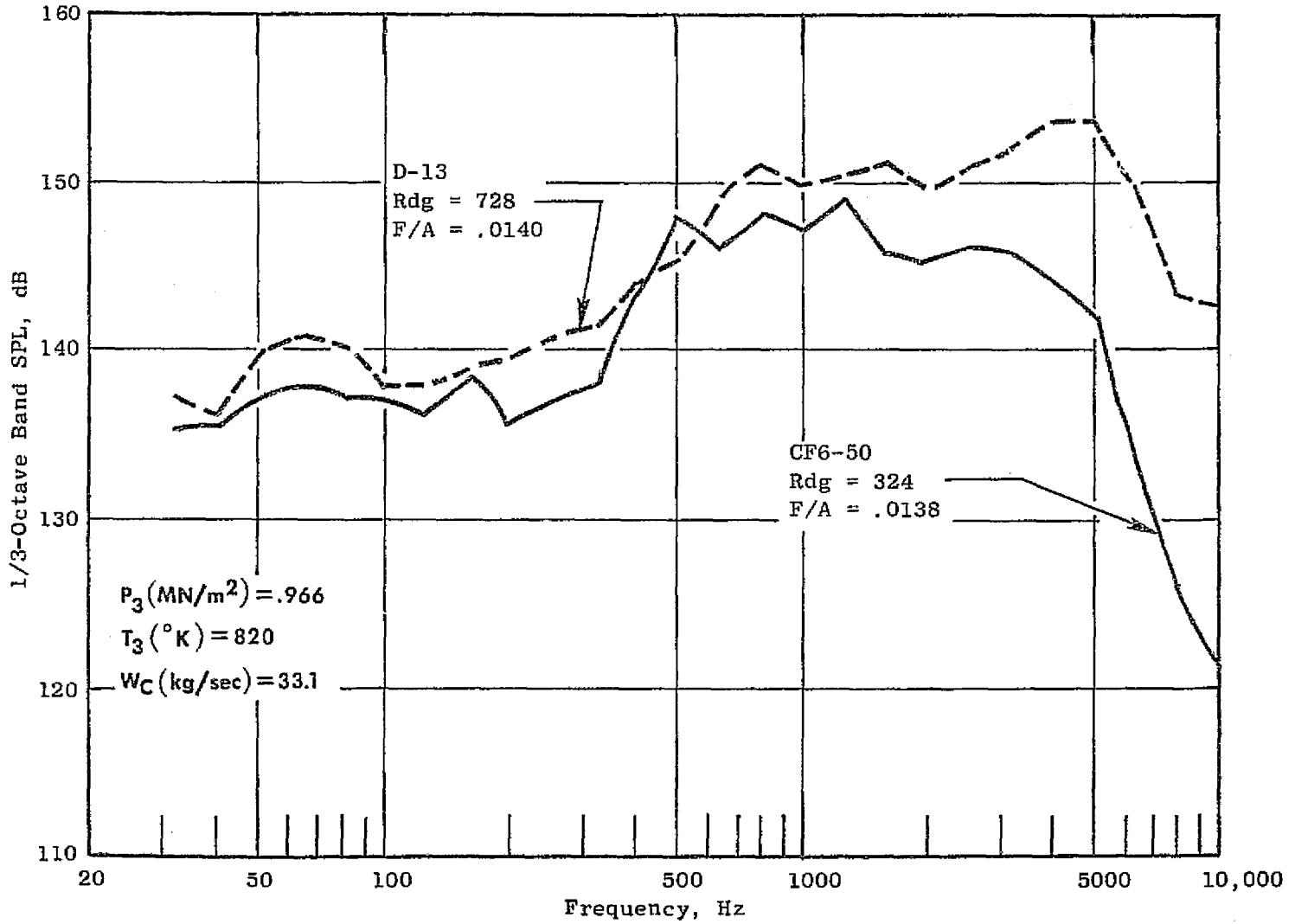

Figure 53. Comparison of CF6-50 to D13 at Takeoff Inlet for Fuel-Air Ratio of 0.0140.

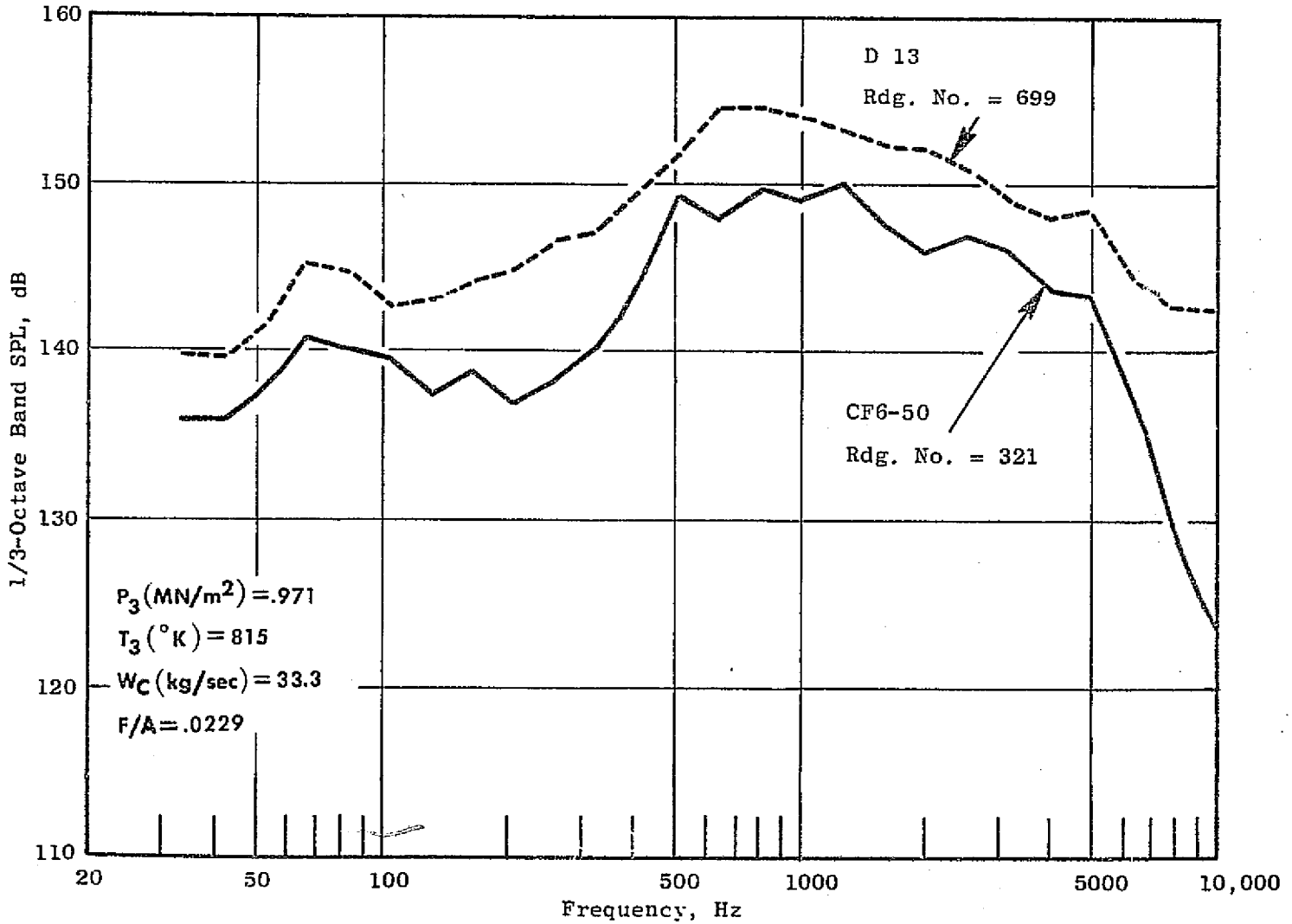

Figure 54. Comparison of CF6-50 to D13 at Takeoff Inlet for Fuel-Air Ratio of 0.0229.

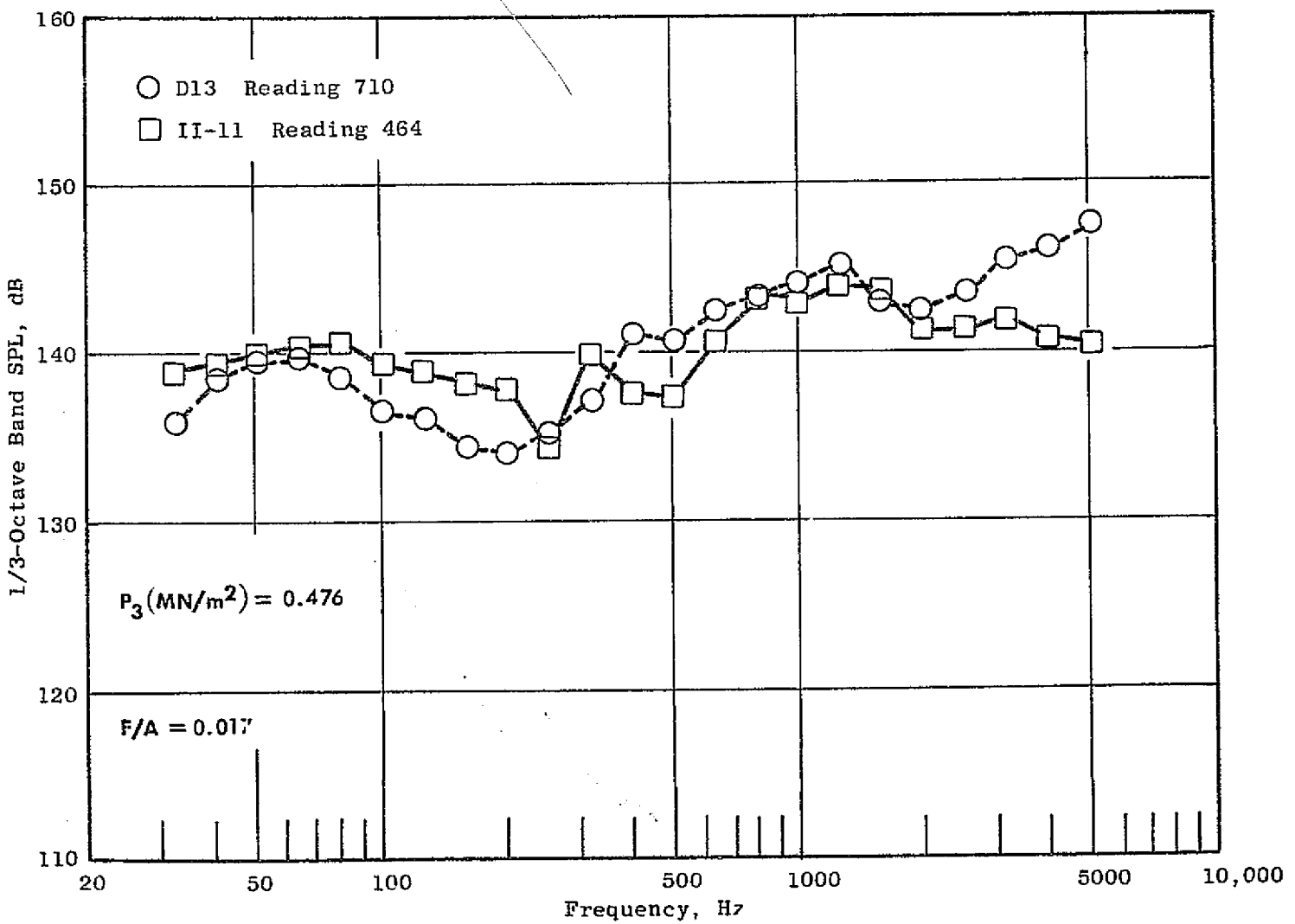

Figure 55. Comparison of Double-Annular Combustor Configurations D13 and II-11 at Takeoff Inlet Conditions.

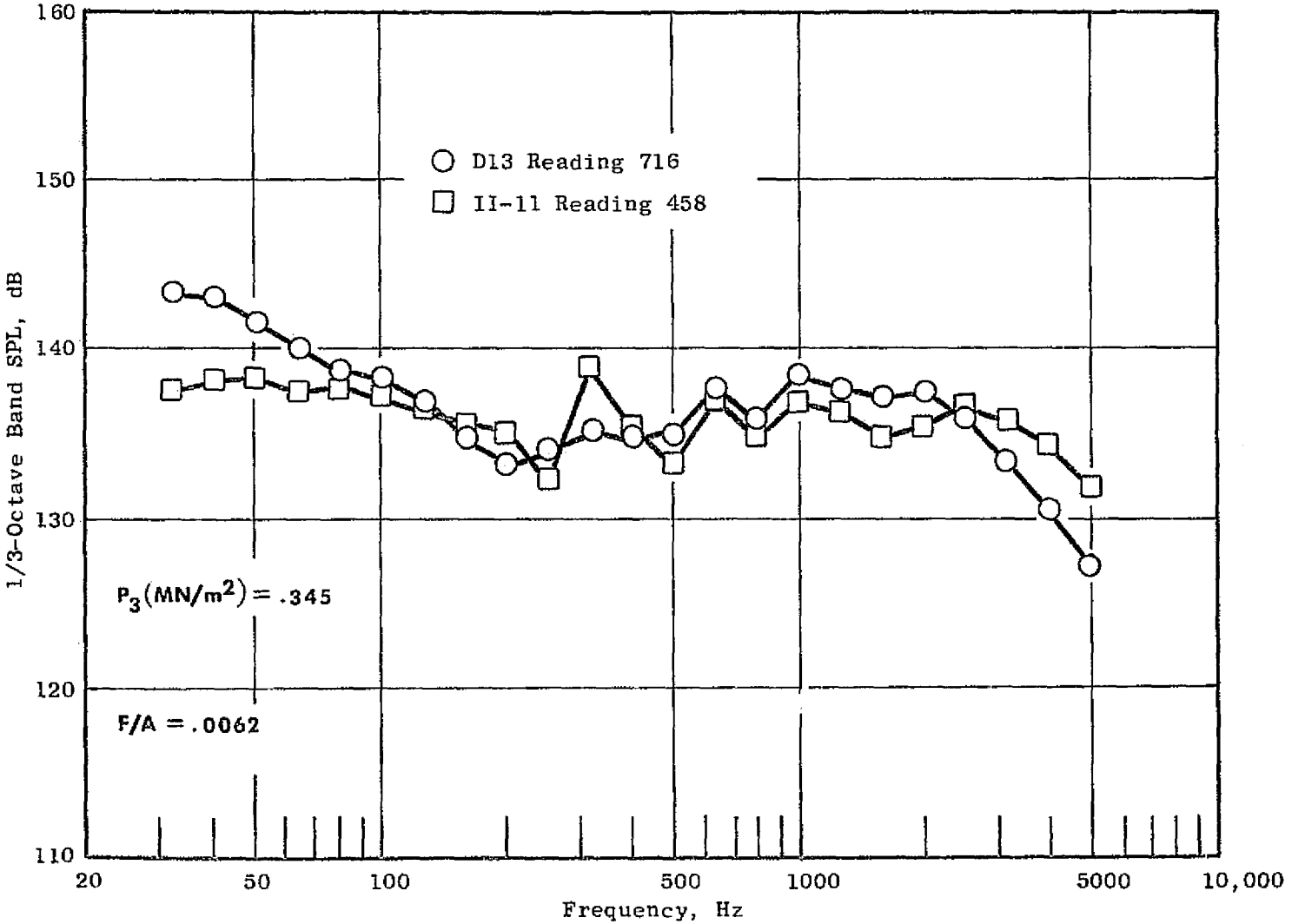

Figure 56. Comparison of Double-Annular Combustor Configurations D13 and II-11 at Approach Inlet Conditions.

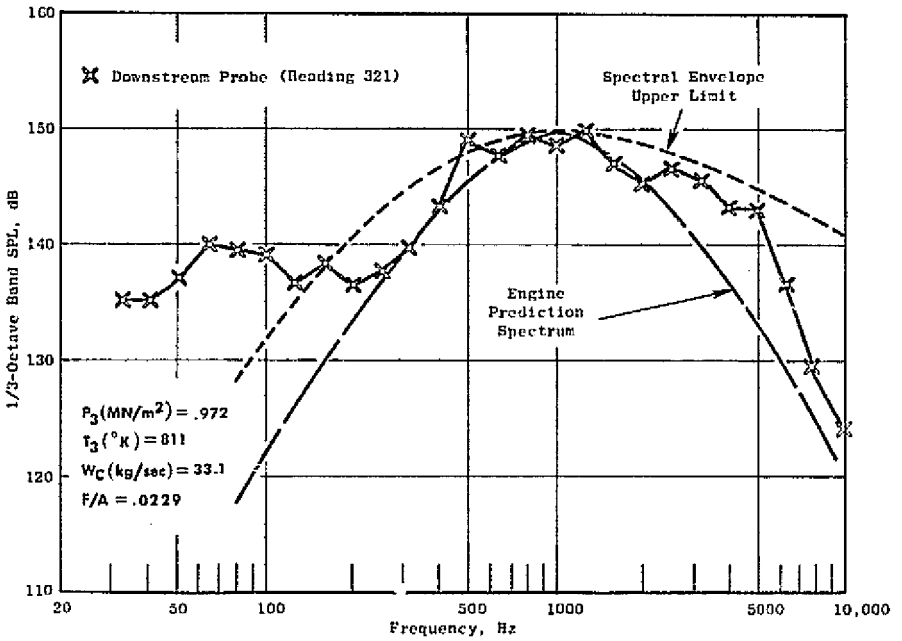

Comparison of CF6-50 Combustor to Prediction Parameter.

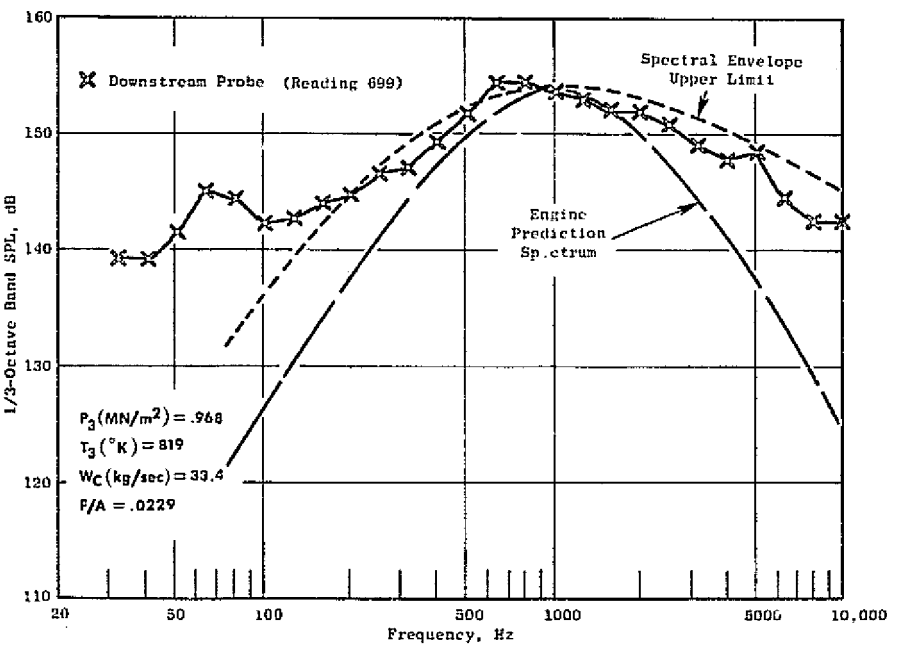

Comparison of D13 Combustor to Prediction Spectra.

Figure 57. Comparison of CF6-50 Combustor and D13 Combustor to the Prediction Spectra.

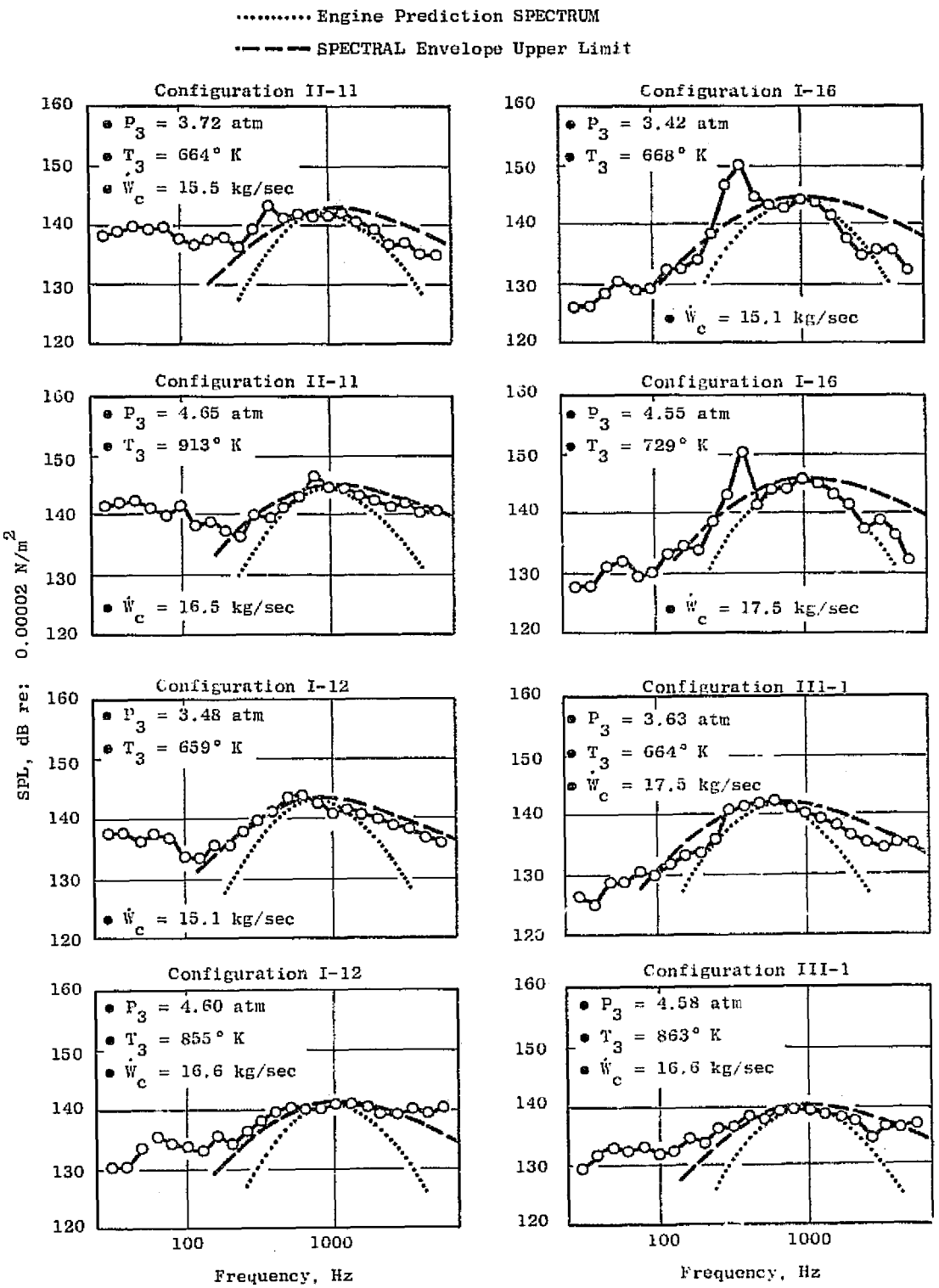

Figure 58. Comparison of Phase I Configurations at Fuel-Air Ratio of 0.0245 to the Prediction Spectra.

Some of the measured combustor noise spectra could be called double humped. Of the two humps the major peak was the broad band hump centered around 1000 Hz. This was believed to be related to the combustion process since its level varied with fuel-air ratio. The second peak was lower in frequency, in the 31.5 to 200 Hz range. It was not possible to determine the cause of this hump. These lower frequency pressure levels were not believed to be combustion related since they were not influenced by the fuel-air ratio as the 1000 Hz hump was. The hump may be related to flow noise generated in the test rig. There were occasions, such as when the fuel-air ratios were below 0.012, that the 1000 Hz levels were as low as the lower frequency hump. When this occurred the overall pressure levels were influenced to some extent. This influence was ignored in the analysis. It was, however, kept in mind that at the lower fuel-air ratios a noncombustion-related source could influence the overall level.

For component noise prediction purposes it is suggested that the engine prediction spectrum also be used for the prediction of combustor noise from a CF6-50 size combustor. The frequency at which the peak should be set is 1000 Hz. The difference between the peak frequency observed in engine data and the component peak frequency may be attributed to the effects of the turbine blade rows and nozzle end impedance.

6.2 ACOUSTIC POWER LEVELS

In order to provide a common basis of comparison of the combustor noise source, it was decided to evaluate the noise on a power level basis. The reason for using the power level was the independence of position or location. However, the use of the power level implied a knowledge of the source of the sound. It was assumed that the noise was generated in the combustor and propagated in the plane-wave mode past the downstream probe. In an engine this would be the acoustic energy that would propagate through the downstream turbine and exhaust nozzle to be radiated to the far field as core noise. The acoustic power levels were calculated based on the measured downstream sound pressure levels which were corrected for the local Mach number, pressure, temperature and annulus area. The overall power levels are based on the overall sound pressure levels and corrected in the same manner. The details of the calculation can be found in Appendix B.

The overall power levels of the combustors from Phase I (Reference 3) and the current tests are plotted as a function of the engine prediction parameter, (Reference 4) in Figure 59. It was observed that the component combustor noise levels were consistently higher than the turbofan engine data, and they appeared to exhibit a somewhat flatter slope than the engine data. This suggested 1) that there was an attenuation of the combustor noise levels as they traveled from the combustor through the turbine blade rows, exhaust nozzle and jet and/or 2) the prediction parameter for component combustor noise is different from the parameter used to predict core noise from engines, possibly because of the absence of the turbine, core nozzle and jet. Thus it may be necessary to determine first a correlation for the combustor noise at the source and then the effect of propagation through the attenuation mechanisms in the engine.

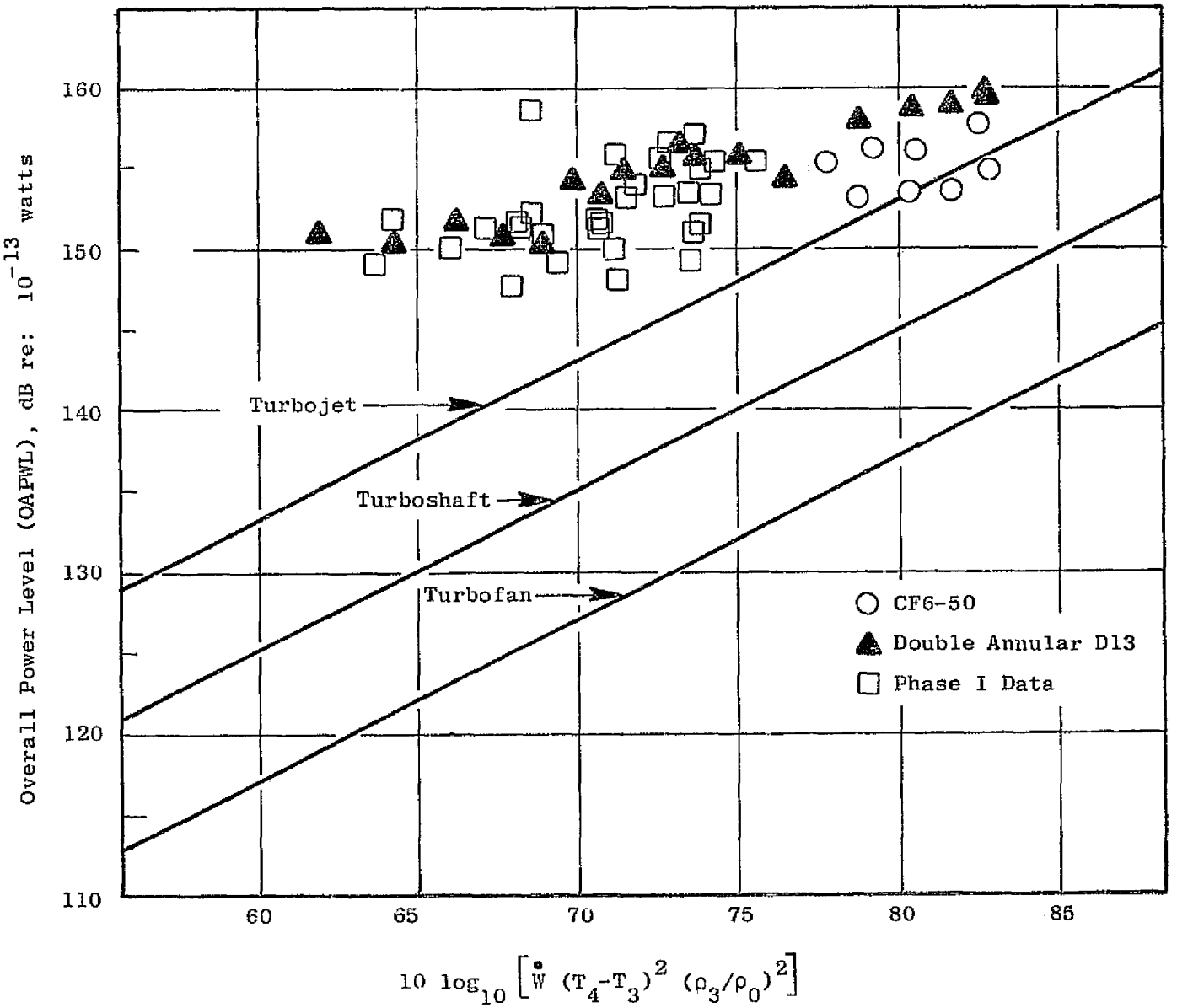

Figure 59. Comparison of Combustor OAPWL to the Engine Prediction Parameter.

The problem of predicting combustor noise using various steady-state and fluctuating aerodynamic parameters has been examined in the literature (References 3 and 4). However, in order to arrive at a prediction capable of being used by an engine designer during the preliminary design of an engine it would be advantageous if only the steady-state parameters determinable from an engine cycle could be used. It was also initially desirable to hold some geometry parameters constant. As a consequence of the basic pollution program that required placement of the final ECCP combustor in a CF6-50 engine, the combustor diffuser duct and the CF6-50 combustor envelope were maintained constant for all of the combustors reported under Phase I (Reference 3) and Phase II. Therefore only the details of the combustor geometry were changed thus eliminating other extraneous effects. The data from Phase I involved some significant geometry changes. There were large variations in the way fuel entered the combustion zone and how it was mixed. Under Phase II, only two combustors were tested, the CF6-50 and Double Annular Configuration D-13. Of the two, Configuration D-13, was tested over a wider range of inlet temperatures, pressures and flow rates than any of the previous combustors. It was felt that a correlation of the noise to the steady-state aerodynamic parameters based on this combustor could be used 1) as a basis to evaluate the effect of modifications in the configuration and 2) to provide a preliminary design prediction parameter.

The parameters that were selected for a final correlation with the overall power level were the air flow rate, $\dot{W}$, the temperature rise, (T_4-T_3), and the inlet temperature, T_3, and the inlet pressure P_3. These variables are sufficiently easy to determine in an engine cycle for preliminary design predictions.

A statistical correlation involving a linear multiple regression analysis was applied to the set of D-13 data. The result of the correlation, was a parameter of the form:

$$OAPWL = 102.7 + 10 \log_{10}\left[\dot{W}^{1.29}(T_4-T_3)^{0.79}\ T_3^{0.48}\right] \qquad (1)$$

The standard deviation from the mean line (Figure 60) was 0.90 dB. The correlation did not require the effect of an inlet pressure to be included separately. This may be because the inlet pressure and temperature are related through the ideal gas law even though they were varied independently. The air flow rate and temperature rise are each approximately to the first power. The product of these two terms is directly related to the heat release rate.

The correlation Equation (1) from D-13 was compared to some of the other combustor configurations. It was observed, Figure 61, that each configuration fell into one of two categories. The first category (Configurations II-11, II-12 and I-16) consisted of data that fell on a single line parallel to the D-13 line but separated by some constant distance. The second category (Configurations I-12, III-1, and CF6-50) fell on two parallel lines each separated by a different constant distance. Of the second category the points

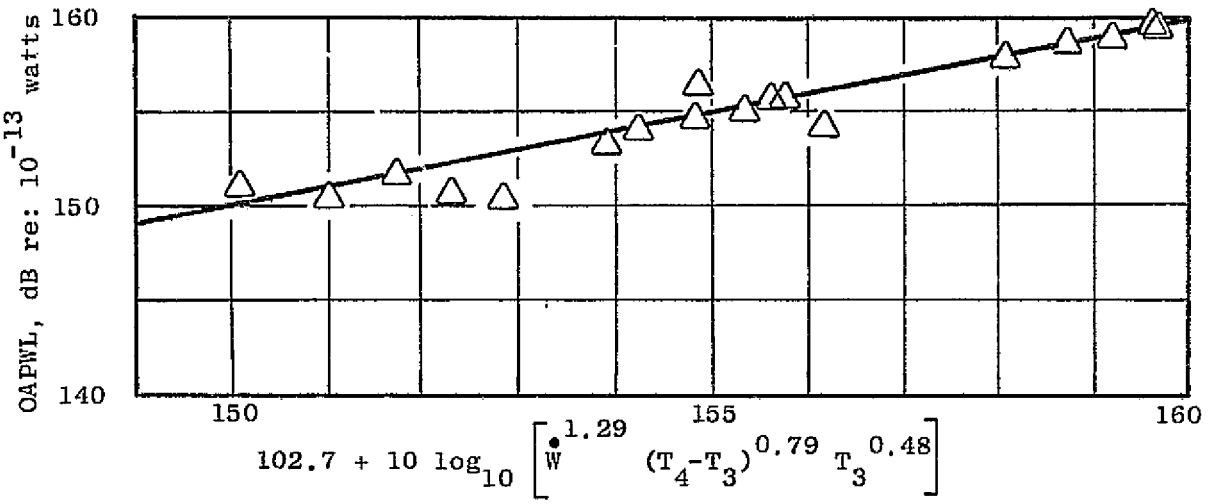

Figure 60. Correlation of Double-Annular Combustor D13 OAPWL.

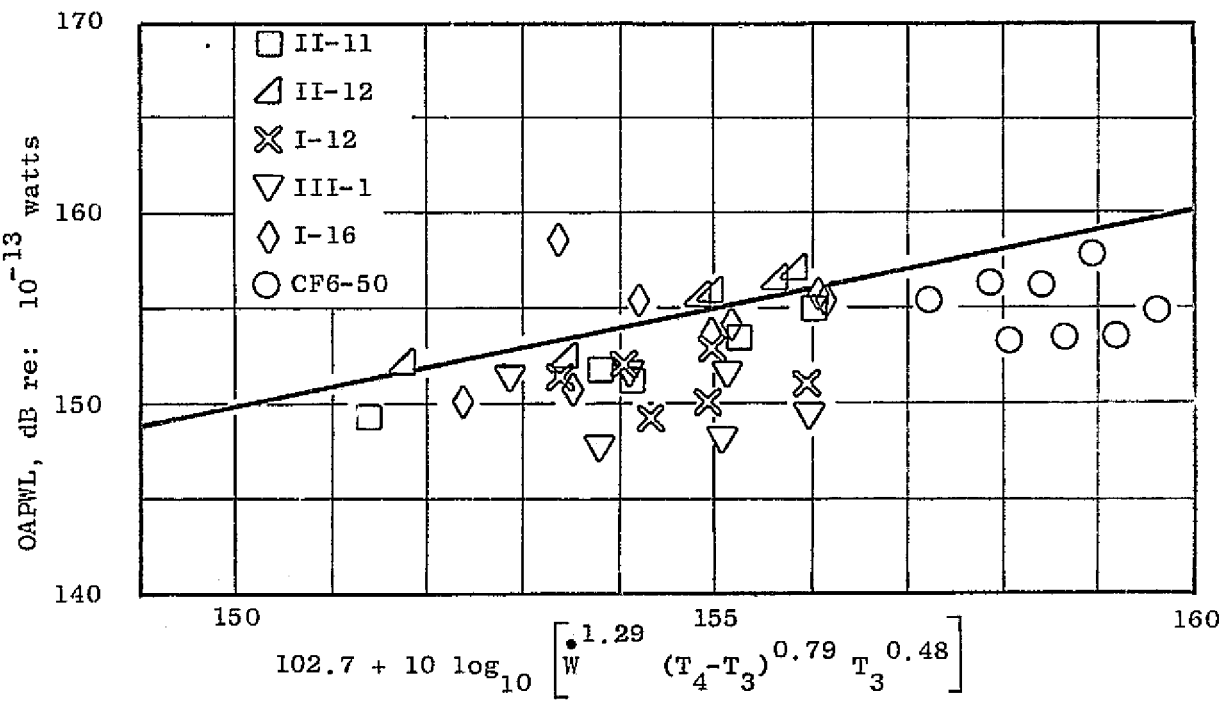

Figure 61. Comparison of Combustor Data to D13 Prediction Line.

at the approach inlet condition were closer to the D-13 correlation line. The takeoff inlet condition noise for those three combustors was noticeably lower than both the D-13 line and their corresponding approach levels. It is suggested that both the difference between configurations and the difference associated with the changed inlet conditions are related to the structure and level of the turbulence generated in each combustor. It is further suggested that the turbulence and its related noise from combustors of the second category is more sensitive to its operating condition than combustors of the first category.

Any general similarity of each category that was exclusive of the other was not immediately evident in the examination of the configurations.

The exponents of the terms in this prediction equation were rounded off. Then the equation becomes:

$$OAPWL = 100.2 + 10 \log_{10}\left[\dot{W} (T_4-T_3)\sqrt{T_3}\right] \qquad (2)$$

The standard deviation from the mean line, Figure 62, was increased to 1.2 dB. The trends and relationships of the other configurations remained essentially unchanged. The simplicity of this equation was attractive and it is recommended as a preliminary design prediction. It should be noted that this equation was based on component combustor data. The effect of a change in end impedance from that which existed in the component test to that which occurs in an engine is not included.

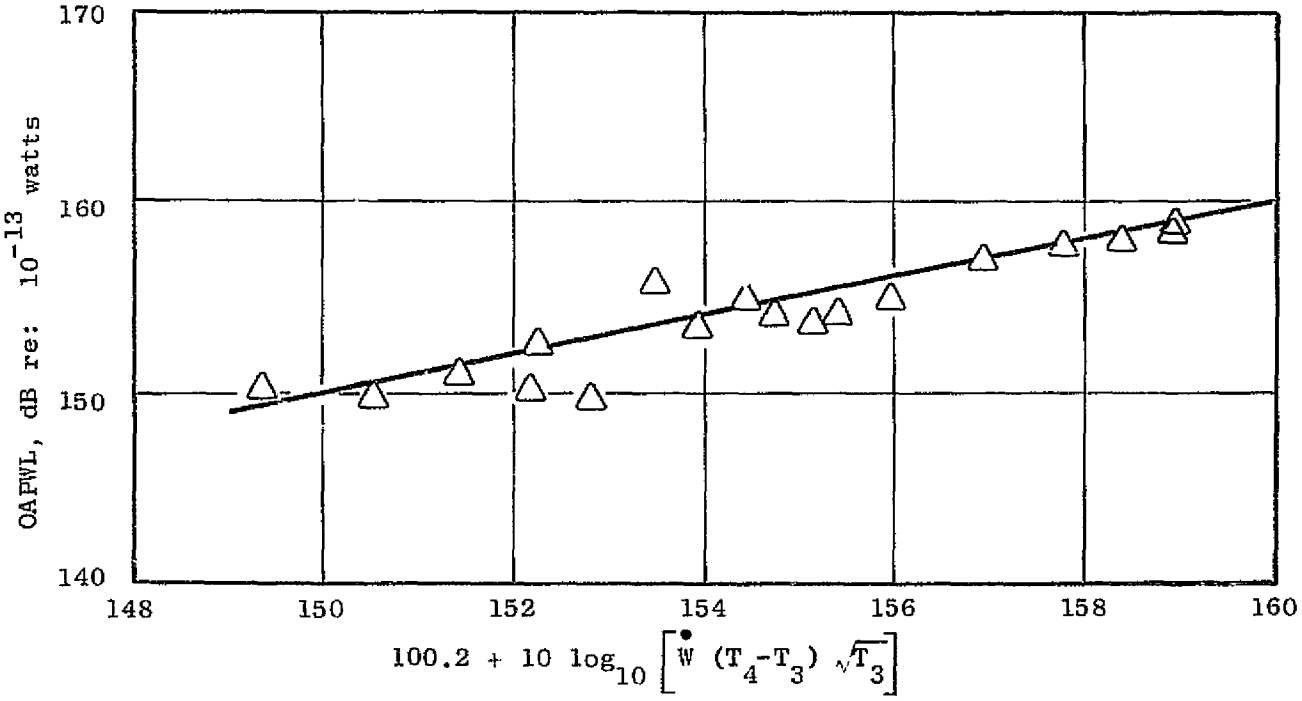

Figure 62. Simplified Correleation of Double-Annular Combustor D13 OAPWL.

SECTION 7.0

ATTENUATION THROUGH TURBINE BLADE ROWS

The attenuation of combustor-generated noise by an engine turbine was suggested in Reference 4. An analysis of the attenuation phenomenon was performed by Bekofske (Reference 5) for subsonic relative flow. This analysis is extended here to include the case where there is subsonic relative flow at the inlet of a blade row but supersonic at the discharge side. The turbine attenuation for the CF6-50 engine was calculated based on this analysis. The calculated attenuation was compared to an estimated value of turbine attenuation. The estimated value was arrived at by first estimating the power level of combustor noise in the engine based on Equation 2. The CF6-50 engine core noise power level based on far-field measurements was then subtracted from the component level. The resulting difference was called the turbine attenuation and was compared to the analytic solution. The comparison showed that the analytic solution over predicts the attenuation.

In addition the analytic prediction method was exercised in a parametric study and a turbine pressure ratio dependency discerned for the plane-wave case.

7.1 EXTENDED ANALYSIS

Introduction

The attenuation of acoustic energy of low frequency waves propagating through a gas turbine stage was analyzed. An earlier investigation of this blade transmission problem (Reference 5) assumed that the relative Mach number was subsonic at both the inlet and discharge sides of the nozzle and bucket row. Results indicated that the attenuation of acoustic energy across typical turbine stages varies from less than 1 dB to more than 10. The present study extends the previously developed theory to account for supersonic relative flow at the discharge of a blade row. Such a choked condition occurs typically in single-stage, high-pressure turbines and highly loaded fan turbines at high power settings. The theory is derived for an isolated blade row. As in the earlier study (Reference 5), Mach number changes and flow turning across a stage element are taken into account.

In actual practice, most of the energy-containing disturbances arising in the combustion chamber of a gas turbine have a characteristic acoustic wavelength which is large compared to both the chord and transverse spacing of a blade row. Core engine noise spectra are presented by Emmerling (Reference 4) and Pickett (Reference 6), which indicate a low frequency peak, identified as combustor noise, centered at about the 400 Hz 1/3-octave band. It is suitable to investigate the transmission of such low frequency

combustor disturbances through a turbine stage element (nozzle or bucket row) using a two-dimensional (cascade plane) actuator disk model. Therefore, as in the previously mentioned study (Reference 5), the analysis will be restricted to low frequency disturbances and the actuator disk model will be employed.

One of the earlier uses of the actuator disk model was by Rannie and Marble (Reference 7). Since the fluid motion in axial flow turbomachinery is three-dimensional, and so complex, it is necessary to use some simple mathematical model in most practical instances. The actuator disk model to be employed here uses a concept borrowed from propeller theory and applied to a blade row within an annular passage. It is assumed that the radial flow is negligible, thus reducing the problem to one of two dimensions (the cascade plane). Further, the actuator disk is a model in which each blade row is assumed to be an appropriate plane of discontinuity in the flow. Thus, the actuator disk method is restricted to low frequency disturbances whose wavelengths are large compared to the chord and transverse spacing of the cascade blade row. A comprehensive discussion of the actuator disk theory in turbomachinery is given by Hawthorne and Ringrose (Reference 8). Pickett (Reference 6) employs the actuator disk model to study the interaction of vorticity and entropy disturbances arising in the combustion chamber with a blade row. Cumpsty and Marble (Reference 9) also use the actuator disk model to investigate the generation of noise by entropy fluctuations into a turbine.

The problem formulation follows closely an unpublished theory by Dr. R. Mani for the discharge reflection coefficient from a blade row at low frequencies and the analysis contained in Reference 5. A sound wave which impinges on the upstream side of a blade row will lead to a reflected wave on the upstream side and a transmitted wave and a vorticity wave on the downstream side of the blade row. The equations necessary to solve for the unknown wave-amplitude coefficients are obtained by requiring continuity of mass flow and energy and, depending on whether the Mach number is subsonic or supersonic at the discharge of the blade row, either applying the Kutta condition at the trailing edge of the blade row or applying the choking condition to the blade row.

Problem Formulation

The actuator disk model is shown in a two-dimensional flow field in Figure 63. A Cartesian coordinate system is fixed with respect to the blade row (nozzle or bucket). The x-axis is in the axial flow direction and the y-axis is tangent to the blade row and positive in the direction of bucket-rotation. It is assumed that the axial Mach number is subsonic on both sides of the blade row. Also, it is assumed that the inlet relative Mach number is subsonic whereas the exit relative Mach number can be either subsonic (Case I) or supersonic (Case II). All quantities (angles and velocities) are taken to be positive when in the direction indicated in Figure 63. The angles α and β are the incident and exit relative stream angles, respectively, measured from the x-axis. Upstream and downstream flow parameters will be indicated by subscripts 1 and 2, respectively.

C-2

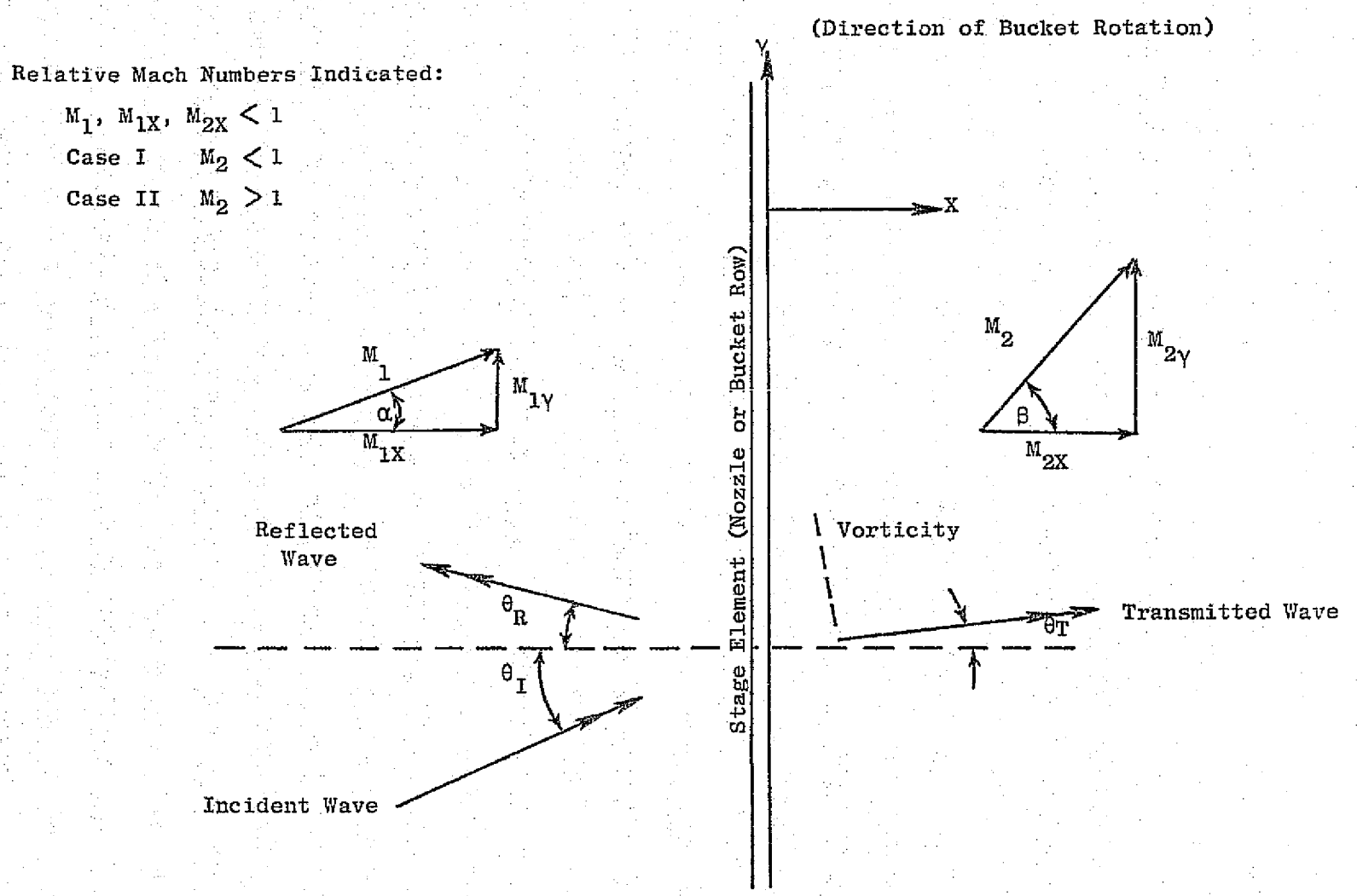

Figure 63. Geometry of Wave Incident on Stage Element.

Wave Description

Consider a sound wave with frequency, ω, and wave number, k_1, which impinges on the upstream side of the blade row at an incident angle, θ_I. Such an incident wave will lead to a reflected wave at angle θ_R and a transmitted wave at angle θ_T. The angles θ_R and θ_T are to be calculated. In addition, a vorticity wave is induced on the downstream side of the blade row.

The physical mechanism by which a "wake" of vorticity is produced by an airfoil in nonuniform motion is described by Karman and Sears(10). Briefly, the unsteadiness in lift gives rise to a wake composed of continuously distributed vortex lines behind the airfoil. Within the approximation of the actuator disk theory (infinitesimal blade spacing) a coalescence of vortex wakes (vorticity wave) is shed from the trailing edge of a blade row on which unsteady distrubances have impinged.

The frequency of each of the above mentioned waves is ω. However, because the temperatures (and, therefore, the speeds of sound) are different upstream and downstream of the blade row, the wave numbers will be different. The wave number is related to the frequency by $k = \omega/a$ where a is the ambient speed of sound. Therefore, the upstream and downstream wave numbers are related by

$$\frac{k_2}{k_1} = \frac{a_1}{a_2} \tag{3}$$

The pressure disturbance associated with the incident acoustic wave can be written as

$$p_I' = P \exp j \left\{ \frac{k_1(x \cos \theta_I + y \sin \theta_I)}{1 + M_{1x} \cos \theta_I + M_{1y} \sin \theta_I} - \omega t \right\} \tag{4}$$

where P is the amplitude of the incident wave, M_{1x} and M_{1y} are axial and tangential components of the upstream relative Mach number, and $j = \sqrt{-1}$. The prime indicates a small deviation from the undisturbed flow field.

The pressures associated with the reflected and transmitted waves can be expressed as

$$p_R' = RP \exp j \left\{ \frac{k_1(-x \cos \theta_R + y \sin \theta_R)}{1 - M_{1x} \cos \theta_R + M_{1y} \sin \theta_R} - \omega t \right\} \tag{5}$$

and

$$p_T' = TP \exp j \left\{ \frac{k_2(x \cos \theta_T + y \sin \theta_T)}{1 + M_{2x} \cos \theta_T + M_{2y} \sin \theta_T} - \omega t \right\} \tag{6}$$

where R and T are unknown coefficients.

The tangential or y dependence of the vorticity wave must be the same as that of the incident wave so that it has the form

$$\exp j\{k_x x + k_y y - \omega t\} \tag{7}$$

where

$$k_y = \frac{k_1 \sin \theta_I}{1 + M_{1x} \cos \theta_I + M_{1y} \sin \theta_I} \tag{8}$$

The x dependence of the vorticity wave is determined by the fact that, in a frame of reference fixed with the fluid ($x_F = x - a_2 M_{2x} t$; $y_F = y - a_2 M_{2y} t$), such a wave appears stationary; that is, its time dependence vanishes. In this frame of reference moving with the fluid, expression (7) is written

$$\exp j\{k_x(x_F + a_2 M_{2x} t) + k_y(y_F + a_2 M_{2y} t) - \omega t\} \tag{9}$$

Since the time dependence must vanish,

$$k_x a_2 M_{2x} + k_y a_2 M_{2y} - \omega = 0$$

or

$$k_x = \frac{k_2 - k_y M_{2y}}{M_{2x}} \tag{10}$$

The vorticity wave is divergence free, so that the velocity components of the vorticity wave must satisfy

$$\frac{\partial u'_Q}{\partial x} + \frac{\partial v'_Q}{\partial y} = 0 \tag{11}$$

Using the expression (7) in equation (11), it follows that

$$\frac{v'_Q}{u'_Q} = - \frac{k_x}{k_y} \tag{12}$$

Therefore, the velocity components of the vorticity wave are given by

$$(u'_Q, v'_Q) = \frac{QP}{\rho_2 a_2} \left(\frac{k_y}{\sqrt{k_x^2 + k_y^2}}, \frac{-k_x}{\sqrt{k_x^2 + k_y^2}}\right) \exp j\{k_x x + k_y y - \omega t\} \tag{13}$$

where Q is an unknown amplitude coefficient and k_y and k_x are given by equations (8) and (10). There are no pressure or density fluctuations associated with the vorticity wave, so that

$$P'_Q = 0 \tag{14}$$

and

$$\rho'_Q = 0 \tag{15}$$

Velocity and density fluctuations associated with the incident, reflected and transmitted waves are given by

$$(u'_I, v'_I) = (\cos\theta_I, \sin\theta_I)\frac{P}{\rho_1 a_1}$$

$$\exp j\{\frac{k_1(x\cos\theta_I + y\sin\theta_I)}{1 + M_{1x}\cos\theta_I + M_{1y}\sin\theta_I} - \omega t\}, \tag{16a}$$

$$\rho'_I = \frac{P}{a_1^2}\exp j\{\frac{k_1(x\cos\theta_I + y\sin\theta_I)}{1 + M_{1x}\cos\theta_I + M_{1y}\sin\theta_I} - \omega t\}, \tag{16b}$$

$$(u'_R, v'_R) = (-\cos\theta_R, \sin\theta_R)\frac{RP}{\rho_1 a_1}$$

$$\exp j\{\frac{k_1(-x\cos\theta_R + y\sin\theta_R)}{1 - M_{1x}\cos\theta_R + M_{1y}\sin\theta_R} - \omega t\}, \tag{17a}$$

$$\rho'_R = \frac{RP}{a_1^2}\exp j\{\frac{k_1(-x\cos\theta_R + y\sin\theta_R)}{1 - M_{1x}\cos\theta_R + M_{1y}\sin\theta_R} - \omega t\}, \tag{17b}$$

$$(u'_T, v'_T) = (\cos\theta_T, \sin\theta_T)\frac{TP}{\rho_2 a_2}$$

$$\exp j\{\frac{k_2(x\cos\theta_T + y\sin\theta_T)}{1 + M_{2x}\cos\theta_T + M_{2y}\sin\theta_T} - \omega t\} \tag{18a}$$

$$\rho'_T = \frac{TP}{a_2^2}\exp j\{\frac{k_2(x\cos\theta_T + y\sin\theta_T)}{1 + M_{2x}\cos\theta_T + M_{2y}\sin\theta_T} - \omega t\}. \tag{18b}$$

Relations expressing θ_R and θ_T in terms of θ_I are found using the fact that the y dependence of the reflected and transmitted waves must also coincide with that of the incident wave. Therefore, from equations (4) - (6)

$$\frac{k_1 \sin \theta_R}{1 - M_{1x} \cos \theta_R + M_{1y} \sin \theta_R} = \frac{k_2 \sin \theta_T}{1 + M_{2x} \cos \theta_T + M_{2y} \sin \theta_T}$$

$$= \frac{k_1 \sin \theta_I}{1 + M_{1x} \cos \theta_I + M_{1y} \sin \theta_I} = k_2 \, G(\theta_I) \tag{19}$$

After some manipulation, it follows that

$$\theta_R = \tan^{-1} \left[\frac{(1 - M_{1x}^2) \sin \theta_I}{(1 + M_{1x}^2) \cos \theta_I + 2M_{1x}} \right] \tag{20}$$

and

$$\theta_T = \tan^{-1} \left\{ \frac{GM_{2x}(1 - GM_{2y}) + G\sqrt{(1 - GM_{2y})^2 - G^2(1 - M_{2x}^2)}}{(1 - GM_{2y})^2 - G^2} \right. \tag{21}$$

where $G(\theta_I)$ is given by equation (19). The reflected and transmitted waves should always appear on the opposite side of the machine axis from the incident wave. Therefore, with the notation and sign conventions of Figure 63, if $\theta_I > 0$, then $\theta_R > 0$ and $\theta_T > 0$, and if $\theta_I < 0$, then $\theta_R < 0$ and $\theta_T < 0$. If $\theta_I = 0$, then $\theta_R = \theta_T = 0$.

Only the acoustic waves for which the normal to the wave crest satisfies

$$|\theta_I| < 90° + \sin^{-1} M_{1x} \tag{22}$$

impinge on the blade row. Other waves are propagating upstream faster than they are convected downstream by the flow. Similarly, only those transmitted waves for which

$$|\theta_T| < 90° + \sin^{-1} M_{2x} \tag{23}$$

are propagating downstream.

When the radical in equation (21) vanishes, i.e.,

$$(1 - GM_{2y})^2 - G^2(1 - M_{2x}^2) = 0, \tag{24}$$

equation (21) leads to

$$\tan \theta_{T,\ \text{cut-off}} = \frac{\pm\sqrt{1 - M_{2x}^2}}{-M_{2x}} \tag{25}$$

where the sign in the denominator has been preserved to identify the quadrant of θ_T. Equation (25) expresses the same limit on θ_T as given in the inequality (23). When the radical in equation (21) becomes negative, the transmitted wave given by equation (6) is decaying exponentially. This downstream cut-off phenomenon leads to a further restriction on the incident angle, θ_I. Solving equation (17) for $\theta_I = \text{fcn}\ (\theta_T)$ and substituting equation (25) gives $\theta_{I,\ \text{cut-off}}$. Acoustic waves whose angles are beyond $\theta_{I,\ \text{cut-off}}$ can impinge on the blade row but are essentially shielded because of condition (23).

Governing Equations

Three equations involving the disturbed flow parameters are necessary to find the unknown amplitude coefficients for the generated waves, T, R, and Q. The flow disturbances must always conserve mass and energy which provide two matching conditions. Furthermore, for the case of subsonic relative velocities on both sides of the blade row, the Kutta condition can be applied at the trailing edge of the blade row (Case I). For the case of subsonic relative velocity at the inlet but supersonic relative velocity at the discharge side of the blade row, the choking condition can be applied to provide the third equation (Case II).

The linearized equation for the continuity of mass flow is given by

$$[U\rho' + \rho u']_1 = [U\rho' + \rho u']_2 \tag{26}$$

The subscripted square brackets indicate evaluation of the quantity on the upstream ($x = 0^-$) and downstream ($x = 0^+$) sides of the blade row, respectively. The linearized equation for the conservation of energy per unit mass, when written in a frame of reference fixed to the blade row, can be written

$$\left[\frac{p'}{\rho} + Uu' + Vv'\right]_1 = \left[\frac{p'}{\rho} + Uu' + Vv'\right]_2. \tag{27}$$

Case I, subsonic relative velocities throughout: the Kutta condition requires that at the trailing edge the flow should be tangent to the exit relative stream angle, β (see Figure 63). The unit vector normal to the flow is

$$\hat{e}_n = -\sin\beta\ \hat{e}_x + \cos\beta\ \hat{e}_y. \tag{28}$$

Then the Kutta condition requires that, at the trailing edge,

$$\underset{\sim}{u}' \cdot \hat{e}_n \Big|_{x = 0^+} = 0. \tag{29}$$

Case II, supersonic relative velocity at the blade row exit: this case assumes that no shock waves occur in the blade passage; the presence of shock waves would allow a subsonic relative velocity at the discharge. The choked condition will manifest itself in the fact that the corrected mass flow is dependent only on the upstream stagnation parameters[11]. A discussion of its application to disturbed flow at a blade row can be found in Reference 9. The choked condition requires that

$$\frac{W}{A\,P_0}\sqrt{\frac{RT_0}{\gamma}} = \text{Constant} \tag{30}$$

where W = mass rate of flow,

A = cross sectional area,

R = gas constant,

γ = ratio of specific heats,

T_0 = stagnation temperature,

and P_0 = stagnation pressure.

The mass rate of flow is $w = \rho AU$. For γ = constant, which will be assumed in this analysis, Equation (30) can be written

$$\rho U\,\frac{\sqrt{T_0}}{P_0} = \text{constant}. \tag{31}$$

Condition (31) is used to obtain the third equation involving disturbed flow parameters when the relative velocity at the blade row exit is supersonic. Introducing

$$T_0 = T\left(1 + \frac{\gamma - 1}{2} M^2_{ab}\right),$$

$$P_0 = p\left(1 + \frac{\gamma - 1}{2} M^2_{ab}\right)^{\gamma/\gamma - 1},$$

and

$$p = \rho RT$$

into Equation (31), where M_{ab} is the <u>absolute</u> Mach number, and taking the logarithmic differential yields

$$\frac{2u'}{U} - \frac{T'}{T} - \frac{\gamma + 1}{\gamma - 1}\,\frac{\mu'}{\mu} = 0 \tag{32}$$

where T' = temperature disturbance,

and

$$\mu \equiv 1 + \frac{\gamma - 1}{2} M_{ab}^2$$

The absolute Mach number is

$$M_{ab} = \frac{C}{\sqrt{\gamma RT}}$$

where C is the absolute flow velocity. Denoting the absolute flow velocity disturbance by c', it follows that

$$-\frac{\gamma + 1}{\gamma - 1} \frac{M'}{M} = \frac{(\gamma + 1)M_{ab}^2}{2[1 + \frac{\gamma - 1}{2} M_{ab}^2]} \left(\frac{T'}{T} - 2 \frac{c'}{C}\right)$$

When this expression is substituted into Equation (32), it becomes

$$(M_{ab}^2 - 1) \frac{T'}{T} + 2M \frac{u'}{U} - (\gamma + 1)M_{ab}^2 \frac{c'}{C} = 0 \qquad (33)$$

The temperature disturbance in isentropic flow is related to the pressure disturbance by

$$\frac{T'}{T} = \frac{\gamma - 1}{\gamma} \frac{p'}{p}.$$

The absolute flow velocity disturbance, c', can be expressed in terms of the relative velocity component disturbances as

$$\frac{c'}{C} = \frac{u'}{C} \cos\phi + \frac{v'}{C} \sin\phi$$

where ϕ is the absolute flow angle, measured from the axial direction. Therefore, equation (33) is written

$$\frac{(\gamma - 1)}{\gamma p} M_{ab}^2 - 1)p' + [\frac{2\mu}{U} - \frac{(\gamma + 1)M_{ab}}{a} \cos\phi]u' - [\frac{(\gamma + 1)M_{ab}}{a} \sin\phi]v' = 0. \qquad (34)$$

It should be noted that in Equation (34), u' and v' can contain, in general, contributions due to both pressure and vorticity waves. This equation will

be applied upstream of the blade row and used as the third condition (choking condition) for the case of supersonic relative flow at the discharge of the blade row.

When equations (4) to (6) and (13) to (18) are substituted into equations (26) and (27) the following two equations result:

$$\frac{a_1}{a_2}[M_{2x} + \cos\theta_T]T + \frac{a_1}{a_2}\frac{k_y Q}{\sqrt{k_x^2 + k_x^2}} + [\cos\theta_R - M_{1x}]R = M_{1x} + \cos\theta_I \tag{35}$$

and

$$\frac{\rho_1}{\rho_2}[1 + M_2\cos(\beta - \theta_T)]T + \frac{\rho_1}{\rho_2}[k_y M_{2x} - k_x M_{2y}]\frac{Q}{\sqrt{k_x^2 + k_y^2}} - [1 - M_1\cos(\alpha + \theta_R)]R = 1 + M_1\cos(\alpha - \theta_I) \tag{36}$$

A third equation is obtained by substituting Equations (4) to (6) and (13) to (18) into either Equation (29) or (34), depending on whether the discharge relative velocity is subsonic or supersonic:

$$[\sin(\theta_T - \beta)]T - [k_y \sin\beta + k_x \cos\beta]\frac{Q}{\sqrt{k_x^2 + k_y^2}} = 0 \text{ (Case I)} \tag{37a}$$

or

$$[(\gamma + 1)M_{1ab}\cos(\phi_1 + \theta_R) - \frac{2\mu_1}{M_{1x}}\cos\theta_R + (\gamma - 1)(M_{1ab}^2 - 1)]R = (\gamma + 1)M_{1ab}\cos(\phi_1 - \theta_I) - \frac{2\mu_1}{M_{1x}}\cos\theta_I - (\gamma - 1)(M_{1ab}^2 - 1) \text{ (Case II)} \tag{37b}$$

Equations (35), (36), and either (37a) or (37b) can be solved for T, Q, and R.

Attenuation of Acoustic Energy

After the transmission coefficient, T, has been determined, it is necessary to relate it to the attenuation of acoustic energy. Using Blokhintsev's[12] results, the acoustic energy density can be written

$$\varepsilon = \frac{p'^2}{\rho a^3}(a + \underset{\sim}{C} \cdot \hat{e}_p) \tag{38}$$

where $\underset{\sim}{C}$ is the absolute flow velocity and $\hat{e}_p$ is the unit vector normal to the wave front. In Equation (38), note that the pressure fluctuation downstream of a blade row is related to the pressure fluctuation of an incident wave by the transmission coefficient, T, in Equation (6).

The intensity flux vector has the expression

$$\underset{\sim}{I} = \frac{p'^2}{\rho a^3} (a + \underset{\sim}{C} \cdot \hat{e}_p)(a\,\hat{e}_p + \underset{\sim}{C}). \tag{39}$$

Then the attenuation of acoustic energy across a blade row is given by

$$\text{Attenuation} = 10 \log_{10} \left(\frac{\underset{\sim}{I}_2 \cdot \hat{e}_x}{\underset{\sim}{I}_1 \cdot \hat{e}_x}\right) \tag{40}$$

where only the axial component of the intensity flux vector is of interest. The attenuation given by (40) is a function of the incidence angle of the wave, θ_I, as well as the other flow parameters.

A listing of the computer program incorporating this extended analysis can be found in Appendix D.

A blade row attenuation computer study was conducted for a single stage high pressure turbine with two different inlet temperatures = 950° F and 350° F. Subsonic cases (Pressure Ratio P_R = 1.9, 2.0, 2.2 and 2.5) for 70, 90, 100, 110% $N/\sqrt{T_{To}}$ were run. The attenuations for normal incidence (θ_I = 0) waves were used. Figure 64 illustrates the results. The overall stage attenuation is indicated as 8 to 9 dB over the entire pressure ratio range.

The prediction program was then exercised for six different turbines over a larger range of operating conditions. There were some definite trends for the plane wave (zero incidence) case. The attenuation increased with the stage pressure ratio (total-to-static) as shown in Figure 65. The trend suggests using (ΔT) or ($\Delta T/T$) as the correlating parameter where:

$$\left(\frac{\Delta T}{T}\right) = 1 - \left(\frac{1}{P_R}\right)^{\frac{\gamma-1}{\gamma}}$$

and T is the turbine inlet temperature.

The last stage of a low pressure turbine offers significantly less attenuation than the preceding stages for the same pressure ratio. This would suggest that the blade turning or exit angle plays a role, but the role is not immediately obvious. The analysis suggests a similar result when a plane wave assumption is made. Using $\theta_I = 0$, $\theta_R = \theta_T = k_y = 0$ and $(k_x/\sqrt{k_x^2+k_y^2}) = 1$, it can be shown that

$$T = \frac{2\,(1+M_{1x})}{\left(\frac{a_1}{a_2} + \frac{\rho_1}{\rho_2}\right)(1+M_{2x}) + \frac{\rho_1}{\rho_2} M_{2x} \tan^2 \beta} \tag{41}$$

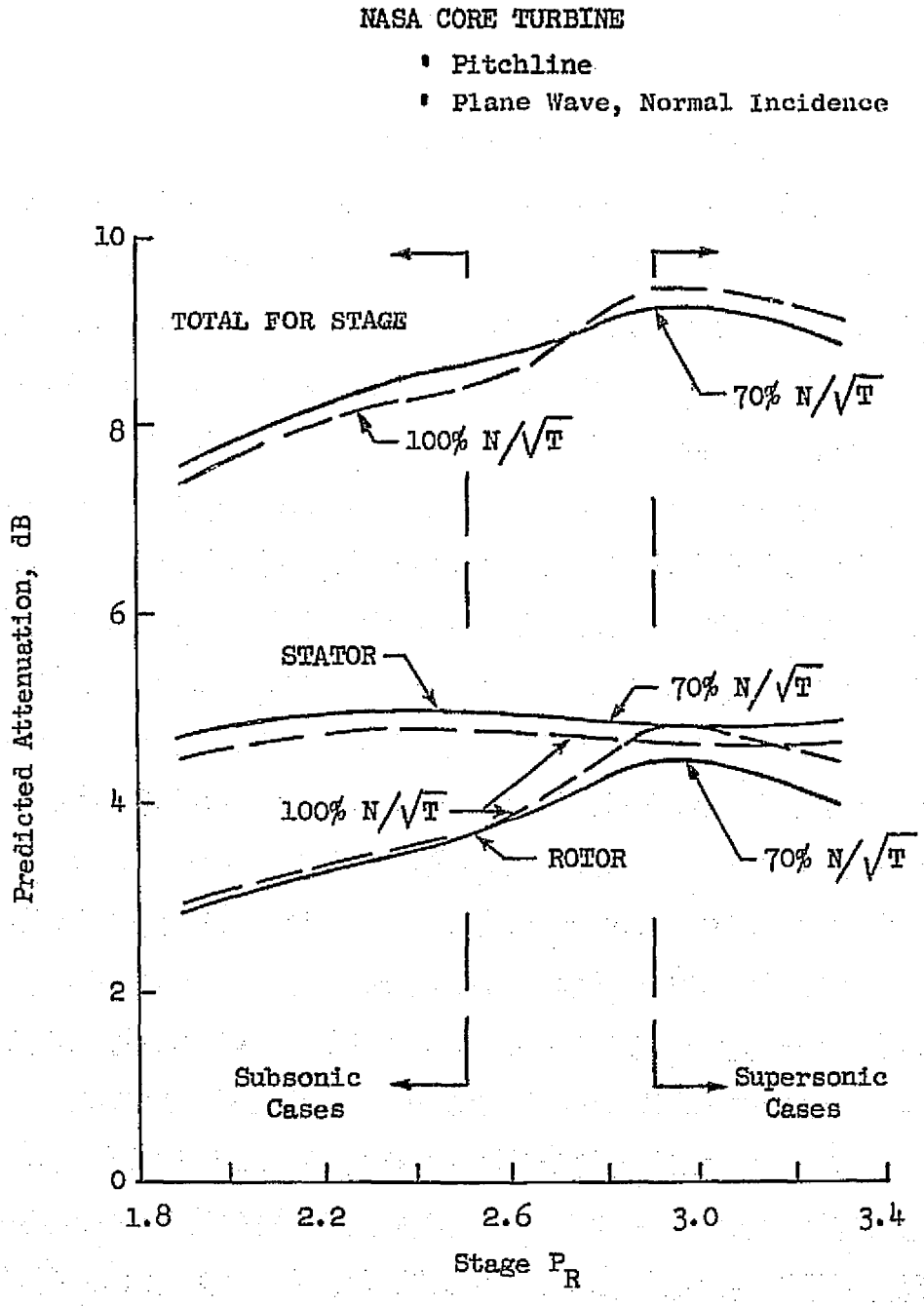

Figure 64. Predicted Attenuation for Subsonic and Supersonic Cases.

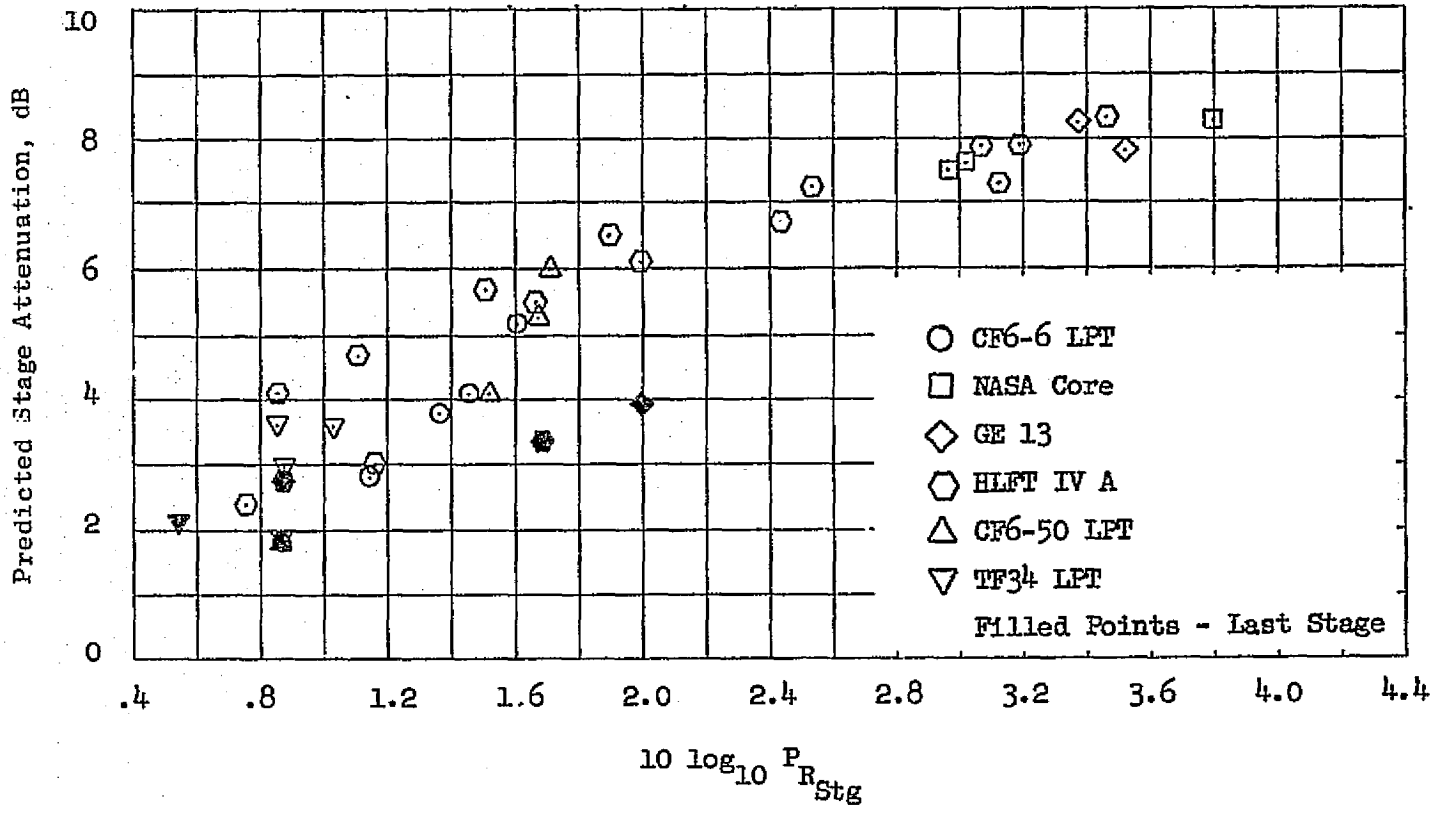

Figure 65. Predicted Attenuation as a Function of Stage Pressure Ratio.

and

$$\Delta = 10 \log_{10} \frac{\rho_2}{\rho_1} \cdot \frac{a_1}{a_2} \frac{1}{T^2} \left(\frac{1+M_{1x}}{1+M_{2x}}\right)^2 \quad (42)$$

where

T = (transmitted/incident) acoustic pressure

Δ = attenuation in dB

β = exit swirl $(\tan^{-1} M_{2y}/M_{2x})$

The quantities (a_1/a_2) and (ρ_1/ρ_2) are related to the work extraction by the turbine and hence to the pressure ratio, P_R. Furthermore, since the axial velocity through a blade row is maintained approximately constant, the ratio $[(1 + M_{1x})/(1 + M_{2x})]$ also becomes, roughly speaking, a function of P_R! Equation (42) can then be recast as

$$\Delta = \text{function } (P_R, \beta)$$

The current prediction method for aircraft engine core noise uses three separate prediction lines for turbojets, turboshafts, and turbofans. The difference between the lines has been attributed, at least in part, to differing low frequency noise attenuation by the turbine stages. The pressure ratio (P_R) dependency indicated by the analysis would suggest inclusion of P_R or $(\Delta T/T)$ in the core noise prediction parameter - in order to collapse the three lines.

7.2 EFFECT OF BLADE ROW ATTENUATION IN THE COMBUSTOR NOISE PREDICTION

The CF6-50 blade row attenuation was calculated using the extended analysis for three engine conditions. The individual stage and total attenuation for the approach, cruise and takeoff conditions are listed in Table VIII. For this operating range, the total calculated attenuation varied between 34 and 37 dB.

For comparison purposes, the component combustor noise was calculated for the same three engine cycle conditions based on equation (2). These extrapolated component combustor overall power levels are listed in Table IX. The CF6-50 engine core noise was then calculated from farfield test data. The engine power levels were based on fitting the combustor noise prediction spectrum with the peak frequency at 500 Hz to the peak angle (120° from the inlet) spectra. The directivity that was used was the one recommended in Reference 4. Subtracting the farfield level from the predicted component combustor level was the attenuation. At approach the attenuation was 14.7 dB while at cruise and takeoff it was greater than 16.6 and 14.8 dB respectively. At the cruise and takeoff condition jet noise dominated the spectra. The maximum level that the combustor noise could assume without effecting the farfield spectra (10 dB below the

Table VIII. Calculated CF6-50 Turbine Stage Attenuation in the Axial Direction.

Turbine	Stage	Approach	Cruise	Takeoff
High Pressure	1	10.6	11.1	11.1
	2	6.3	7.3	7.3
Low Pressure	1	5.9	5.6	5.6
	2	5.3	5.6	5.6
	3	4.1	4.9	4.9
	4	1.8	2.4	2.3
Total Attenuation	=	34.0	36.9	36.8

Table IX. Combustor Noise Attenuation in the CF6-50 Engine.

	Approach	Cruise	Takeoff
Component Combustor OAPWL	159.4	162.8	164.0
Farfield Engine Core OAPWL	144.7	<146.2	<149.2
Attenuation	14.7	>16.6	>14.8

measured level) were listed. The core noise must be at that level or less for those two cases.

The discrepancy between analysis and indicated experimental results could be due to either the unique end impedance condition involved in the component tests or the simplifying assumptions involved in the analysis, perhaps both. The latter invokes an actuator disk assumption and also uses an isolated stage - thus neglecting the effect of reflections from upstream and downstream stages. A study is currently being performed under NASA Contract (No. NAS3-19435) in an attempt to resolve some of these questions.

SECTION 8.0

CONCLUSIONS

Although it remains to be proven that the pressure levels recorded during this test were entirely acoustic pressures, conclusions may be drawn assuming that the peak levels are indeed combustor noise.

- A wall static probe may be used to measure combustor noise, however locally turbulent test conditions may occur which may generate pressures in excess of the acoustic pressure levels.
- The frequency of the peak noise was observed to be 1000 Hz in the component tests rather than 400 Hz ± one-third octave band observed from engine data (see Reference 4).
- The overall power level was found to be a function of the heat release rate and the inlet temperature.
- The attenuation of combustor noise was found to be significant (greater than 14 dB).
- The blade row attenuation analysis as it is presently structured over-predicts the apparent attenuation based on component combustor tests. This may be due to an initial assumption in the analysis and/or the change in combustor exit impedance due to the addition of a turbine when going from component data to engine data.

SECTION 9.0

REFERENCES

1. "Experimental Clean Combustor Program Phase II Final Report," NASA CR .

2. Iberal, Arthur S.; "Attenuation of Oscillatory Pressures in Instrument Lines," Journal of Research of the NBS, Vol. 45, pp. 85-108, July 1950.

3. Emmerling, J.J.; "Experimental Clean Combustor Program Noise Measurement Addendum," Phase I Final Report NASA CR 134853, July 1975.

4. Kazin, S.B., Matta, R.K., et. al.; "Core Engine Noise Control Program, Final Report Volume III Prediction Methods," Report No. FAA-RD-74-125, III, August 1974.

5. Bekofske, K., "Attenuation of Acoustic Energy Across a Turbine Stage With Subsonic Relative Flow," ASME Publication 75-GT-17, 1975.

6. Pickett, G.F.; "Turbine Noise Due to Turbulence and Temperature Fluctuations," presented at 8th International Congress on Acoustics, London, July, 1974.

7. Rannie, W.D., and Marble, F.E.; "Unsteady Flows in Axial Turbomachines," ONERA, Comptes Rendus des Journées Internationales des Sciences Aeronautiques, Part 2, Paris, May, 1957, pp. 1-21.

8. Hawthorne, W.R., and Ringrose, J.; "Actuator Disk Theory of the Compressible Flow in Fre-Vortex Turbomachinery," Proceedings of the Institution of Mechanical Engineers, 1963-64, Vol. 178, Pt. 31(ii), Paper 5, pp. 1-13.

9. Cumpsty, N.A., and Marble, F.E.; "The Generation of Noise by the Fluctuations in Gas Temperature into a Turbine," University of Cambridge Report No. CUED/A TURBO/TR57, 1974.

10. Karman, Th. von and Sears, W.R.; "Airfoil Theory for Non-Uniform Motion," Journal of the Aeronautical Sciences, Vol. 5, No. 10, August, 1938, pp. 379-390.

11. Shapiro, A.H.; "Compressible Fluid Flow," Vol. I, Chapter 4, The Ronald Press Co., New York, 1953.

12. Blokhintsev, D.I.; "Acoustics of a Nonhomogeneous Moving Medium," NACA TM 1399, 1956 (Russian original Leningrad 1946).

13. Clemons, A., Hehmann, H., Radecki, K., "Quiet Engine Program Turbine Noise Suppression," NASA CR-134499, Volume II, 1973.

APPENDIX A

SYMBOLS

NOMENCLATURE

a	Speed of sound
A	Cross sectional area
B	Fuel nozzle spacing
c'	Absolute flow velocity disturbance
C	Absolute flow velocity
$\hat{e}$	Unit vector
D	Downstream, Engine Station 3.9
f/a	Fuel Air Ratio
G	Defined by Equation (17)
H	Height
$\underset{\sim}{I}$	Intensity flux vector
j	$\sqrt{-1}$
k	Wave number
L	Length
M	Relative Mach number
M_{ab}	Absolute Mach number
P_R	Turbine stage pressure ratio
p	Pressure (atmospheres)
p'	Pressure disturbance
P, Q, R, T	Amplitude coefficients
R	Gas constant
RDG	Reading number of test

NOMENCLATURE (Continued)

T	Temperature (° K)
T'	Temperature disturbance
t	Time
u'	Axial velocity component disturbance
U	Upstream, Engine Station 3.0 or mean axial velocity component
v'	Tangential velocity component disturbance
V	Mean tangential velocity component
$\dot{W}$	Mass rate of flow
x	Axial Cartesian coordinate (fixed to blade row)
y	Tangential Cartesian coordinate (fixed to blade row)
α	Incident relative stream angle
β	Exit relative stream angle
γ	Ratio of specific heats
Δ	Increase or decrease
ε	Acoustic energy density
θ	Wave propagation angle
μ	$1 + \frac{\gamma-1}{2} M_{ab}^2$
ρ	Mean density
ρ'	Density disturbance
ϕ	Absolute flow angle (relative to axial direction)
ω	Frequency

SUBSCRIPTS

B	Burner
C	Combustor
D	Dome

SUBSCRIPTS (Continued)

F	Fixed with respect to fluid
f	Fuel
I	Incident wave
n	Normal to flow
p	Normal to wave front
Q	Vorticity wave
R	Reflected wave
S	Static
T	Transmitted wave or total
W	Wall
x	Axial
y	Tangential
0	Stagnation value or ambient condition
1	Upstream of blade row
2	Downstream of blade row
3.0	Engine station upstream of the combustor
3.9	Engine station downstream of the combustor

APPENDIX B

POWER LEVEL CALCULATION

The acoustic power levels were calculated using the measured sound pressure levels from a probe located in an annular duct with mean flow. The acoustic power levels were calculated (Reference 13) for the downstream probe only. For this probe the acoustic waves were traveling in the direction of the flow and all of the energy was assumed to be concentrated in the plane-wave mode. If A was the annulus area in square meters at the probe sensing plane, the power level correction equation in dB re. 10^{-13} watts was:

$$PWL = SPL + 9.9 + 10\log_{10}\left(\left[1+M_{ab}\right]^2\right) + 10\log_{10}\left[\frac{P_o}{P}\sqrt{\frac{T}{T_o}}\right] + 10\log_{10}\,[A]$$

The pressures and temperatures were static but, because the Mach number was low, the total pressure and total temperature may be used without appreciable error.

The above equation was derived from the definition of power.

$$\text{Watts} = \frac{p^2 A}{\rho c}$$

The pressure squared term was contained in the SPL and the characteristic impedance ρc was corrected to standard day conditions by:

$$\left[\frac{P_o}{P}\sqrt{\frac{T}{T_o}}\right]$$

The correction for the flow incorporated the square of one plus the Mach number. This was a simplification of the correction suggested by Blokhintsev (Reference 12):

$$(1 + M_{ab}\cos\theta)(\cos\theta + M_{ab})$$

For the plane-wave mode these corrections are identical.

APPENDIX C

NARROWBAND SPECTRA

All of the spectra in this section are from 0 to 5000 Hz with constant 10 Hz band width. The sample length was 12.8 seconds. These spectra are not corrected for probe losses. Those corrections can be found in Section 3.3.

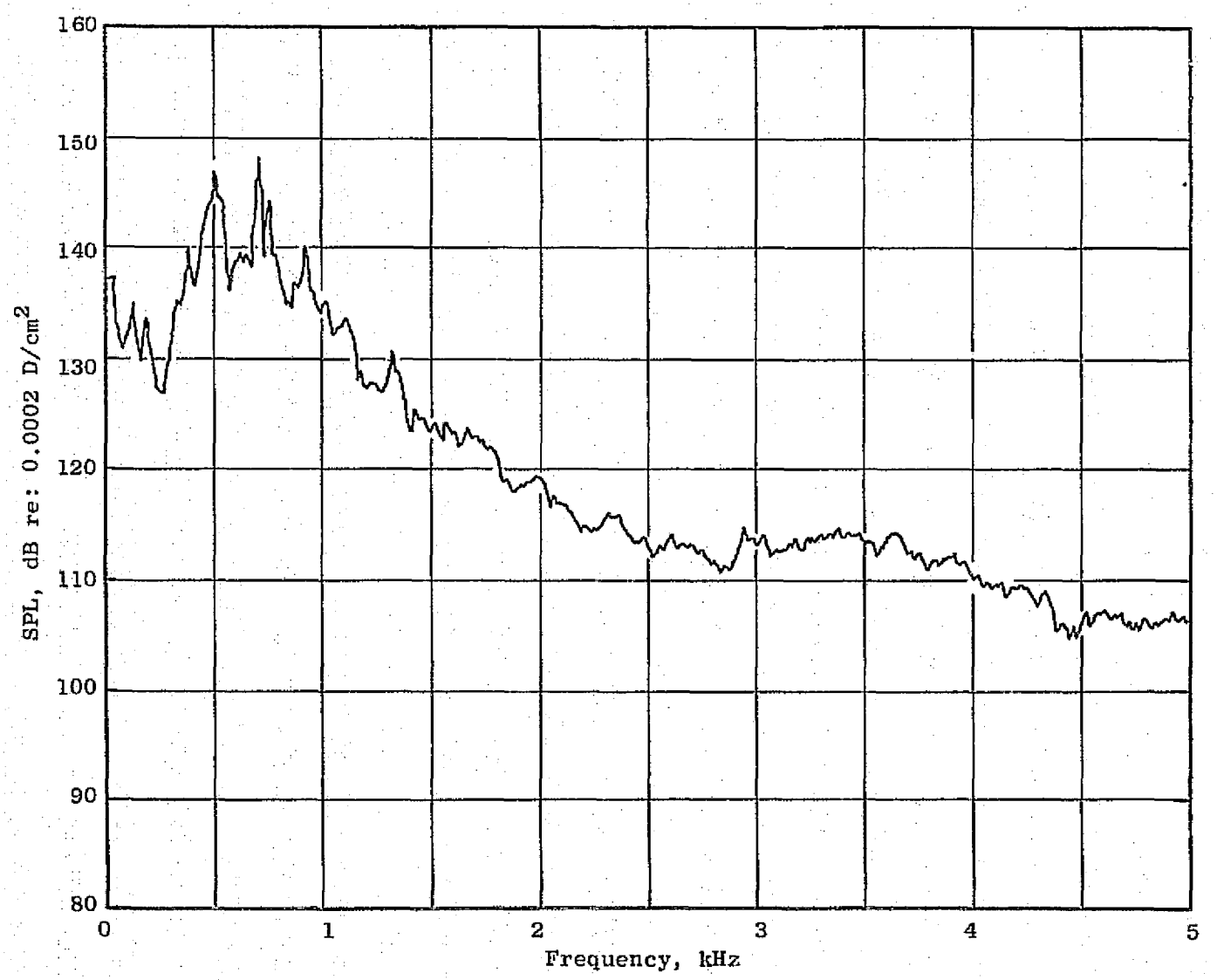

Figure C-1. CF6-50 Combustor Reading 317 Upstream Probe Narrowband Spectrum.

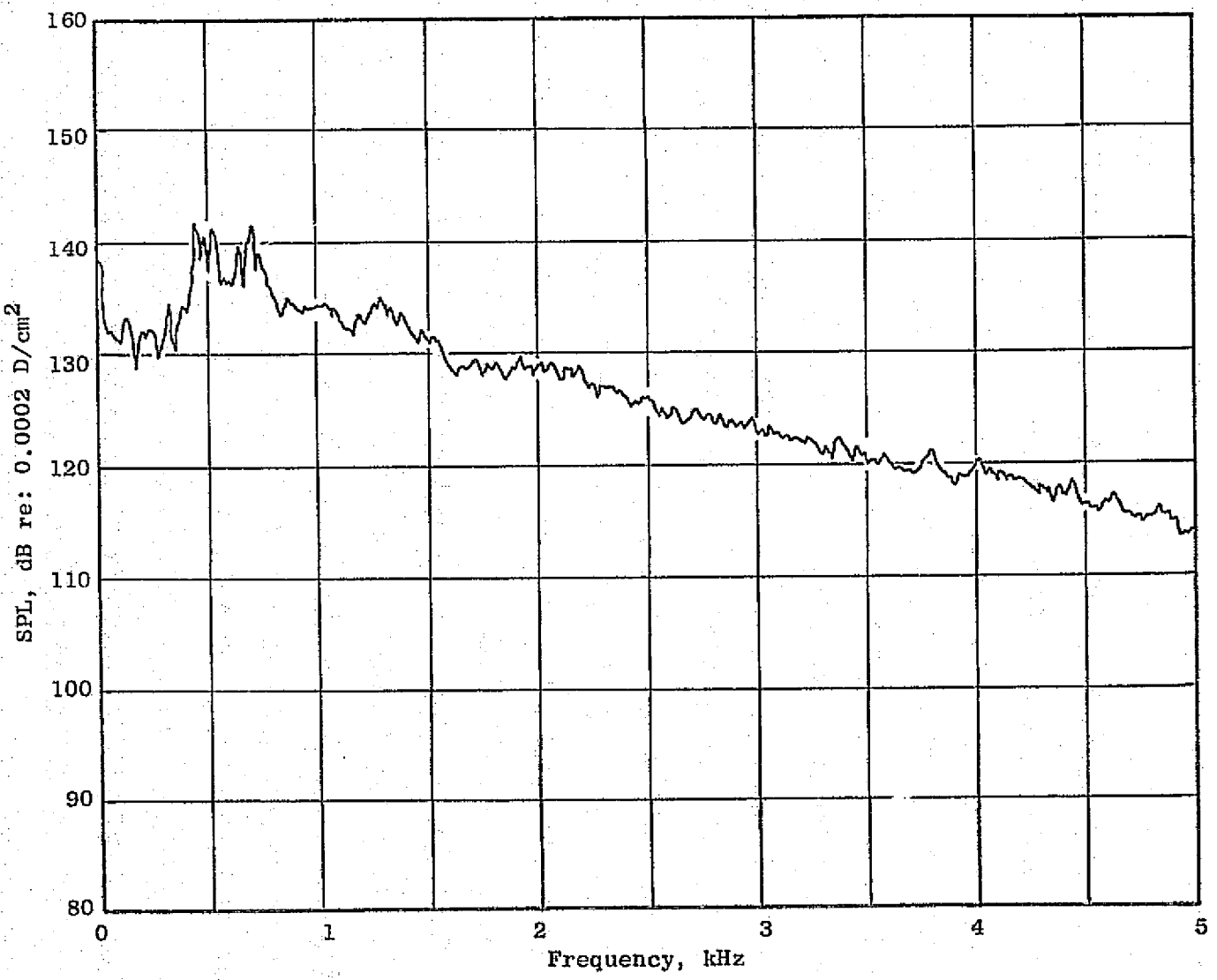

Figure C-2. CF6-50 Combustor Reading 317 Downstream Probe Narrowband Spectrum.

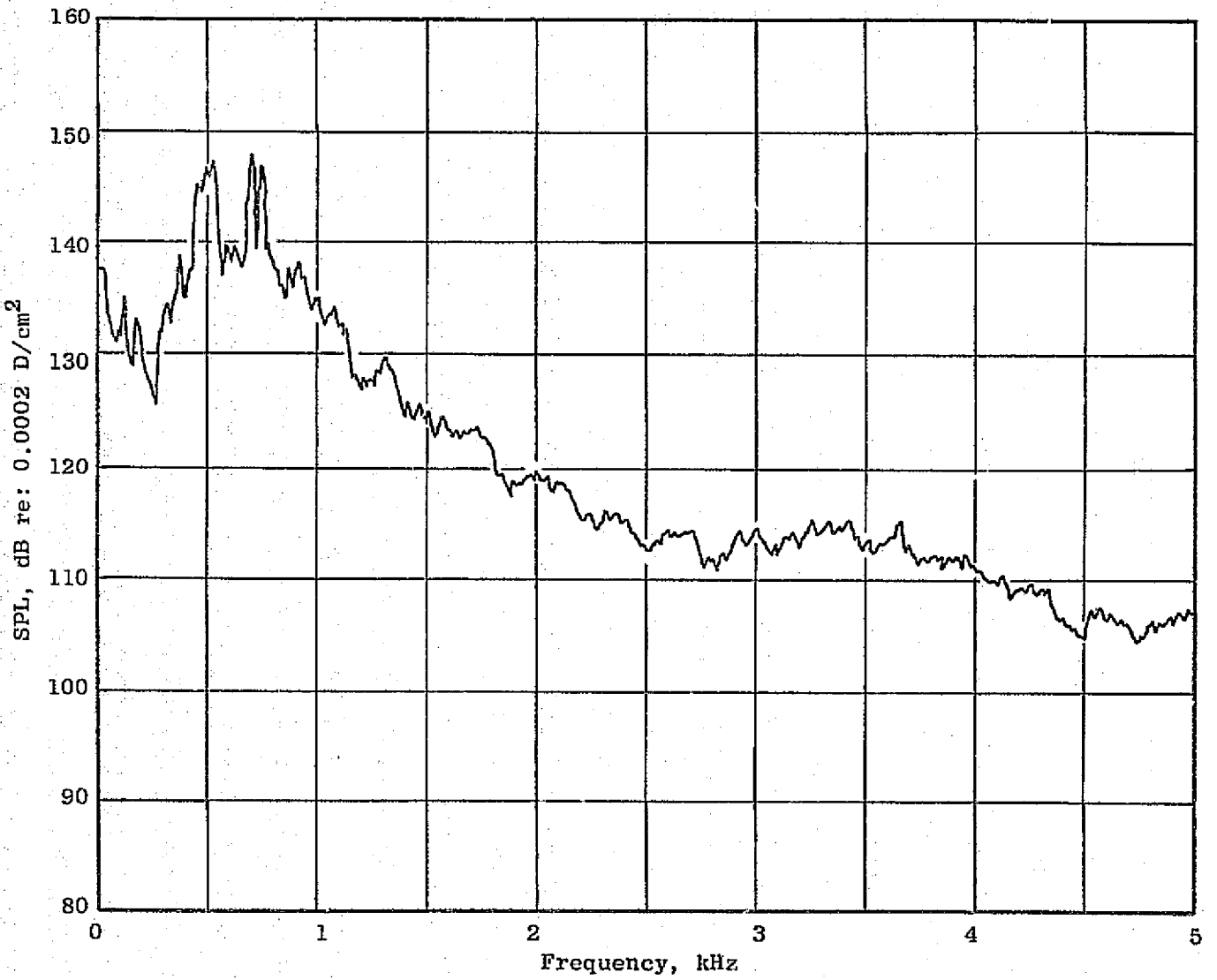

Figure C-3. CF6-50 Combustor Reading 318 Upstream Probe Narrowband Spectrum.

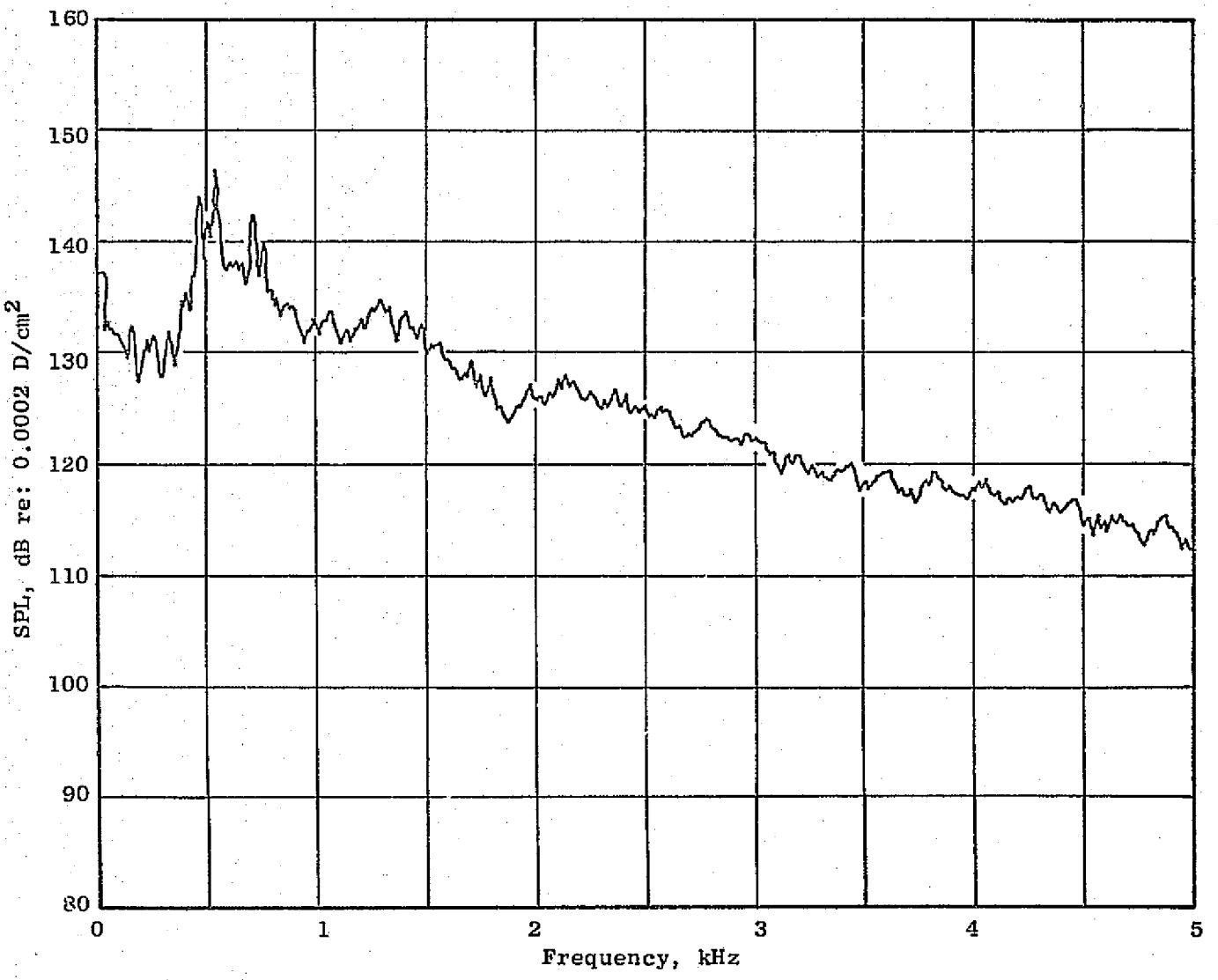

Figure C-4. CF6-50 Combustor Reading 318 Downstream Probe Narrowband Spectrum.

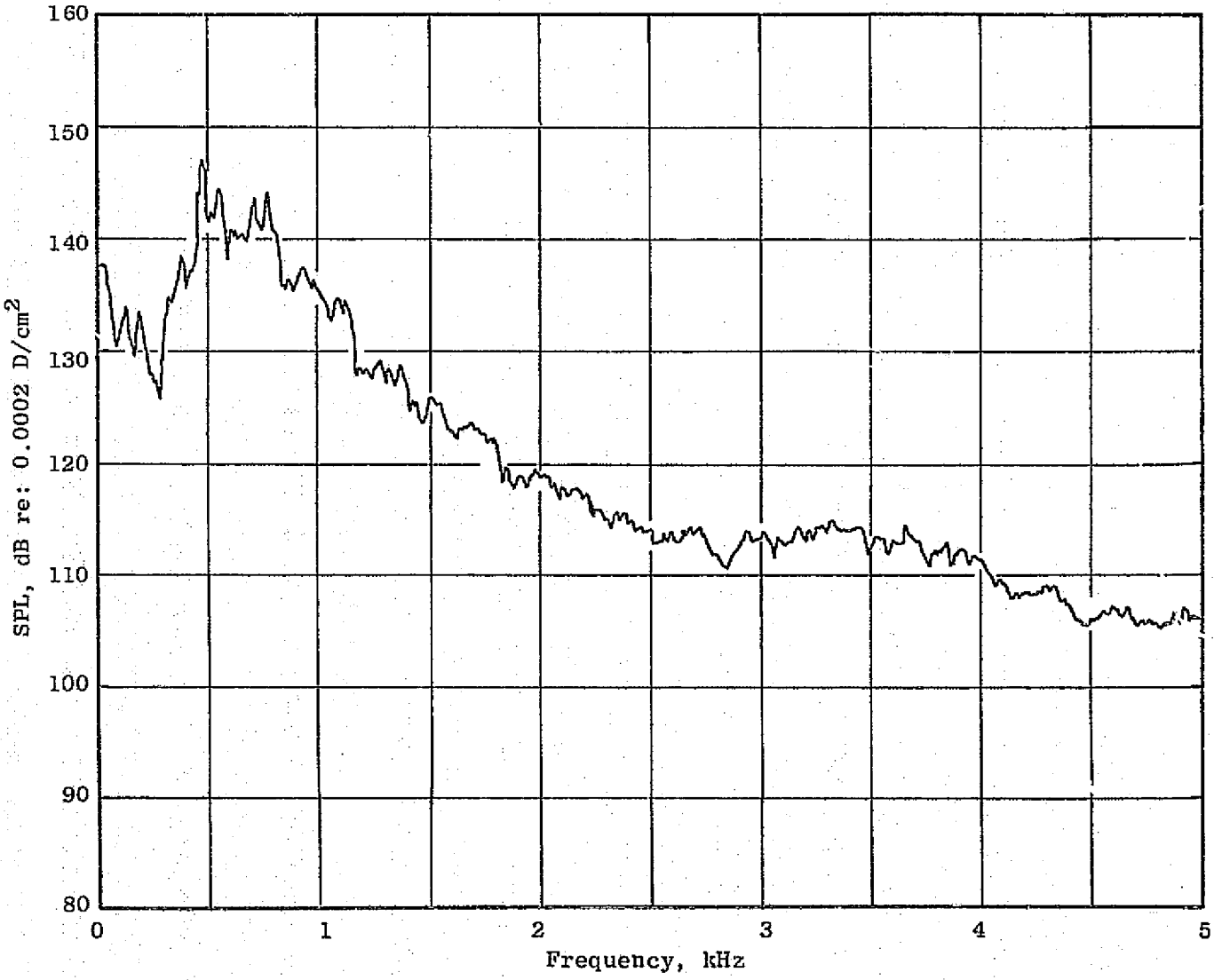

Figure C-5. CF6-50 Combustor Reading 319 Upstream Probe Narrowband Spectrum.

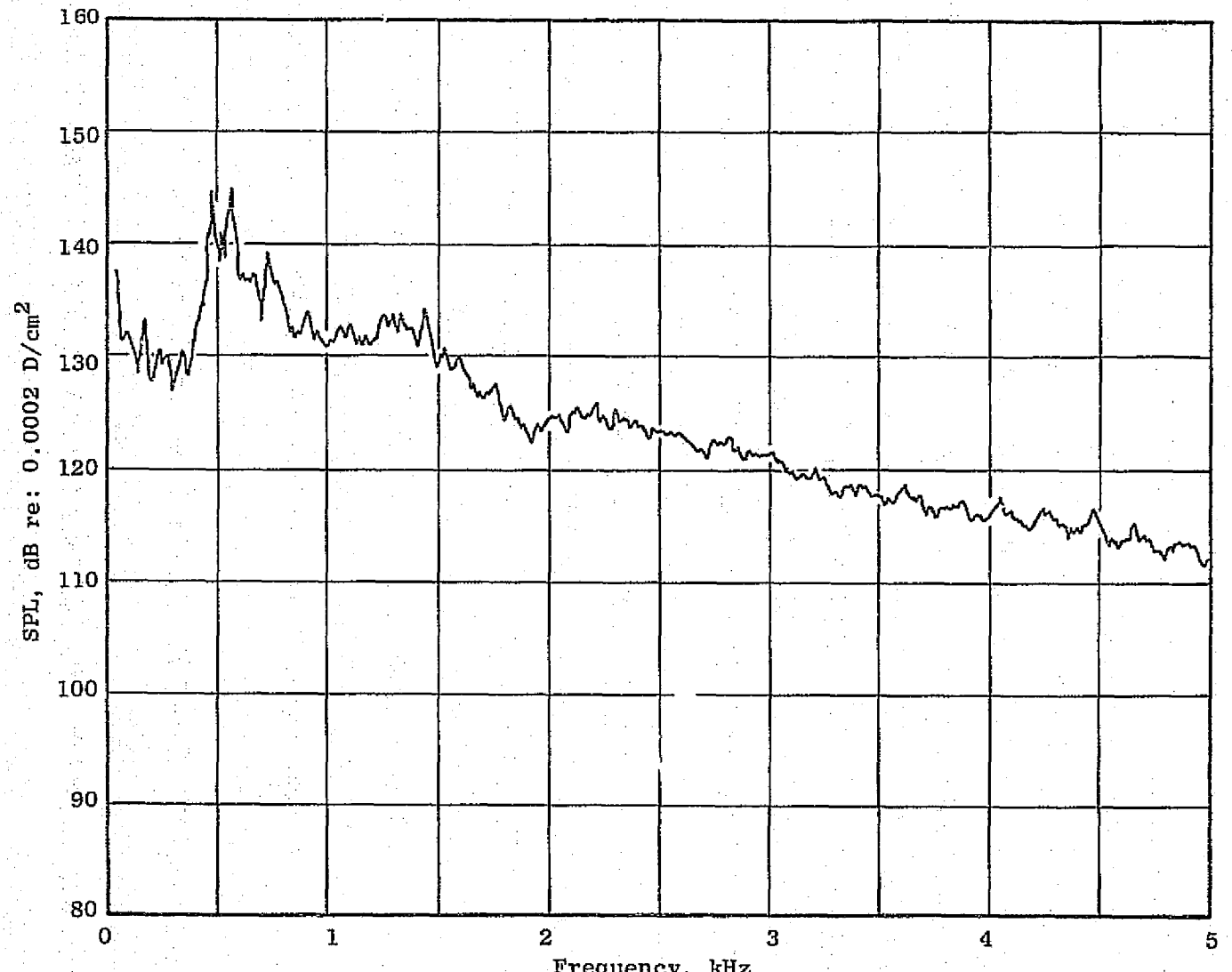

Figure C-6. CF6-50 Combustor Reading 319 Downstream Probe Narrowband Spectrum.

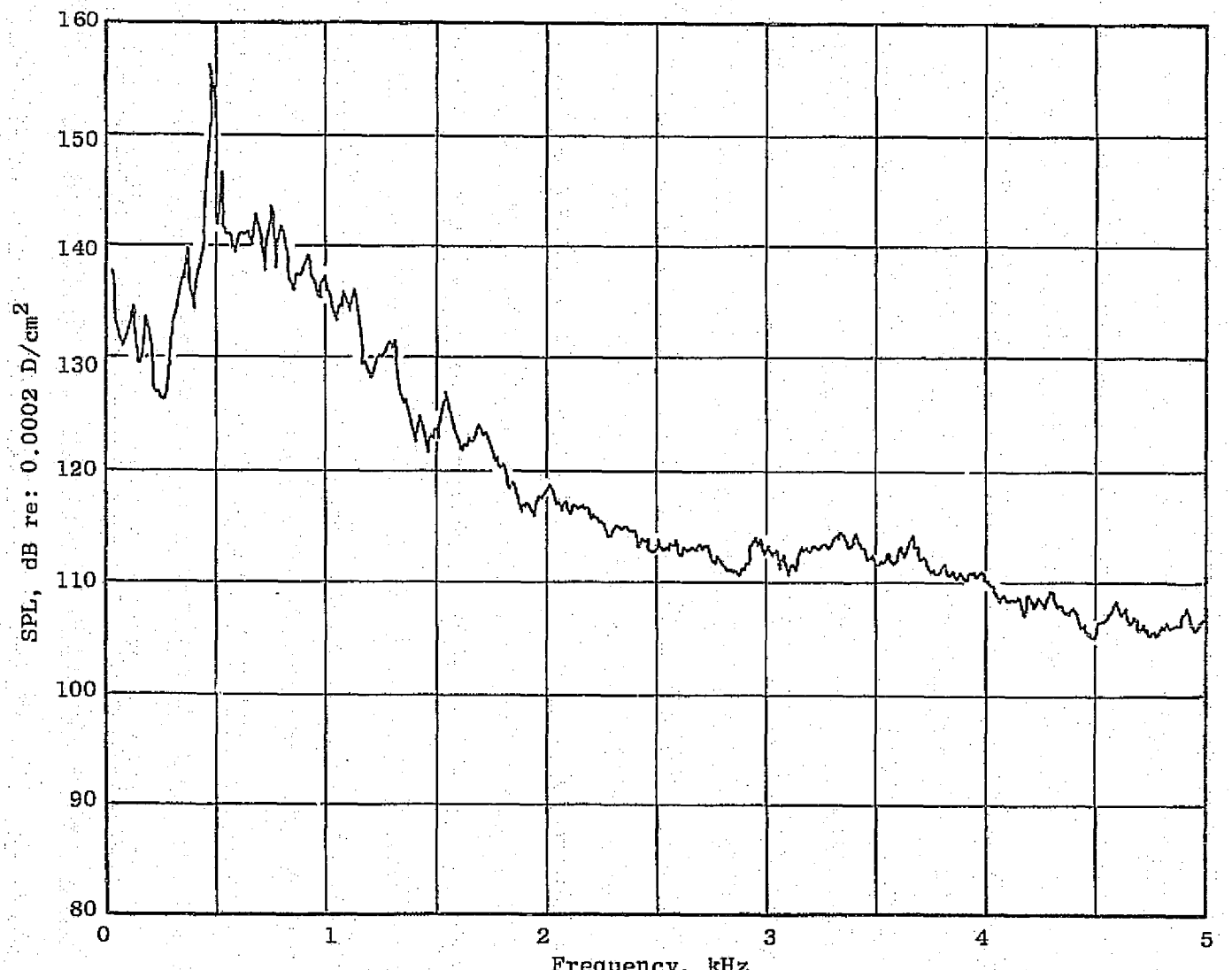

Figure C-7. CF6-50 Combustor Reading 320 Upstream Probe Narrowband Spectrum.

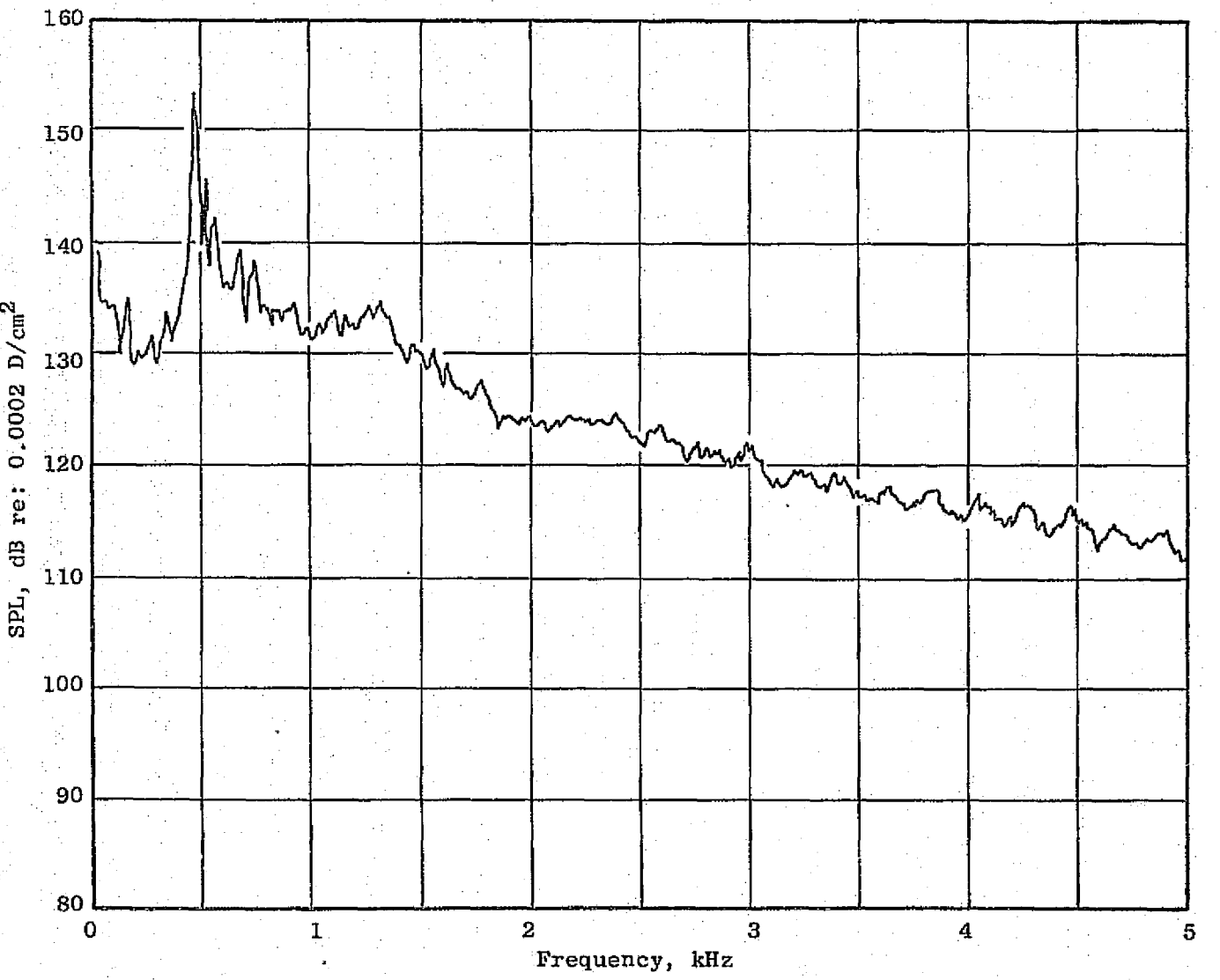

Figure C-8. CF6-50 Combustor Reading 320 Downstream Probe Narrowband Spectrum.

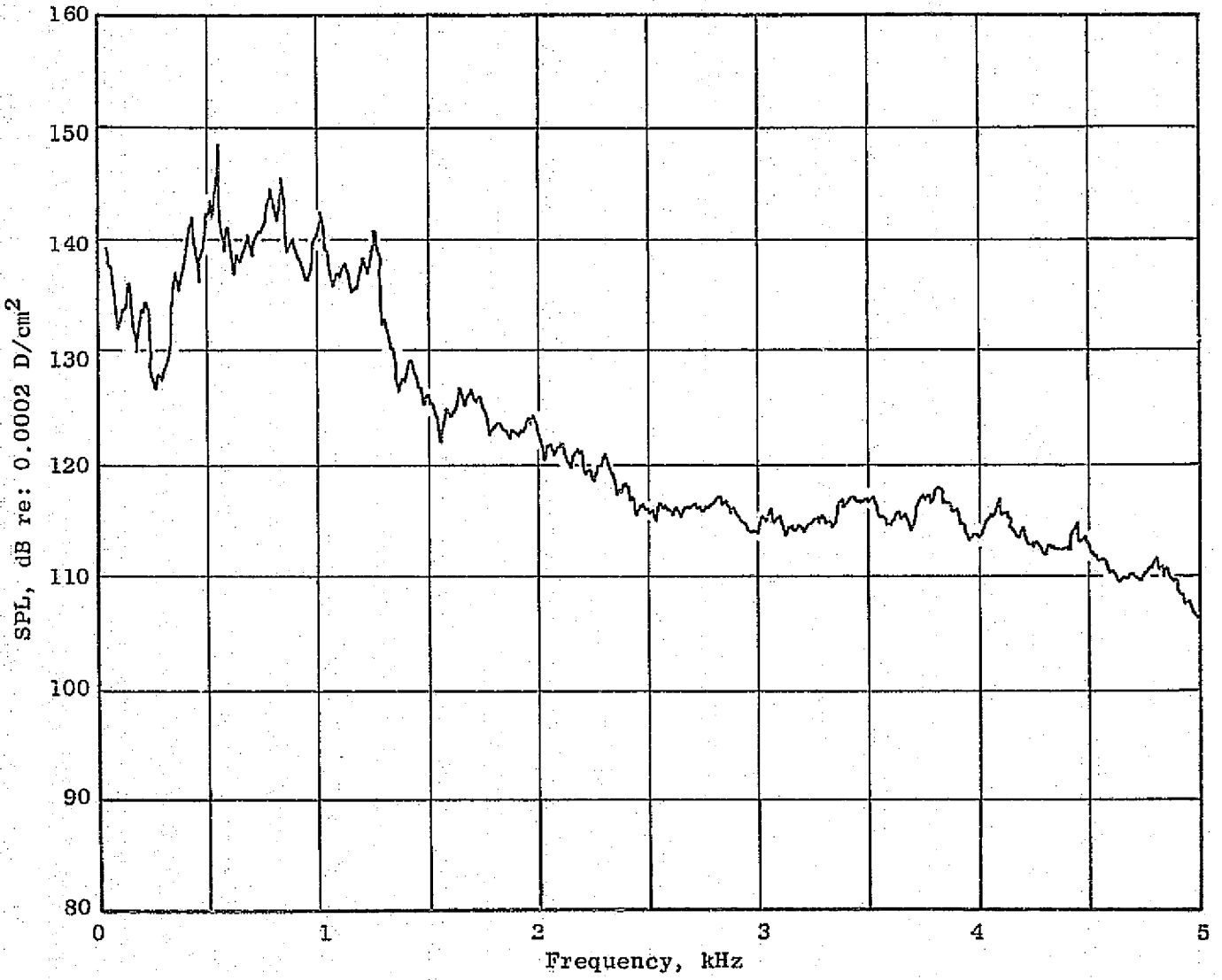

Figure C-9. CF6-50 Combustor Reading 321 Upstream Probe Narrowband Spectrum.

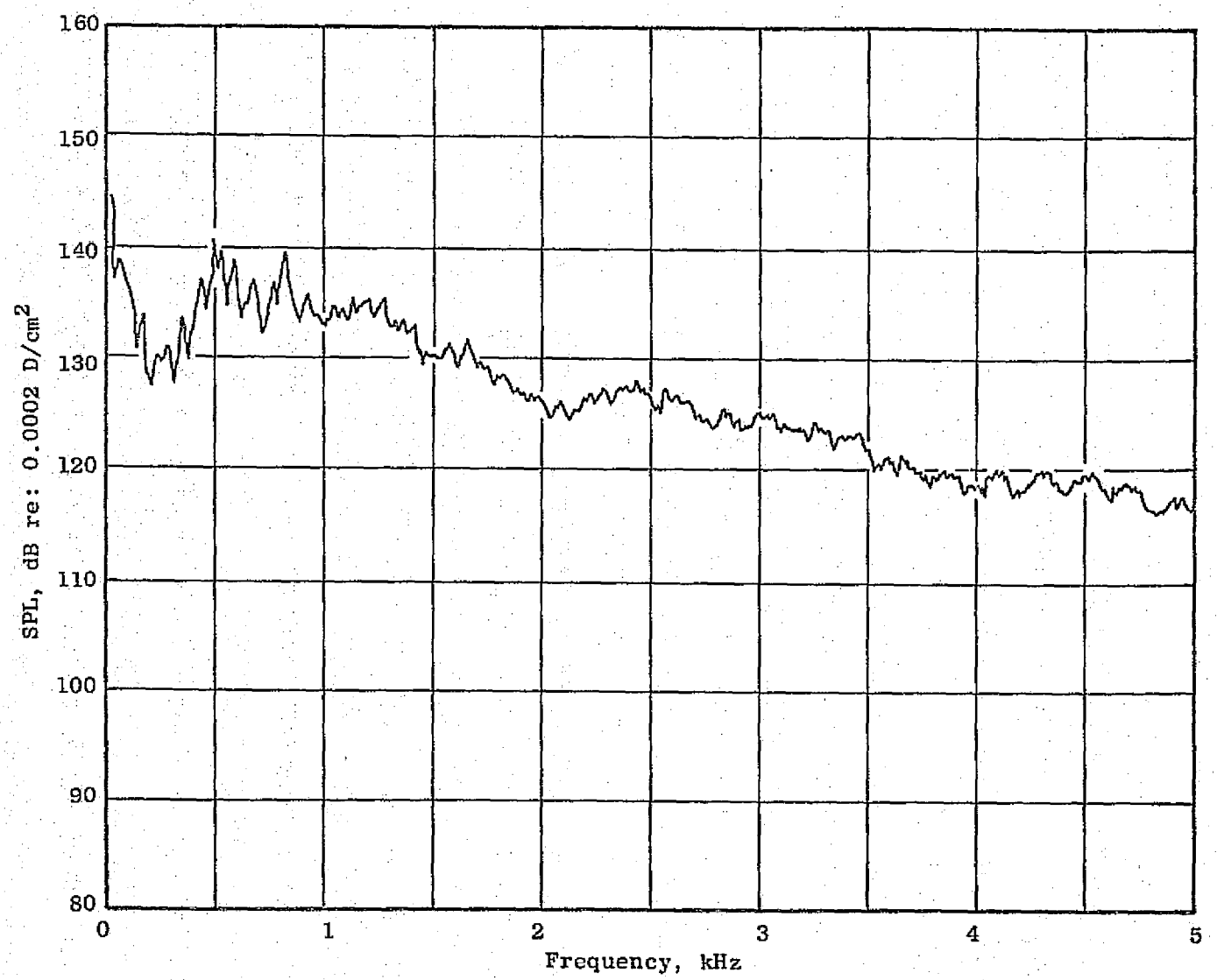

Figure C-10. CF6-50 Combustor Reading 321 Downstream Probe Narrowband Spectrum.

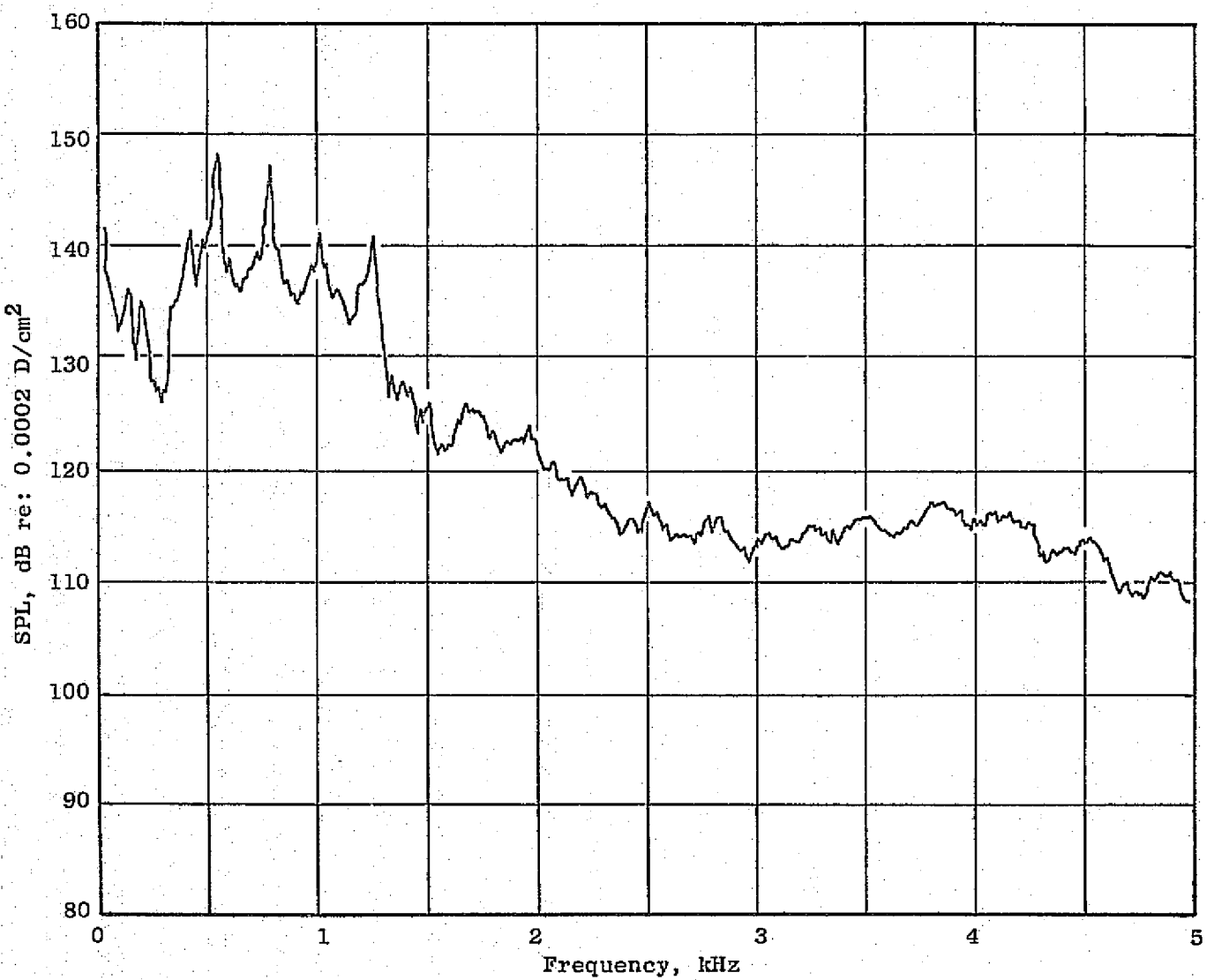

Figure C-11. CF6-50 Combustor Reading 322 Upstream Probe Narrowband Spectrum.

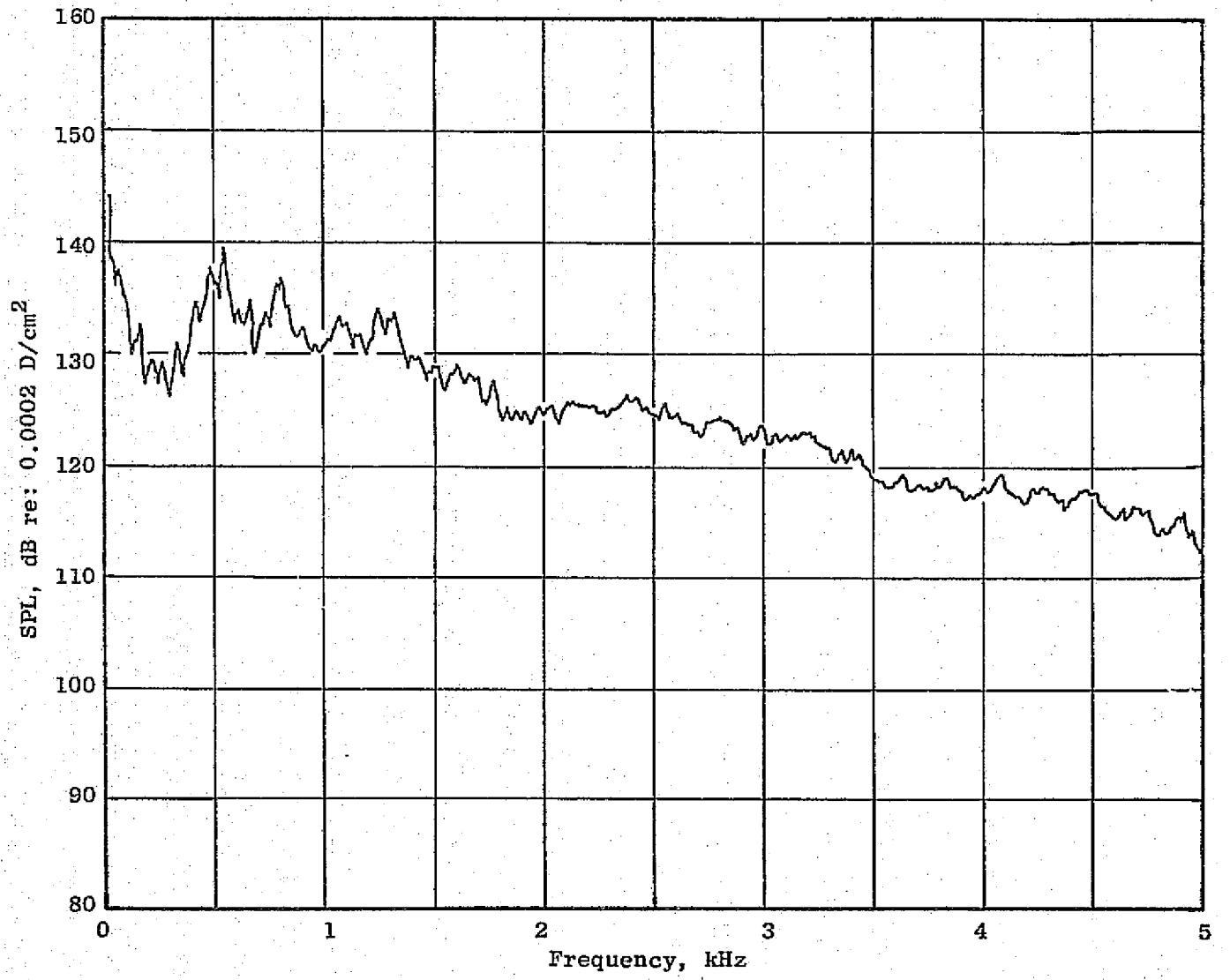

Figure C-12. CF6-50 Combustor Reading 322 Downstream Probe Narrowband Spectrum.

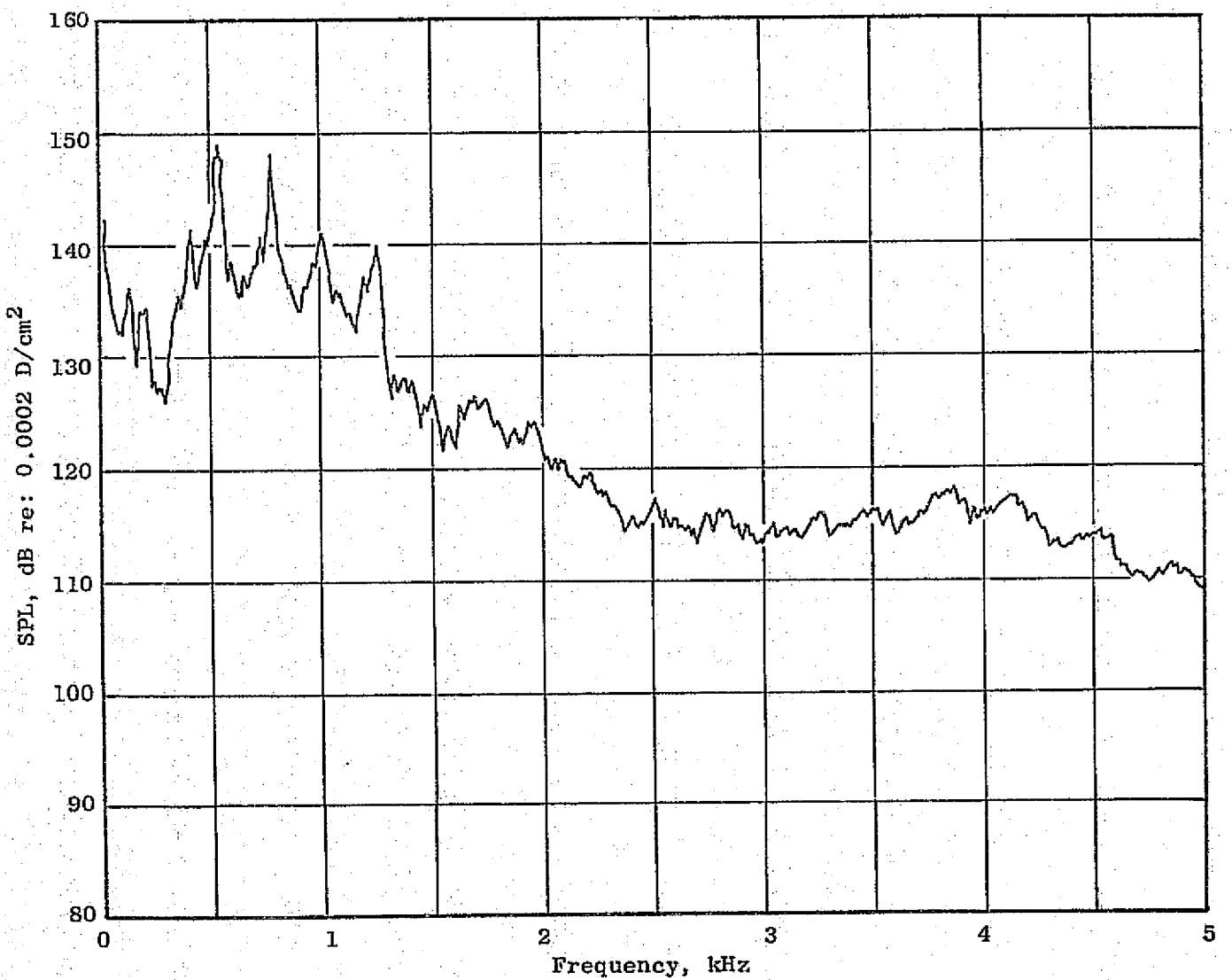

Figure C-13. CF6-50 Combustor Reading 323 Upstream Probe Narrowband Spectrum.

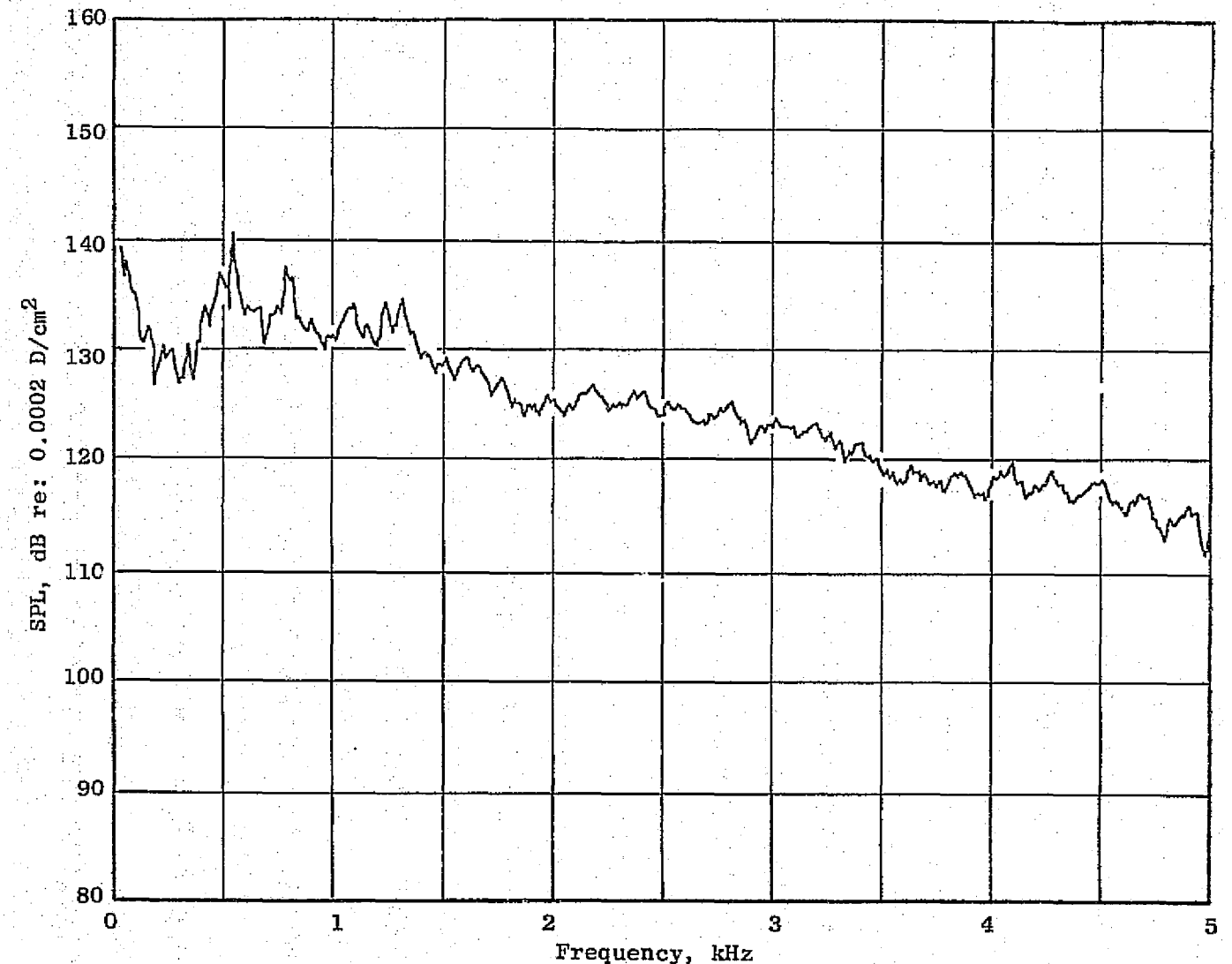

Figure C-14. CF6-50 Combustor Reading 323 Downstream Probe Narrowband Spectrum.

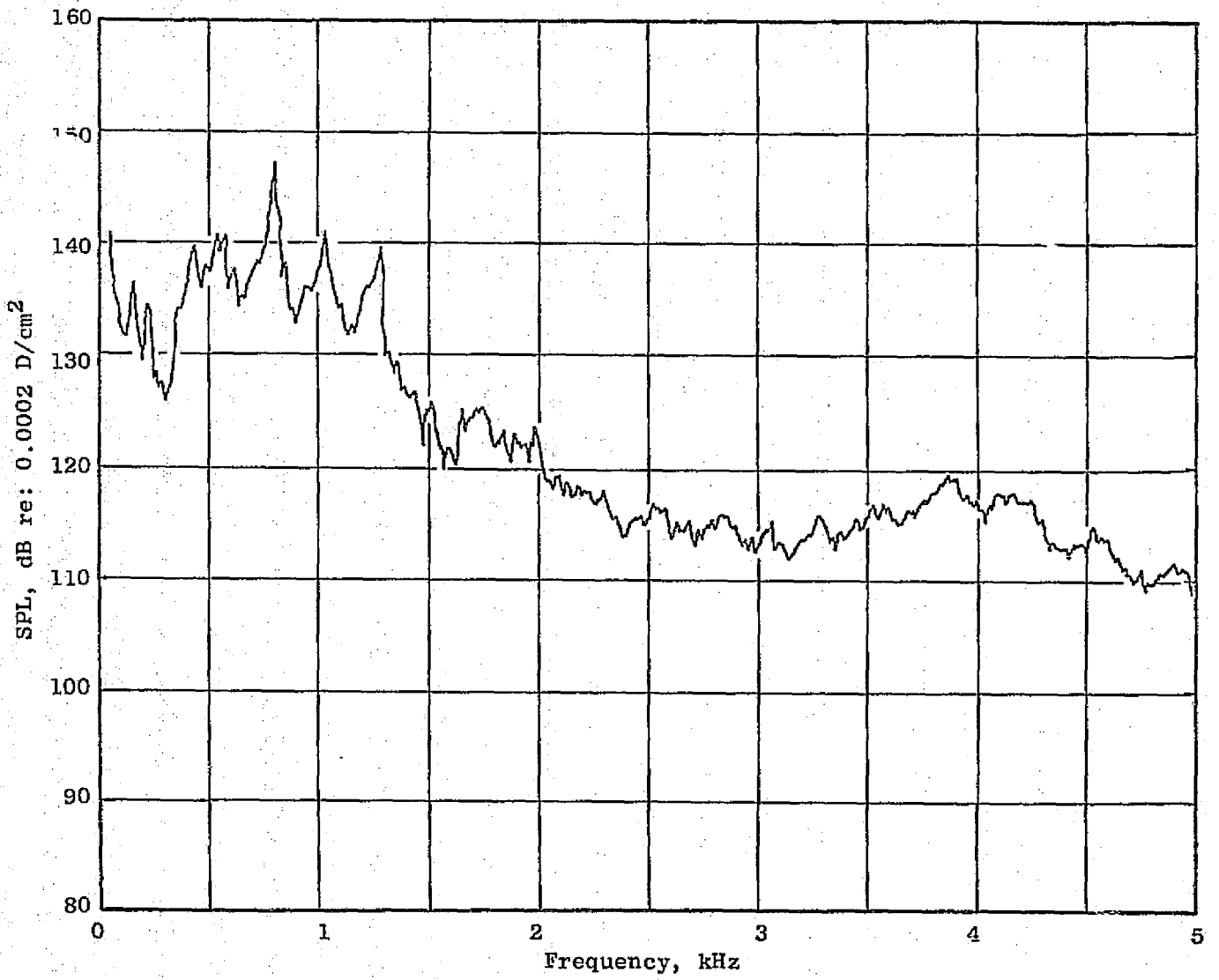

Figure C-15. CF6-50 Combustor Reading 324 Upstream Probe Narrowband Spectrum.

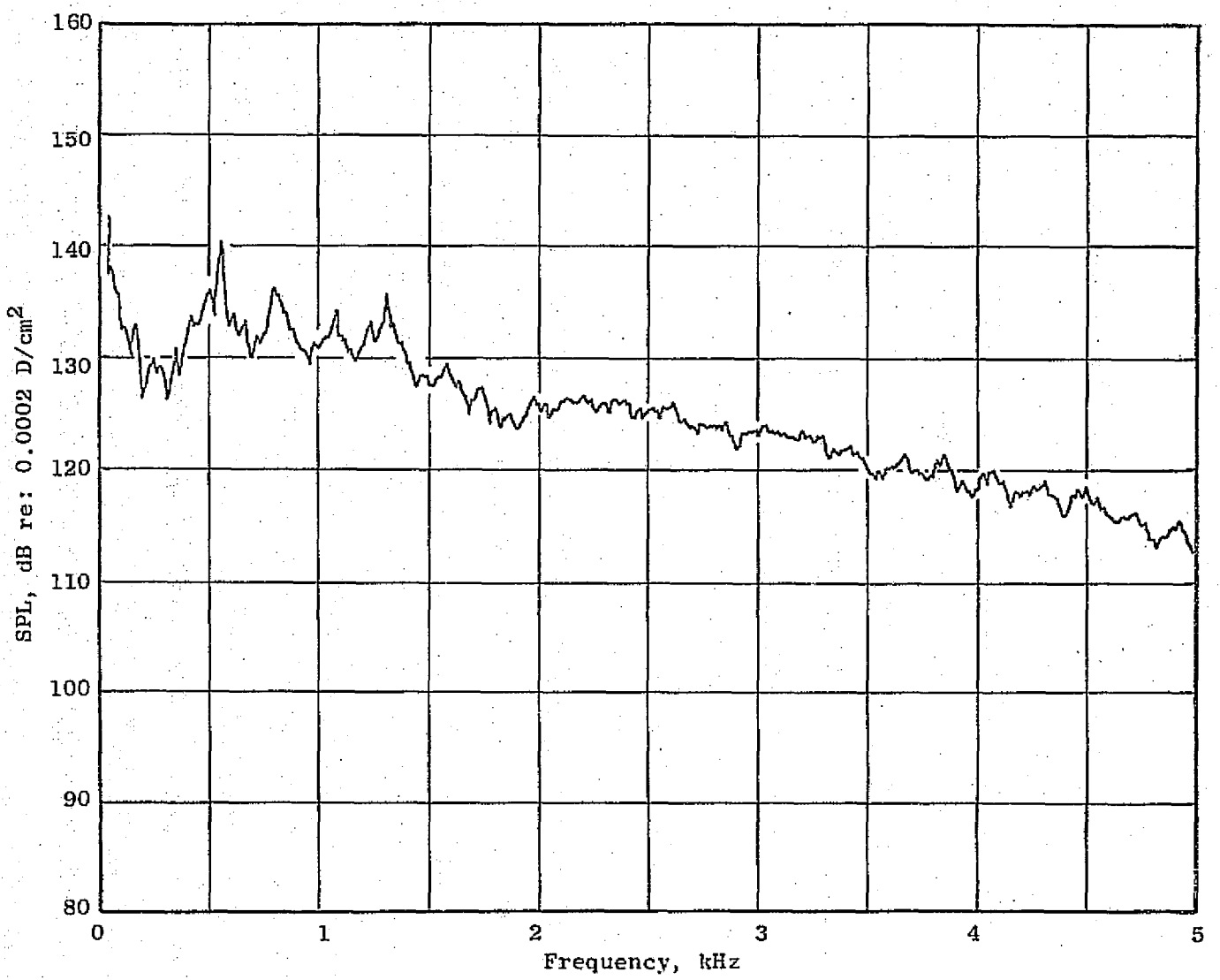

Figure C-16. CF6-50 Combustor'Reading 324 Downstream Probe Narrowband Spectrum.

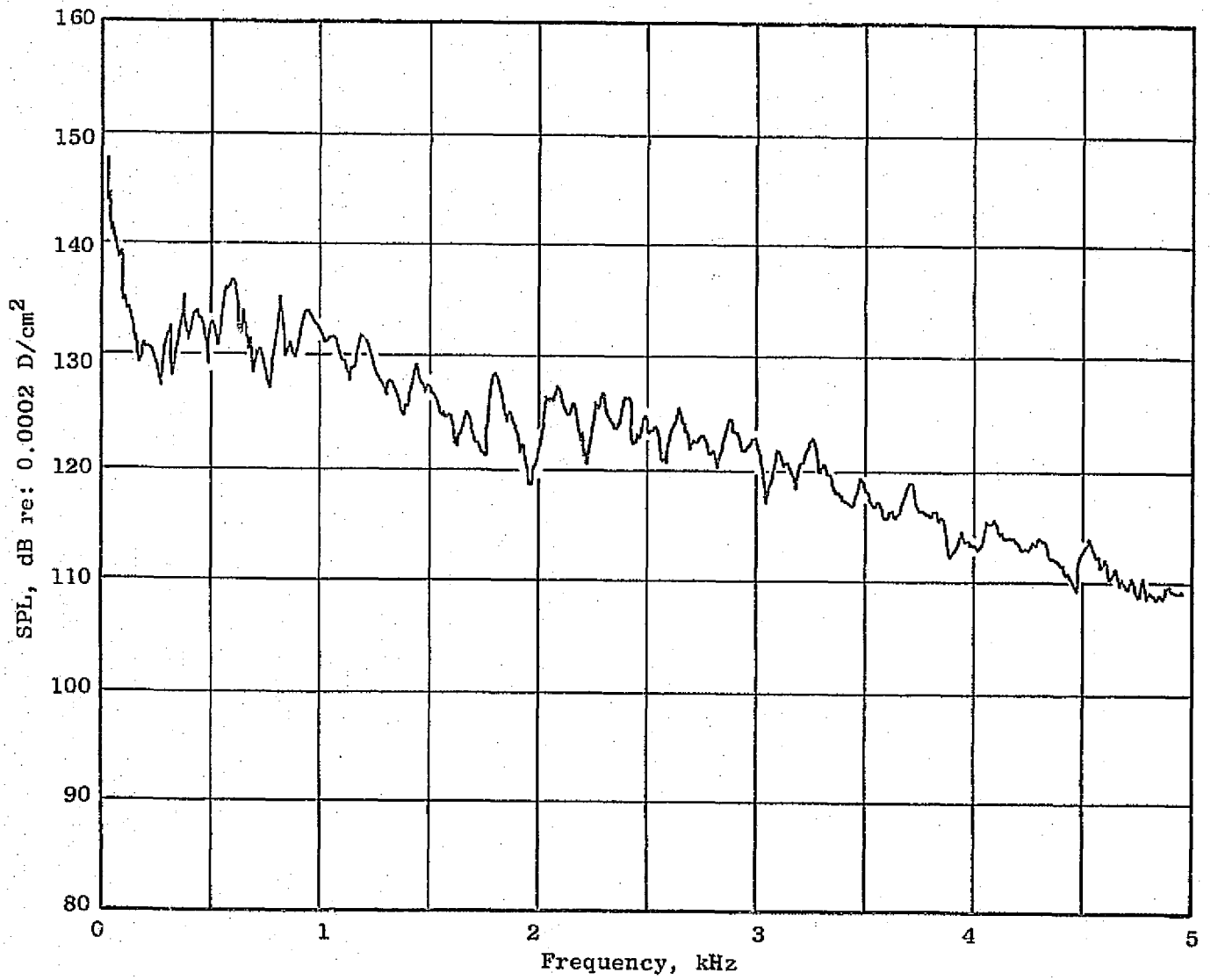

Figure C-17. Configuration D13 Reading 705 Downstream Probe Narrowband Spectrum.

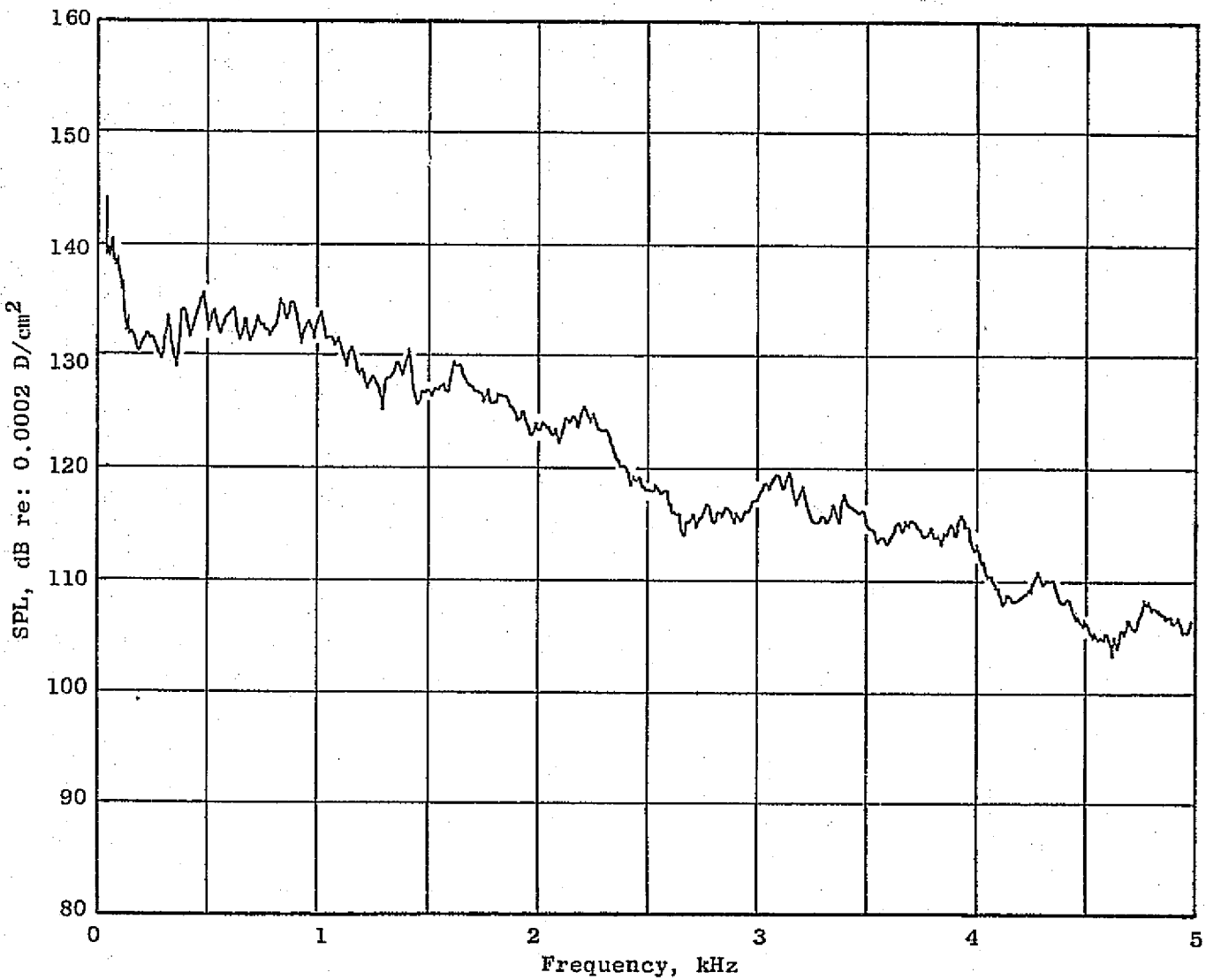

Figure C-18. Configuration D13 Reading 705 Downstream Wall Narrowband Spectrum.

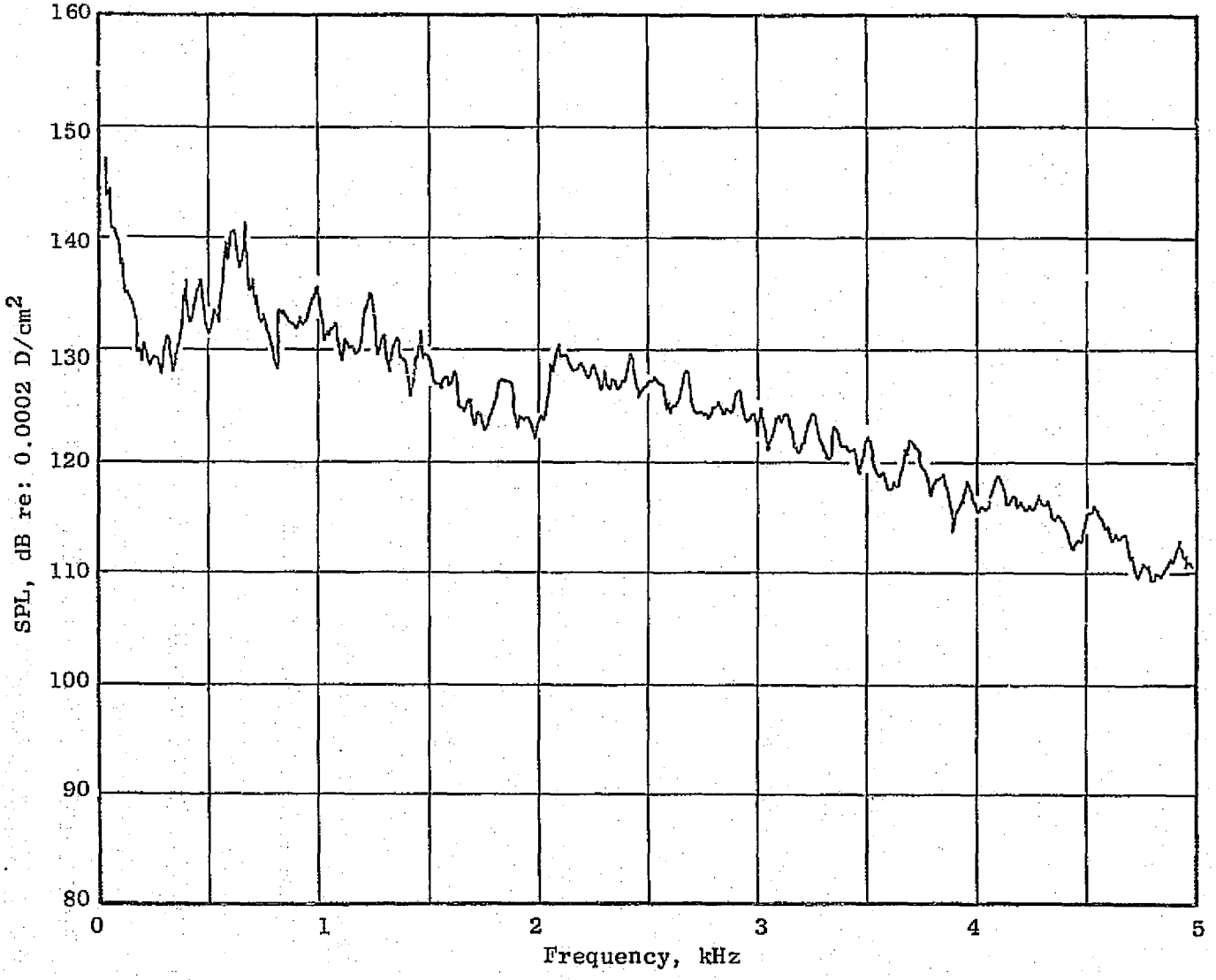

Figure C-19. Configuration D13 Reading 706 Downstream Probe Narrowband Spectrum.

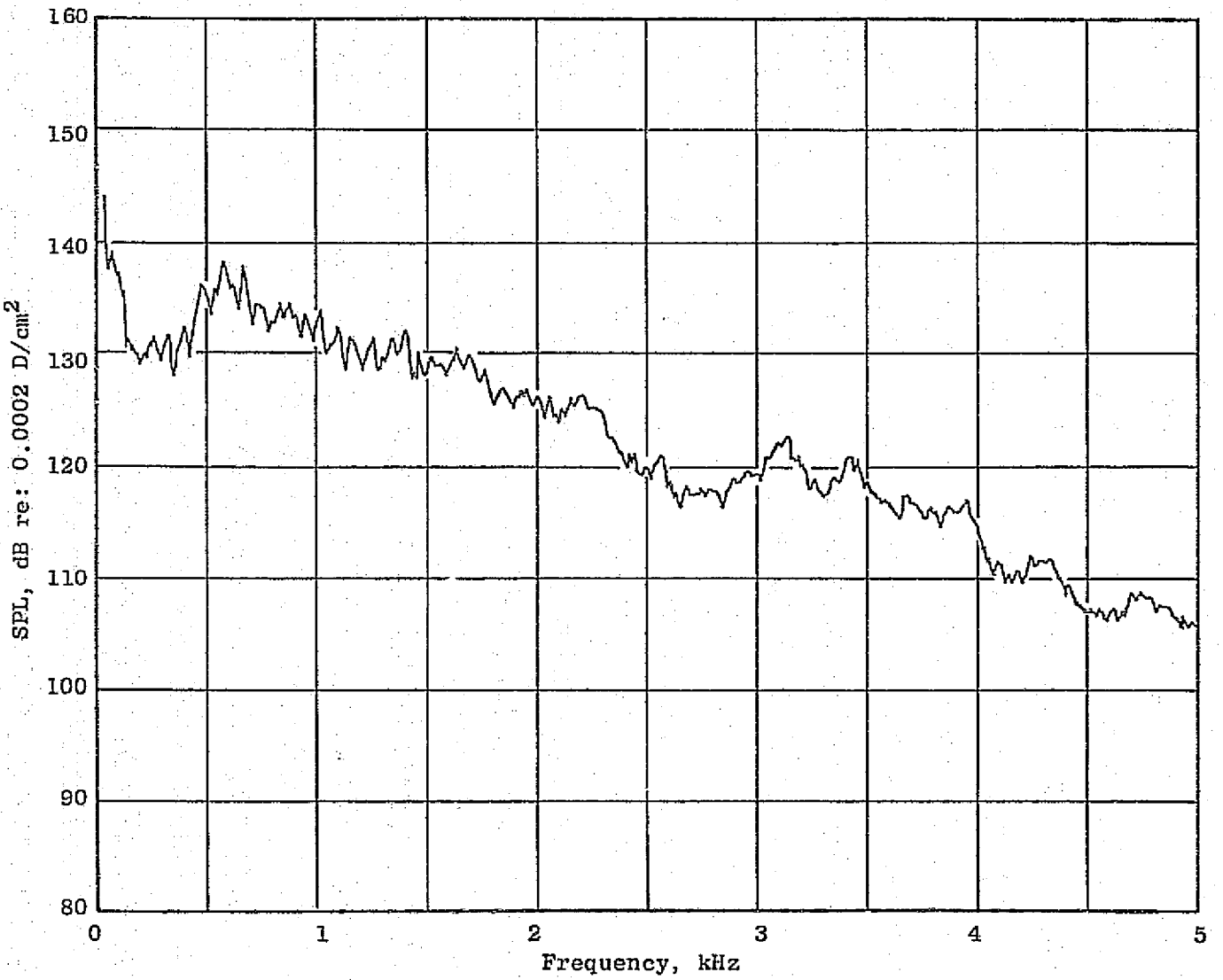

Figure C-20. Configuration D13 Reading 706 Downstream Wall Narrowband Spectrum.

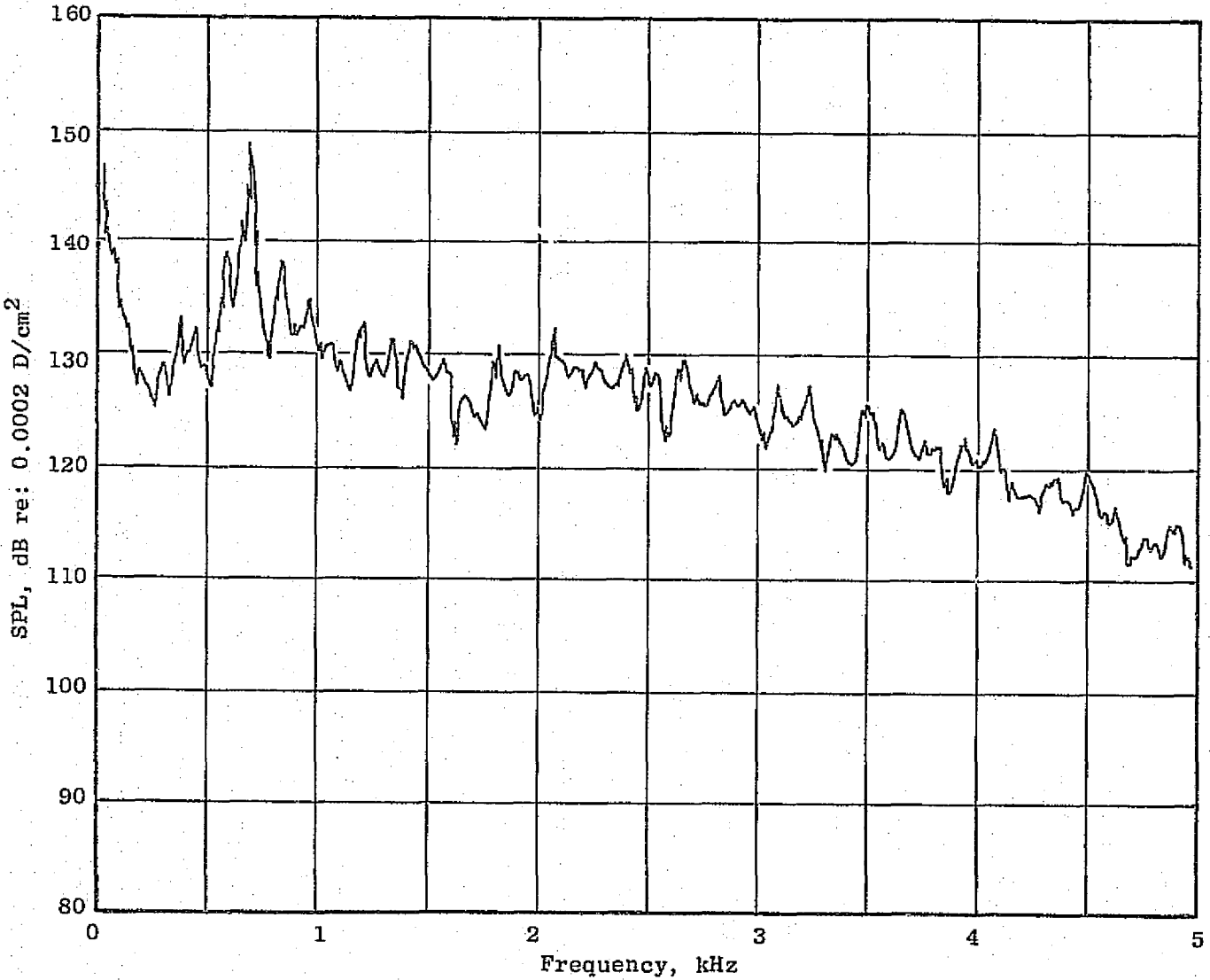

Figure C-21. Configuration D13 Reading 707 Downstream Probe Narrowband Spectrum.

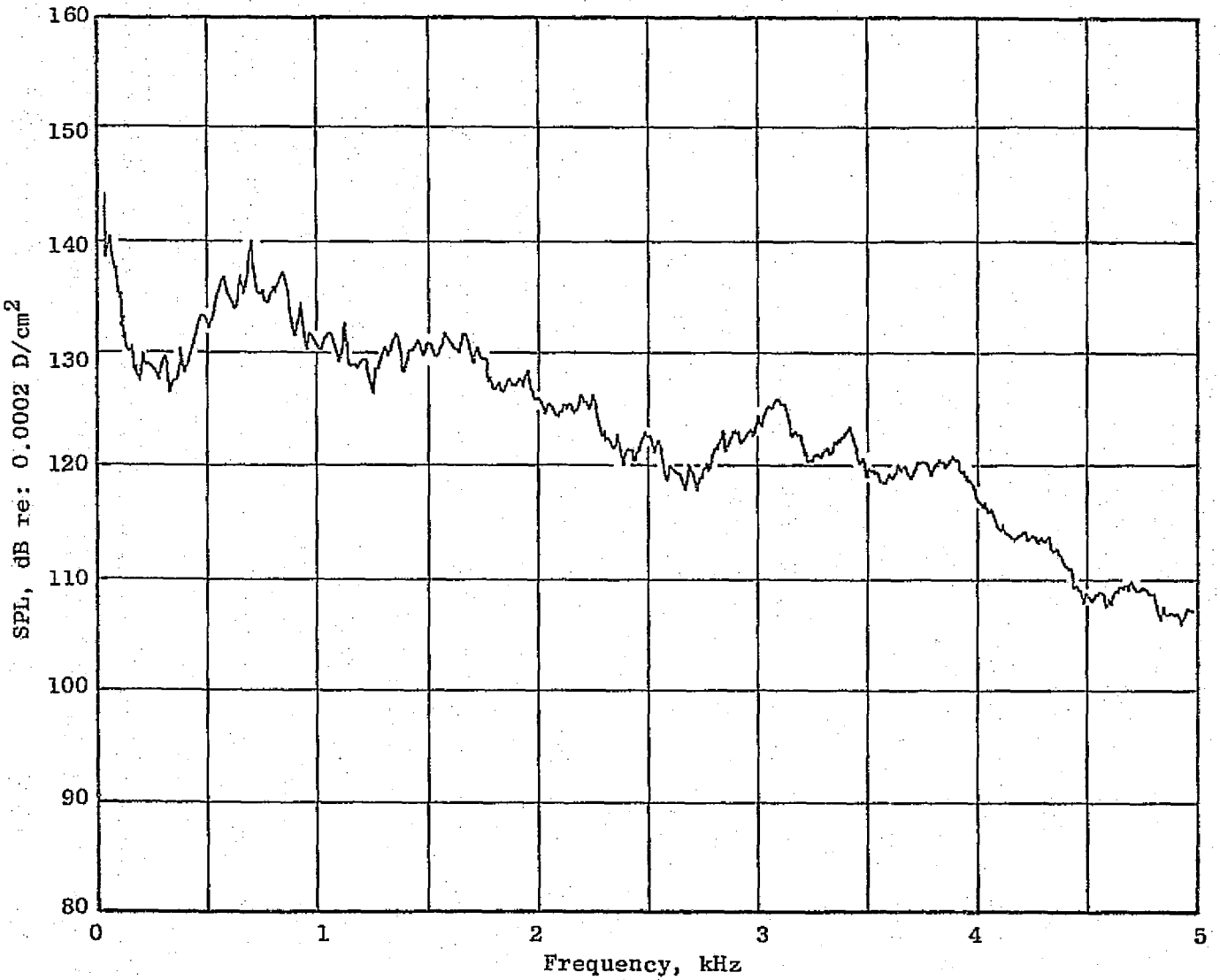

Figure C-22. Configuration D13 Reading 707 Downstream Wall Narrowband Spectrum.

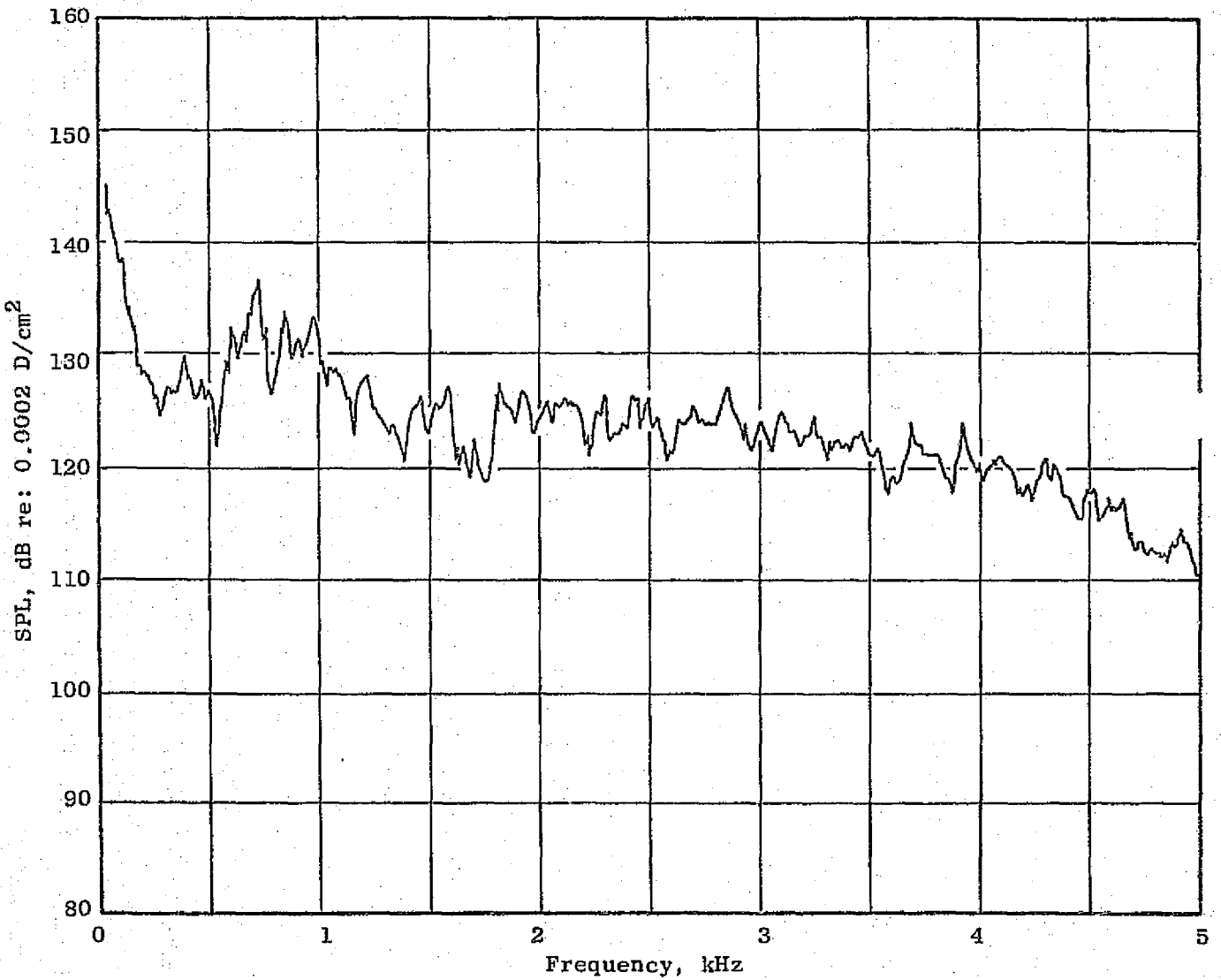

Figure C-23. Configuration D13 Reading 708 Downstream Probe Narrowband Spectrum.

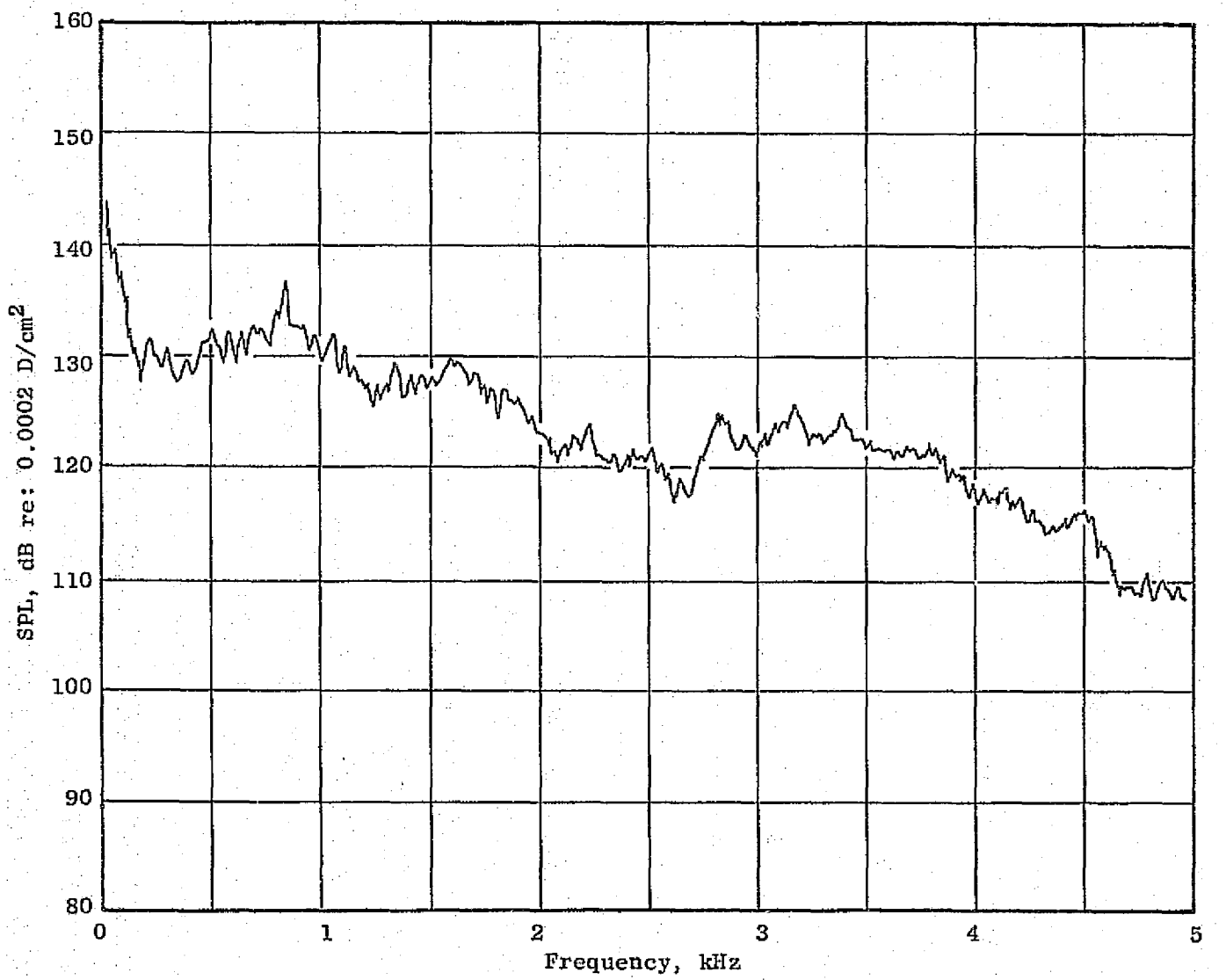

Figure C-24. Configuration D13 Reading 708 Downstream Wall Narrowband Spectrum.

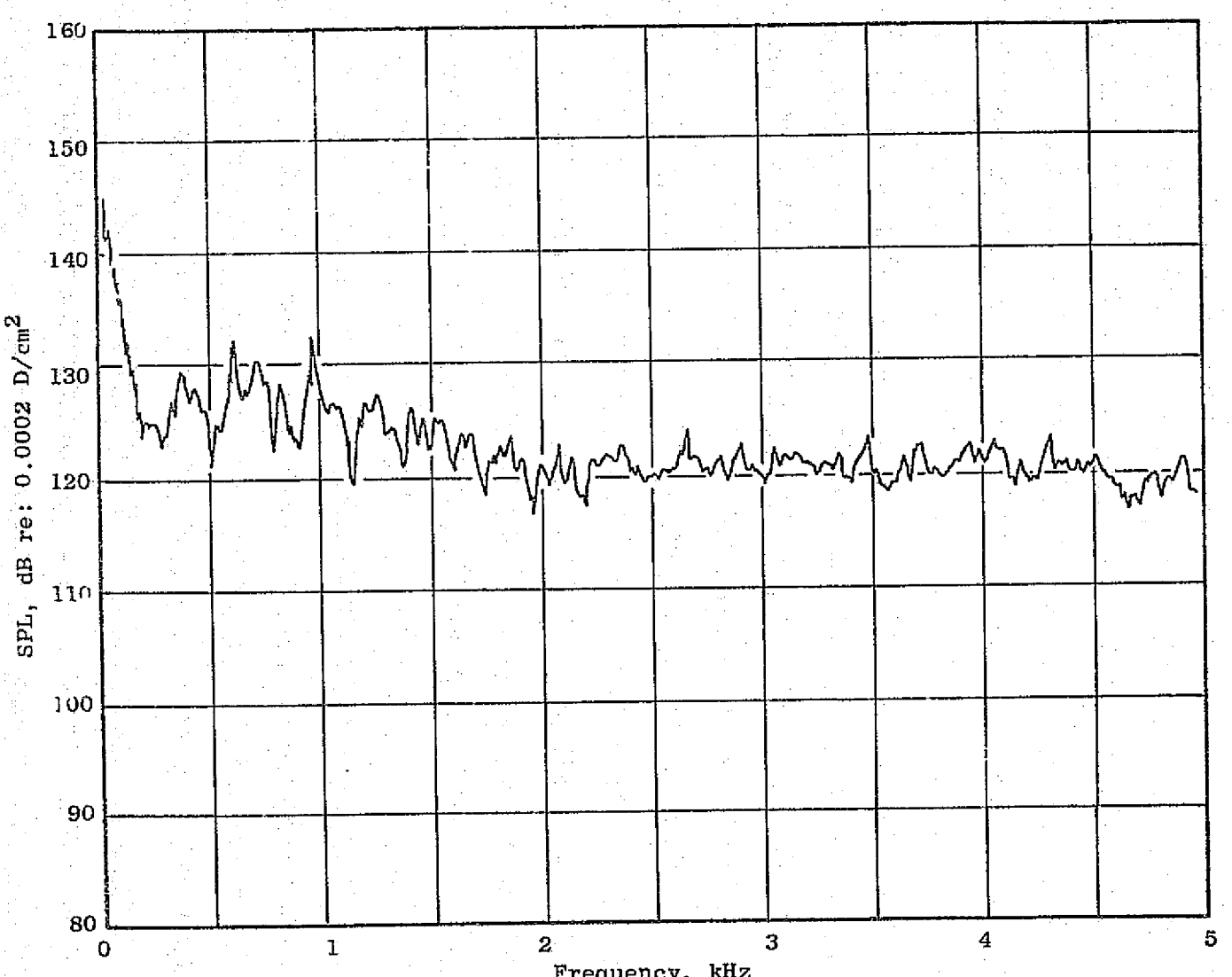

Figure C-25. Configuration D13 Reading 709 Downstream Probe Narrowband Spectrum.

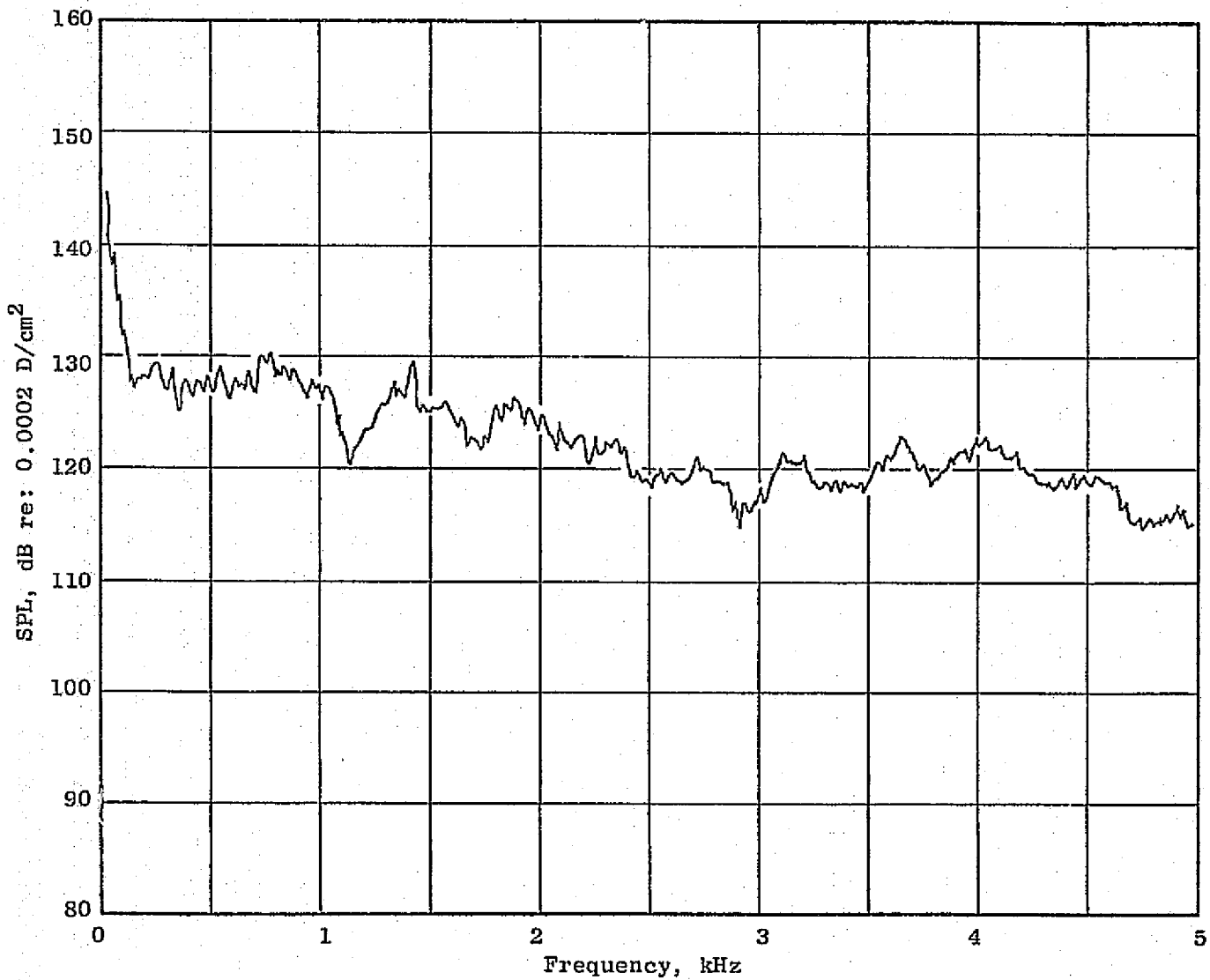

Figure C-26. Configuration D13 Reading 709 Downstream Wall Narrowband Spectrum.

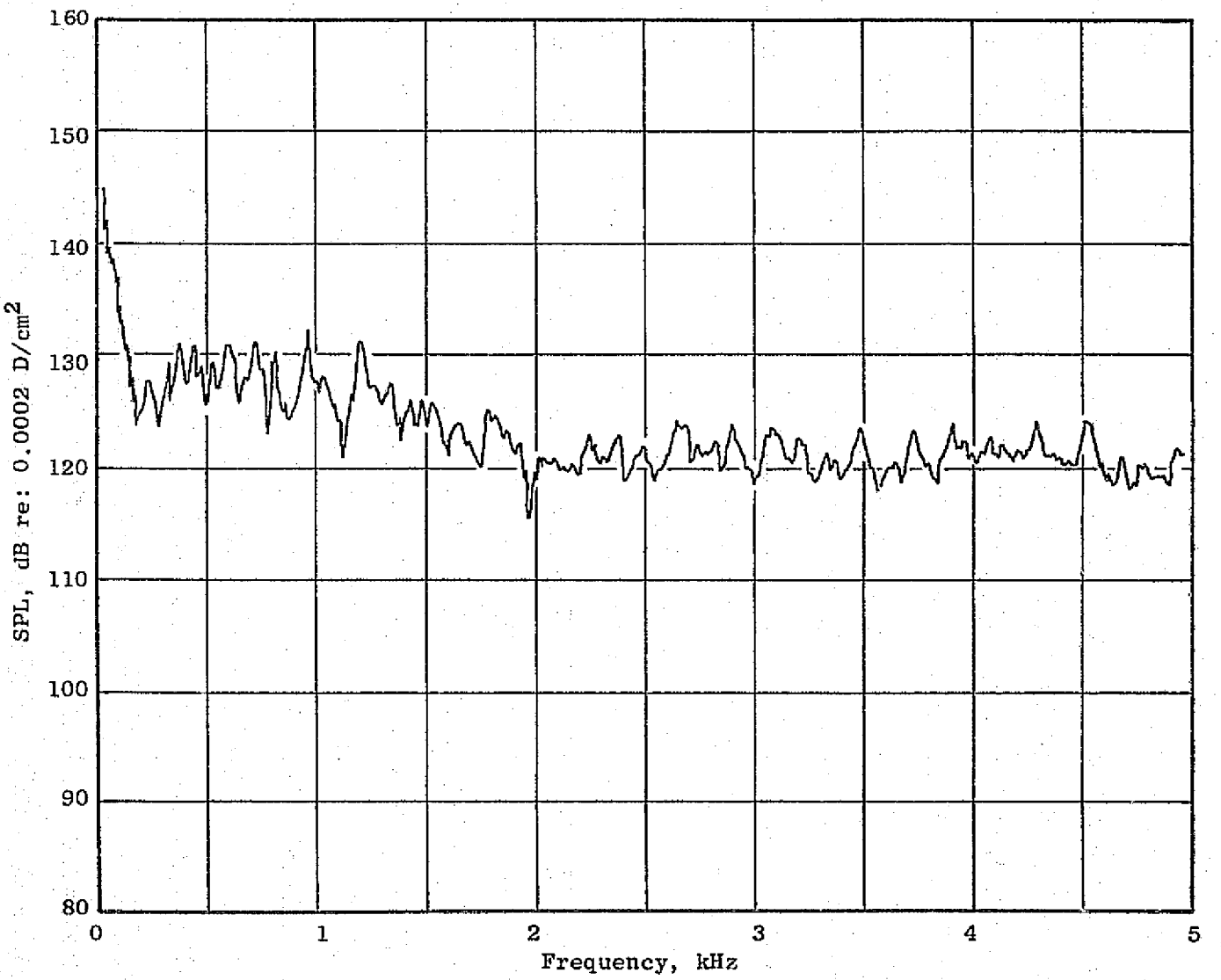

Figure C-27. Configuration D13 Reading 710 Downstream Probe Narrowband Spectrum.

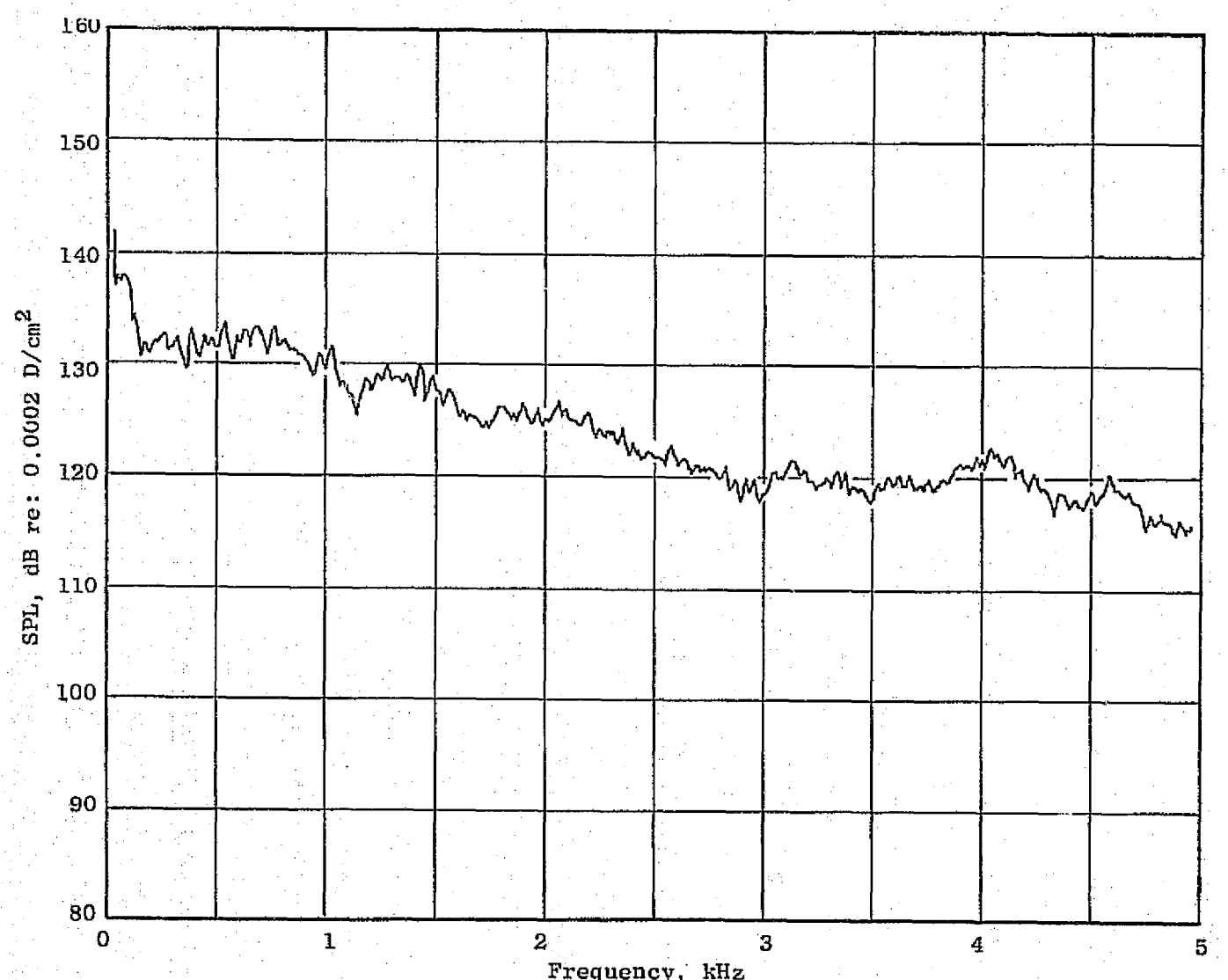

Figure C-28. Configuration D13 Reading 710 Downstream Wall Narrowband Spectrum.

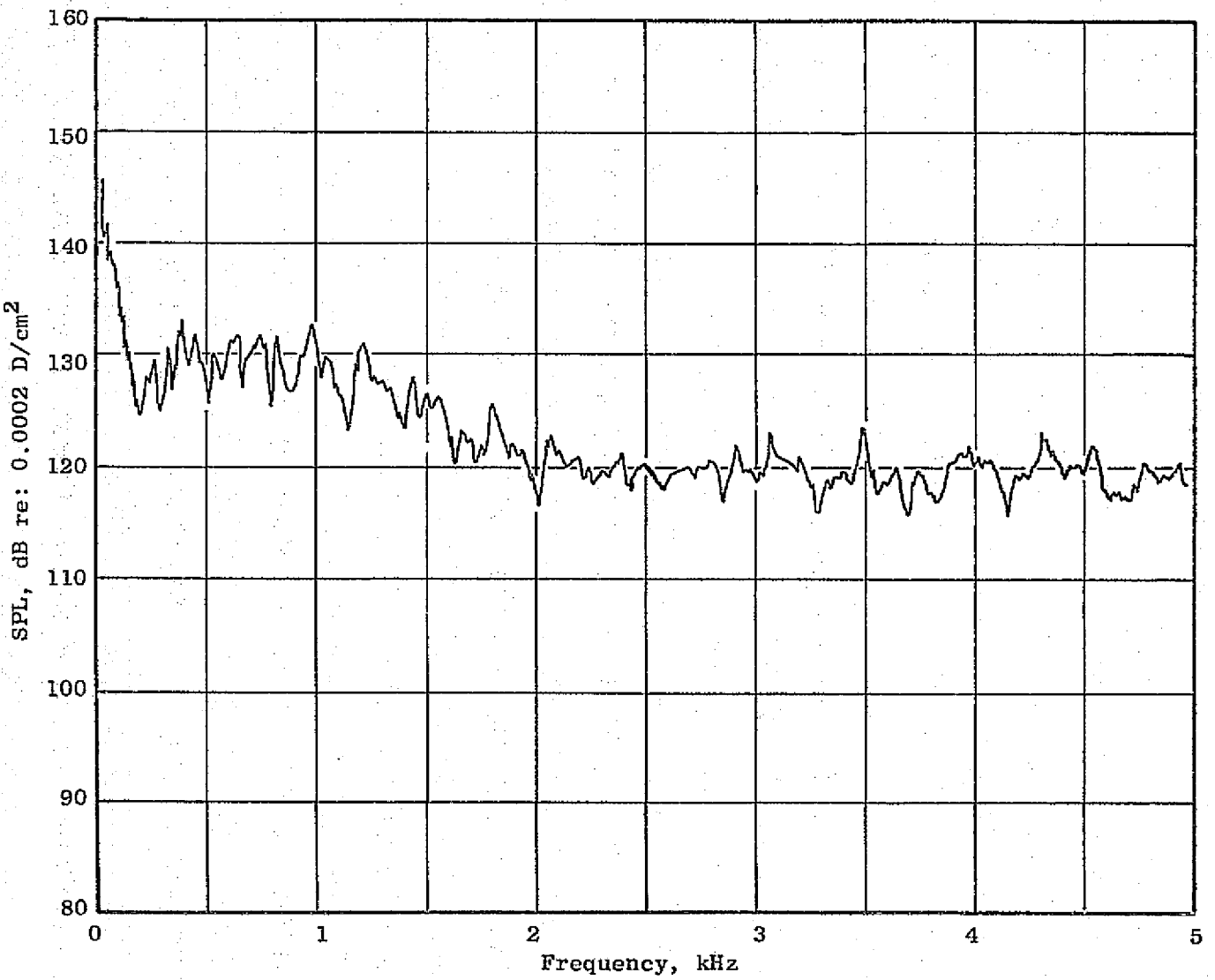

Figure C-29. Configuration D13 Raeding 711 Downstream Probe Narrowband Spectrum.

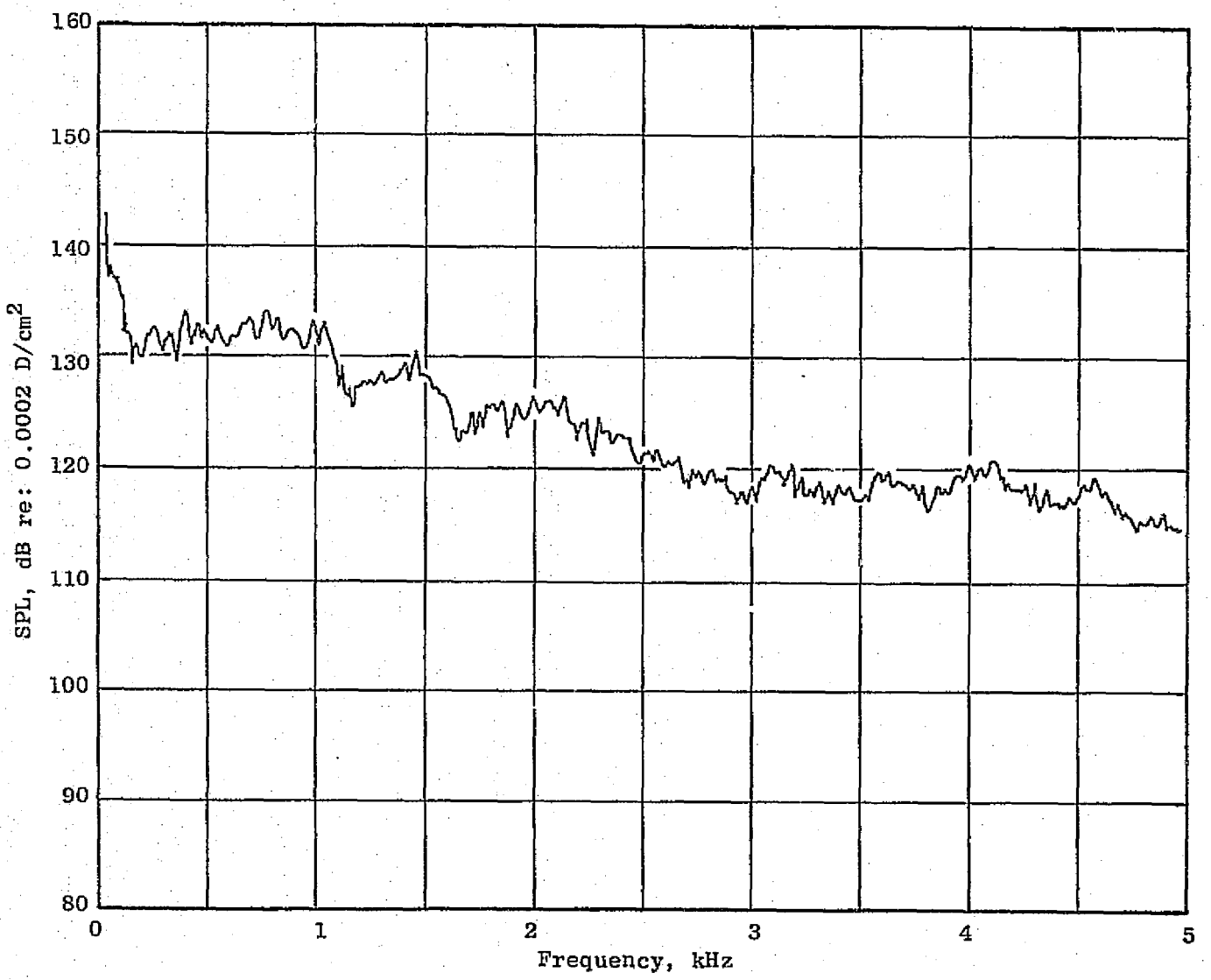

Figure C-30. Configuration D13 Reading 711 Downstream Wall Narrowband Spectrum.

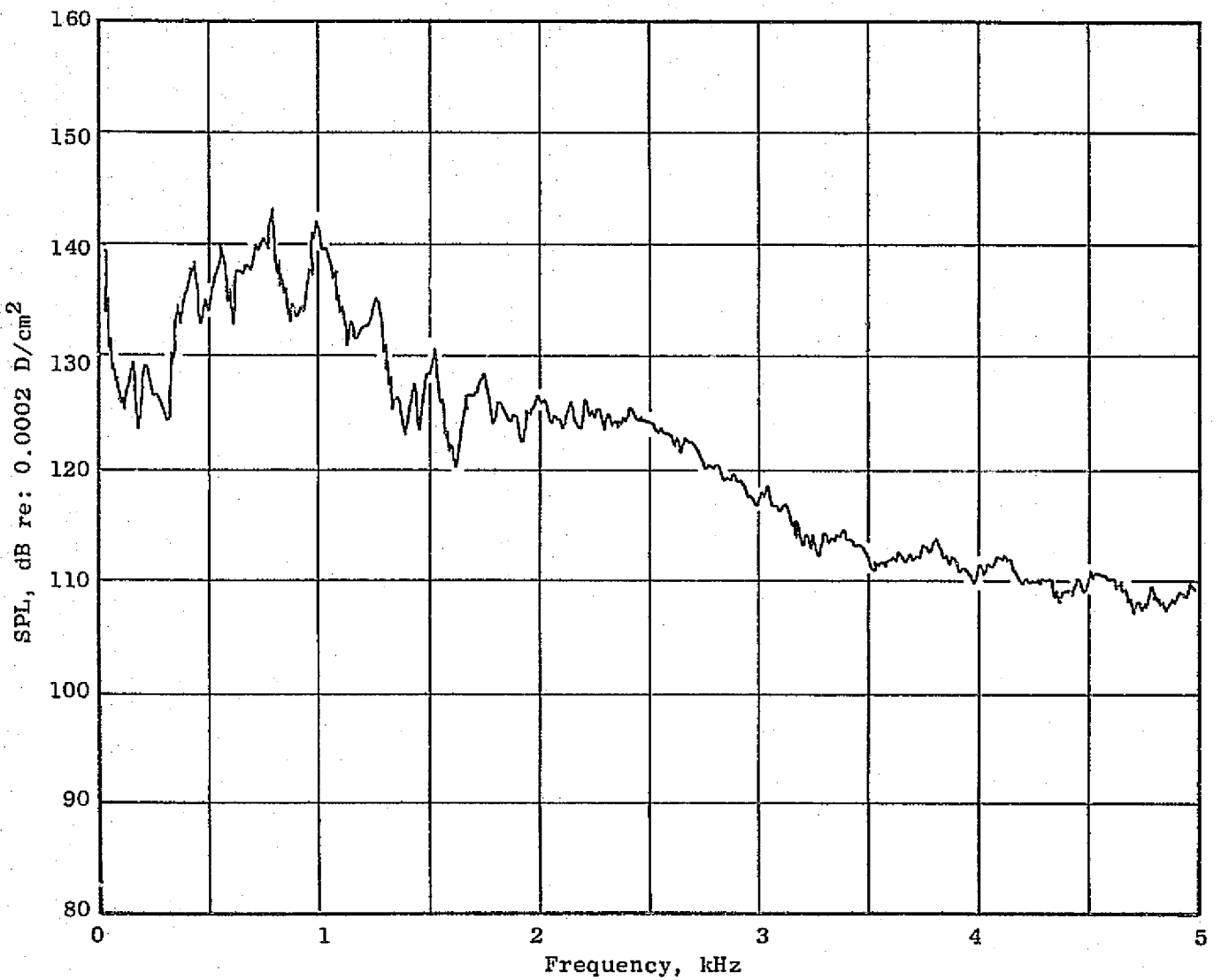

Figure C-31. Configuration D13 Reading 748 Upstream Probe Narrowband Spectrum.

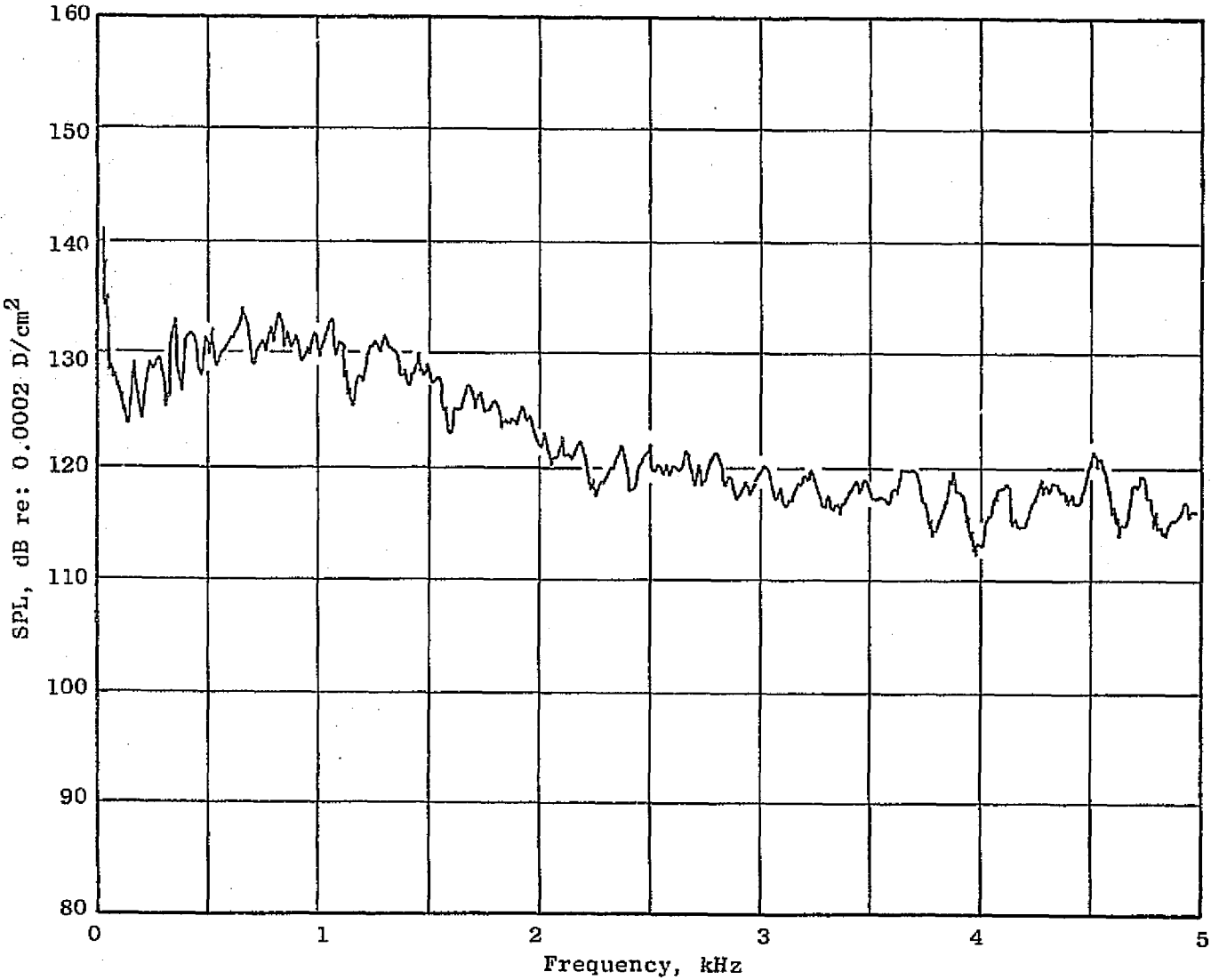

Figure C-32. Configuration D13 Reading 748 Downstream Probe Narrowband Spectrum.

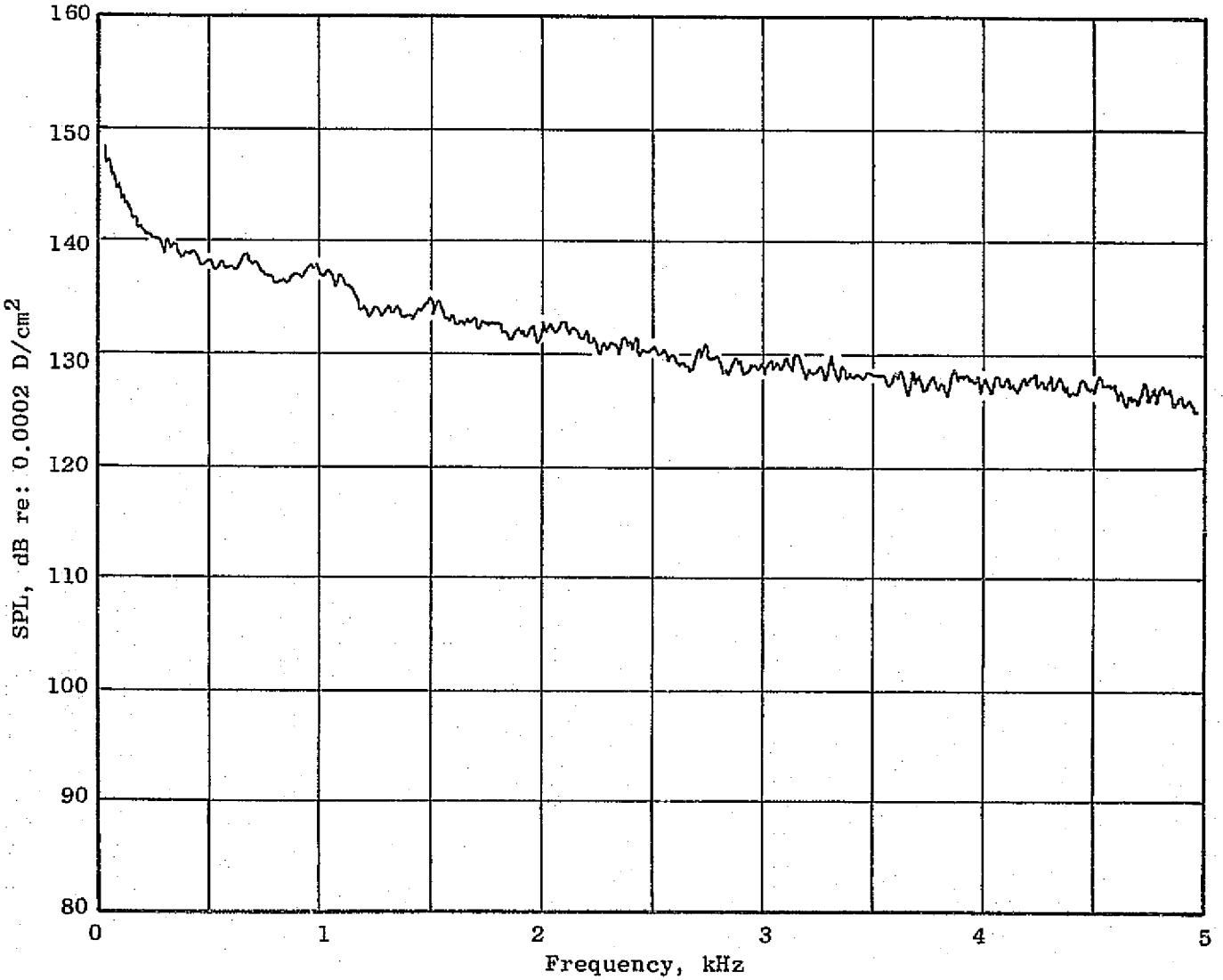

Figure C-33. Configuration D13 Reading 748 Downstream Wall Narrowband Spectrum.

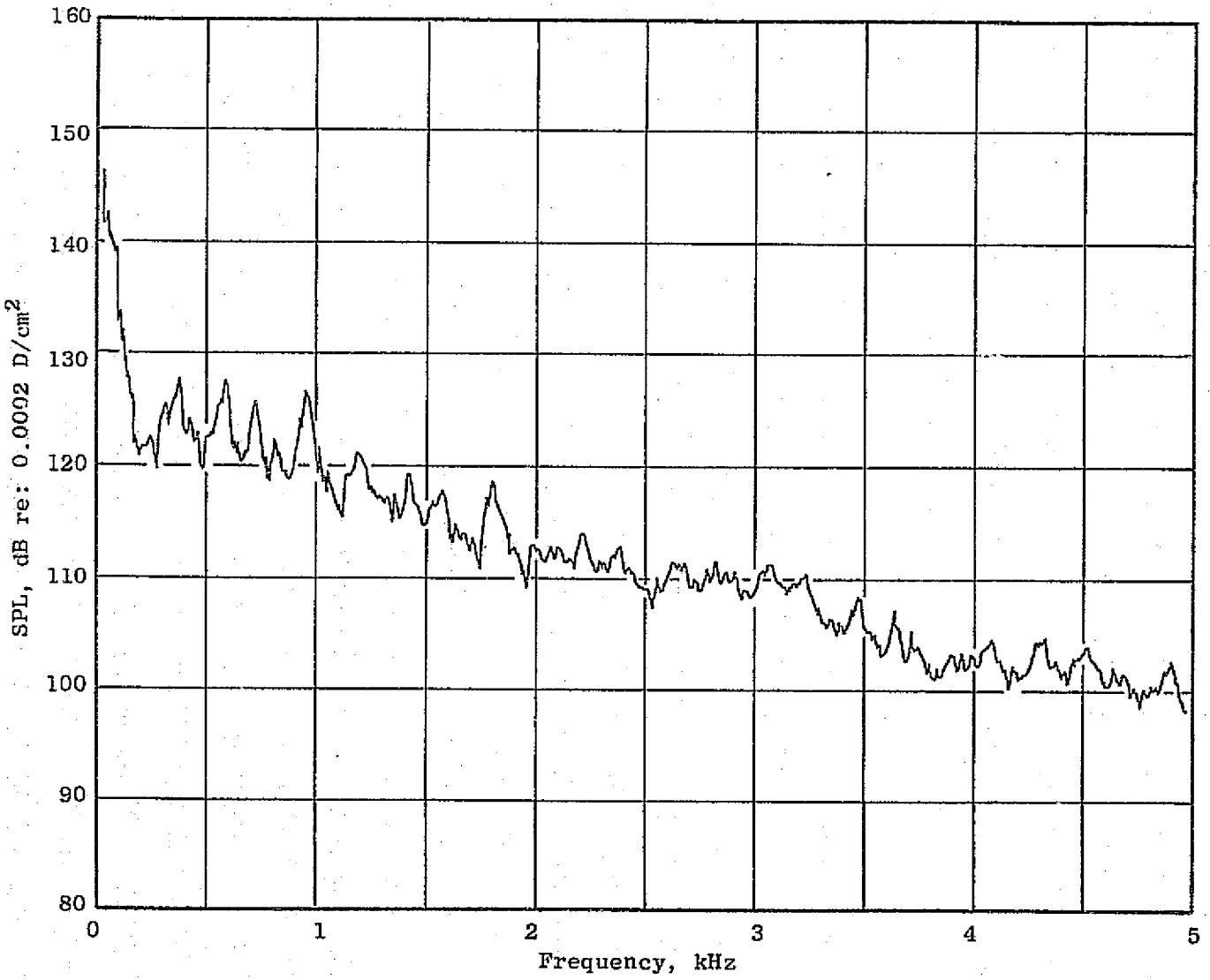

Figure C-34. Configuration D13 Reading 712 Downstream Probe Narrowband Spectrum.

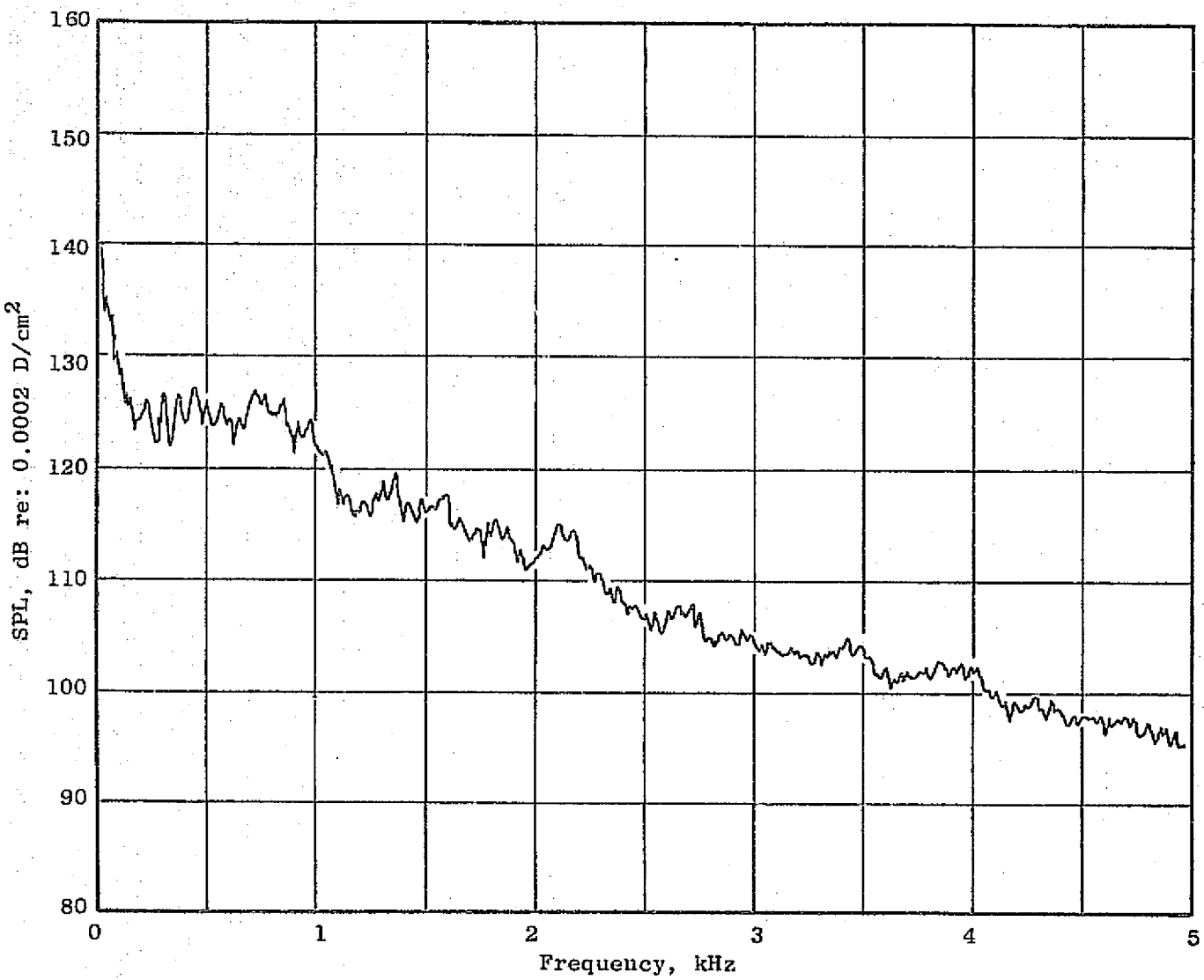

Figure C-35. Configuration D13 Reading 712 Downstream Wall Narrowband Spectrum.

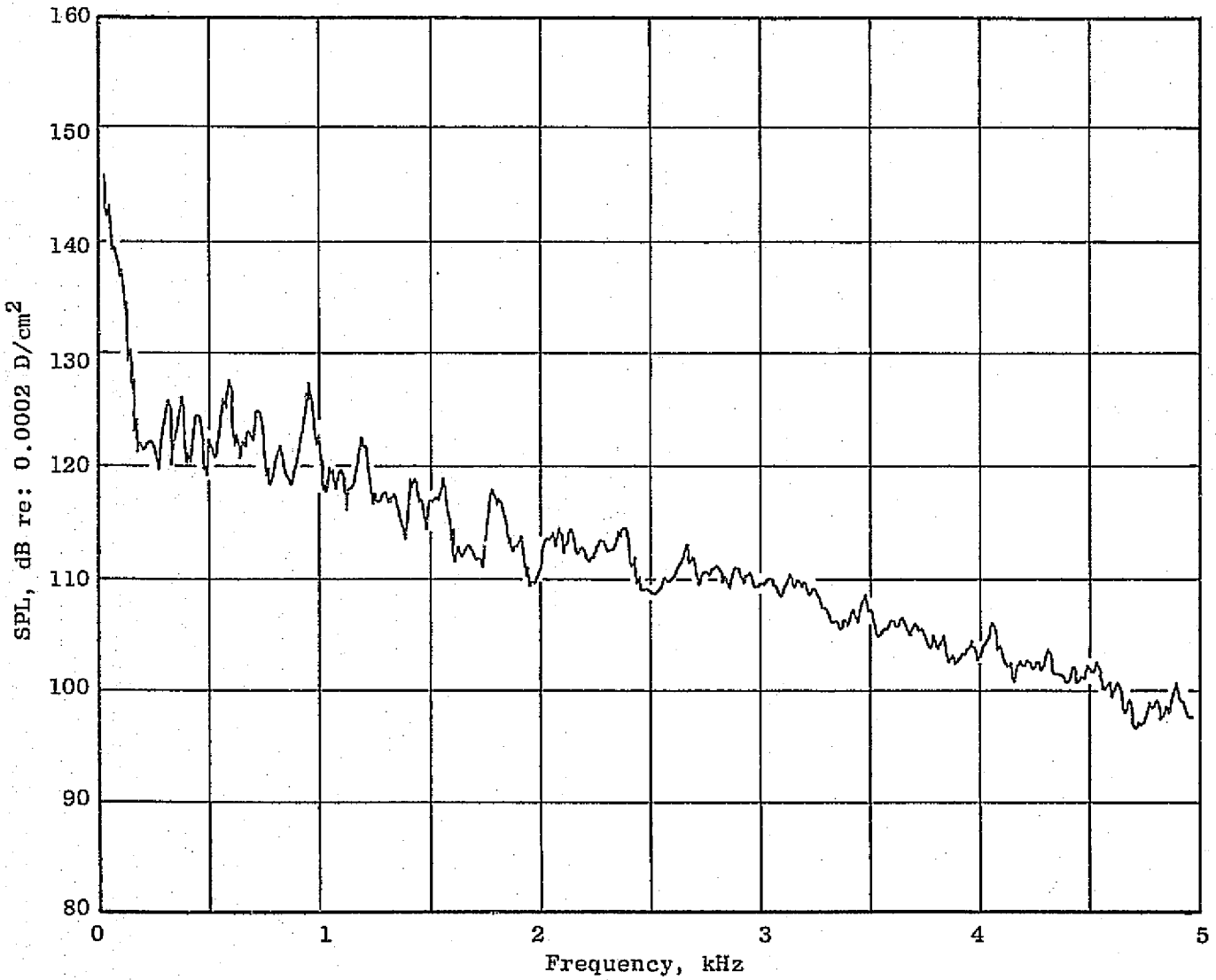

Figure C-36. Configuration D13 Reading 713 Downstream Probe Narrowband Spectrum.

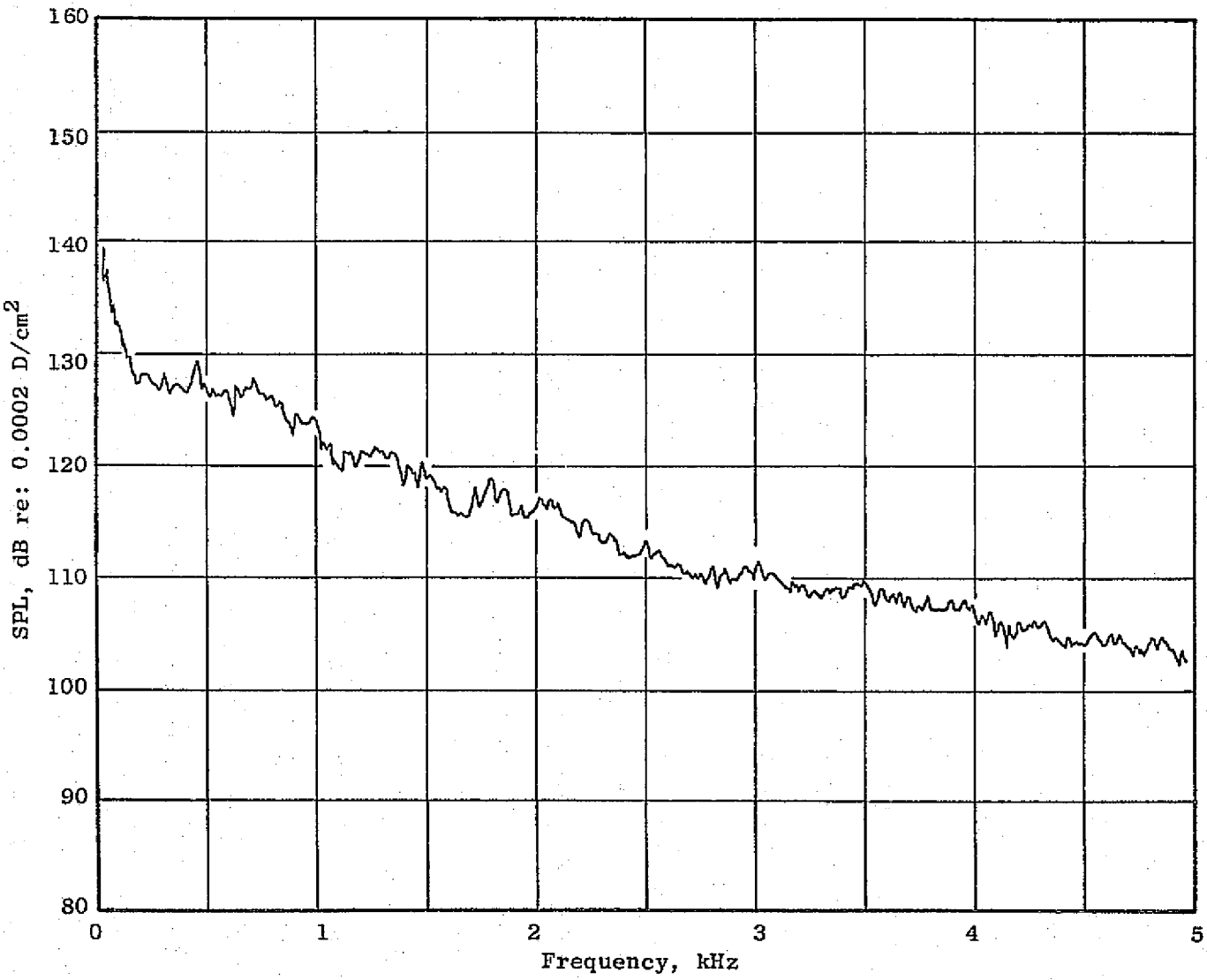

Figure C-37. Configuration D13 Reading 713 Downstream Wall Narrowband Spectrum.

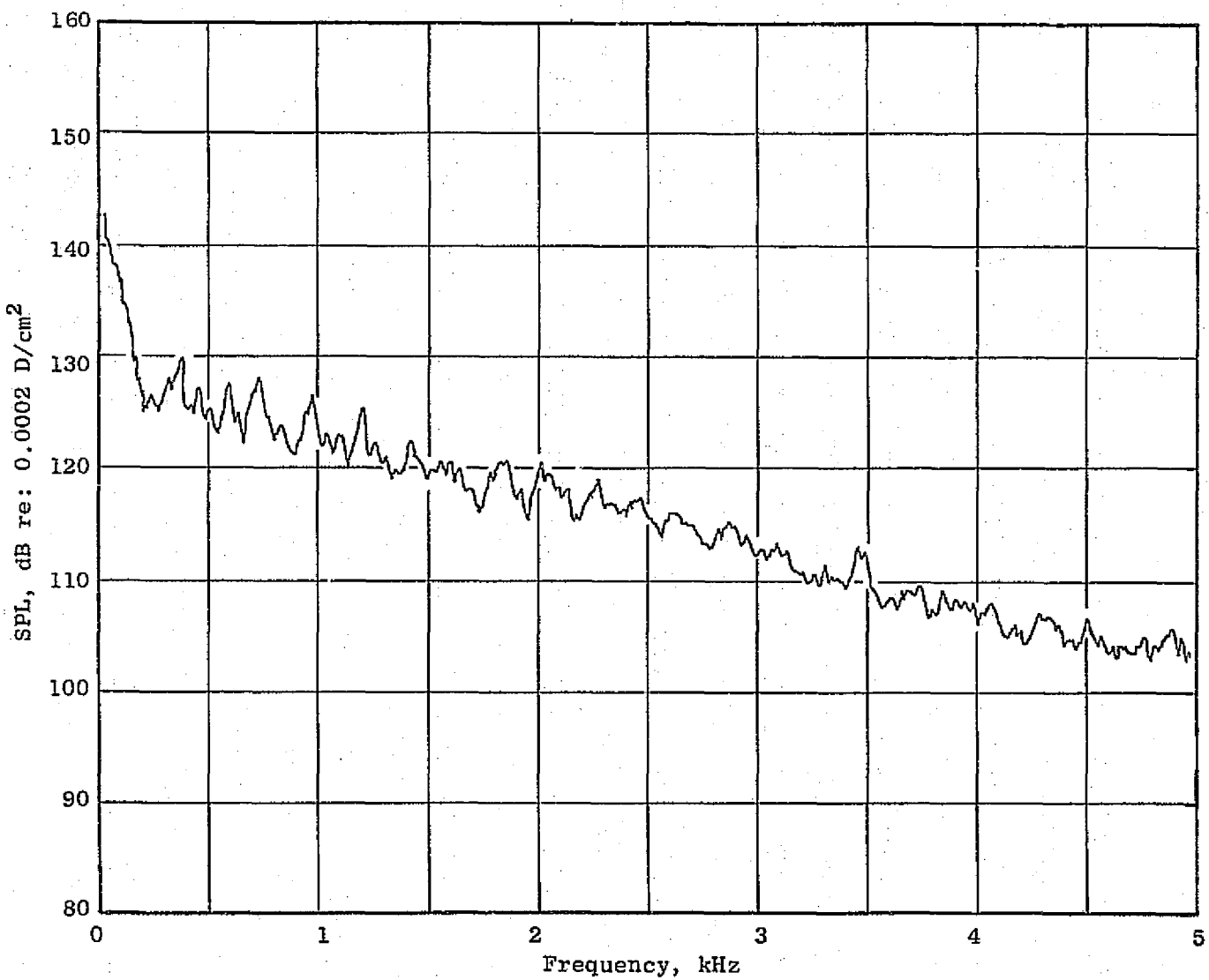

Figure C-38. Configuration D13 Reading 714 Downstream Probe Narrowband Spectrum.

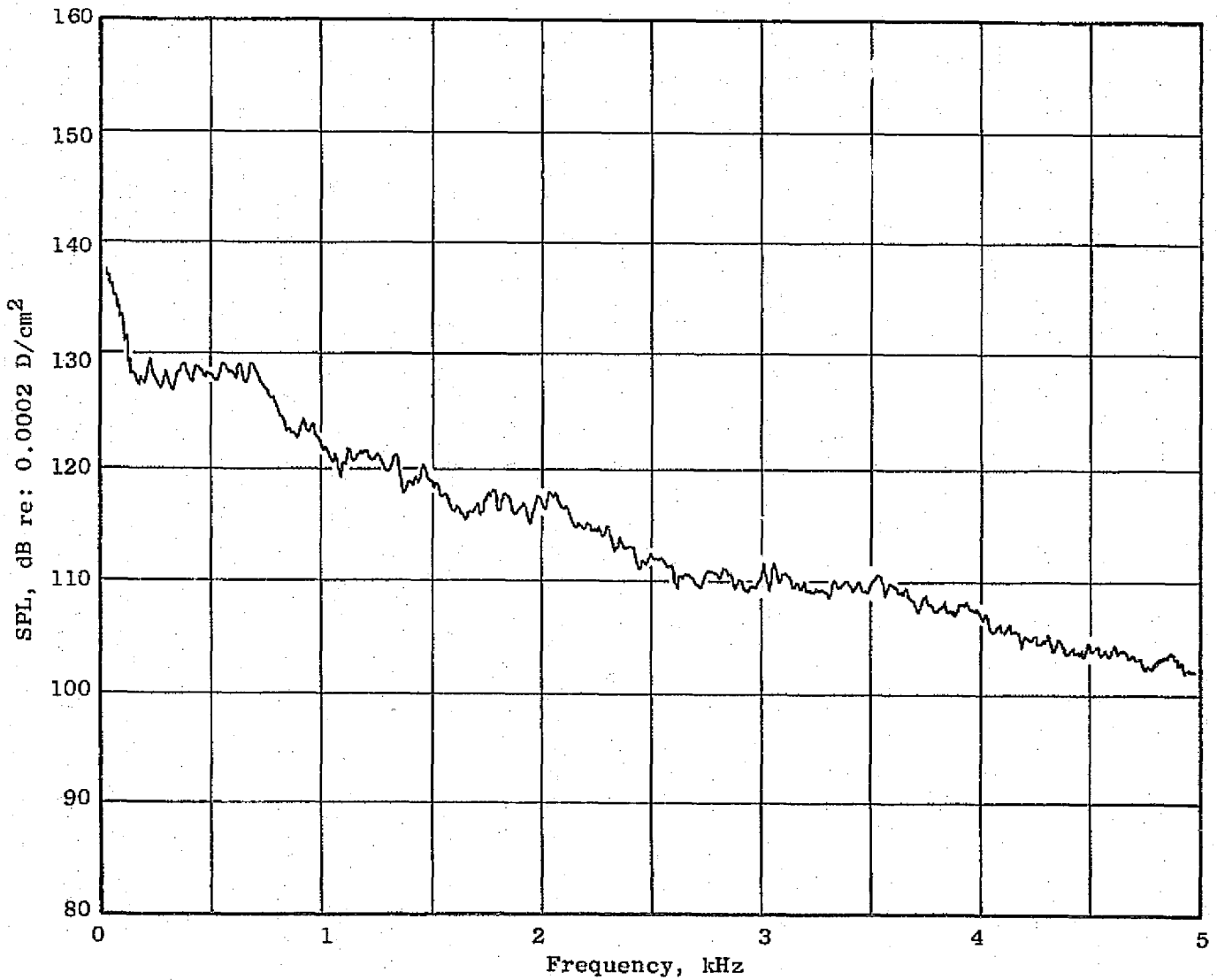

Figure C-39. Configuration D13 Reading 714 Downstream Wall Narrowband Spectrum.

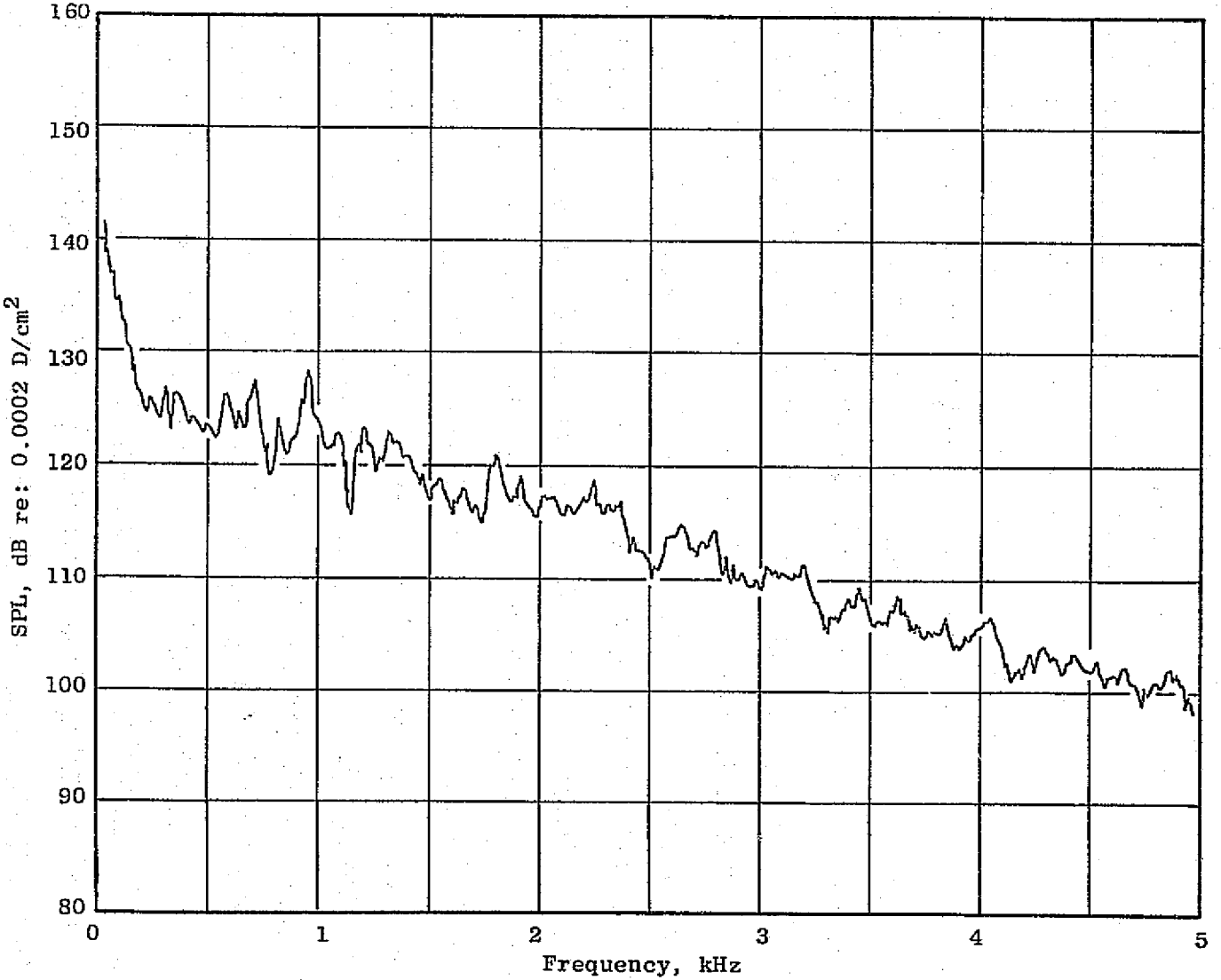

Figure C-40. Configuration D13 Reading 715 Downstream Probe Narrowband Spectrum.

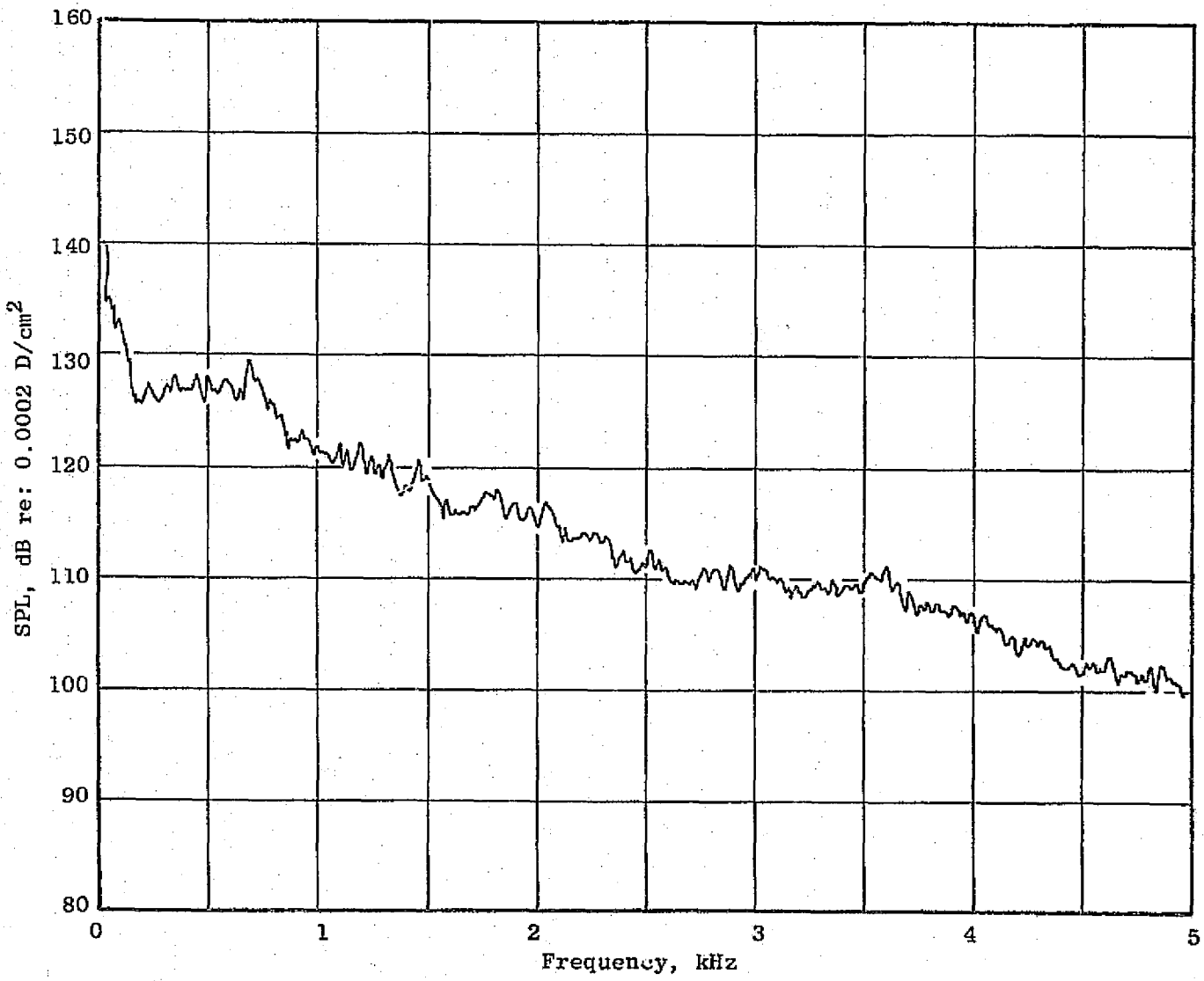

Figure C-41. Configuration D13 Reading 715 Downstream Wall Narrowband Spectrum.

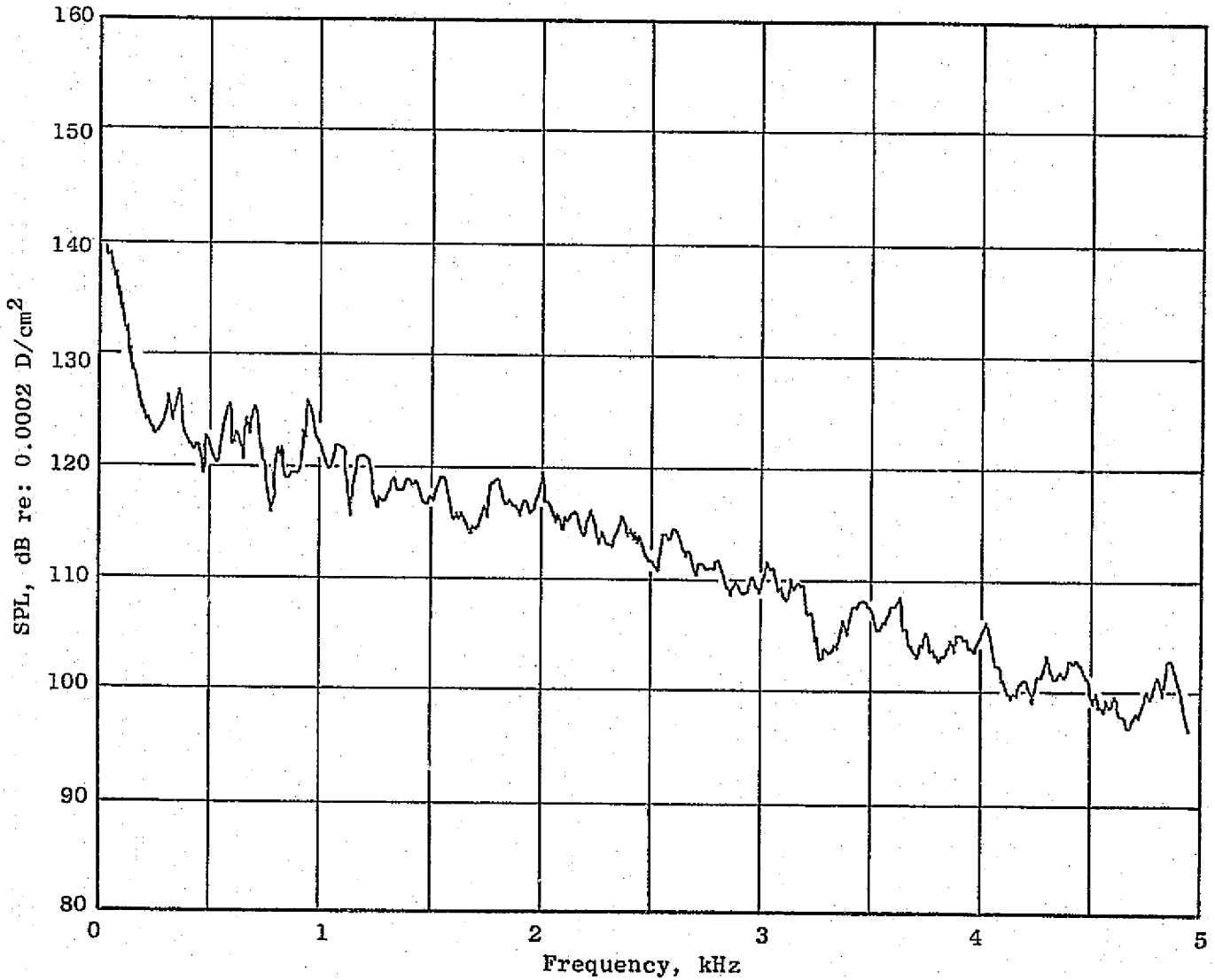

Figure C-42. Configuration D13 Reading 716 Downstream Probe Narrowband Spectrum.

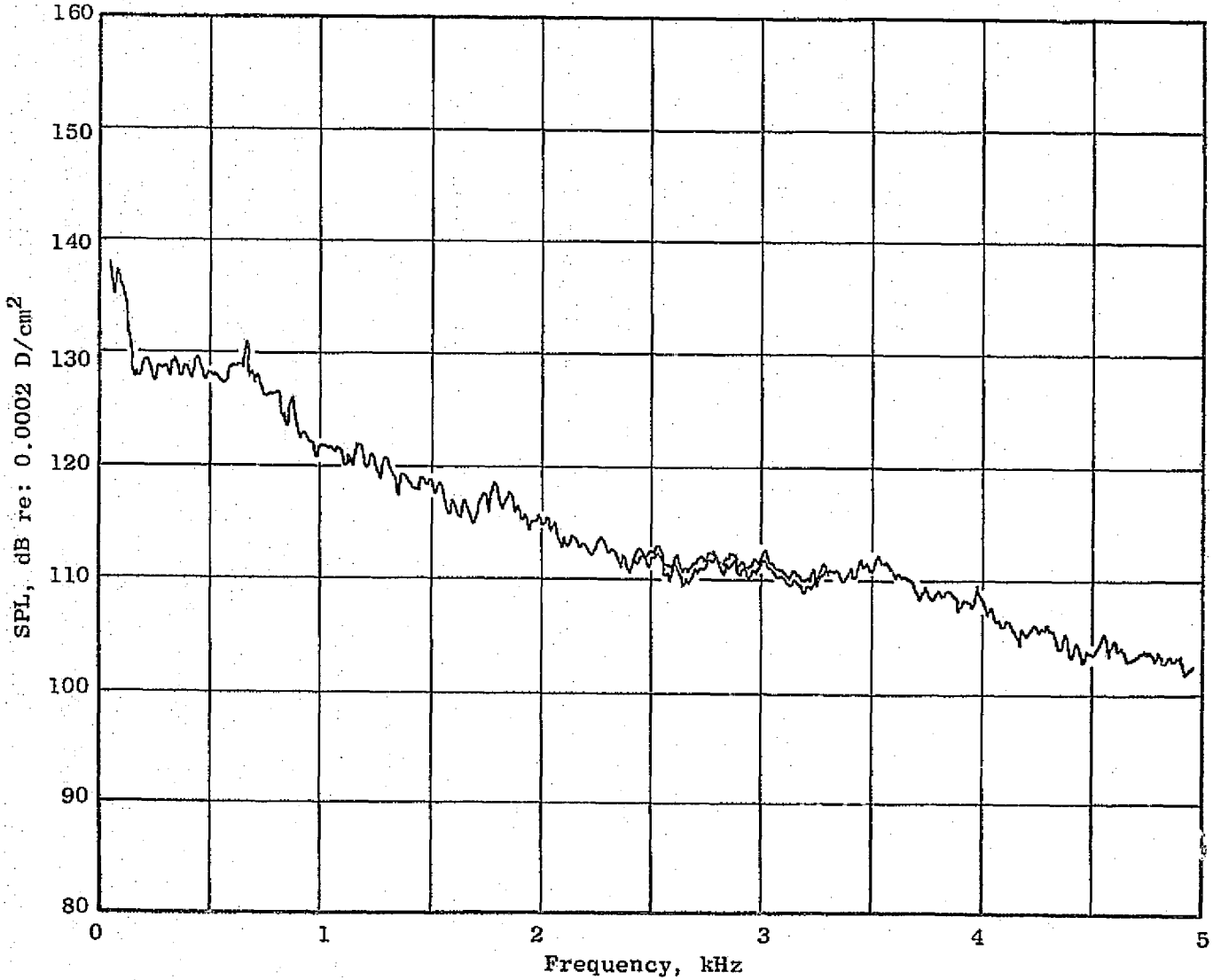

Figure C-43. Configuration D13 Reading 716 Downstream Wall Narrowband Spectrum.

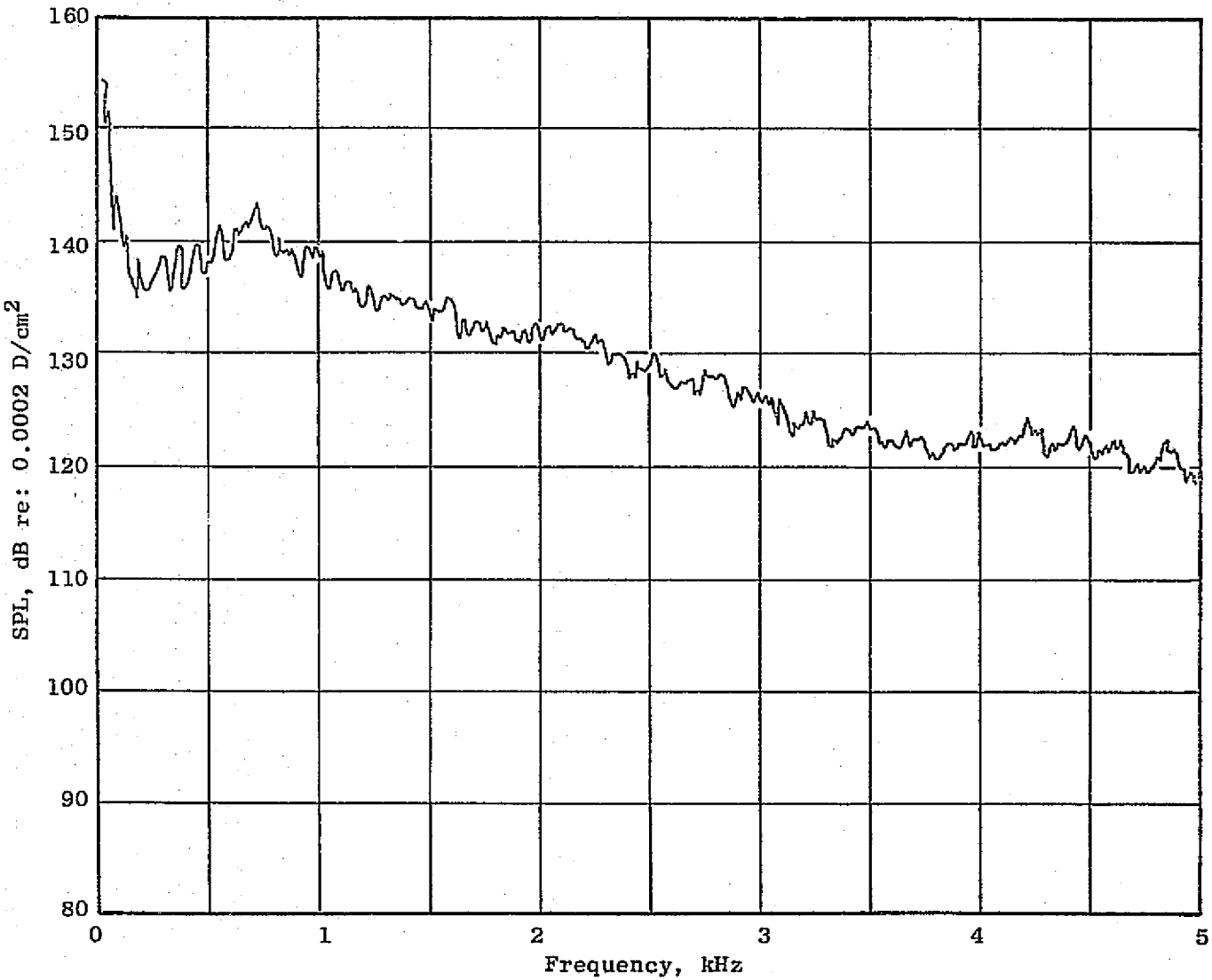

Figure C-44. Configuration D13 Reading 699 Downstream Probe Narrowband Spectrum.

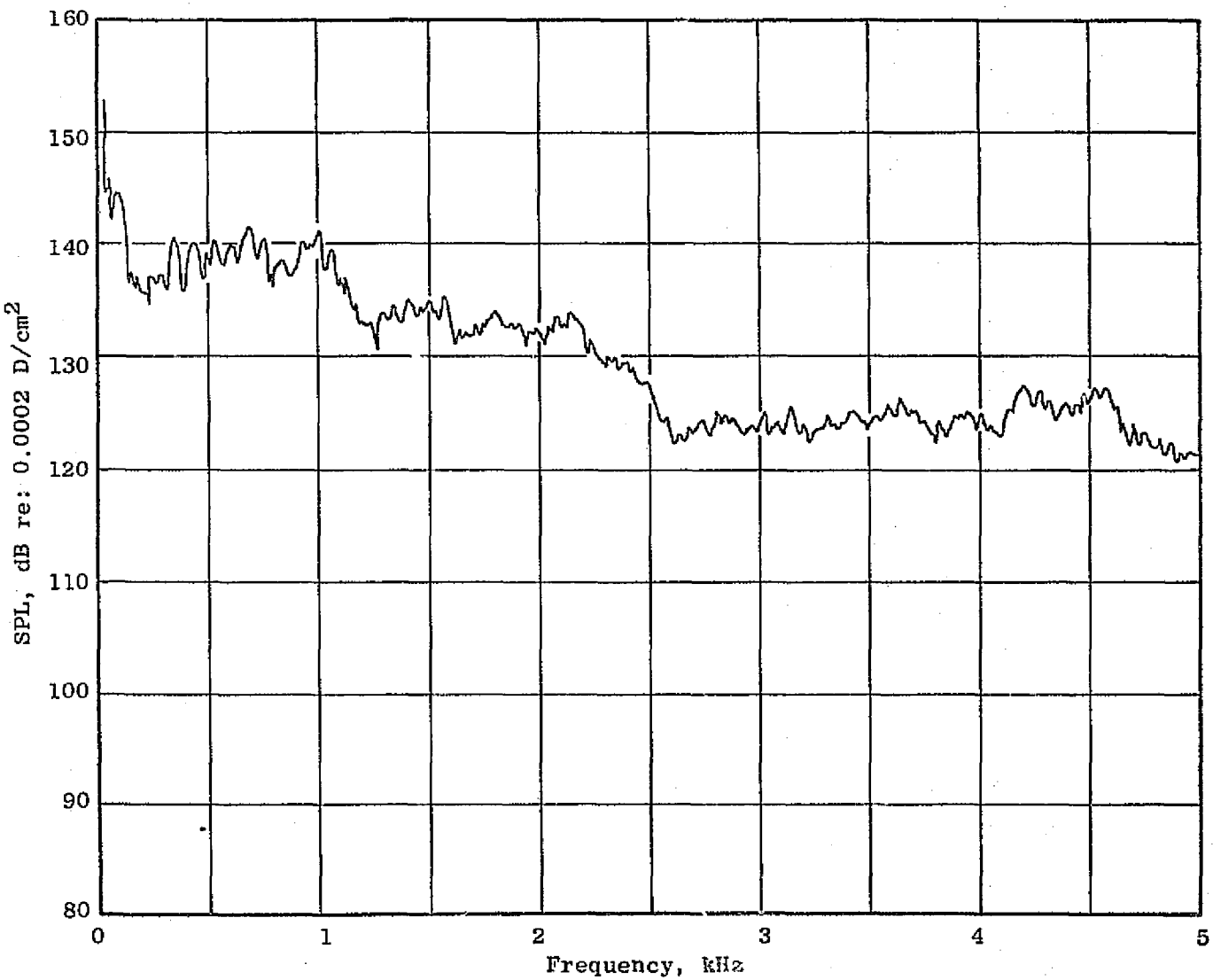

Figure C-45. Configuration D13 Reading 699 Downstream Wall Narrowband Spectrum.

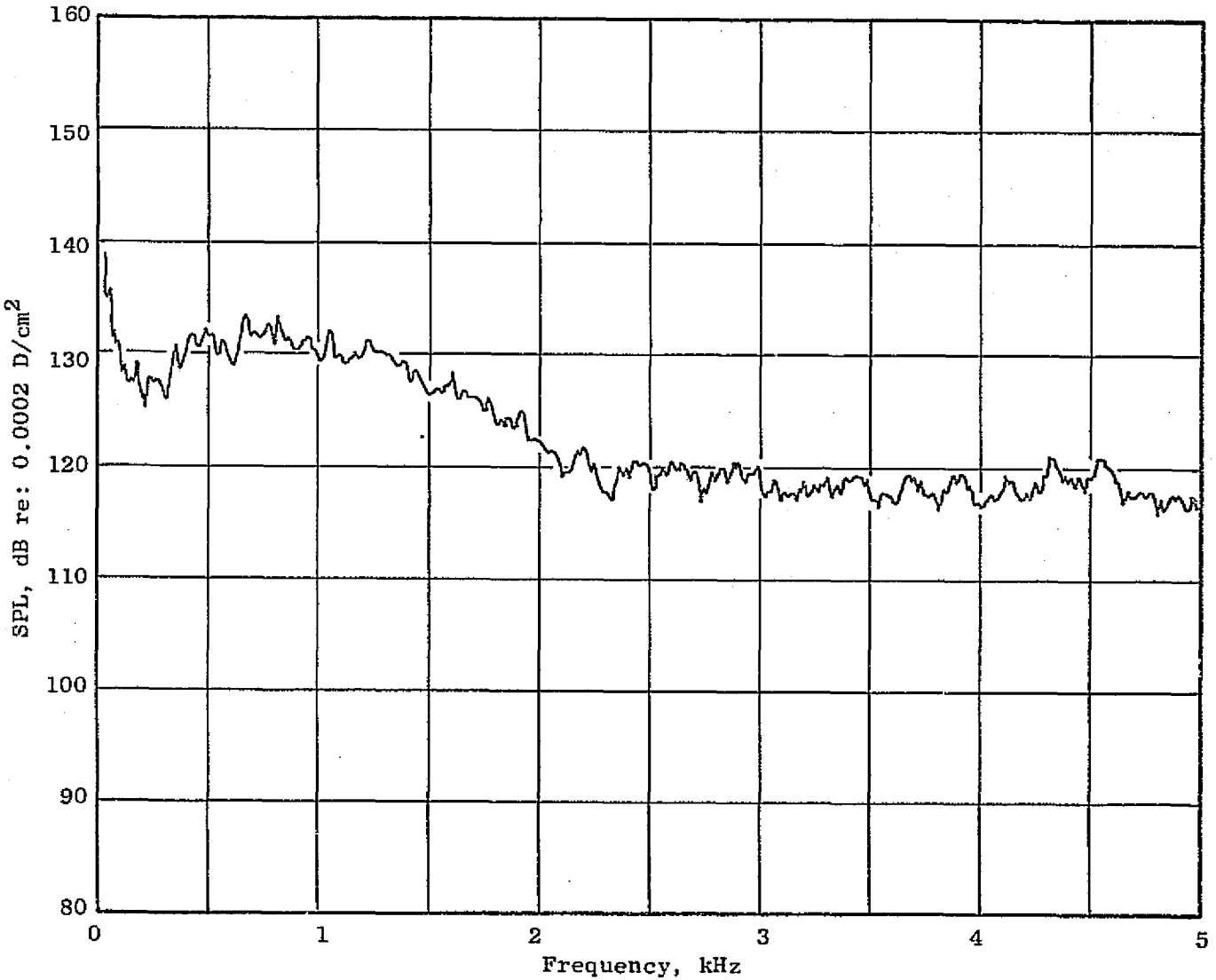

Figure C-46. Configuration D13 Reading 723 Downstream Probe Narrowband Spectrum.

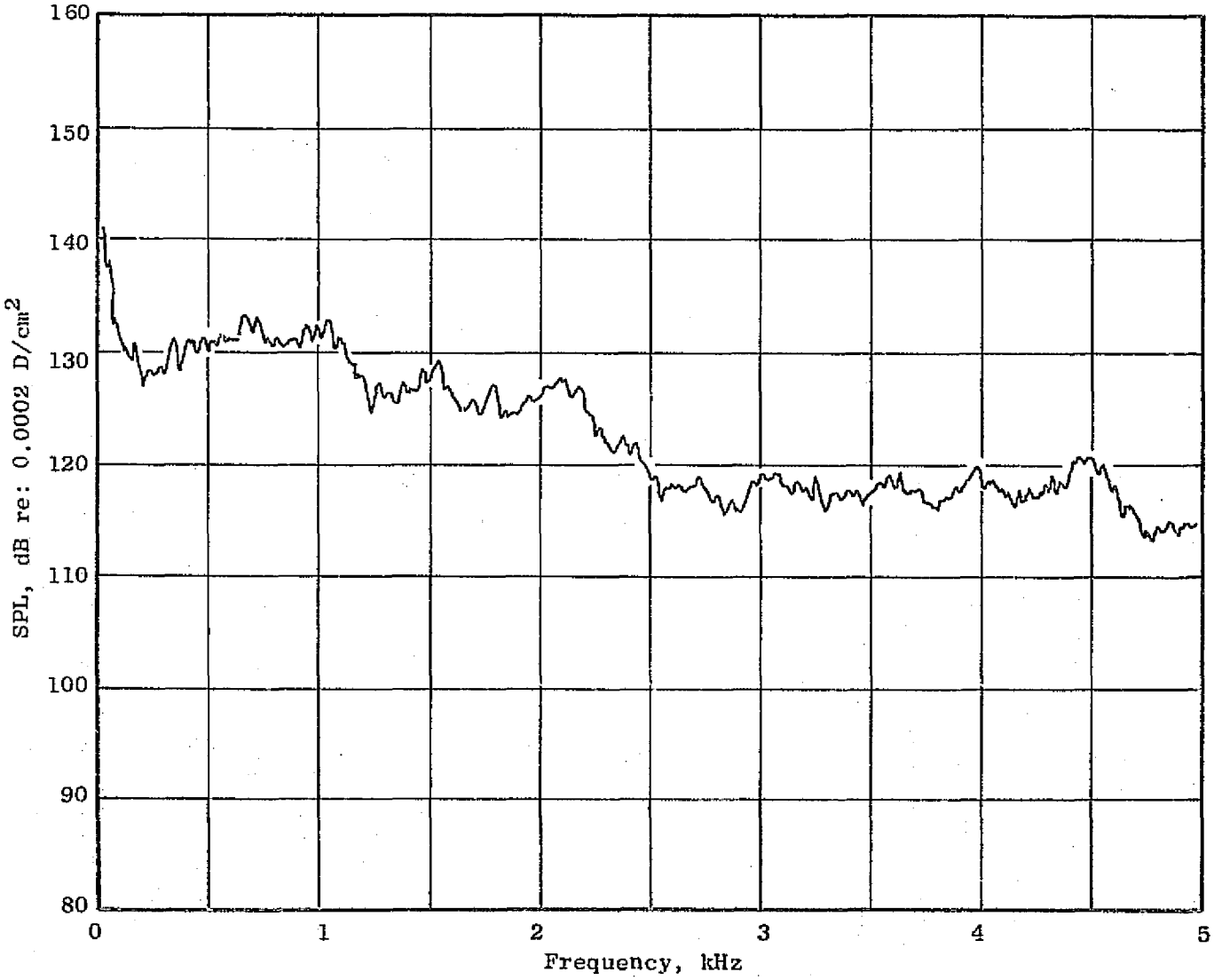

Figure C-47. Configuration D13 Reading 723 Downstream Wall Narrowband Spectrum.

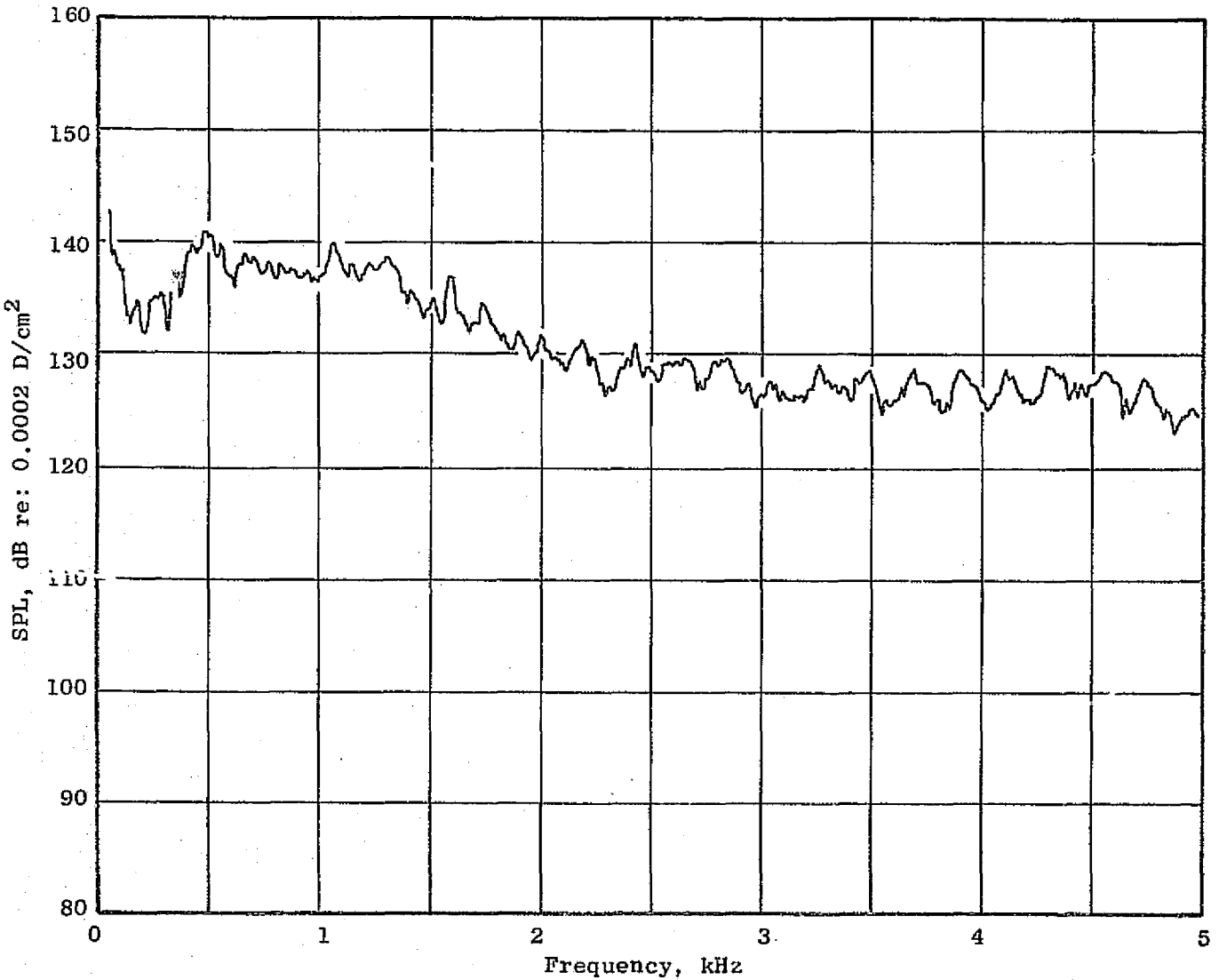

Figure C-48. Configuration D13 Reading 726 Downstream Probe Narrowband Spectrum.

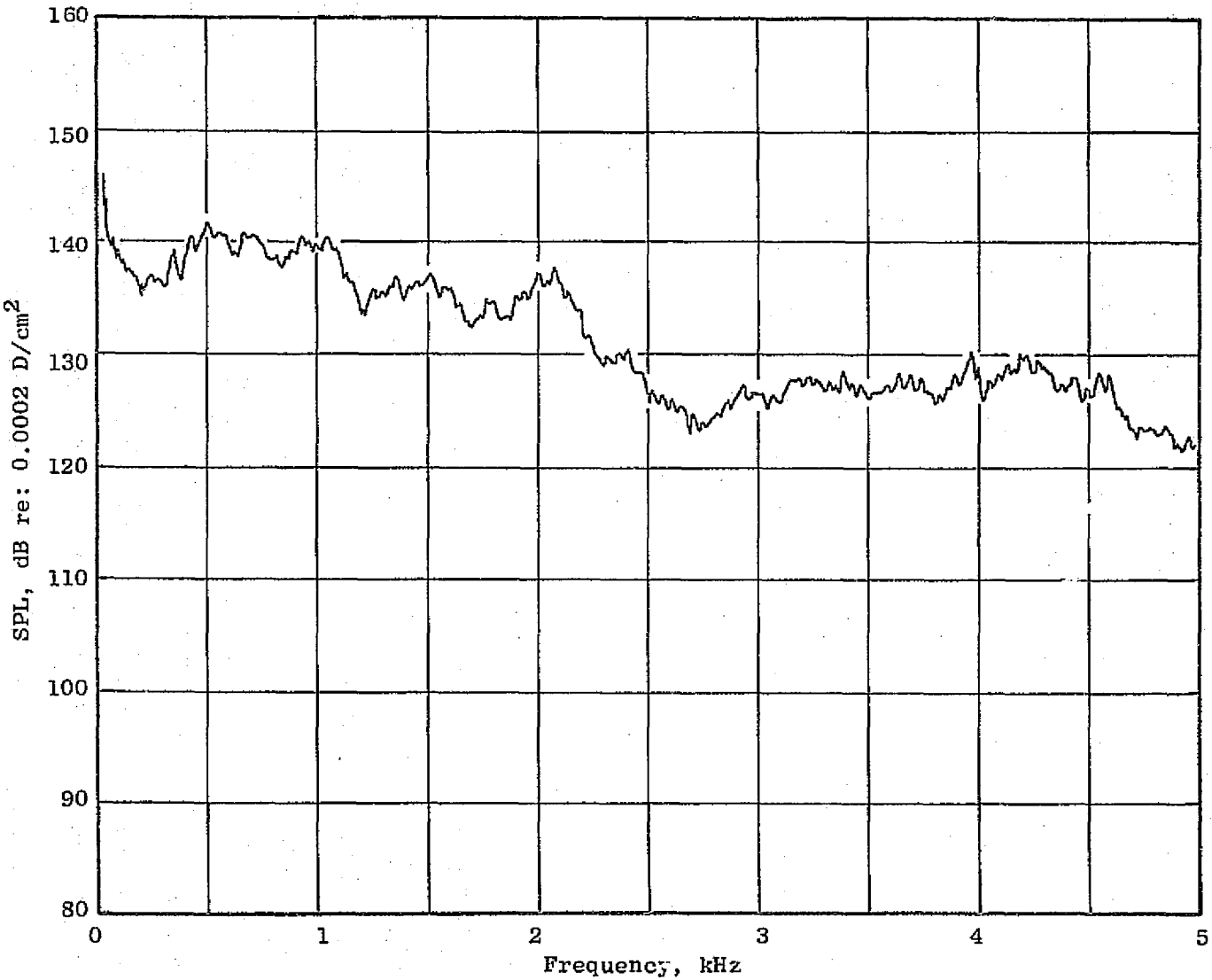

Figure C-49. Configuration D13 Reading 726 Downstream Wall Narrowband Spectrum.

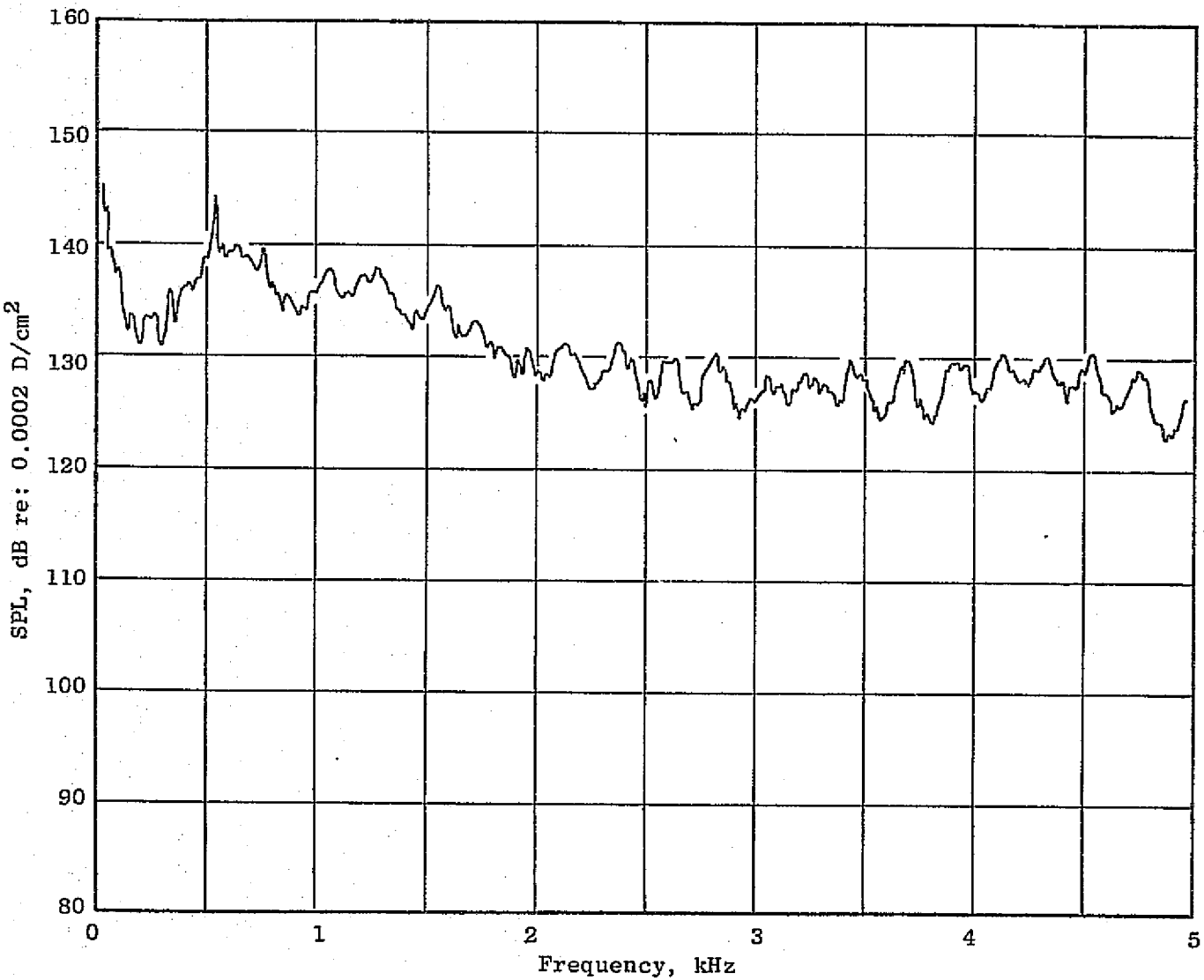

Figure C-50. Configuration D13 Reading 727 Downstream Probe Narrowband Spectrum.

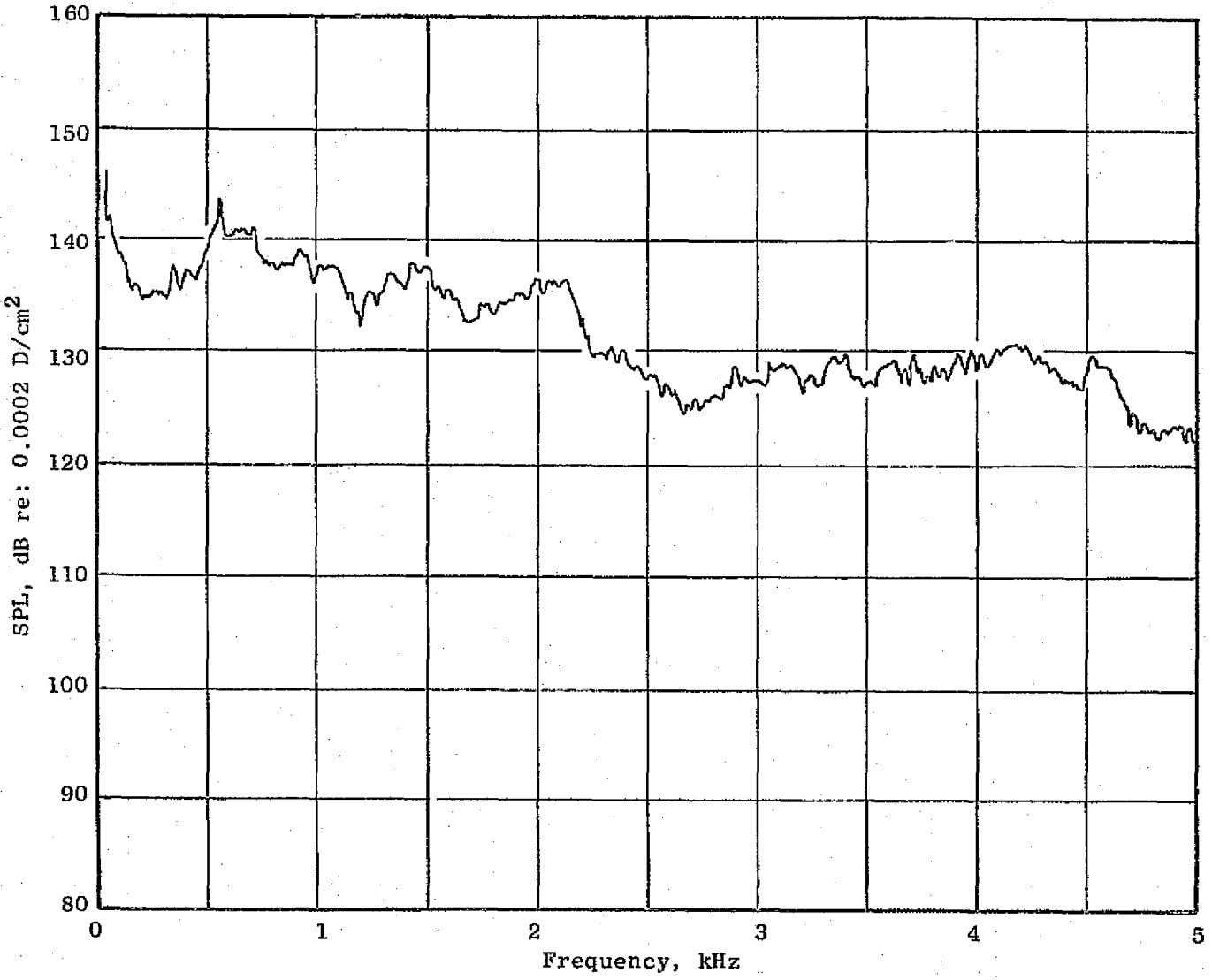

Figure C-51. Configuration D13 Reading 727 Downstream Wall Narrowband Spectrum.

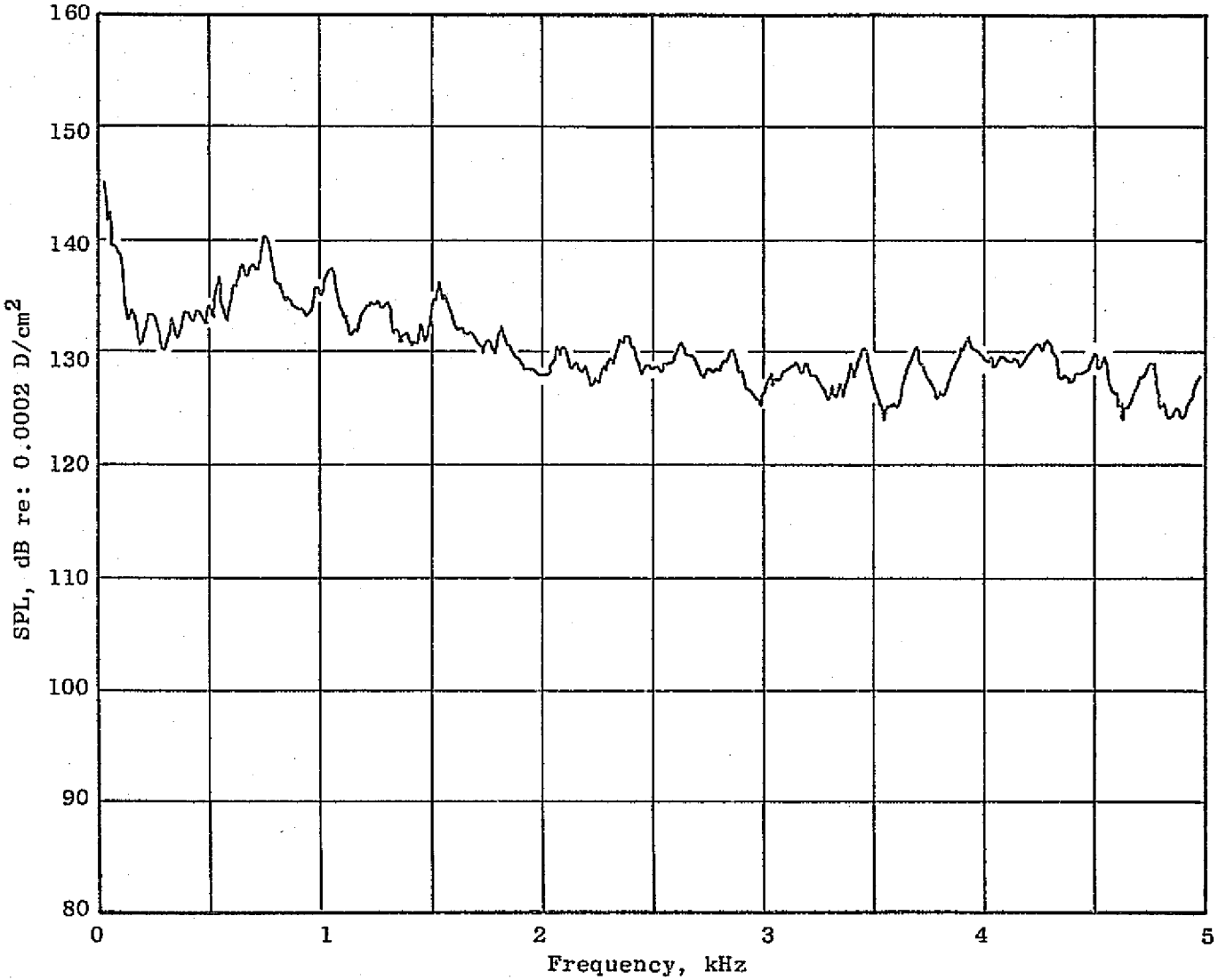

Figure C-52. Configuration D13 Reading 728 Downstream Probe Narrowband Spectrum.

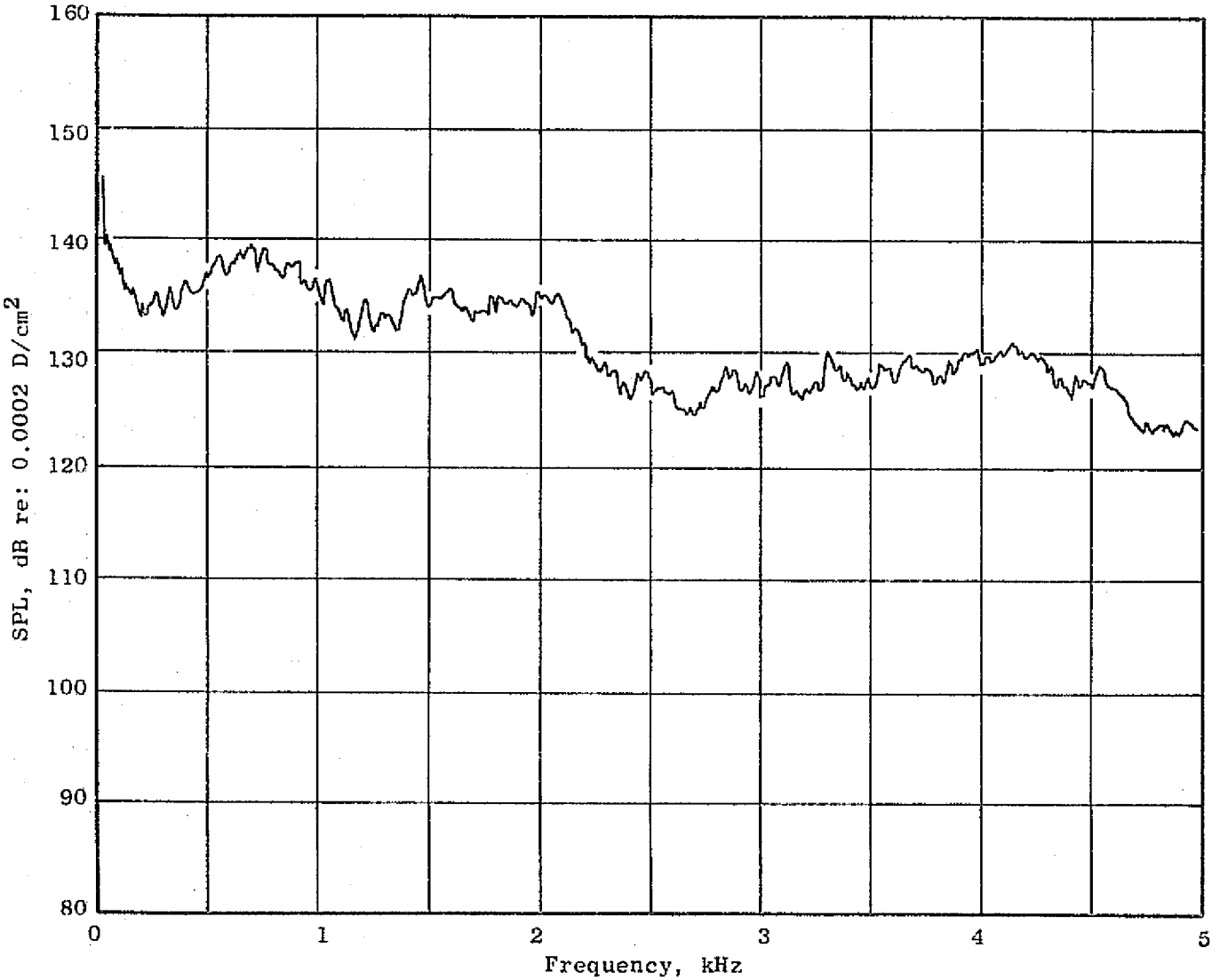

Figure C-53. Configuration D13 Reading 728 Downstream Wall Narrowband Spectrum.

APPENDIX D

BLADE ROW ATTENUATION COMPUTER PROGRAM

The computer program listed here is based on the extended analysis described in Section 7.1.

```
00010 REAL K1,K2,KRA,KXOVKY,M1,M2,M1A,M2A,M1T,M2T
  020 REAL M3A, M4A, M3T, M4T
00030 DIMENSION QQ(100),ATTEN1(100),ATTEN2(100),QQSAVE(100)
00031 DIMENSION X1CORD(100),X2CORD(100),X1(100),X2(100 )
00032 DIMENSION X3(100),Y1(100),Y2(100),Y3(100)
00035 INTEGER E,F
00040 PI=3.1415927 ;GRAV=32.17405 ;CONV=778.26
00050 GAMMA=1.32 ;RGC=0.06854
00060 PRINT:"ABSOLUTE VELOCITIES ARE INPUT IN OPTION 1"
00070 PRINT:"RELATIVE MACH NUMBERS ARE INPUT IN OPTION 2"
00080 PRINT:"SELECT OPTION 1 OR 2  " ;READ: INPUT
00090 IF(INPUT .EQ. 2) GO TO 130
00100 PRINT:"ABSOLUTE VELOCITIES ARE IN FEET/SECOND" ;PRINT 1460
00110 PRINT:"ABSOLUTE FLOW ANGLES ARE IN DEGREES RELATIVE TO FACE PLANE"
00120 PRINT:"  AND NEGATIVE IF FLOW DIRECTION OPPOSITE WHEEL ROTATION"
00130 130 PRINT 1460 ;PRINT:"PRESSURES ARE IN PSIA"
00140 PRINT 1460 ;PRINT:"TEMPERATURES ARE IN DEGREES RANKINE"
00150 150 N=0 ;PRINT 1460
00160 DO 170 I=1,100,1
00170 170 ATTEN2(I)=0.
00180 IF(INPUT .EQ. 2) GO TO 290
00190 PRINT:"INPUT DATA UPSTREAM OF NOZZLE"
00200 PRINT:"AXIAL VELOCITY, ABSOLUTE FLOW ANGLE" ;READ: V1A,PSI1
00210 PRINT:"STATIC PRESSURE, TOTAL TEMPERATURE" ;READ: PS1,TZ1
00220 PRINT:"INPUT DATA BETWEEN NOZZLE AND BUCKET"
00230 PRINT:"AXIAL VELOCITY, ABSOLUTE FLOW ANGLE" ;READ: V2A,PSI2
00240 PRINT:"STATIC PRESSURE, TOTAL TEMPERATURE" ;READ: PS2,TZ2
  250 PRINT:"INPUT DATA DOWNSTREAM OF BUCKET"
00260 PRINT:"AXIAL VELOCITY, ABSOLUTE FLOW ANGLE" ;READ: V3A, PSI3
00270 PRINT:"STATIC PRESSURE, TOTAL TEMPERATURE" ;READ:PS3, TZ3
00280 PRINT:"INPUT WHEEL SPEED(FPS)" ;READ: UW23 ;UW=0.
00290 290 IF(INPUT .EQ. 1) GO TO 420
00300 PRINT:"INPUT DATA UPSTREAM OF NOZZLE"
00310 PRINT:"AXIAL AND TANGENTIAL RELATIVE MACH NUMBERS";READ:M1A,M1T
00320 PRINT:"STATIC TEMPERATURE AND PRESSURE" ;READ: TEMP1,PS1
00330 PRINT:"INPUT DATA DOWNSTREAM OF NOZZLE"
00340 PRINT:"AXIAL AND TANGENTIAL RELATIVE MACH NUMBERS";READ:M2A,M2T
00350 PRINT:"STATIC TEMPERATURE AND PRESSURE" ;READ: TEMP2,PS2
00360 PRINT:"INPUT DATA UPSTREAM OF BUCKET"
00370 PRINT:"AXIAL AND TANGENTIAL RELATIVE MACH NUMBERS";READ:M3A,M3T
00380 TEMP3=TEMP2 ;PS3=PS2
00390 PRINT:"INPUT DATA DOWNSTREAM OF BUCKET"
00400 PRINT:"AXIAL AND TANGENTIAL RELATIVE MACH NUMBERS";READ:M4A,M4T
00410 PRINT:"STATIC TEMPERATURE AND PRESSURE" ;READ: TEMP4,PS4
00420 420 IF(INPUT .EQ. 2) GO TO 440
00430 PSI1=PI*PSI1/180. ;PSI2=PI*PSI2/180. ;PSI3=PI*PSI3/180.
00440 440 N=N+1 ;IF(INPUT .EQ. 2) GO TO 530
00450 V1T=V1A/TAN(PSI1) ;V2T=V2A/TAN(PSI2)
00460 V1=SQRT(V1A*V1A+V1T*V1T) ;V2=SQRT(V2A*V2A+V2T*V2T)
00470 W1A=V1A ;W2A=V2A ;W1T=V1T-UW ;W2T=V2T-UW
00480 W1=SQRT(W1A*W1A+W1T*W1T) ;W2=SQRT(W2A*W2A+W2T*W2T)
00490 AZ1=SQRT(GAMMA*GRAV*RGC*CONV*TZ1)
  500 AZ2=SQRT(GAMMA*GRAV*RGC*CONV*TZ2)
00510 TEMP1=TZ1*(1.-(GAMMA-1.)*(V1A*V1A+V1T*V1T)/(2.*AZ1*AZ1))
```

```
00520 TEMP2=TZ2*(1.-(GAMMA-1.)*(V2A*V2A+V2T*V2T)/(2.*AZ2*AZ2))
  530 530 A1=SQRT(GAMMA*GRAV*RGC*CONV*TEMP1)
00540 A2=SQRT(GAMMA*GRAV*RGC*CONV*TEMP2)
00550 ARA=A1/A2 ;;KRA=1./ARA
00560 IF(INPUT .EQ. 2) GO TO 580
00570 M1A=W1A/A1 ;M2A=W2A/A2 ;M1T=W1T/A1 ;M2T=W2T/A2
00580 580 M1=SQRT(M1A*M1A+M1T*M1T) ;M2=SQRT(M2A*M2A+M2T*M2T)
00590 QTC1=ATAN2(SQRT(1.-M2A*M2A), -M2A)
00600 QTC2=ATAN2(-SQRT(1.-M2A*M2A), -M2A)
00610 GTC1=SIN(QTC1)/(KRA*(1.+M2A*COS(QTC1)+M2T*SIN(QTC1)))
00620 GTC2=SIN(QTC2)/(KRA*(1.+M2A*COS(QTC2)+M2T*SIN(QTC2)))
00630 GTC=GTC1 ;QTC=QTC1 ;M=0
00640 640 M=M+1 ;QQTC=180.*QTC/PI
00650 ATC=(1.-GTC*M1T)*(1.-GTC*M1T)-GTC*GTC
00660 BTC=-2.*GTC*M1A*(1.-GTC*M1T)
00670 CTC=-GTC*GTC*(1.-M1A*M1A)
00680 X=BTC*BTC-4.*ATC*CTC
00690 IF(X .LT. 0.) GO TO 820
00700 DDTC=(-BTC-SIGN(1.,BTC)*SQRT(BTC*BTC-4.*ATC*CTC))/2.
00710 QC=ATAN2(DDTC,ATC) ;QQC=180.*QC/PI ;PRINT 1460
00720 IF(N .EQ. 2) GO TO 740
00730 PRINT;"NOZZLE ATTENUATION" ;PRINT 1460 ;GO TO 750
00740 740 PRINT;"BUCKET AND STAGE ATTENUATION" ;PRINT 1460
00750 750 PRINT;"UPSTREAM CUT-OFF OCCURS AT INCIDENCE ANGLES OF"
00760 CUTOFF=90.+180.*ARSIN(M1A)/PI ;PRINT 1430, CUTOFF
00770 CUTOFF=-CUTOFF ;PRINT 1430, CUTOFF ;PRINT 1460
 0780 PRINT;"DOWNSTREAM CUT-OFF OCCURS AT A TRANSMISSION ANGLE OF"
00790 PRINT 1430, QQTC ;PRINT 1460
00800 PRINT;"THE CORRESPONDING INCIDENCE ANGLE IS"
00810 PRINT 1430, QQC ;PRINT 1460
00820 820 IF(M .EQ. 2) GO TO 840
00830 GTC=GTC2 ; QTC=QTC2 ; GO TO 640
00840 840 IF(M1 .LT. 1. .AND. M2 .LT. 1.) GO TO 860
00850 PRINT;"SUPERSONIC RELATIVE FLOW" ;GO TO 1400
00860 860 IF(N .EQ. 1) GO TO 890
00870 PRINT;"THETA   THETA T   T     V      R   "
00880 GO TO 900
00890 890 PRINT;" THETA I  THETA T    T      V      R    ATTEN"
00900 900 RHORA=PS1*TEMP2/(PS2*TEMP1)
00910 ALPHA=ATAN2(M1T,M1A) ;BETA=ATAN2(M2T,M2A)
00920 GO TO (930, 1050), N
00930 930 QQ(1)=90.+180.*ARSIN(M1A)/PI ;QQMIN=-QQ(1) ;S=10.
00940 QQHOLD=10.*AINT((QQ(1)+10.)/10.)
00950 IF(QQC .LT. 0.) GO TO 980
00960 QQ(1)=-90.-180.*ARSIN(M1A)/PI ;QQMAX=-QQ(1) ;S=-10.
00970 QQHOLD=10.*AINT((QQ(1)-10.)/10.)
00980 980 DO 1040 J=2,100,1
00990 QQ(J)=QQHOLD-S ;QQHOLD=QQ(J)
01000 IF(ABS(QQ(J)-QQC) .LT. ABS(1.1*S)) S=0.1*S
01010 IF(ABS(S) .LT. 0.0001) GO TO 1050
01020 IF(QQC .LT. 0.) GO TO 1040
01030 IF(QQ(J) .GT. QQMAX) GO TO 1050
01040 1040 IF(QQ(J) .LT. QQMIN) GO TO 1050
01050 1050 DO 1330 K=1,100,1
```

```
01060 IF(N .EQ. 1) QQSAVE(K)=QQ(K)
01070 IF(QQ(K) .LT. QQC .AND. N .EQ. 2) GO TO 1330
01080 IF(K .EQ. (J+1)) GO TO 1340
01090 Q=PI*QQ(K)/180.
01100 IF(ABS(QQ(K)) .GT. 0.001) GO TO 1110 ;KXOVKY=100000. ;GO TO 1120
01110 1110 KXOVKY=((1.+M1A*COS(Q)+M1T*SIN(Q))/(KRA*SIN(Q))-M2T)/M2A
01120 1120 QR=ATAN((1.-M1A*M1A)*SIN(Q)/((1.+M1A*M1A)*COS(Q)+2.*M1A))
01130 G=KRA*SIN(Q)/(1.+M1A*COS(Q)+M1T*SIN(Q))
01140 A=(1.-G*M2T)*(1.-G*M2T)-G*G ;B=-2.*G*M2A*(1.-G*M2T)
01150 C=-G*G*(1.-M2A*M2A) ;DD=(-B-SIGN(1.,B)*SQRT(B*B-4.*A*C))/2.
01160 QT=ATAN2(DD,A) ;QQT=180.*QT/PI
01170 T1=ARA*(M2A+COS(QT)) ;V1=ARA ;R1=COS(QR)-M1A ;C1=M1A+COS(Q)
01180 T2=RHORA*(1.+M2*COS(BETA-QT)) ;V2=RHORA*(M2A-KXOVKY*M2T)
01190 R2=M1*COS(ALPHA+QR)-1. ;C2=1.+M1*COS(ALPHA-Q)
01200 T3=SIN(QT-BETA) ;V3=-(SIN(BETA)+KXOVKY*COS(BETA)) ;R3=0.;C3=0.
01210 D= T1*V2*R3+V1*R2*T3+R1*T2*V3-R1*V2*T3-T1*R2*V3-V1*T2*R3
01220 T=(C1*V2*R3+V1*R2*C3+R1*C2*V3-R1*V2*C3-C1*R2*V3-V1*C2*R3)/D
01230 V=(T1*C2*R3+C1*R2*T3+R1*T2*C3-R1*C2*T3-T1*R2*C3-C1*T2*R3)/D
01240 R=(T1*V2*C3+V1*C2*T3+C1*T2*V3-C1*V2*T3-T1*C2*V3-V1*T2*C3)/D
01250 V1A=M1A*A1 ;V1T=M1T*A1 ;V2A=M2A*A2 ;V2T=M2T*A2
01260 Z1=(A1+V1A*COS(Q)+V1T*SIN(Q))*(A1*COS(Q)+V1A)
01270 Z2=(A2+V2A*COS(QT)+V2T*SIN(QT))*(A2*COS(QT)+V2A)
01280 ATTEN=-4.342945*ALOG(T*T*RHORA*ARA*ARA*ARA*ABS(Z2/Z1))
01290 ATTEN2(K)=ATTEN2(K)+ATTEN
01300 GO TO (1310,1320),N
01310 1310 PRINT 1450,QQ(K),QQT,T,V,R,ATTEN ;GO TO 1330
01320 1320 PRINT 1440, QQ(K),QQT,T,V,R,ATTEN,ATTEN2(K),QQSAVE(K)
01330 1330 QQ(K)=QQT
01340 1340 GO TO (1350, 1400),N
01350 1350 IF(INPUT .EQ. 2) GO TO 1380
01360 V1A=V2A ;V2A=V3A ;PSI1=PSI2 ;PSI2=PSI3
01370 PS1=PS2 ;PS2=PS3 ;TZ1=TZ2 ;TZ2=TZ3 ;UW=UW23 ;GO TO 440
01380 1380 M1A=M3A ;M2A=M4A ;M1T=M3T ;M2T=M4T
01390 TEMP1=TEMP3 ;TEMP2=TEMP4 ;PS1=PS3 ;PS2=PS4 ;GO TO 440
01400 1400 PRINT 1460
01410 PRINT: "MORE INPUT? (YES=1, NO=2)  " ;READ: MORE
01420 GO TO (150, 1470), MORE
01430 1430 FORMAT(F10.3)
01440 1440 FORMAT(2F9.3, 5F7.3, F9.3)
01450 1450 FORMAT(2F9.3, 4F7.3)
01460 1460 FORMAT(/)
01465 111 FORMAT(1X,2(F8.3,1X))
01470
01480 1470 CONTINUE
01490 END
```